STUDIES ON LASER PRODUCED TRANSIENT PHOTOPLASMA IN ELECTROMAGNETIC FIELD

By

BISWAJIT JANA

ENROLLMENT NO.: PHYS 01200804022

BHABHA ATOMIC RESEARCH CENTRE, MUMBAI.

A thesis submitted to the Board of Studies in Physical Sciences

In partial fulfillment of requirements for the Degree of

DOCTOR OF PHILOSOPHY

Of

HOMI BHABHA NATIONAL INSTITUTE, MUMBAI

DECEMBER, 2015.

Homi Bhabha National Institute

Recommendations of the Viva Voce Board

As members of the Viva Voce Board, we certify that we have read the dissertation prepared by **Shri Biswajit Jana** entitled "**Studies on Laser Produced Transient Photoplasma in Electromagnetic Field**" and recommend that it may be accepted as fulfilling the dissertation requirement for the Degree of Doctor of Philosophy.

Sudeep Bhattacharjee		11/12/15
Chairman:	**Prof. Sudeep Bhattacharjee**	**Date:**
		11/12/2015
Guide/Convener:	**Prof. A. K. Das**	**Date:**
A Chaturvedi		11/12/15
Member 1:	**Prof. S. Chaturvedi**	**Date:**
Lj Dhareshwar		11/12/15
Member 2:	**Dr. L. J. Dhareshwar**	**Date:**
S Basu		11.12.15
Member 3:	**Prof. S. Basu**	**Date:**

Final approval and acceptance of this dissertation is contingent upon the candidate's submission of the final copies of the dissertation to HBNI.

I hereby certify that I have read this dissertation prepared under my direction and recommend that it may be accepted as fulfilling the dissertation requirement.

Date:

Place:

11/12/2015

Guide: Prof. A. K. Das.

STATEMENT BY AUTHOR

This dissertation has been submitted in partial fulfillment of requirements for an advanced degree at Homi Bhabha National Institute (HBNI) and is deposited in the Library to be made available to borrowers under rules of the HBNI.

Brief quotations from this dissertation are allowable without special permission, provided that accurate acknowledgement of source is made. Requests for permission for extended quotation from or reproduction of this manuscript in whole or in part may be granted by the Competent Authority of HBNI, when in his or her judgment the proposed use of the material is in the interests of scholarship. In all other instances, however, permission must be obtained from the author.

Biswajit Jana

DECLARATION

I, hereby declare that the investigation presented in the thesis has been carried out by me. The work is original and has not been submitted earlier as a whole or in part for a degree / diploma at this or any other Institution / University.

Biswajit Jana

LIST OF PUBLICATIONS ARISING FROM THE THESIS

Journals:

1. "Decay of a finite-sized transient photoplasma in an electric field", B. Jana, A. Majumder, K. B. Thakur and A. K. Das., *Eur. Phys. J. D*. **2015**, *Vol. 69*, 62 (11 pp).
2. "Measurement of photoionization yield in low density barium photoplasma study", B. Jana, P. T. Kathar, A. Majumder, K. B. Thakur and A. K. Das., *Meas. Sci. Technol*. **2014**, *Vol. 25*, 15003 (9 pp).
3. "Design principles of a linear array multi-channel effusive metal vapor source", B. Jana, A. Majumder, K. B. Thakur and A. K. Das, *Review of Scientific Instrument*, **2013**, *Vol. 84*, 106113 (3pp).
4. "Motion of finite-sized low-density photoion bunch in electrostatic potential wells", B. Jana, A. Majumder, P. T. Kathar, A. K. Das and V. K. Mago, *IEEE Transactions on Plasma Science*, **2012**,*Vol.40, Issue.6*, 1643-1649.
5. "Ionization yield of two-step photoionization process in an optically thick atomic medium of barium", B. Jana**,** A. Majumder, P. T. Kathar, A. K. Das and V. K. Mago, *Applied Physics B, Laser and Optics* , **2011**, *Vol. 102*, 841–849.
6. "Effect of electrode temperature on the evolution of photoplasma under electric field", B. Jana, A. Majumder, P.T. Kathar, V.K. Mago, *J.Phys.:conf.ser*, **2010,** *Vol. 208*, 012096 (8pp).
7. "Two dimensional expansion of finite size barium photoplasma in an electrostatic field", A. Majumder, B. Jana, P. T. Kathar, A. K. Das and V. K. Mago, *Phys. Plasmas* , **2008**, *Vol. 15*,123508 (8pp).

Conferences:

1. "Response of electrons in a transient photoplasma to an external electric field", B. Jana, A. Majumder, P. T. Kathar, S. Baruah, G. K. Sahu, K. B. Thakur and A. K. Das, *DAE-BRNS National Laser Symposium (NLS -22), MIT, Manipal University, Manipal, Karnatak,* **January 2014**.
2. "Scaling of ion extraction time with applied potential in finite-sized barium photoplasma study", B. Jana, A. Majumder, P.T. Kathar, S. Baruah, G. K. Sahu, K.B.Thakur and A.K.das, *DAE-BRNS National Laser Symposium (NLS -21), Bhabha Atomic Research Centre, Mumbai;* **January 2013**.

3. "1-D PIC Simulation of Finite-size Transient Photoplasma", B. Jana, A. Majumder, S. Baruah, G. K. Sahu, K. B. Thakur and A. K. Das, *27th National Symposium on Plasma Science & Technology (Plasma-2012), Pondicherry University, Punducherry,* **December 2012**. **(It was selected for the awards of best paper).**
4. "Estimation of photoionization yield in optically thick medium of barium", B. Jana, A. Majumder, P. T. Kathar and V. K. Mago, *DAE-BRNS National Laser Symposium (NLS -19), Raja Ramanna Centre for Advanced Technology, Indore*; **December 2010**.
5. "Motion of finite sized plasma in plate-grid-plate geometry using 1d PIC simulation", B. Jana, A. Majumder, P. T. Kathar A. K. Das and V. K. Mago, *25th National Symposium on Plasma Science and Technology (Plasma-2010), Institute of Advanced Study in Science and Technology, Guwahati,* **December 2010.**
6. "Motion of low-density photoplasma in accelerating zones", B. Jana, A. Majumder, P. T. Kathar and V. K. Mago, *DAE-BRNS National Laser Symposium (NLS -09), Bhabha Atomic Research Centre, Mumbai*; **January 2010.**
7. "Sheath movement on Photoplasma motion under electric field", B. Jana, A. Majumder, P. T. Kathar and V. K. Mago, *DAE-BRNS National Laser Symposium (NLS -08), Laser Science and Technology Centre, Delhi;* **January 2009.**
8. "On re-evaporation of barium and electrical conduction in its vapor in photoplasma studies", A. Majumder, B. Jana, P. T. Kathar, A. K. Das and V. K. Mago. *Proceedings of XXVIII International Conference on Phenomena in Ionized Gases, (ICPIG) Prague,Czech Republic,* **2007,** 1957-59.
9. "Diffusion dominated two-dimensional motion of barium photoplasma between Parallel Plate Electrodes", B. Jana, A. Majumder, P. T. Kathar, A. K. Das and V. K. Mago. *21st National Symposium on Plasma Science & Technology (Plasma-2006), Malaviya National Institute of Technology, Jaipur,* **December 2006.**
10. "Density dependent effects in decay of laser photoionized barium plasma under an electrostatic field",B. Jana, A. Majumder, P. T. Kathar and V. K. Mago, *DAE-BRNS National Laser Symposium (NLS -06), Raja Ramanna Centre for Advanced Technology, Indore*, **December 2006**.

Biswajit Jana.

Dedicated to my grandparents……..

Late Bimala Rani Jana

And

Late Amulya Ratan Jana

ACKNOWLEDGEMENTS

First of all, I would like to express my special appreciation and thanks to my thesis advisor Prof. A. K. Das for his immense knowledge, valuable guidance, motivation and encouragement. I am extremely grateful to Dr. V. K. Mago and Dr. A. Majumder for their constant support, guidance and fruitful suggestions during all the time of research works as well as writing of this thesis. A special thanks to Dr. K. B. Thakur, Dr. K. Dasgupta and Dr. L. M. Gantayet for their continuous support and help to pursue this research work.

I would like to acknowledge my colleague Mr. P. T. Kathar for his kind cooperation and enormous supports during the course of experiments. My special thanks to Dr. K. Patel for his valuable suggestions during the use of his developed two-dimensional particle-in-cell code to validate the experimental results. I extend my thanks to my doctoral committee members: Prof. S. Chaturvedi, Prof. A. K. Chakrabarti and Dr. L. J. Dhareshwar for their encouragement, keen assessment and invaluable suggestions. I would also like to recognize all of my great teachers and professors who taught me the beauty of science and encouraged me to pursue a scientific research work.

I am grateful to my colleagues Dr. G. K. Bhowmick, Dr. Vasdev, Dr. Salesh Kumar, Dr. A. K. Phulani, Dr. G. K. Sahu, Dr. B. Dikshit, Dr. R. C. Das, Dr. M. L. Shah for their valuable suggestions, supports in writing of this thesis. I would also like to thank my colleagues cum friends Dr. S. Baruah, P. Mandal, A. Ghosh, A. Singh, A. Khattar, A. Wahid, T. Garg, D. Saraswat for their help and cooperation during the course of writing this thesis. My sincere thanks to all technical staff of MDRS, LPTD for their help and support required during the course of work.

I am extremely grateful to my father Mr. Sukesh Jana, mother Smt Dulali Jana, father-in-law and mother-in-law for their moral support and numerous blessings. A

special thanks to my brothers (Ranajit and Surajit), brother-in-law (Rinku) and sister-in-law(Jolly) for their love and continuous support to cheer me up. At the end, I am specially thankful to my wife (Mrs Archana) for her endless support, love and inspiration. Without her emotional support and faith in me, it would not be possible to complete this work. I dedicate this work to my little princess (Bhumee) whose smiles always inspired me to do all difficult jobs in an easy manner.

Biswajit Jana

ABSTRACT

Plasma produced through resonant photoionization technique by shining laser pulses onto a collimated atomic beam is known as photoplasma. It is a special class of plasma which is transient in nature and it has a finite size with the sharp plasma density gradients at its boundary. In general, the photoplasma is generated by laser pulses of time duration ~10 ns while it lasts for few tens of microseconds. During its decay in an externally applied electric field, the photoplasma passes through the various transient stages. To investigate its motion in the electrostatic field, both experiments and numerical simulations on barium photoplasma have been carried out in this thesis. The entire works of the thesis are broadly divided into two parts. The first part describes the generation of the finite-sized photoplasma inside a long collimated barium atomic beam. The second part discusses the evolution of photoplasma in the applied external electrostatic field.

A long wedge-shaped and collimated atomic beam of barium has been generated using a collinear array of multichannel effusive source. The barium atomic beam has been characterized by measuring its line of sight averaged atom density at the height of laser-atom interaction region. A finite-sized barium photoplasma has been produced through two-step resonant photoionization method by shining laser pulses onto the collimated atomic beam. To study the kinetics of two-step photoionization process in the optically thick atomic medium of barium, a model based on rate equations has been developed. The estimated photoionization yield from the model is compared with results obtained from the experiments.

The decay of barium photoplasma has been studied under in the applied electrostatic field with different electric field configurations. To understand the dynamics of photoplasma evolution, a fully kinetic one dimensional model based on standard PIC (particle-in-cell) technique has been developed. Using the plate-grid-plate geometry, a

linear electrostatic potential well was created. The motion of low-density barium photoplasma has been studied in the potential well to realize the transition of plasma behavior from its independent particle motion to its collective effect. The experimentally measured photoionization signal has been compared with the results obtained from the PIC model. The various physical processes involved during the transient decay of photoplasma are investigated using the PIC model. In a parallel plate geometry, with the help of a series of Faraday cups placed behind the electrodes, the two dimensional evolution of the photoplasma and photoion audit at different location of the electrostatic-ion-extractor have been carried out. The measured results are compared with 2d PIC simulation.

SYNOPSIS

It is a fact that plasma is the most common form of matter. Very often it is known as the fourth state of the matter. In the universe, more than 99% of the matters are in the plasma state. Plasma is defined as a collection of charge particles along with neutral species. It is macroscopically quasi-neutral and exhibits a collective behavior due to the long range Coulomb interactions among the charged particles. The plasma exists in nature as well as it is produced in the laboratory with wide range of plasma density from 10^{9} m^{-3} to 10^{26} m^{-3} and electron temperature from a fraction of eV to few keV. In nature, the plasma is created at high temperature through the process of thermal ionization, whereas in the laboratory it is produced by the process of either photoionization or electron impact ionization of gas molecules. In the photoionization process, the ionization occurs by absorption of incident photons whose energy is greater than or equal to the ionization potential of the absorbing atoms or molecules. Photoplasma is a special class of plasma which is generated through a technique of multi-step resonant photoionization method by shining the laser lights onto a collimated atomic beam. The neutral atoms resonantly interact with the laser photons of either same color or different colors in multi-step process. They get excited by absorbing the laser photons. When the energy absorbed by the atoms is greater than their ionization energy, they get ionized and produce a pair of electron and ion. Thus it generates the plasma which is known as “photoplasma”.

The multi-step resonant photoionization technique used for generation of the photoplasma is extremely selective and highly efficient. So the photoplasma of a particular element or isotope is produced with a large photoionization yield. The photoplasma finds application in many areas of research and technology like laser based isotope separation through atomic route, purification of materials in nuclear and medical applications, laser based ion source in ion beam technology, plasma based ion

implantations, photoionization spectroscopy and fundamental studies of ultra-cold neutral plasmas. In these above applications, a collimated atomic beam of the alloy or elements under consideration is generated in an evacuated vessel. The atomic beam is illuminated by the appropriate laser lights. The atoms resonantly interact with the incident laser photons and they are selectively ionized to produce the photoplasma of a particular species. The photoions are extracted from the photoplasma in an efficient way by applying an external electromagnetic field. They are collected at a desired location in the ion-extractor. Therefore the photoplasma plays the central role in above applications.

Photoplasma has unique characteristics which are different from that of the conventionally produced thermal plasma and discharge plasma. Usually the photoplasma is generated within a time scale of nano-sec (i.e. laser pulse duration ~ 10 ns) while it lasts for few tens of microseconds ranging from 10-100 μs. So the photoplasma is transient or pulsed in nature. It has a finite size and shape of either rectangular or cylindrical depending on the cross sectional area of the incident laser beams. It is surrounded with the vacuum boundary and it has a sharp plasma density gradient at its boundary. The initial density distribution in the photoplasma depends on the resultant intensity profile of the combined laser beams used in multi-step photoionization method as well as the atom density distributions in the atomic beam. The ion density in the photoplasma is determined by knowing the neutral atom density at the laser-atom interaction region and the ionization yield of the photoionization process. Typically the photoplasma density varies in the range of ~ 10^{12} to 10^{17} m^{-3} with ionization yield of ~ 10^{-2} -10^{-1}. Though the photoplasma is embedded inside the atomic beam, the collisions of charge particles with the neutral background atoms are negligible. Thus the photoplasma behaves like fully ionized plasma. This type of plasma has low electron temperature of ~ 0.1 - 0.5 eV and the charge species are weakly coupled. As the photoplasma is generated

through the photoionization process, the excess absorbed energy of the atom over its ionization energy is shared among the products i.e. electrons and photoions. The mass of electrons are very less compared to that of the photoions and the excess energy mostly goes to the electrons. As a result, all electrons in the photoplasma initially have the same kinetic energy. They get equilibrated through the electron-electron interactions and define the electron temperature in the photoplasma. Since the photoplasma is created inside the atomic beam, it has a bulk motion along the direction of vapor flow and the plasma bulk velocity is nearly equal to the average velocity of atoms in the atomic beam.

In the last few decades, both theoretical as well as experimental studies were carried out on the motion of photoplasma. The studies were focused on the processes of ion extractions from the photoplasma in various ion-extraction regimes over a wide range of plasma density and applied electric field. The photoions were extracted from the finite-sized photoplasma and collected in an efficient manner at a desired location of an ion-extractor. To optimize the ion-extraction efficiency, the evolution of the photoplasma was studied in different electric field configurations these are produced by various geometry like parallel plate geometry, π-type geometry, M-type geometry and plate-grid-plate geometry. The spatial and temporal evolutions of the photoplasma were investigated using laser induced fluorescence (LIF) technique and with the help of electrical current measured on electrodes and Faraday cups placed behind the electrodes. Numerical simulations using both particle-approach and fluid-approach were also carried out to understand the time dependent evolution of the photoplasma as well as to estimate the individual contributions of various mechanisms involved in the decay of photoplasma.

Though the photoplasma is extensively studied in the different field configurations with the wide range of plasma densities, the dynamics of the finite-sized photoplasma evolution and its complex transient behaviors are not clearly understood. During its decay

under an externally applied electric field, the photoplasma undergoes through the various transient stages which are not fully explained. The thesis has mainly concentrated on the evolution of the finite-sized transient photoplasma in an applied electrostatic field. The aim is to investigate the various physical processes involved in the transient decay of the photoplasma and to study the photoion extraction from the photoplasma in the electrostatic ion-extractors. Starting from the atomic beam generation and photoplasma production through resonant photoionization process, the evolutions of photoplasma in the electrostatic ion-extractors have been investigated in details.

The works under the thesis have been broadly divided into two parts. In the first part, it is discussed the generation of a long wedge-shaped barium (Ba) atomic beam and production of photoplasma inside the atomic beam through two-step resonant photoionization method. In experiments, barium element has been chosen because of two reasons. The barium has reasonable vapor pressure at relatively lower elevated temperature (~ 1000 K). The atomic beam of high neutral atom density is easily produced. Also its low lying electronic energy levels have the large values of excitation cross-sections. They are readily accessed by the wavelengths of commercial lasers to produce the photoplasma through two-step resonant photoionization. In the second part, the evolution of photoplasma in the externally applied electrostatic field is described. A linear electrostatic potential well is created by the plate-grid-plate geometry. The motion of low-density photoplasma is studied inside the potential well and it is highlighted the transition of plasma behavior from the single particle kinetics to its collective phenomena. A fully kinetic 1d model based on particle-in-cell (PIC) simulation is developed to study the dynamics of photoplasma under the constant electromagnetic field. During its transient decay in the electric field, the finite-sized photoplasma passes through the various physical processes. They are investigated using the PIC model. Two dimensional

features of the photoplasma motion are investigated in the electrostatic ion-extractor produced by parallel plate configuration. The contributions of various processes in two dimensional motion of the photoplasma have been quantified.

The thesis is organized in nine chapters to discuss the different aspects of the present work in a systematic manner. The contents of the chapters are summarized as follows.

The chapter 1 provides a general introduction to the laser produced transient photoplasma and its study in an electromagnetic field. The unique characteristics of the photoplasma are stated. Its primary role in the process of laser based isotope separation via atomic route is discussed along with a brief summary of literature survey on its study. The salient features of its motion under the externally applied various electric field configurations are briefly explained. The use of various diagnostic techniques like simple current measurement on electrodes, Faraday cups and sophisticated technique of laser based fluorescence are described to identify the various decay processes during its evolutions in the two dimensions. The theoretical studies of computer simulations which are applied to understand the complex behavior of the photoplasma are also discussed. The problems of the thesis work is defined and elucidated in subsequent chapters.

The chapter 2 describes the details of the experimental set-ups used for the barium photoplasma study in the electrostatic field. It consists of various sub-systems. They are (i) experimental chamber, (ii) atomic vapor source with resistively heated furnace to produce a long wedge-shaped atomic beam, (iii) hollow cathode lamp based absorption set-up to characterize the atomic beam, (iv) laser systems to generate the photoplasma, (v) electrostatic ion-extractor for evolution of the photoplasma and (v) various diagnostic tools to study the photoplasma decay. Two types of ion-extractors are used in the present study. In the first case, a linear electrostatic potential well is produced by plate-grid-plate

configuration whereas in second case, two parallel plate electrodes create the uniform electric field. The designing features of the different sub-systems used in the experiments and their role to investigate the photoplasma motions are discussed.

The chapter 3 deals with the generation and its characterizations of a long wedge-shape barium atomic beam. A linear array multichannel atom source has been designed to produce the atomic beam. Based on the design parameters, the crucible lid has been fabricated. The pieces of barium metal are kept inside the crucible and the crucible is heated by a resistively heated furnace. The atoms are effused through the channels and collimated by a set of linear slits. Thus it forms the vertically expanding wedge-shaped atomic beam. An attempt has been made theoretically to characterize the atomic beam in the collision-free vapor flow regime. At a height of ~ 70 mm from the crucible lid (i.e. at the laser-atom interaction region) the various parameters of the atomic beam like its length, width, average neutral atom density and the distribution of density along its length have been calculated. An absorption setup based on hollow cathode lamp (HCL) has been developed where the Ba-Ar HCL is used as the emission source. The line of sight integrated average barium atom density in the atomic beam is measured at different crucible temperatures. The measured values agree in well with the values obtained from the theory.

The chapter 4 talks about the generation of barium photoplasma using two-step resonant photoionization schemes and the kinetics of two step photoionization process. In the first step, the Ba atoms get resonantly excited from their ground state ($6s^2$: $^1s_0$) to an intermediate excited state (6s6p: $^1p_1$) by 553.5 nm radiation. The resonant line is obtained from a dye laser pumped by the second harmonic of Nd: YAG laser. In the second step, the excited atoms are subsequently ionized from their excited state (6s6p: $^1p_1$) to continuum by absorbing the 355 nm radiation of Nd: YAG laser. The two laser beams are

propagated collinearly and overlapped with the atomic beam to generate the photoplasma inside the atomic beam. A model based on the rate equation approach has been developed to study the kinetics of two-step photoionization process in the optically thick atomic medium of barium. In the model, the absorption of exciting radiation is taken into account along its propagation direction (optically thick). Whereas the atomic medium is assumed to be optically thin for the ionizing radiation as the photoionization cross-section has very low value compared to that of bound to bound level excitation. Numerical simulations are carried out to estimate the ionization yield for the time varying Gaussian shaped laser pulses. The required energy density of the laser pulse is estimated to saturate the excitation transition throughout the entire thick atomic medium. The effect of the optical delay between two laser beams on the ionization yield is also simulated. The calculated ionization yields from the simulations are compared with the measured values from the experiments.

The chapter 5 discusses the development of one dimensional model based on particle-in-cell technique (1d PIC) to study the decay of a finite-sized transient photoplasma in the applied electric and magnetic field. The photoions and electrons of the photoplasma are represented by super-particles. The computational volume (i.e. a linear box in one dimension) is discretized into grids by sets of uniformly spaced points. At grid points, the charge density is calculated from the particle's positions by applying first-order linear weighting scheme. Using the charge density, the Poisson's equation is solved to get the potentials at different grid points. The forces on the super-particles are calculated using the Lorentz equation. The velocity and position of the particles are estimated by solving Newton's equation of motion using the leap-frog integration method. The iterative execution of the above steps self-consistently calculates the electric field due to both space charge field and external electric field. Thus it describes the

evolution of the photoplasma in the externally applied electromagnetic field. The temporal and spatial variations of various parameters like distribution of density, potential, electric field, energy, particles' positions, velocities are saved in the files for the post-run analysis.

The chapter 6 presents the motion of low density barium photoplasma in a linear electrostatic potential well created by the plate-grid-plate geometry. The experimentally observed photoionization signal is compared with the results obtained from the PIC model. The observations show that for density range ~ ($1x10^{13}$- $3x10^{14}$) m^{-3}, the applied electric field ($\leq 1x10^{4}$ V/m) is sufficient to remove all the electrons from the photoplasma within a time of few ns. As a result the photoion-bunch remains left and it evolves in the linear potential well. A damped oscillation is observed on the current signal recorded on grid electrode. The structure of current signal is explained by the single particle behavior of the photoion bunch. For densities > $3x10^{14}$ m^{-3}, the frequency of oscillation in potential well depends on both the externally applied electric field and the internal field produced by the space-charge interactions among the charge particles. As the plasma density increases, the collective behavior of the plasma dominates and the dynamics of charge particle motion is governed by the space charge interactions. Thus the transition of single particle motion to plasma collective behavior as the plasma density increases is realized by studying the motion of photoplasma in the linear potential well.

The chapter 7 discusses the various physical processes involved in decay of the finite-sized photoplasma under an electrostatic field. The mono-energetic electrons produced in the photoplasma get equilibrated through the electron-electron collisions. The plasma space potential initially oscillates with plasma electron frequency and it attains a stable value close to the anode potential. Within a few cycles of plasma electron oscillation, an electron sheath is formed between the anode plate and the plasma

boundary. The plasma is polarized in a fashion so that the internal field in plasma shields the applied external electric field. Therefore the entire applied potential drops between the plasma and the cathode. Towards the cathode, the photoions move and form a sheath of photoions and their motion is governed by the space-charge limited Child-Langmuir law. The Child-Langmuir flux at the plasma-sheath boundary is supplied by the Bohm flux in the plasma region. The difference in the value of Bohm flux and Child-Langmuir flux at the plasma-sheath boundary governs the motion of plasma-sheath boundary. Due to the ambipolar diffusion, the finite-sized plasma expands toward the anode. As the photoplasma decays with time, its density decreases. The plasma sheath boundary moves towards the plasma region i.e. in the opposite direction of the photoion motion to balance the Child-Langmuir flux. Initially the sheath boundary moves fast, stagnates and again moves slowly away from the cathode surface. As the density further decreases with time, the plasma (i.e. collections of charge particles) is unable to shield the external potential. Hence it behaves like single charge particle. The processes of ion-extraction from the photoplasma in an electrostatic-ion-extractor are investigated. The efficiency of photoion collection on the electrodes is studied over the wide range of plasma density and applied electric field.

The chapter 8 describes the two dimensional features of photoplasma evolutions in the electrostatic ion-extractor. The distributions of photoions due to plasma expansion in 2d are studied using a series of Faraday cups placed behind the cathode along the central vertical line. The ions audit at different locations of the ion-extractor are also examined both experimentally and using 2d PIC model. Several physical processes like bulk motion, ambipolar diffusion, bounded diffusion, Coulomb repulsion, Child–Langmuir flux which contribute in the extraction of photoions from the photoplasma have been identified. Their relative contributions are also quantified with the help of

photoionization signals recorded on electrode and Faraday cups. The results are compared with the 2d PIC simulations. These processes are superimposed and their relative magnitudes decide the evolution of the photoions. When the external field dominates, a significant fraction of photoions reach the cathode with negligible vertical spread. The plasma motion can be considered as one-dimensional. However, when the plasma collective effects are dominant, then the different mechanisms become comparable and the photoplasma expands in two dimensions. The spread of photoions at different locations in the electrostatic ion-extractor has been determined as a function of plasma density.

The chapter 9 concludes with a summary of works and discusses briefly the future directions of the photoplasma study. The achievements of the works under thesis are summarized as follows.

- A linear array multichannel effusive metal vapor atom source has been designed to produce a long wedge-shaped high density effusive atomic beam.
- A model using rate equations has been developed to study the two-step resonant photoionization (TSRPI) process in an optically thick atomic medium of barium.
- The kinetics of TSRPI process on barium has been studied and the model has been validated with the experimentally measured photoionization yield.
- A one dimensional model based on particle-in-cell (PIC) simulations has been developed to study the decay of finite-sized photoplasma in the externally applied electrostatic field.
- The transition of plasma behavior from the single particle regime to plasma regime has been observed in the experiments as the plasma density increases.
- The various physical processes involved in decay of the photoplasma like thermalization of mono-energetic electrons, oscillation of plasma space potential

before attain a stable value close to the anode potential, formation of electron sheath and photoion sheath, motion of plasma-sheath boundary, plasma expansion have been investigated.

- The two dimensional evolutions of the finite-sized photoplasma in the electrostatic ion-extractor has been studied using 2d- PIC code developed in our group and the code has been validated with the experiments done on the barium photoplasma.
- The relative contributions of processes like bulk motion, ambipolar diffusion, bounded diffusion; Coulomb repulsion and Child-Langmuir flux involved in the 2d evolutions have been quantified.

The most of the results under the thesis work are published in the peer reviewed journals.

LIST OF FIGURES

Figure no.	Figure Captions	Page no
Figure 1.1:	Several ionization schemes involved in multi-step resonant photoionization method.	**5**
Figure 1.2:	Listing of physical processes occurred in atomic vapor laser isotope separation method.	**9**
Figure 1.3:	Different types of geometry used in photoplasma study: (a) Parallel plate geometry, (b) PI type geometry, (c) M type geometry and (d) Plate-grid-plate geometry.	**17**
Figure 1.4:	Overviews of works carried out in the thesis	**20**
Figure 2.1:	Schematic linkage of various sub systems used in photoplasma study.	**24**
Figure 2.2:	Isometric view of various components in the atomic vapor generating source.	**26**
Figure 2.3:	Photographs of crucible lid with different sized holes, collimating slits and resistively heated electrical furnace.	**28**
Figure 2.4:	Schematics of a hollow-cathode lamp based optical absorption set-up for measurement of atom-density in a long wedge-shaped atomic beam.	**30**
Figure 2.5:	Schematics of laser systems and laser beam transportations for generation of barium photoplasma through two-step resonant photoionization schemes.	**32**
Figure 2.6:	Electrostatic in-extractor produced by two parallel plate electrodes along with electrical circuit diagrams to measure the photoionization signals.	**33**
Figure 2.7:	Schematic layout of plate-grid-plate assembly along with signal detection circuit and atomic vapor generating furnace.	**35**
Figure 2.8:	Schematics of plate-plate ion-extractor along with Faraday cups for studying the two dimensional evolution of the photoplasma.	**36**
Figure 2.9:	Photograph of Faraday cups arrangements placing behind the electrodes in parallel plate assembly.	**37**

Figure 3.1:	Schematics of geometrical configurations for estimating the neutral atom density at any point P from a multi-channel atom source.	**42**
Figure 3.2:	Normalized angular distributions of atoms effused through a single cylindrical channel for different β values of the channel.	**44**
Figure 3.3:	Variation of half width at half intensity (i.e. $\theta_{1/2}$) of angular distribution as a function of β.	**45**
Figure 3.4:	Variations of channel's transmission probability with its aspect ratio (β).	**46**
Figure 3.5:	Density distribution profile along the length of atomic beam: (a) single channel of β=0.4, (b) three identical channels of β=0.4 and (c) channels with centre one having larger aspect ratio of β=0.8.	**47**
Figure 3.6:	(a) Variation of beam-width (FWHM) and (b) average atom density with relative distance between the central channel and the end channels for the case of Fig. 3.5 (c).	**48**
Figure 3.7:	Density distributions along the length of atomic beam from a collinear array of 31 channels. (data points are from the experiments)	**49**
Figure 3.8:	Average atom density at various heights from the source.	**50**
Figure 3.9:	Effect of collimating slit in the spatial density distribution of atomic beam along its length direction.	**51**
Figure 3.10:	Distributions of atom density along the width of atomic beam produced by collinear array.	**52**
Figure 3.11:	Crucible temperature at different electrical power fed to the resistively heated furnace. Same is plotted in log-log scale (inset).	**53**
Figure 3.12:	Variation of neutral vapor density inside the crucible (i.e. vapor reservoir) with its temperature.	**54**
Figure 3.13:	Variation of absorbance 'A_s' with optical density (i.e. K_0L) for various value of γ.	**58**
Figure 3.14:	Emission profile of barium 553.5 nm resonant line when Ba-	**59**

HCL is operated at ~15 mA current.

Figure 3.15: Relative instrumental error (i.e. $\Delta n/n$) in measurement of atom density against the absorption coefficient as the intensity is measured by photo-emissive detector like PMT. **60**

Figure 3.16: Measured average atom density in the laser-atom interaction region at different source temperature. **61**

Figure 4.1: (a) Low-lying singlet energy levels of BaI and (b) geometry for laser-atom interaction involved in two-step photoionization process. **66**

Figure 4.2: (a) Schematic of laser-atom interaction region. 1. Crucible, 2. Atomic beam, 3. Laser beams, 4. Photoplasma, 5.Parallel plate electrodes (b) Width view. **67**

Figure 4.3: Temporal profile of 355 nm pulse from the third harmonic of Nd-YAG laser. **68**

Figure 4.4: Typical photoionization signal recorded on the cathode plate biased at -500 V with crucible temperature of ~ 850 K. **71**

Figure 4.5: Measured photoions collected on the cathode plate at different applied electric field. **71**

Figure 4.6: (a) Variation of excitation energy density and (b) the corresponding change in photoionization yield along the length of thick medium, $N_0 \sigma_1 L_0 \sim 1$ for $N_p \sim 1$. **76**

Figure 4.7: Variation of average photoionization yield with incident number of photons per atom (i.e. N_p) for an optically thick medium of $N_0 \sigma_1 L_0 \sim 1$. **77**

Figure 4.8: Variation of ionization yield with time delay between two co-propagating laser beams. **78**

Figure 4.9: Time dependent variation of normalized population density in ground state (n_0), excited state (n_1) and ionized state (n_i) with the measured values of different experimental parameters. **79**

Figure 5.1: Schematics of one dimensional computational linear box discretized into uniformly spaced grid points. **86**

Figure 5.21: A computational cycle for one time step in a particle simulation program. The grid points are numbered as i=0, 1, 2…N and the particles are numbered as j = 1, 2, …..N_P. **87**

Figure 5.3: Sketch of leap-frog integration method showing the time-centering of force F while advancing velocity (v) and that of 'v' while advancing position (x). **89**

Figure 5.4: The V_x, V_y plane showing the magnetic force q(vxB) force normal to **V** which results in a rotation of **V** with no change in speed with $\frac{d\theta}{dt} < 0 \; for \; \left(\frac{q}{m}\right) > 0, B_0 > 0$. **91**

Figure 5.5: Backward movement of particles' initial velocity by a half time-step (shown by solid line) using the field at time t=0 to fit in the time flow in leap-frog method. **92**

Figure 5.6: Charge assignment to grid points from particle's position using the first order linear charge weighting scheme. **94**

Figure 6.1: Potential distribution in symetric potential well (a) and asymmetric potential wells (b and c).obtained from analytical solution (⋯⋯) in absence of ion bunch, PIC simulation (——) with ion-bunch of density ~$2x10^{13}$ m^{-3} **104**

Figure 6.2: Trajectory of photoion in phase-space plane for different potential wells shown in figure 6.1. **105**

Figure 6.3: Time dependent current signal recorded on various electrodes when the photoion bunch of density ~ $2x10^{13}$ m^{-3} is evolved in the symetric potential well as shown in figure 6.1(a): ⋯⋯ analytical solution, ---------- PIC simulation and —— experiement. **107**

Figure 6.4: Current signal of grid electrode when the photoion bunch of density ~ $2x10^{13}$ m^{-3} is undergone in an assymetric potential well shown by figures 6.1(b) and 6.1(c): ⋯⋯ analytical solution, ---------- PIC simulation and —— experiement. **108**

Figure 6.5: Photoion current signal measured on grid electrode for different width of photoion bunch of density ~ $2x10^{13}$ m^{-3} evolved in **109**

symetric potential well shown by figure 6.1(a): _____ experiment and --------- PIC model.

Figure 6.6: Variation of oscillation frequency with the applied negative voltage on grid for the photoplasma of density $1x10^{14}$ m^{-3} evolves in symetric potential well. **111**

Figure 6.7: Variation of oscillation frequency with plasma density during the evolution of photoplasma in symmetric potential well produced by biasing -500 V on the grid electrode. **112**

Figure 7.1: Density distribution of plasma particles in photoplasma between two electrodes at t=0. **116**

Figure 7.2: Velocity distribution functions of plasma electrons at time: (a). t = 0, (b). $t = 5\omega_{pe}^{-1}$, (c). $t = 5x10^{1}\ \omega_{pe}^{-1}$ and (d). $t = 1x10^{2}\ \omega_{pe}^{-1}$. The fitted one dimensional Maxwell velocity distributions are shown by red color. **117**

Figure 7.3: Temporal variation of electrons' average thermal energy when the applied electric field is (a) $E_0 = 0$, (b) $E_0 \sim 2.8x10^{3}$ V/m and (c) $E_0 \sim 1.4x10^{4}$ V/m. **118**

Figure 7.4: Oscillatory motion of the plasma space potential before it attains a stable value close to the anode potential. **120**

Figure 7.5: Spatial variations of potential profile between two electrodes before obtaining a stable profile. **121**

Figure 7.6: Density distribution of plasma electrons (n_e) and photoions (n_i) at time $t = 1x10^{2}\ \omega_{pe}^{-1}$. **122**

Figure 7.7: Distribution of (a) electron density (n_e) and photoion density (n_i), (b) potential and electric field at time $t = 4x10^{3}\ \omega_{pe}^{-1}$. **124**

Figure 7.8: Time dependent (a) position and (b) velocity of the plasma-sheath boundary during the decay of photoplasma. **126**

Figure 7.9: Distributions of electron density (n_e), photoion density (n_i) and potential near sheath boundary at time (a) $t = 2x10^{4}\ \omega_{pe}^{-1}$, (b) $t = 4\ x10^{4}\ \omega_{pe}^{-1}$, (c) $t = 6\ x10^{4}\ \omega_{pe}^{-1}$, (d) $t = 8\ x10^{4}\ \omega_{pe}^{-1}$. **128**

Figure 7.10: Temporal variations of simulated currents obtained from 1d PIC model: (a). photoion current to the cathode (I_{iC}), (b). photoion **129**

current to the anode (I_{iA}), (c). electron current to the anode (I_{eA}) and (d). total current on the cathode ($I_T = I_{iC} - I_{iA} + I_{eA}$).

Figure 7.11: Normalized fraction of total photoions collected on the cathode and anode plate at different normalized density (ρ). (Simulations, data points are from the experiments). **132**

Figure 8.1: Various mechanisms contributing to two-dimensional expansion of photoplasma. 1: bulk motion, 2: ambipolar free diffusion, 3: Coulomb repulsion, 4: Child-Langmuir flux and 5: bounded diffusion. **137**

Figure 8.2: Temporal variation of current signal as recorded by Faraday cups with photoplasma density ~ $5x10^{15}$ m^{-3} and applied potential ~ 100 volts. **139**

Figure 8.3: Measured photoion current signal on top plate while the photoplasma of density ~ $2x10^{15}$ m^{-3} decays in absence of electric field. **141**

Figure 8.4: Distribution of photoions over the Faraday cup locations in the vertical direction at different ρ values. (Red lines represent the results of 2d simulation and data points are from experiments). **142**

Figure 8.5: PIC simulated temporal dependence of uncompensated ions responsible for Coulomb repulsion. **144**

Figure 8.6: Photoions collected on the cathode and the anode plate as sampled by Faraday cups placed behind the electrode for different ρ values. **146**

Figure 8.7: Snapshots (a-k) of the 2d evolution of photoplasma at different time obtained from PIC simulation. (Green dots represent electrons and red dots represent photoions). **147**

LIST OF TABLES

Table 4.1:	Comparisons between experimentally measured and numerically estimated ionization yield of two-step photoionization process	**81**
Table 7.1:	Input parameters for 1d PIC simulations of the finite-sized photoplasma	**115**
Table 7.2	Calculated plasma parameters of the above photoplasma	**115**
Table 8.1:	Percentage distribution of photoions on different locations as a function of plasma density when +1kV is applied. The values have error of ~10%. The values in parenthesis are that of 2D-PIC simulation	**150**

CONTENTS

Abstract **x**

Synopsis **xii**

List of Figures **xxiii**

List of Tables **xxix**

1. Introduction **1**

1.1 Photoplasma 2

1.2 Unique Characteristics of Photoplasma 2

1.3 Multistep Resonant Photoionization method 3

1.4 Applications of Photoplasma 7

1.4.1 Laser based Isotope Separation 7

1.4.2 Purification of Metals 9

1.4.3 Laser Ion Source 10

1.4.4 Ultra-Cold Neutral Plasma 11

1.5 Literature Survey on Photoplasma Study 13

1.5.1 Photoion Extraction by Electrostatic field 13

1.5.1.1 Theoretical Study 13

1.5.1.2 Experimental Observations 14

1.5.1.3 Numerical Simulations 15

1.5.2 Different Electric Field Configurations 16

1.5.3 Photoion Extraction by RF Resonance Electric Fields 18

1.5.4 Photoion Extraction by Electromagnetic Fields 19

1.6 Scope of Thesis 19

1.7 Organization of the Thesis 21

2. Experimental Systems for Photoplasma Study **23**

2.1 Experimental Set-up 23

2.2 Experimental Chamber 24

2.3 Atomic Vapor Source 25

2.4 Atom Density Measurement Setup 28

2.5 Laser Systems 30

2.6 Electrostatic Ion-Extractors 32
2.6.1 Plate-Grid-Plate configuration 34
2.6.2 Plate-Plate Configurations 35
2.7 Summary 37

3. Long Collimated Atomic Beam: Design, Generation and its Characterization
3.1 Introduction 39
3.2 Design Principles of a Linear Array Multichannel Atom Source 41
3.2.1 Collision-Free Flow through a Cylindrical Channel 41
3.2.2 Flow Characteristics of a Single Channel 43
3.2.3 Linear Array of Channels 45
3.2.4 Inter -Channel Separation 47
3.2.5 Linear Array Multichannel Atom Source 48
3.2.6 Average Atom Density with Height from Source 50
3.2.7 Effect of Collimating Slits 51
3.3 Generation of a Long Wedge-Shaped Atomic Beam 53
3.4 Methodology of Atom Density from Optical Absorption Method 55
3.5 Measurement of Averaged Atom Density inside the Atomic Beam 57
3.6 Summary 62

4. Photoplasma Generation and Estimation of Photoionization Yield 63
4.1 Introduction 63
4.2 Two-Step Photoionization Method 64
4.3 Relevant Atomic Parameters of Barium 65
4.4 Experiments 67
4.4.1 Generation of Barium Photoplasma 67
4.4.2 Estimation of Ion Density from Charge Collection Method 69
4.5 Kinetics of Two-Step Photoionization Process 72
4.5.1 Formulation of Rate Equations 72
4.5.2 Numerical Simulation 74
4.5.3 Features of Optically Thin/ Thick Medium 75
4.5.4 Effect of Time Delay between Pulses 77
4.5.5 Population Dynamics of Barium Atoms 79
4.6 Comparison of Photoionization Yield 80

4.7 Summary 81

5. Developed One Dimensional Plasma Model Based on PIC Technique 83

5.1 Introduction 83

5.2 Formulation of Mathematical Problem 84

5.3 PIC Simulation 85

5.4 Integration of Field Equation 88

5.5 Integration of Equations of Motion 89

5.6 Charge Assignment 89

5.7 Field Interpolation 95

5.8 Simulation Algorithm 95

5.9 1D PIC Code 97

5.10 Summary 98

6. Motion of Low-density Photoplasma in a Linear Electrostatic Potential Wells

6.1 Introduction 100

6.2 Theoretical Description 101

6.2.1 Analytical Solution 101

6.2.2 PIC simulation 102

6.3 Removal of Electrons from Low-Density Photoplasma 103

6.4 Motion of Ion Bunch in Potential Wells 104

6.5 Experimental Observations 106

6.6 Effect of Photoplasma Width 109

6.7 Space-Charge Effect(Collective Behavior) 110

6.8 Summary 113

7. Decay of Photoplasma in an Electrostatic Field 114

7.1 Introduction 114

7.2 Input Parameters to PIC simulation 114

7.3 Relaxation of Electrons' Velocity Distribution 116

7.4 Transient Effect in Plasma Potential 119

7.5 Formation of Photoion-Sheath and its Structure Analysis 123

7.6 Motion of Plasma-Sheath Boundary 125

7.7 Plasma Expansion towards Anode 127

7.8 Temporal Shape of Current Signal 128
7.9 Collection of Photoions 131
7.10 Summary 133

8. Two Dimensional Evolution of Photoplasma in Electrostatic-Ion-Extractor
8.1 Introduction 135
8.2 Physical Picture of Photoplasma Evolution in 2d 136
8.3 2d PIC Simulations 137
8.4 Bulk Plasma Motion 138
8.5 Free Ambipolar Diffusion 140
8.6 Coulomb Repulsion 141
8.7 Child Langmuir Flux and Bounded Diffusion 145
8.8 2d Evolution from PIC Simulation 147
8.9 Audit of Photoions in Ion-Extractor 149
8.10 Summary 151

9. Conclusions and Future Directions 153
9.1 Summary of present studies: Contributions 153
9.2 Future Scope 159

Bibliography 163

Chapter 1

Introduction

Plasma produced through resonant photoionization process by shining laser pulses onto a collimated atomic beam is known as photoplasma. It is a special class of plasma having unique characteristics which are different from that of conventionally produced thermal plasma and discharge plasma. The photoplasma is pulsed in nature and it has a finite size and volume with the sharp plasma density gradient at its boundary. Since the resonant photoionization technique is extremely selective and highly efficient, the photoplasma of a particular species is generated in an efficient manner. The photoplasma finds applications in many important areas of science and technology. It plays a vital role in the applications of laser based isotope separation, material purification and laser ion sources. During its evolution in an externally applied electrostatic field, the photoplasma passes through the different transient stages. The aim of the thesis is to investigate the various physical processes involved in the transient decay of photoplasma under an electrostatic field and to study the temporal as well as spatial evolutions of photoions in an electrostatic ion-extractor.

This chapter starts with a general introduction of photoplasma and its unique characteristics. It discusses the process of multi-step resonant photoionization through which the photoplasma is generated. It briefly describes the different areas of applications where the photoplasma is involved and the literature survey of photoplasma study. At last, the chapter is concluded with the scope of work and organization of the works under this thesis.

1.1 Photoplasma

Plasma is defined as an ensemble of charge particles along with the neutral species which is ‘macroscopically quasi-neutral’ and exhibits ‘collective behavior’. The words ‘macroscopically quasi-neutral’ means the net resulting electric charge over a macroscopic region of the plasma volume is nearly zero. The ‘collective effect’ in the plasma occurs due to the long range Coulomb interactions among the charged particles [Bittencourt, 2004, Chen, 1984]. Each charge particle interacts simultaneously with a considerable number of other charge particles. It results an important collective motions of the particles which is primarily responsible for the physical phenomena occurred in the plasma. The plasma is generated through the ionization of neutral species (i.e. atoms or molecules). In the process of ionization, the neutral species absorb energy, when the absorbed energy of neutral species is greater than their ionization energy; they create positive ions and free electrons to produce plasma. Depending upon the supply of external energy to the neutral species, the ionization process is termed as thermal ionization, electron impact ionization, photoionization. In photoionization process, the energy is supplied by the incident photons. Today, LASER provides the intense and tunable monochromatic radiations. While the laser photons incident on an atomic beam, the neutral atoms interact resonantly with the incident laser photons of same color or different colors in step-wise interactions. They get excited by absorbing the laser photons. When the energy absorbed by the atoms is greater than their ionization energy, they get ionized and generate plasma which is termed as ‘photoplasma’.

1.2 Unique Characteristics of Photoplasma

The photoplasma is as special class of plasma and it has unique characteristics. Usually the photoplasma is generated within a timescale of nano-sec (i.e. pulse duration of laser ~ 10 ns) while it lasts for a few microseconds ranges from 10-100 μs. Thus the

photoplasma is transient or pulsed in nature. It has a finite size and shape of either rectangular or cylindrical type depending upon the cross-sectional area of incident laser beams. It is surrounded with the vacuum boundary and has a sharp plasma density gradient at its boundary. The initial density distribution of photoions depends on the resultant intensity profile of the laser beams and the atom density distribution profile in the collimated atomic beam. The photoion density is determined from the neutral atom density at the laser-atom interaction region and the ionization yield of the photoionization process. The photoplasma density varies typically in the range of ~ 10^{12} to 10^{17} m^{-3} with ionization yield of ~ 10^{-2} -10^{-1}. The collisions of charge particles with the neutral background atoms are negligible and the photoplasma behaves as fully ionized plasma. In photoionization process of atoms, the excess absorbed energy of atom over its ionization energy is shared among the products i.e. electrons and photoions. As the mass of electrons are very less compared to that of the photoions, the excess energy mostly goes to the electrons. Therefore all electrons in the photoplasma initially have same kinetic energy. They get thermalized through the electron-electron collisions and defined an electron temperature of the photoplasma. The photoplasma has low electron temperature of ~ 0.1 - 0.5 eV and the charge species are weakly coupled. Since the photoplasma is embedded inside the atomic beam, it has a bulk motion along the direction of vapor flow. The flow velocity is nearly equal to the average velocity of atoms in the atomic beam.

1.3 Multi-step Resonant Photoionization Method

An isolated atom has many discrete electronic energy levels. While it interacts with laser photons, the atom absorbs the photons as the energy of photon is matched with the difference of energy between two atomic levels i.e.

$$E_2 - E_1 = h\gamma \qquad (1.1)$$

where E_2 and E_1 are the energy of atom's upper level and lower level and $h\gamma$ is the energy of incident photon. The electronic transition between two atomic levels is governed by the spectroscopic selection rule. Thus the atoms get resonantly excited from their ground level to an intermediate excited level. In subsequent step, the atoms of excited level absorb laser photons of same color or different color. When the atoms' absorbed energy is greater than their ionization energy, they get ionized and produce positive ions and free electrons. At each step, the atom interacts resonantly with a single photon as the incident energy of laser beam is relatively low (~ 10^{10} -10^{11} W/m^2). The contribution of non-resonant interaction and multi-photon absorption are negligible and hence they are not considered.

Typically the ionization energy of metal atoms lies in the range of ~ 5 eV to 9 eV. The neutral atom can be photoionized through either two-step or three-step resonant photoionization method. In each step the required photon energy is nearly 2 eV to 3 eV. The colors of laser photons are in visible or ultraviolet region of the optical spectrum. Figure 1.1 shows the typical schemes involved in the multistep resonant photoionization process. In two-step photoionization scheme as shown in figure 1.1(a), the atoms of ground level are resonantly excited to an intermediate excited level and subsequently photoionized in the second step. The resonant excitation process of atom is the transition of electrons between two bound levels while the ionization process is the transition of electron from a bound level to continuum (i.e. infinitely extended). Therefore the value of cross-section in the excitation process is large compared to that of ionization. The typical value of excitation cross-section is order of ~ 10^{-16} to 10^{-17} m^2 whereas the photoionization cross-section is nearly 10^{-21} to 10^{-22} m^2.

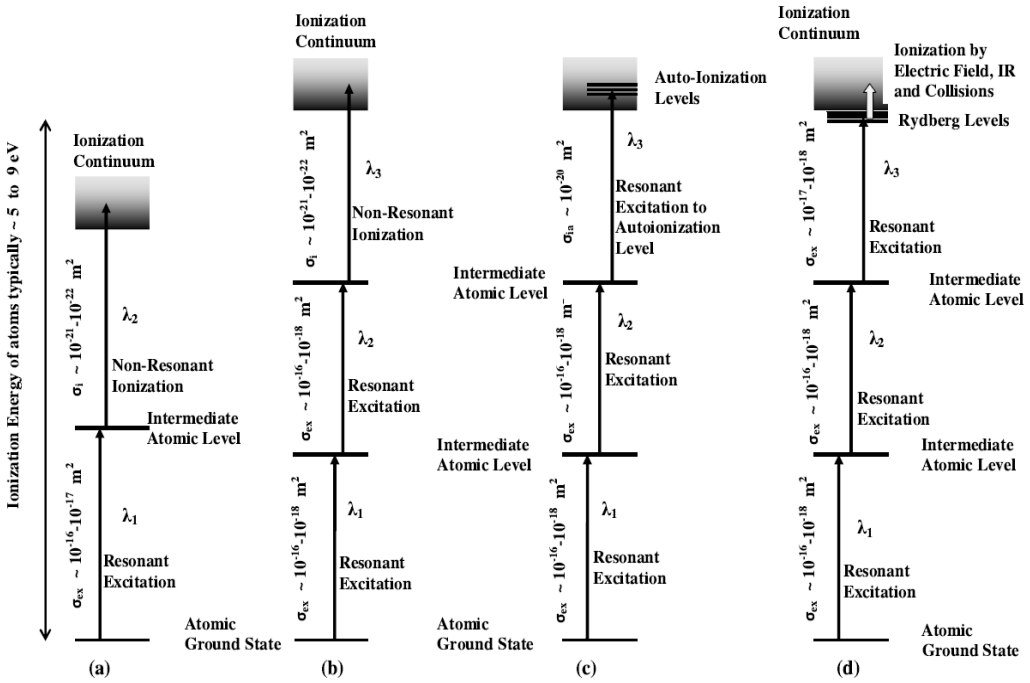

Figure 1.1: Several ionization schemes involved in multi-step resonant photoionization method.

Various schemes of the three-step photoionization process are shown in figure 1.1(b-d). In the first step, atoms get excited from their ground level to an intermediate excited level. The atoms of excited level are further excited to their higher excited level in the second step and get ionized in the third step. Fig. 1.1(b) shows that the excited atom absorbs a photon in third step and gets ionized through non-resonant photoionization. The ionization step of the excited atom is expressed by equation 1.2

$$A^* + h\gamma_3 \rightarrow A^+ + e^- + \Delta E \qquad (1.2)$$

where A* represents the atoms in the higher excited level and $h\gamma_3$ is the energy of photon in the third step (i.e. ionization step). As the probability of the electron transition from the bound excited level to continuum is very less compared to that of the resonant excitation, the ionization yield is very less in the process of 1.1(b).

To increase the efficiency of photoionization in the third step, the excited atom is resonantly excited to a high lying Rydberg level above the ionization limit known as super excited level. The life time of super excited levels is very short ~ 10^{-13} sec. The atoms spontaneously decay from the super excited level to the state of ionization as shown in figure 1.1(c). This process is known as autoionization. The super excited states or autoionization states lie energetically above the lowest ionization threshold and they are embedded in the continuum. The energy requirement of the autoionization level is satisfied by the simultaneous excitation of two outer shell valence electrons. The autoionization process has a large value of cross-section compared to those of ordinary non-resonant photoionization. The typical value of autoionization cross-section is ~ 10^{-20} m^2 and it is almost one order higher than that of the typical photoionization cross-section.

When the atom excites to a highly excited Rydberg levels which lies closely below the ionization limit, the required energy to ionize the atom is very less. The value is nearly hundreds of meV which is comparable to the energy of thermal motion [Letokhov, 1987]. The highly excited atom can be ionized with continuous or pulsed electric field or with electromagnetic radiation in the microwave or infrared ranges as shown in fig. 1.1(d). Even the collisions among the atoms can supply the above energy to ionize the atoms. In presence of external electric field, the potential energy curve of the valence electron is modified and it changes the electronic spectrum of the highly excited Rydberg levels which are closest to the ionization limit. The levels become autoionized. The decay probability of the level rises with an increase in the principal quantum number. This method is particularly efficient if the excited level is a long lived, highly excited Rydberg state with large principle quantum number ($n > 10$) and applied external electric field is ~ 10^6 V/m. The required external electric field may even lower for complete ionization due to the quantum mechanical tunneling effect [Letokhov, 1987].

The ionization yield of the multistep-resonant photoionization process is much larger than that of thermal ionization and electron impact ionization. It is very efficient technique that is used to ionize the atoms in the laboratory. In general, the available photons in the multi-step resonant ionization processes are supplied by lasers. Today the laser provides a very intense, tuned monochromatic radiation. It is easy to efficiently target and ionize a particular atom in the mixture of isotopes or in any mixture like alloys. Thus the multi-step resonant photoionization technique is extremely selective and highly efficient. The photoplasma of a particular element or isotope is being generated in the laboratory with a large value of photoionization yield.

1.4 Applications of Photoplasma

The photoplasma finds applications in many scientific and technological areas like laser based purification of materials for nuclear and medical application, laser based ion source and ion implantation, fundamental study of ultra-cold strongly coupled neutral plasma and photoionization spectroscopy. Some of the above applications are briefly discussed below.

1.4.1 Laser based Isotope Separation

Laser based isotope separation through atomic route [Greenland, 1990; Bokhan et al, 2006] is a promising technology to enrich a particular isotope of an elements. It exploits the difference in the quantum mechanical properties of the element. The small mass differences among the isotopes cause a small isotope shift in their atomic spectra. The isotope shift of a transition arises due to the difference in nuclear mass, nuclear volume (size) and nuclear spin [Greenland, 1990]. In the spectra of light elements, the main contribution is made by the change of nuclear mass whereas for heavy atoms, the

main role is played by the isotope volume shift as well as by the difference in the hyperfine structure of various isotopes.

Due to the strong interaction among the atoms, the optical isotope shift is masked in their solid and liquid phase. Whereas the atom-atom interactions are negligible in the vapor phase and the atomic spectra of individual atoms remain unaffected. So it is easy to access the atomic spectra of a particular isotope in the vapor phase through the tunable laser radiations.

The method of laser based isotope separation through atomic route consists of several physical processes [Paisner, 1988] shown in figure 1.2. They are listed below.

i. Evaporation of target material
ii. Formation of well defined collimated atomic beam
iii. Interaction of the targeted isotope with laser photon
iv. Generation of photoplasma through multi-step resonant photoionization
v. Extraction of photoions from the plasma as product
vi. Collection of product and tails as liquid in continuous process

The photoplasma of a particular isotope is produced through multi-step photoionization method and the photoions are extracted to a desire location for enrichment of the particular isotope. The isotopes of many elements in periodic table are separated using the technique of laser based isotope separation. Laser based enrichment of U^{235} from the mixture of U^{235} and U^{238}, cleanup of hard Gama ray emitter U^{232} from mixture U^{232} and U^{233} are the promising method in fuel cycle of nuclear reactors. The enriched U^{235} is used as low cost fuel in the light water reactor. In same fashion, many isotopes having important applications in various fields of science and technology are also separated. The particular isotope of Gadolinium (Gd), Samarium (Sm) and Europium (Er) are used as the burnable poison in power reactors; Zirconium (Zr) is used as cladding

for nuclear fuel element. An isotope of Mercury (Hg) is more efficient in fluorescent lamps. The precious metals like Rhodium (Rh), Palladium (Pa) and Platinum (Pt) [Paisner, 1988] are recovered from the nuclear waste using laser isotope separation technique.

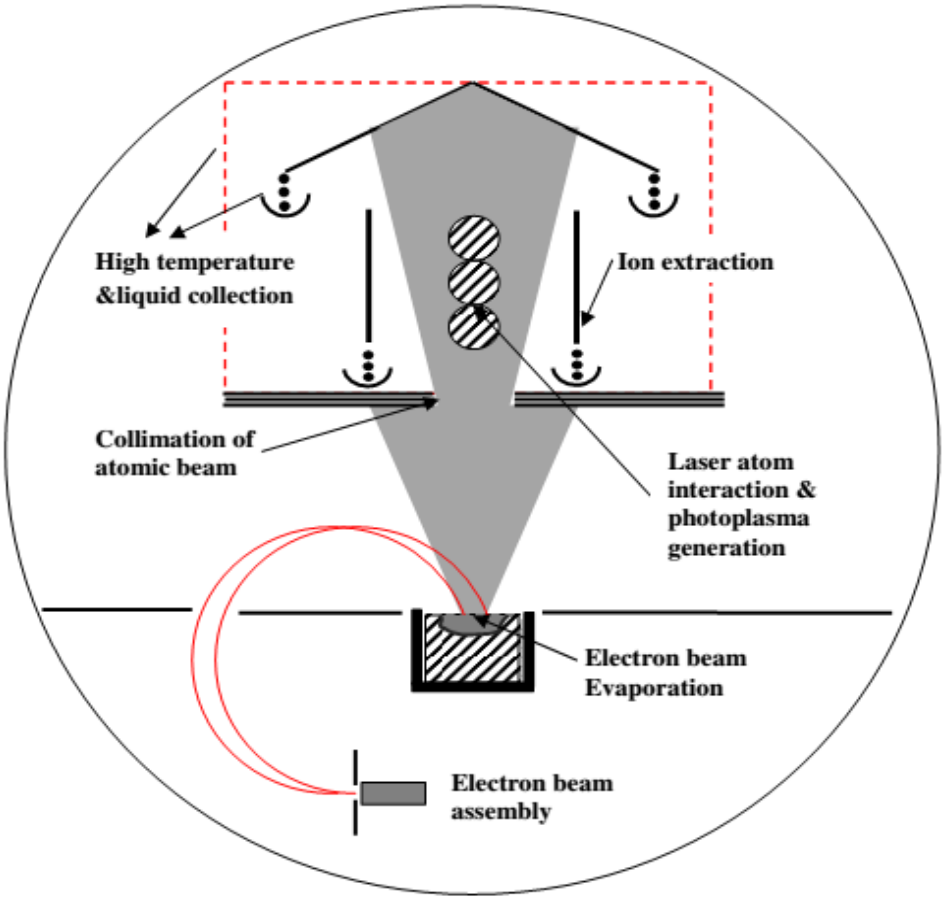

Figure 1.2: Listing of physical processes occurred in atomic vapor laser isotope separation method.

1.4.2 Purification of Metals

Laser based metal purification process is also based on the multi-step resonant photoionization method. It uses the differences in atomic spectra of the individual element (i.e. a property of isolated atom). Whereas the conventional purification methods exploit differences in thermodynamic properties such as vapor pressure, solubility of the materials etc. The laser based purification method has an extremely high selectivity and produces elements with a large degree of purification. It has a distinct advantage from the

conventional purification method. It is a quite universal method and applied for almost all elements, independent of their respective physical and chemical properties.

The laser based purification in alloy system of AgIn, CuNi [Mori et al, 1997] etc was experimentally demonstrated. As an example, the alloy of $Ag_{0.90}In_{0.10}$ was vaporized by electron beam heating in a vacuum evaporator. The Ag atoms were photoionized using three-step photoionization methods [Ishikawa et al 1997]. The photoions were collected on negatively biased gold substrate. The impurity concentration of Indium i.e. [In/ (In +Ag)] was reduced from 10.3 % in the vapor phase to 5.4 % in the deposited thin film. The impurity in the product was mainly due to neutral scattering away from the atomic beam to the substrate. The impurity was further reduced using the method of time division collection [Mori, 1998] where a high speed rotating disc was used to suppress the impurity level. The rotating disc and the pulsed lasers were synchronized in time. Using this new technique, a high quality Ag film of 0.11 % In impurity concentration was achieved from the starting alloy AgIn of 6.08 % In.

1.4.3 Laser Ion Source

Laser based ion source plays a vital role in applications of high energy Radioactive Ion Beam (RIB) generation. In an Isotope Separator On Line (ISOL) facility, the main requirements of the ion sources are high ionization efficiency, element selectivity and rapidity i.e. short delay times. These requirements are ideally fulfilled by a Resonance Ionization Laser Ion Source (RILIS) for many elements. The ions of a particular element are produced in the laser ion source by laser radiations through multi-step resonant ionization technique. Today, the RILIS are the most commonly used ion source at the online mass separator facilities like ISOLDE in CERN Geneva [Fedoseyev et al, 2000], IGISOL (Ion Guide Isotope Separation On Line) in Jyvaskyla Finland [Moore et al, 2005] and at many other RIB facilities worldwide. B A Marsh [2014] has

described the recent RILIS developments and the worldwide current status of laser ion sources. The RILIS is considered as one of the major prerequisites in atomic and nuclear spectroscopy to measure the isotope shift, hyperfine structure of atomic transitions for many rare short lived isotopes. The high elemental selectivity of resonance ionization techniques also provides an inherent suppression of unwanted isobaric contamination at the ion source. In addition to the isobaric suppression, the RILIS provides a unique chance to produce intensive beams of separated nuclear isomers which was impossible with other ion sources.

The high intense radioactive ion beam of many elements like Yb, Ag, Mn, Ni, Zn, Be, Cu, Cd and Sn were produced at ISOLDE with the resonance ionization laser ion source (RILIS). The entire list of radio nuclides and radioactive ion beams delivered for atomic and nuclear physics were discussed by Fedosseev et. al. [2012]. The nuclear isomer separation of Ag and Cu [Fedoseyev et al 2000] and the study of hyperfine splitting of CuI [Fedosseev et al, 2012] were also achieved in the ion source by appropriate tuning of the laser wavelength.

1.4.4 Ultra-Cold Neutral Plasma

Ultra-cold neutral plasma is a uniquely different class of plasma produced by step-wise photoionization method of ultra-cold atoms. It occupies an exotic regime of plasma physics where it extends the normal boundaries between plasma, neutral gases and condensed matter [Killian, 2007]. To reach the ultra-cold regime, the atoms are cooled by lasers. They are trapped in a magneto optical trap (MOT) [Simien et al, 2004] and formed an atomic cloud. A typical ~ 10 ns laser pulse of a narrow bandwidth laser irradiates the atomic cloud and produces the ultra-cold plasma. Alkali, alkaline-earth and noble gas atoms are the most common choice for ultra-cold neutral plasma studies. Using the MOT lasers, the atoms get excited from their ground state to an excited metastable state. In

subsequent step, the excited atoms are ionized by absorbing photons from a narrow band-with pulsed dye laser. The pulsed laser wavelength is tuned just above the ionization threshold to get the electron temperature order of few Kelvin to a few thousand Kelvin. The ultra-cold plasmas have typical parameters like plasma density ~ 10^{15} – 10^{16} m^{-3}, plasma size ~ 1 mm, electron temperature ~ 10 -1000 K and ion temperature ~ 10 μK [Killian et al, 1999; Simien et al, 2004)]. The coulomb coupling parameter is an important quantity in the ultra-cold plasma and it is defined as the ratio of particle's electrical interaction energy to its thermal energy. The thermal energy of the charged particles in the ultra-cold plasma is less than the coulomb interaction energy between nearest neighbors. It makes the plasma strongly coupled. The coulomb parameter for both electrons and ions in ultra-cold plasma are greater than unity. It is distinctly different from the conventional plasma where the thermal energy dominates and the value of coulomb parameter is very less than unity.

In some extreme environments such as the core of Jupiter, the crust of a neutron star, shock waves produced by laser implosion, laser produced high-energy density plasma etc., the plasma density is so high that the coulomb parameter becomes larger than unity. Thus the ultra-cold neutral plasma creates the identical conditions in the laboratory to explore the basic understandings of the strongly coupled physics at very low densities compared to high-energy densities experiments, which typically work at close to solid densities. At low densities, the important time scales of the problem, such as the time between collisions and 1/ W_{pi} (plasma ion oscillation frequency), are orders of magnitude longer. It makes easier to study the phenomena occurred in the high density plasma. In addition, the ultra-cold neutral plasma provides a 'clean' system where the initial density profile, energy and ionization state are accurately known and controllable. The optical probes have proven powerful for obtaining precise measurements of plasma properties

[Killian, 2007]. Thus the ultra-cold neutral plasma provides a powerful and flexible environment to test the fundamental understanding of the plasma physics. The studies of plasma formation [Killian et al 1999], excitation of plasma oscillation [Kulin et al, 2000], dynamics of plasma expansion [Simien et al, 2004], collisional recombination into Rydberg atomic state [Mazevet et al, 2002] were demonstrated in ultra-cold neutral plasma.

1.5 Literature Survey on Photoplasma Study

Photoplasma was first experimentally produced by two-step resonant photoionization method on rubidium atoms [Ambartzumian and Leokhov, 1972]. Using the technique of multi-step photoionization method, the photoplasma of any elements in the periodic table can be generated. Letokhov et al [1977] discussed the kinetics of two-step and three-step resonant photoionization process through which the photoplasma is generated. In the last few decades, the photoplasmas were studied both theoretically and experimentally. The studies on photoplasma were mainly focused on the process of photoion extractions from the photoplasma and its evolutions in an electrostatic ion-extractor.

1.5.1 Photoion Extraction by Electrostatic Field

1.5.1.1 Theoretical Studies

The work was first started by Chen [1982] on decay of semi infinite plasma in an electric field. He had analytically explained the effect of various mechanisms on the ion-extraction-time by taking into account the motion of plasma-sheath boundary during the plasma decay. Somewhat his result was restricted in the applicable density range, particularly for the low density limit. Later on Okano [1992] extended the applicable density range from a very low density to high density of photoplasma. He derived the

scaling formulas of ion-extraction-time in a convenient dimensionless form over the wide density range. The reliability of Okano's formulas on the ion-extraction-time was verified by Watanabe and Okano [1993] using the plasma simulations. Murakami and Nishihava [1993] presented a simple analytical model to describe the sheath dynamics during the evolution of photoplasma. They highlighted that the ion-extraction-time is reduced when the electron temperature in the photoplasma is increased. Tkachev and Yakovlenko [1993] studied the ion behavior in the photoplasma under an intense pulsed electric field and showed a coulomb explosion of the net positive charge within the plasma. Litvinov [1997] proposed a refined model of the extraction processes taking place in case of high density plasma in the electrostatic ion extractors. He analytically calculated the initial profile of ion current to the cathode and also estimated the integrated contribution of ionic current to the anode.

1.5.1.2 Experimental Observations

In experiments, Chen and Borzileri [1981] measured the initial electronic state distribution of laser produced uranium ions employing the method of laser induced fluorescence (LIF). They also observed the decay of laser induced uranium plasma by monitoring the LIF signal as function of time. Using LIF, Yamada et al [1990] studied the time evolution of two dimensional ion density distributions in barium photoplasma under the electrostatic field. They investigated the various ion extraction characteristics in the electric field and showed that the ion behavior in the plasma is determined by the overlapping effect of three mechanisms: Bulk plasma flow, plasma diffusion and ion extraction by electric field. Using the same technique, the ion behavior was investigated in Ba and U photoplasma by Yamada et al [1993] in the electrostatic ion-extractor produced by two parallel plates. They explained the ion extraction process in various distinct stages and compared the results with numerical model. Similar studies were

carried out by Oruga et al [1993] on gadolinium photoplasma using multichannel Faraday cups placed behind the electrodes. A scaling relation i.e. parametric dependency of ion-extraction-time was experimentally established by Yamada et al [1991a] with an accuracy of 15 % in Ba photoplasma produced between parallel plate electrodes. Oruga and Shibata [1994] measured the kinetic energy of photoions collected on the electrodes using time of flight method. Furtlehner et al [1994] studied experimentally and theoretically the time evolution of electron temperature in Ba photoplasma which expands freely into a vacuum. In our group, the motion of a finite-sized barium photoplasma was studied in an electrostatic ion-extractor to investigate the various ion extraction processes using the Faraday cups placed behind the electrodes [Majumder et al. 2008]. The distributions of photoions in the ion-extractor were also measured at different values of plasma density, external field and they were compared with the simulations.

1.5.1.3 Numerical Simulations

Numerical simulations were also carried out to understand the evolution of photoplasma in better way. Two approaches are used to simulate the plasma. One is particle approach where the finite-sized photoplasma is replaced by a number of both positive and negative super particles. Another is fluid approach and the plasma is considered as a mixture of interpenetrating electron and ion fluid. Anisimov and Medveda [1990] solved the kinetic equations numerically by the particle in cell method and studied the expansion of finite-sized plasma cloud into vacuum under an electric field. Doneddu [1993] simulated the plasma dynamics regarding the ion extraction process in the ion-extractor. Watanabe and Okano [1993] estimated the ion-extraction-time over a wide range of plasma density. Oruga et al [1993] studied the two dimensional evolution of plasma using 2d PIC simulation and investigated the variations of ion-extraction-time with different plasma parameters like electron temperature, plasma potential and initial

plasma density. Patel and Mago [1995] simulated the spatial and temporal evolution of finite-sized Ba plasma and explained the motion of electrons and ions during the decay of plasma under the external electric field. They also highlighted the motion of plasma-sheath boundary in various conditions. Patel [1997] observed the ion wave during the transient evolution of photoplasma. Zidhkov [1998] extended the PIC method by incorporating the particle elastic collisions like electron-electron, electron-ion and resonance charge exchange collisions. He discussed the process of ion extraction from the weakly collisional plasma and showed the evolution of the net positive charge in the photoplasma.

Based on fluid approach, Vitello et al [1992] developed two dimensional one fluid model where the plasma electrons were assumed as having a Maxwell Boltzman distribution. They simulated the ion extraction process during the transient evolution of the plasma in two dimensions. Hasegawa et al [2001] extended the model by incorporating the charge exchange process and evaluated the influence of charge exchange on ion collection from the photoplasma. Kurusaga et al [2001] used the one dimensional two fluid models to investigate the motion of plasma electrons under the external field and to study the details evolution of plasma potential. They described the influence of different plasma parameters (i.e. electron temperature, plasma density and applied voltage) on the plasma potentials.

1.5.2 Different Electric Field Configurations

To optimize the efficiency of ion extractions from the photoplasma, its evolutions were studied in various electric field configurations produced by different geometry like PI type, M type and plate-grid-plate geometry as shown in figure 1.3. The PI type geometry (fig. 1.3 (b)) was produced by placing a new plate electrode above the parallel plate electrodes where the above plate was biased with positive potential and others were

grounded. Yamada et al [1991b] experimentally measured the ion extraction characteristics of barium photoplasma in the PI type geometry using the method of LIF.

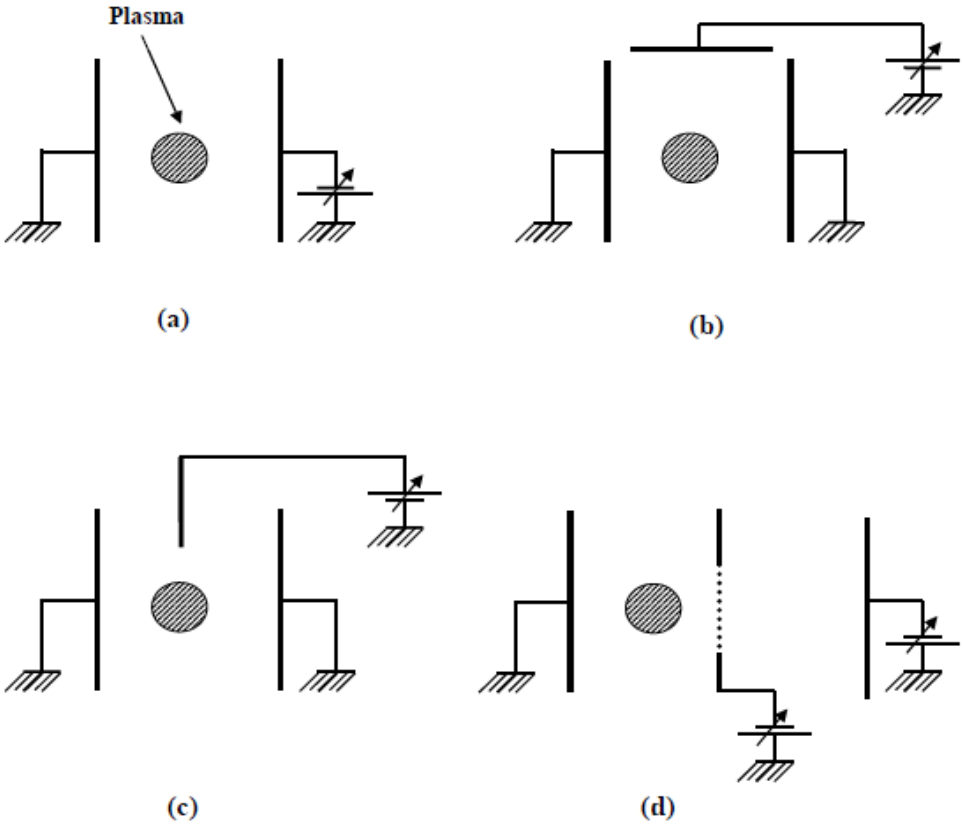

Figure: 1.3 Different types of geometry used in photoplasma study: (a) Parallel plate geometry, (b) PI type geometry, (c) M type geometry and (d) Plate-grid-plate geometry.

They provided a scaling relation i.e. parametric dependencies of ion-extraction-time by external electric field for PI type geometry and showed that the PI type configuration improved the ion-extraction-time by maximum factor of 2.6 than that in the parallel plate geometry.

The M type geometry (fig. 1.3(c)) was configured in a fashion where a positive biased wire electrode or plate electrode placed vertically between two parallel plate electrodes. Oruga et al [1992] experimentally studied the ion collection method using

Gadolinium plasma in the M type geometry. Using a positively biased wire electrode, they demonstrated that the ions were collected from the laser induced plasma in a shorter time at the same applied potential or by lower electric potential in the same ion-collection-time compared with the conventional parallel electrode method. Nishio et al [1995] investigated the two dimensional evolution of photoplasma using Faraday cups in the M type geometry. They compared the ion-collection-time from PI type, M type and parallel plate geometry. They concluded that a more rapid ion transport can be achieved by the M type electrodes compared with parallel electrodes and PI type electrode. The same results were also investigated numerically using fluid model by Hasegawa et al [2001]. They also simulated the influence of resonance charge exchange on collection of ions in various geometries. Kurusawa et al [2002] showed that the photoions in the M type geometry were collected twice as fast as in the conventional parallel plate electrode system.

Golyatina et al [1998] studied the ion extraction from the low density plasma through grid meshes. Savelev et al [1997] showed the passage of low density plasma through transparent grids in the plate-grid-plate geometry (fig. 1.3(d)). Majumder et al [2003] also experimentally investigated the motion of low-density photoion bunch in a linear electrostatic potential well created by plate-grid-plate geometry.

1.5.3 Photoion Extraction by RF Resonance Electric Field

When the plasma density is high, the applied external electric fields do not penetrate inside the plasma. The plasma shields the external fields within the Debye screening length from the plasma boundary. So the ions at the boundary are only affected by the electric field. The ion inside the plasma volume remains unaffected. In order to raise the efficiency of ion collection, Matsui et al [1997a] proposed a method of ion extraction from the plasma using radio frequency resonance electric field. The resonance

frequency of the RF field was chosen to excite an Eigen mode of the plasma wave in a low magnetic field. It was experimentally observed on xenon discharge plasma that the RF electric field was penetrated inside the plasma at resonance. The obtained ion current by RF method is twice that of the ion saturation current in the electrostatic ion-extractor. The mechanisms of ion collection from the plasma using RF resonance electric field were also studied [Matsui et al, 1997b] using 1d PIC simulation. The simulations showed that the large electric field penetrates into the plasma at resonance. Consequently the ions are accelerated in plasma as well as ion-sheath regions which are formed in front of both electrodes. They are extracted rapidly from the photoplasma. It indicates that the restriction of the plasma shielding effect was overcome by the RF electric field.

1.5.4 Photoion Extraction by Electromagnetic Fields

Apart from the electric field, a combination of electric field and magnetic field were also used for ion extraction study. For fast ion extraction, Hazak et al [1980] presented the ExB scheme using an analytical solvable model and a numerical simulation. Zhidkov [1998] simulated the ion extraction process in weakly collision plasma by various kinds of electromagnetic field such as electrostatic, cross electric and magnetic (ExH), RF field and alternating magnetic field. He compared the characteristics of various ion extractors relevant to the application of laser based isotope separation through atomic route. He proposed that the ion extraction by alternating magnetic field seems to have good prospects for the laser based isotope separation applications.

1.6 Scope of Thesis

Though the photoplasmas are extensively studied in the different external field configurations with the wide range of plasma density, the dynamics of the finite-sized photoplasma evolution and its complex transient behaviors are not clearly understood.

During its decay under the external electric field, the photoplasma evolves through the various transient stages which are not fully explained. Therefore the aim of the thesis is to investigate the processes through which the transient photoplasma decays under the externally applied electrostatic field. Starting from the atomic beam generation and photoplasma production through resonant photoionization, the evolutions of photoplasma in the electrostatic ion-extractors have been investigated in details. The overview of entire works carried out under the thesis is schematically shown in figure 1.4.

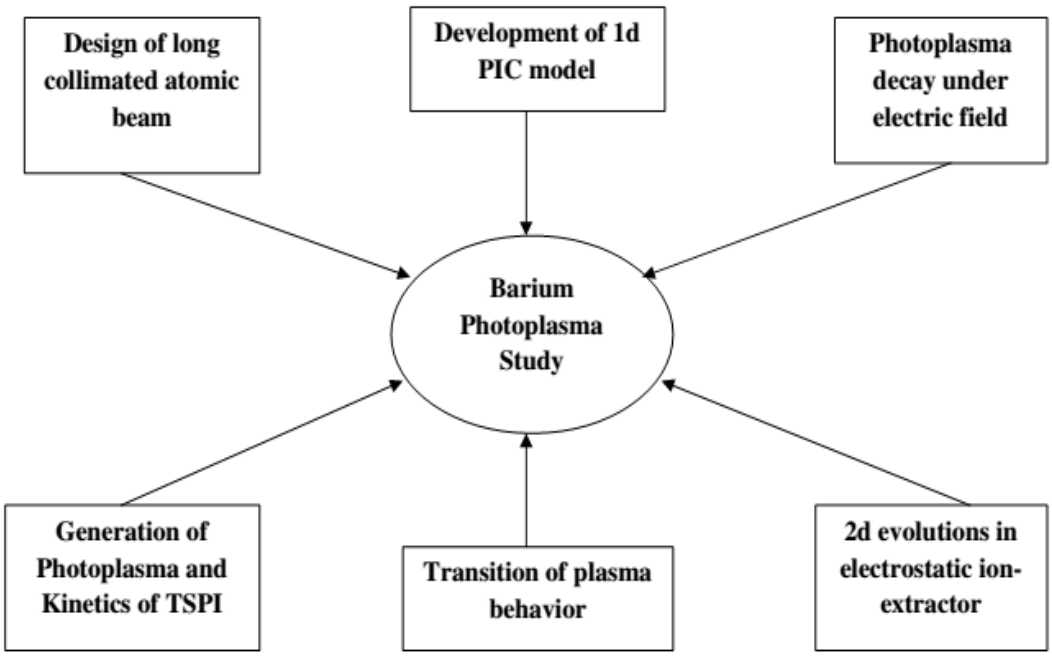

Figure 1.4: Overviews of works carried out in the thesis.

The works under the thesis have been broadly divided into two parts. In the first part, it has been discussed about the generation of a wedge-shaped barium atomic beam and the production of the barium photoplasma inside the atomic beam through two-step photoionization method. In the second part, it has been described the motion of low-density photoplasma in the linear electrostatic potential wells created by the plate-grid-plate configuration. By increasing the plasma density in the experiments, the transition of

the plasma behavior from the single particle kinetics to its collective phenomena is highlighted. The various physical phenomena involved in the transient decay of photoplasma under the electric field are investigated. Two dimensional evolution of photoion density in the electrostatic ion-extractor are discussed. The various processes that contributed to the two dimensional motion of photoplasma are identified and their individual contributions are quantified. A fully kinetic 1d model based on standard particle-in-cell (PIC) simulation has been developed to study the dynamics of photoplasma under the constant electromagnetic field.

1.7 Organization of the Thesis

To discuss the different aspects of the present work in a systematic manner, the works under the thesis is organized in nine chapters. The contents of the chapters are summarized as follows. The chapter 2 describes the details of experimental setups that were used for the barium photoplasma study in the electrostatic field. The set-up consists of various sub-systems. The designing features of the sub-systems and their role to investigate the photoplasma motions are discussed. The chapter 3 deals the design principle of a long wedge-shaped atomic beam using collinear effusive channels. It discussed the generation and its characterizations of the long collimated barium atomic beam for the photoplasma study. The chapter 4 discusses about the generation of barium photoplasma using two-step photoionization schemes and the detail kinetics of the photoionization process occurred in the optically thick medium of barium. The chapter 5 talks about the development of one dimensional PIC (particle-in-cell) model to study the decay of a finite-sized transient photoplasma in an electromagnetic field. The chapter 6 presents the motion of low density photoplasma in a linear electrostatic potential well created by plate-grid-plate geometry. The results obtained from the PIC model are compared with the experimentally observed photoionization signal. It discusses the

transition of plasma behavior from the single particle kinetics to collective behavior as the plasma density increases. The chapter 7 discusses the various physical processes through which the transient photoplasma passes during its decay in an electrostatic field. The chapter 8 describes the two dimensional features of the photoplasma evolutions in the electrostatic ion-extractor. Various processes contributed to the two dimensional motions are identified and their individual contributions are quantified based on the data observed from experiments and numerical simulations. The chapter 9 concludes with a summary of works and discusses briefly the future directions of the photoplasma study.

Chapter 2

Experimental Systems for Photoplasma Study

In this thesis work, both experiments and numerical simulations have been carried out to investigate the evolutions of barium photoplasma in the electrostatic field. In the experiments, a long collimated and wedge-shaped atomic-beam of barium was produced. The average atom density of the atomic beam was measured by an optical absorption method. By shining the laser pulses onto the atomic beam, a finite-sized photoplasma was generated inside the atomic beam. The spatial and temporal evolutions of the photoplasma were studied in the electrostatic ion-extractor. This chapter describes the details of experimental systems which were used to study the evolution of barium photoplasma in the electrostatic field.

2.1 Experimental Set-up

The experimental set-up was made of several sub-systems and diagnostic tools. They were (i) a resistively heated furnace for generation of a long wedge-shaped atomic beam, (ii) a hollow cathode lamp based optical absorption sensor to measure the average atom density in the atomic beam, (iii) a laser systems to produce the photoplasma inside the atomic beam, (iv) an electrostatic ion-extractor for evolution of the photoplasma in the externally applied electric field. Figure 2.1 shows the schematic linkage of various subsystems which were used to study the barium photoplasma in the electrostatic ion-extractor. The sub-systems of heating furnace and ion-extractor assemblies were kept inside a vacuum chamber.

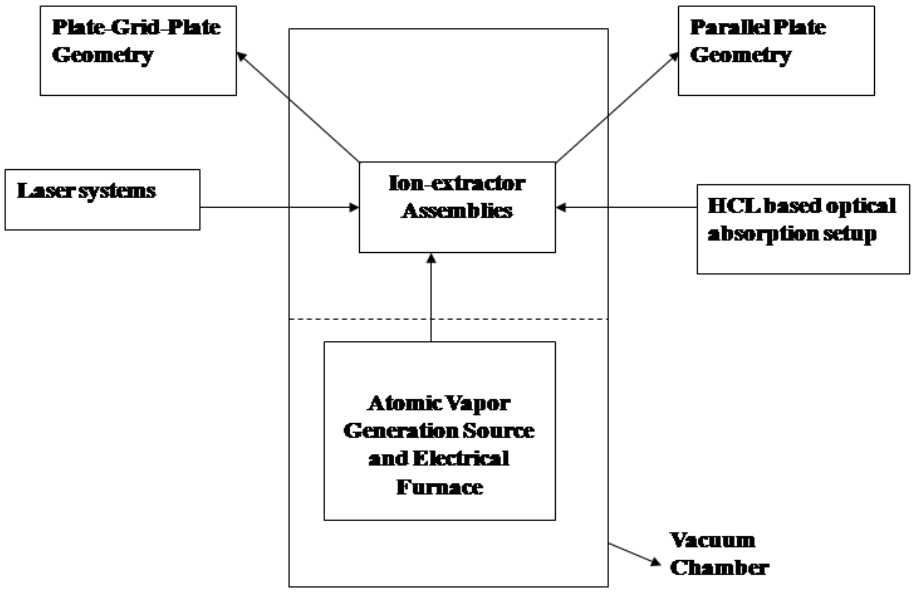

Figure 2.1: Schematic linkage of various sub systems used in photoplasma study.

2.2 Experimental Chamber

The experimental chamber was vertically placed a stainless steel (SS 304) made cylindrical chamber. It had dimensions of height 600 mm, internal diameter 450 mm and wall thickness 6 mm. The top and bottom ends of the chamber were closed with 10 mm thick stainless steel flanges. Each flange has two welded ribs to strength the mechanical structure. The flanges had a series of feed-through that were used for electrical connections and other diagnostic purposes. Copper limpet coils were brazed on the chamber body and the flanges. The chamber was cooled by water flowing through the copper limpet coils. The vertical chamber was divided into two compartments. The lower part contained the vapor-generating furnace assembly while the upper part was used as the laser-atom interaction zone for photoplasma study. There were four equi-spaced

circular ports at the middle height of the chamber. Two of the diagonally opposite ports were used for the entry / exit of the laser beams and also for characterization of the atomic beam. The other two orthogonal ports were used for various purposes such as electrical connections, vacuum leak testing. Sometimes they were also used as the view port of the chamber.

The experimental chamber had a volume of ~ 95 liter. It was evacuated by two set vacuum pumps of diffusion-rotary pump combinations. The water cooled diffusion pumps having pumping speed of 1000 lit/sec and 2000 lit/sec were connected in parallel to the chamber's lower part and upper part respectively through the high vacuum compatible gate valves. The diffusion pumps were backed by two rotary pumps. The pumping speeds of the rotary pumps were 500 lit/min and 750 lit/min respectively. High capacity pumping systems were specially designed to take care of out-gassing load from the high temperature furnace and also to reduce the initial pump-down time. In our case, the initial pump down time is nearly 45 minutes. The typical operational vacuum in the chamber during experiments was $\sim 2.0 \times 10^{-5}$ torr.

2.3 Atomic Vapor Source

The atomic vapor source produced a long collimated atomic beam that expands vertically upwards. The vapor source was made of a resistively heated electrical furnace, a rectangular crucible and a set of linear rectangular collimating slits. Figure 2.2 shows the isometric view of various components in the vapor generating source.

The electrical furnace had a heating filament of 1 mm diameter tantalum (Ta) wire. The filament wire was configured in a fashion like the wire wound in an incandescent bulb, at the vertical planes from all side surrounding the crucible. The Ta wire was supported by a series of 2 mm diameter tungsten rods. At one end, the rods were shaped in the form of hooks and the filament wire was supported by the hooks. All

supporting rods were electrically insulated and had arrangements by which their heights could be adjusted. This design basically took care the plastic deformations of Ta filament wire occurred in repeated heat cycles and also to minimized its deformation during thermal expansion. A rectangular frame of Ta foils acted as thermal heat shields were covered the crucible from the four sides. To reduce the heat loss, two set of separate Ta sheets were placed on top and bottom of the crucible. The lower Ta sheet had a series of holes for passing the supporting rods of filament wire and crucible stand. The upper one had a linear rectangular slit for passage of vapors to form the collimated atomic beam. Thus it formed an enclosed rectangular hot zone which had a volume of ~ 0.85 liter.

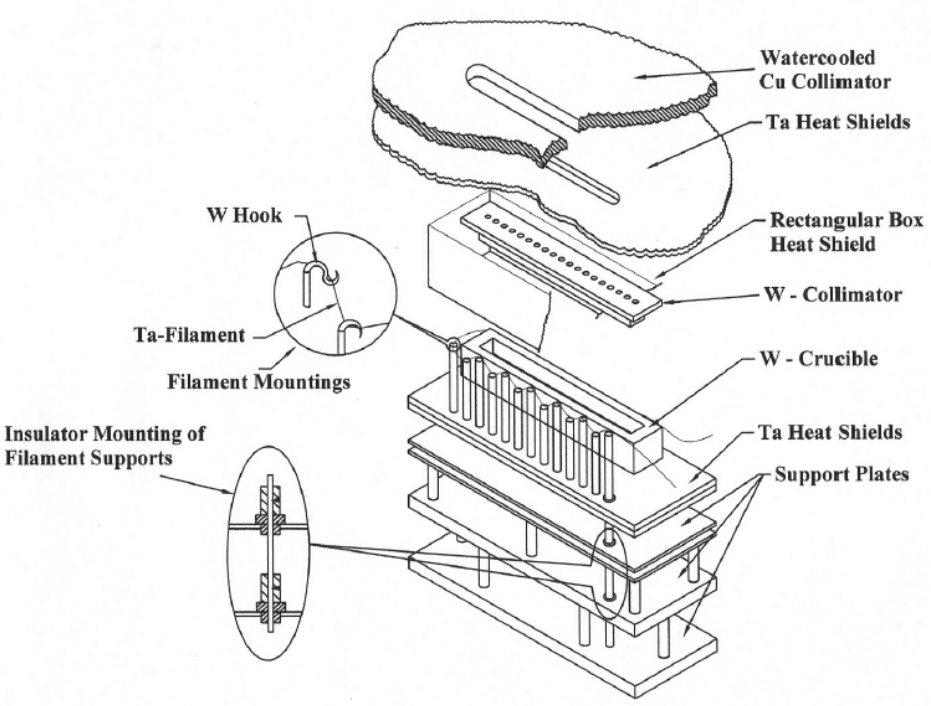

Figure 2.2: Isometric view of various components in the atomic vapor generating source.

A 3 mm thick base plate of inconel 600 was placed on top of the hot zone. It provided a base platform on which the ion-extractor assemblies were supported. The plate also acted as an outer heat shield of the hot zone and it separated the hot zone of the furnace from

the laser-atom interaction zone. The base plate and the top sheets had a narrow aperture of 100 mm long and 8 mm width.

The rectangular crucible was made of tungsten. It had a length of 120 mm, width of 18 mm, height of 18 mm and 3 mm wall thickness. A smoothly fitted 5 mm thick tungsten lid covered the crucible. The lid had a collinear array of 31 cylindrical channels / tubes, which were drilled along the length of crucible. The apertures of channels (i.e. holes in the lid) were of different shapes and size as shown in figure 2.3. The middle hole was oval shaped with 6 mm length and 2 mm width. Two sets of three holes located on either side of it were also oval shaped with length of 4 mm and width of 2 mm. Another two set of three holes having 3 mm length and 2 mm width were located symmetrically on both sides of that. All other remaining holes were circular. The hole-sizes were chosen in a way that the centrally located holes had large divergence compared to the holes placed at the extreme having less divergence. The series of collinear channels contributed additively to achieve the spatial uniformity of density distributions along the length of the crucible.

The filament was heated directly by passing current through it. A step down transformer of 20 V, 100 A was used for supplying the electrical power to the filament. The thermal radiation at high temperature from the filament heated the crucible. The crucible contained small pieces of barium (Ba) (99.5% purity) granules of weight about 22 g. The Ba vapors effused through the holes and were collimated by the linear rectangular slits of the inconel base plate and Ta sheets placed on the above of the crucible. Thus it formed a well collimated atomic beam. The neutral vapor density in the atomic beam was varied by changing the temperature of crucible. The temperature of crucible was measured by K-type thermocouple placed very near the crucible.

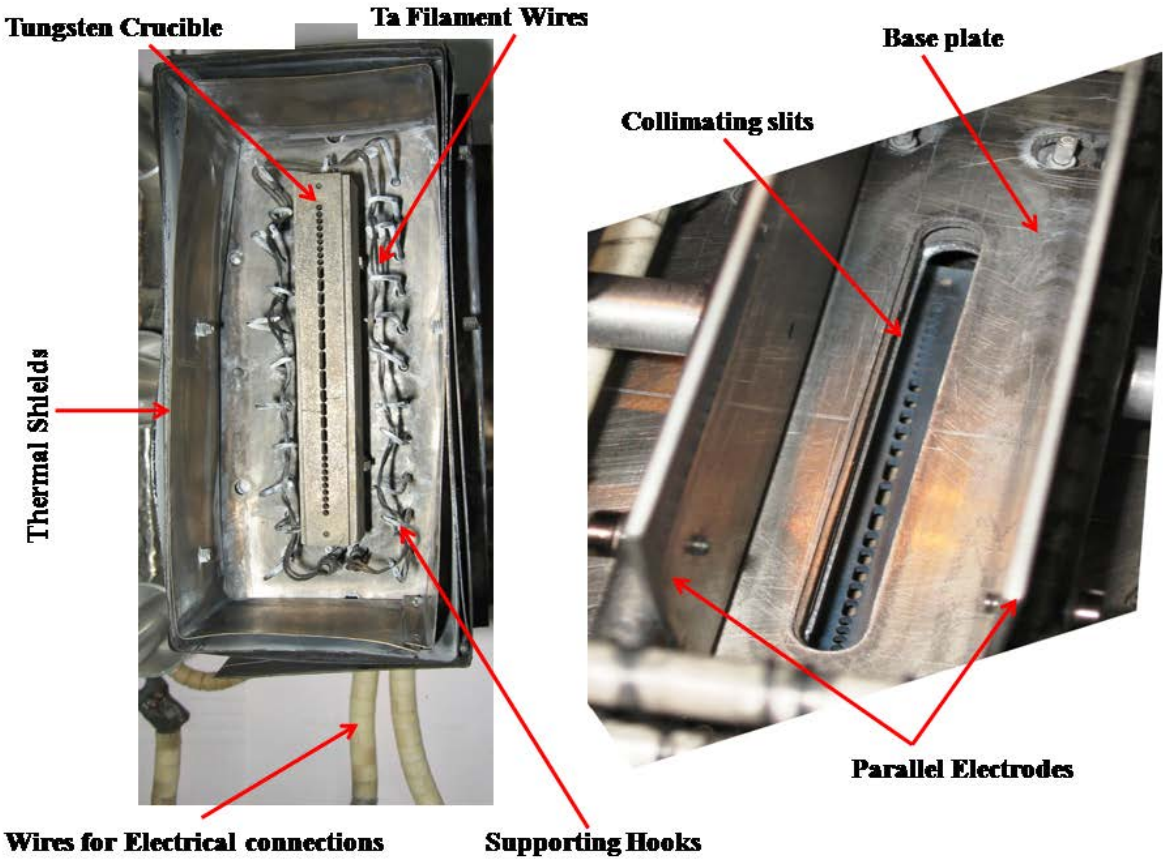

Figure 2.3: Photographs of crucible lid with different sized holes, collimating slits and resistively heated electrical furnace.

The barium metal is highly reactive. It reacts easily with air and water. So it required to take some precautions for its safe handling. The barium rods were stored in an inactive liquid like paraffin. The rod was cut into small pieces under kerosene and the barium pieces were transferred to the crucible along with a little amount of kerosene. It minimized the reactions of Ba pieces with air during the preparation stage of experiments before the vacuum pumps started.

2.4 Atom Density Measurement Setup

The integrated atom density over the length of atomic beam was measured at the height of laser-atom interaction region using the optical absorption method. Figure 2.4 shows the schematics of atom density measurement set-up. The setup had an emission

light source, beam guided optics and detection systems. A commercial Ba/Ar hollow cathode lamp (Ba-HCL) (make: Heraeus, model: 3BAXBa) was used as the emission source. The light emitted from Ba-HCL was guided by a lens and right angled prisms, after that it was transported through the atomic beam inside the vacuum chamber. The transmitted light was focused on an optical fiber coupled with a monochromator (make: Oriel, model: 77200) having a resolution of 0.1 nm and a focal length of ¼ meters. The monochromator was set at a particular reading to allow the resonant line of BaI at 553.5 nm radiation. The monochromator was connected with a photomultiplier tube (PMT) (make: Oriel, model: 70680) biased at approximately - 800 V. The optical light incident on PMT was converted into an electrical signal. The signal was processed by a digital lock-in-amplifier (make: Perkin Elmer, model: 7265), which was locked at a reference frequency of the optical chopper. The dc output from the lock-in-amplifier was recorded in the data logging computer.

The reference intensity (I_0) was measured by recording the light intensity in absence of atomic vapor at the interaction region. In presence of the atomic vapor, a fraction of incident light intensity was resonantly absorbed by atoms and remaining fraction was transmitted through the atomic beam which was referred as transmitted intensity (I_t). There was a possibility of vapor coating on the optical window of the vacuum chamber and the transparency of the optical window could be changed during the measurement cycle. To minimize the measurement error, the reference intensity (I_0) was cross-checked at certain time interval during the experiments and the averaged value of several measurements was considered as the reference intensity. It was found that the corresponding change in the reference intensity was negligible in our case. The average atom density was estimated by comparing the transmitted intensity (I_t) with the reference

intensity (I_0). Thus the measurements of atom density in the atomic beam were carried out at different crucible temperature.

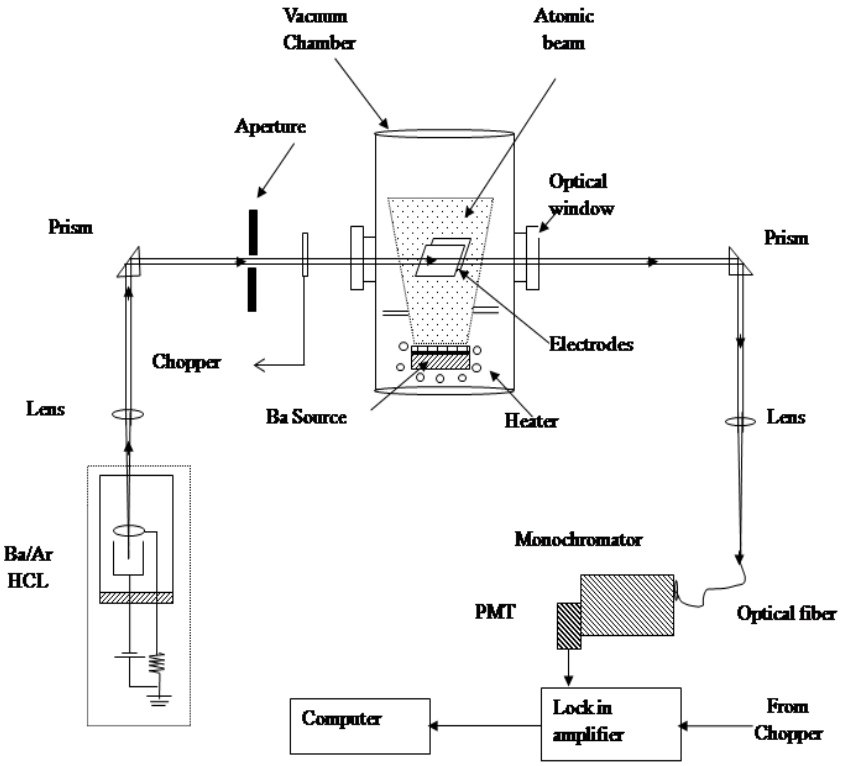

Figure 2.4: Schematics of a hollow-cathode lamp based optical absorption set-up for measurement of atom-density in a long wedge-shaped atomic beam.

2.5 Laser Systems

The laser system made of a Q-switched Nd: YAG laser (make: Quantel, YG980 series) operating at 10 Hz pulse repetition rate along with its harmonic generation unit and a tunable pulsed dye laser (make: Quanta-ray). They were used for two-step, two-color photoionization of barium atoms. The second harmonic of the Nd: YAG laser at 532 nm radiation pumped the Rhodamine 6G dye in the dye cell. The Rhodamine 6G dyes dissolved in methanol solvent. The dye concentrations for oscillator and amplifier were ~ 62.2 mg/ lit and ~ 14.8 mg/lit respectively. The dye laser was tuned to provide the first-

step excitation pulse at λ_1 = 553.5 nm. In the second step, the third harmonic of the Nd: YAG laser at λ_2 = 355 nm radiation pulse was used to ionize the excited Ba atoms. Although Ba has a lot of autoionization levels, the 355 nm radiation was used for the ionization step because it was easily available from the Nd: YAG laser. No further dye laser was required for the second step.

The laser beams were transported over a distance of ~10 meters from the laser systems to the vacuum chamber in a co-propagation configuration with the help of optical components like right-angled prisms, optical beam combiner etc. The schematic of the laser-beam transportation is shown in figure 2.5. The two laser radiation pulses were combined at the optical beam combiner. The beam combiner reflected 355 nm radiations almost fully at 45^o angle of incidence and efficiently transmitted 553.5 nm radiations. The combined optical beam co-propagated and then spatially overlapped with the long wedge-shaped atomic beam at the interaction zone. An adjustable iris was located in front of the co-propagating laser beams just before they entered the vacuum chamber. The spot size of the combined laser beam was decided by the aperture of the iris. In our case the aperture's diameter was ~ 10 mm.

The pulse durations (FWHM) of both the laser pulse were measured using fast photodiode. The values were ~7 ns for 553.5 nm radiation and ~ 9 ns for 355 nm radiations. The combined pulses were temporarily overlapped. An optical delay of 4 ns (less than the life time of excited level ~ 8.37 ns) was introduced between the excitation pulse and the ionization pulse such that the ionizing pulse arrived at the atomic beam after the exciting pulse. The spectral line width (FWHM) of laser radiations was ~ 9 GHz for 553.5 nm while it was ~ 17 GHz for 355 nm. The excitation radiation was broadband and all isotopes of Ba atom were excited and ionized. The average pulse energy was measured by power meter (make: Ophir, model: Nova P/N IJ06013) in front of the vacuum chamber

and the values were ~ 2 J/m^2 and ~ 50 J/m^2 for excitation and ionization steps respectively.

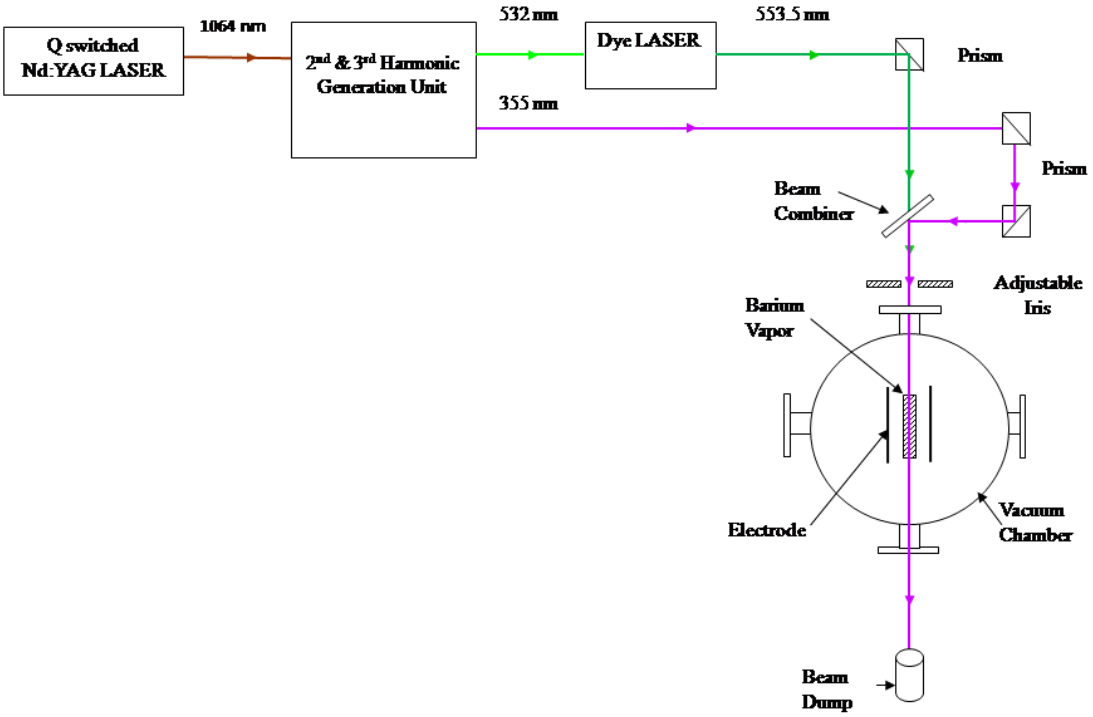

Figure 2.5: Schematics of laser systems and laser beam transportations for generation of barium photoplasma through two-step photoionization process.

2.6 Electrostatic Ion-Extractors

The evolutions of barium photoplasma were studied in an electrostatic ion-extractor. Figure 2.6 shows the schematics of an ion-extractor produced by two parallel plate electrodes. The plates had dimensions of 130 mm length, 110 mm height and 2 mm thick. They were placed on both side of the wedge shaped atomic beam with a separation gap of ~ 35 mm. A negative potential was applied on one plate and other one was grounded. It created a uniform electrostatic field between two electrodes. The series resistors (1 kΩ, 2W) were connected to the electrodes. The voltage drop across the resistor was measured to estimate the photoion current flowing in the circuit. The photoplasma was produced at

the center location between the plates. The photoion density in the photoplasma was measured by the method of total charge collection.

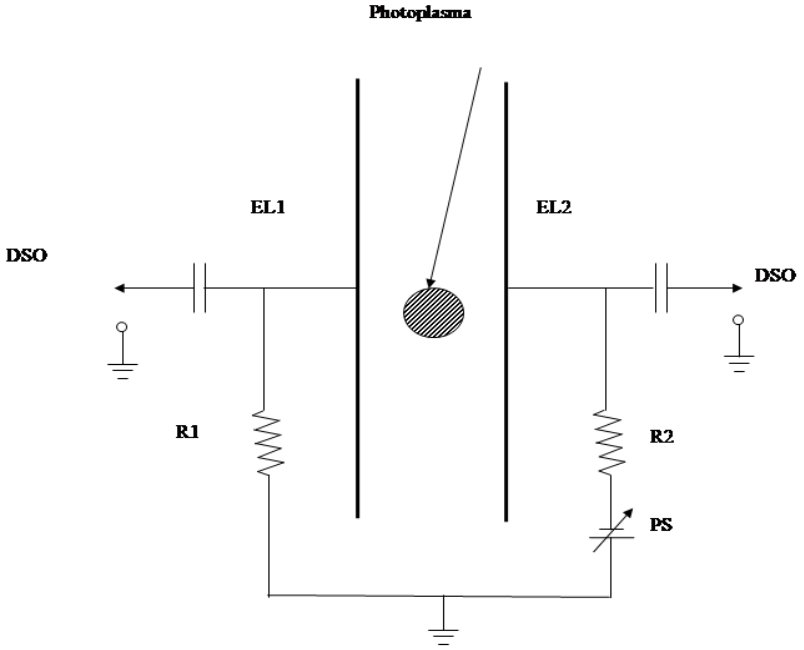

Figure 2.6: Electrostatic ion-extractor produced by two parallel plate electrodes along with electrical circuit diagrams to measure the photoionization signals.

The pulsed photoionization signal was recorded on an oscilloscope of 100 MHz bandwidth (make: Tektronix, model: TDS 224) which was triggered with the Q-switch pulse of Nd: YAG laser. The integrated area of the photoionization current signal provided the total photoions collected on the electrode. The plasma density was estimated from the total charge collected on electrodes by knowing the volume of the finite-sized plasma. The plasma density was varied from 10^{12} m^{-3} to 10^{17} m^{-3} by changing the atom density at the laser-atom interaction region.

2.6.1 Plate-Grid-Plate Configuration

To demonstrate the transition of plasma behavior from its single particle kinetics to collective motions, the photoplasma was studied in a linear electrostatic potential well produced by plate-grid-plate configuration. The grid was fabricated on a stainless steel frame (45 mm high x 110 mm wide) with 5 mil tungsten wires horizontally spot welded on it. The grid element was about 1 mm in the vertical direction. The geometrical transmission of grid structure was obtained from the ratio of the open area of frame, which was not blocked by the grid wire to the total area of frame itself. The estimated geometrical transmission factor of the grid was about 75%. The plate electrodes had the dimension of 118 mm height and 140 mm length. The grid frame was mounted on the lower side of the plate having similar dimensions as that of the electrodes so that the laser-interaction zone was at the middle of grid structure. The separation between the plates was 70 mm and the grid frame placed in the middle. Figure 2.7 shows the schematic layout along with the circuit diagram of the plate-grid-plate configuration. The photoplasma was produced between plate No. 1 and the grid at a height that is at the center with respect to the grid in the vertical direction. Physically this configuration created two independent zones (I and II) and they were connected to each other through the grid window. In zone I, the atomic beam traversed and interacted with the laser radiations. The photoplasma was formed in zone I. In zone II, the photoplasma evolved in a clean vapor free environment. To create a linear potential well, the plate no. 1 was grounded through 1 kΩ resistor whereas the grid and plate no. 2 were connected through 1 kΩ resistors with different negative or positive biased voltage. The currents were individually measured across the resistors. The structures of measured current signal showed the nature of the photoplasma motions in the electrostatic wells.

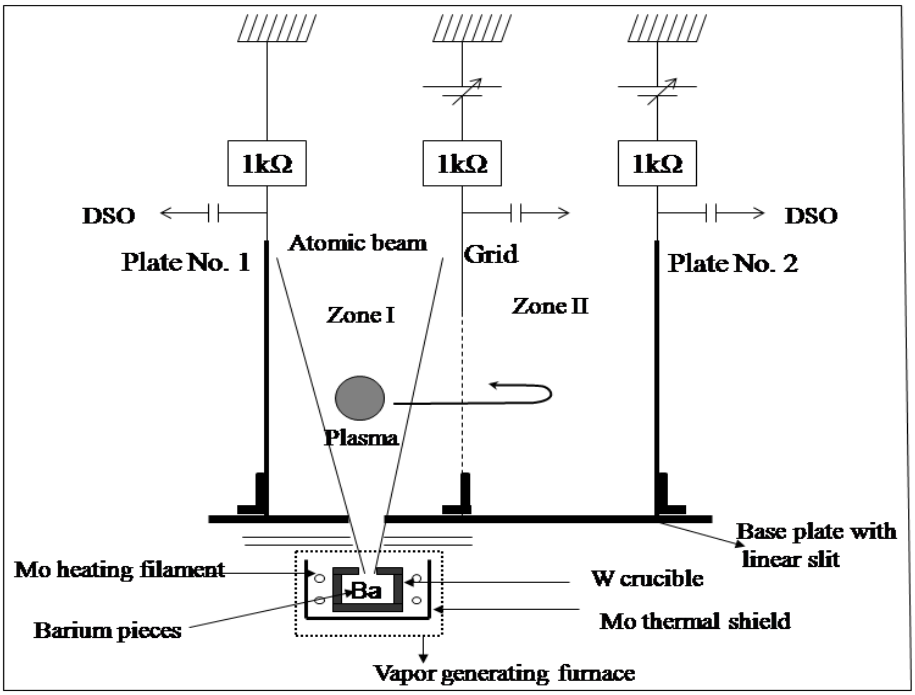

Figure **2.7**: Schematic layout of plate–grid–plate assembly along with signal detection circuit and atomic vapor generating furnace.

2.6.2 Plate-Plate Configuration

To investigate the decay of photoplasma under external electric field, the ion-extractor was produced by two parallel plates. The schematic setup of this configuration is shown in figure 2.8. The Faraday cups were placed behind the electrodes to study the two dimensional evolutions of the photoplasma in the middle cross-sectional plane. A series of five holes having 2.5 mm diameter were drilled along the height. Widthwise the holes were located in the middle of plate no.1. The separation between two consecutive holes was ~ 18 mm along the vertical direction. The lowermost hole was at the height of 20 mm from top of the base plate on which the photoion extractor was supported. A single hole was drilled in plate no.2 at 38 mm height from top of the base plate. It was located at the midway along the width but at the same height as the photoionization region. The Faraday cups behind the plate no.1 were labeled serially from F1 to F5 with

the numbering starting from the bottom. Behind plate no.2 one Faraday cup was placed at the height of F2 and labeled as F6.

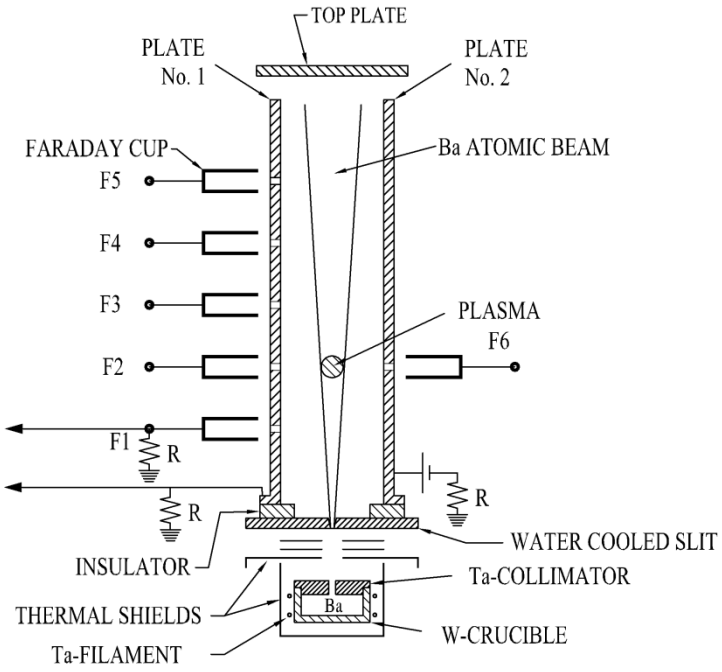

Figure 2.8: Schematics of plate-plate ion-extractor along with Faraday cups for studying the two dimensional evolution of the photoplasma.

Figure 2.9 shows the photograph of Faraday cups placed behind the electrodes in parallel plate assembly. The Faraday cups were designed and fabricated in house. In order to record fast signals faithfully, the Faraday cup had a coaxial design and was assembled on a BNC connector. The Faraday cups were grounded through 10 KΩ, 2W series resistors. The photoionization took place at the height of the F2 and F6. The photoplasma was produced at the centre location between the two plates. A top plate was kept on the above of the two electrodes at 150 mm from the base plate. While the photoions reached at the electrode, some fraction of them were passed through the holes and collected on the Faraday cups. The current signals were individually recorded on the Faraday cups and electrodes by measuring the potential drops across the series resistors using a digital

oscilloscope. The charge collected on Faraday cups provided the two dimensional features of finite-sized photoplasma motions.

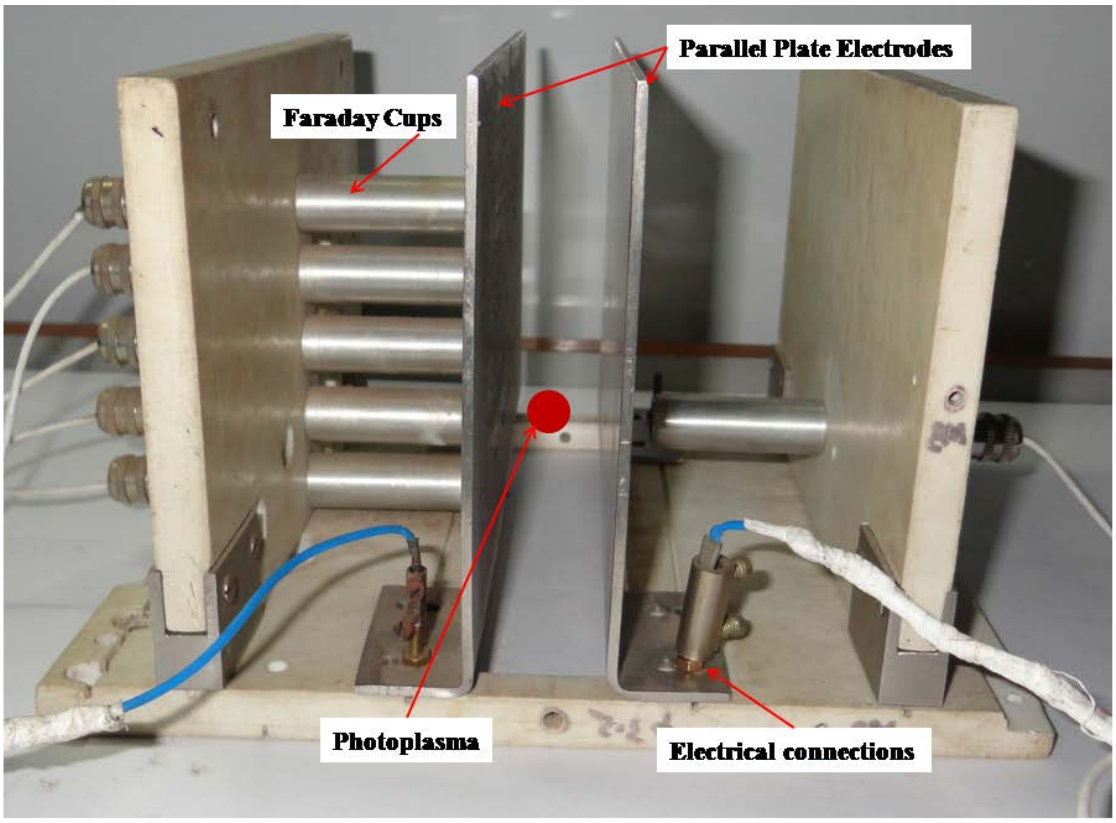

Figure 2.9: Photograph of Faraday cups arrangements placing behind the electrodes in parallel plate assembly.

2.7 Summary

The details of various sub-systems used to investigate the barium photoplasma motion have been described. Using the atomic vapor source a long collimated and wedge-shaped barium atomic beam has been produced. The integrated atom density in the atomic beam has been measured by the optical absorption based sensor. With the help of laser systems, a finite-sized cylindrical shaped photoplasma has been created inside the atomic beam through two-step photoionization scheme. The photoplasma evolution has been studied under electric field with plate-plasma-grid-plate configuration and plate-plasma-plate

configuration. Using a series of Faraday cups placed behind the extractor plates, the two dimensional features of photoplasma evolution have been investigated.

Chapter 3

Long Collimated Atomic Beam: Design, Generation and its Characterization

This chapter describes in details the design, generation and its characterization of a long extended atomic beam. Starting from the vapor flow under collision-free conditions through a single finite-length cylindrical channel to the characteristics of a linear array of multichannel has been discussed. Parametric studies of various parameters like aspect ratio of the channel, inter-channel separation, beam width and vertical height from the source plane etc have been carried out to optimize the design. Based on the design parameters, the atom source has been fabricated. Using the atom sources, a long collimated atomic beam of barium element has been generated. The line of sight averaged atom density in the barium atomic beam has been measured by an optical absorption method. The measured values have been compared and validated with the values obtained from theory.

3.1 Introduction

Since atoms have the least inter-atomic interactions among themselves in their vapor phase, they behave as isolated particles in the ensemble. They allow an excellent platform for many detailed studies of their properties as well as their interactions with particles and fields. Thus an atomic vapor source plays an important role in many areas of atomic physics, chemical physics and surface science. The atomic vapor sources are designed in several ways depending upon their uses. In the applications of laser based isotope separation and material purification, the primary object is to get a clean and resolved atomic spectra of the interested isotopes or elements so that the photoplasma of the

selected species is only produced by multistep resonant photoionization method. In vapor phase, the atoms provide relatively the clean spectra of the element than that in their liquid phase or solid phase. In general the isotope shift of the element is masked by the Doppler width in its vapor phase. Therefore it is necessary to reduce the Doppler width less than the isotope shift for selection of a particular isotope from its mixture [Letokhov et al, 1977]. Doppler width can be decreased through reducing the width of thermal velocity distribution by allowing the vapors to flow through the long channel. The vapors get directed flow in the vertical direction and produce an atomic beam with less Doppler width from that of source. The atoms are further collimated by a narrow rectangular slit or aperture and the Doppler width of vapors again reduces in the collimated atomic beam.

In photoplasma study, a long extended atom source having a uniform atom density along its length is preferred for better utilization of the incident photon flux in an efficient way. The spot size of the incident laser beam is decided by the width of atomic beam. The maximum permissible number density of the atomic beam is decided by the process of resonance charge exchange [Greenland, 1990] between the selectively produced photoions and the neutral background atoms in the atomic beam. There should be no inter-atomic collisions among themselves in the atomic beam because it can populate some low lying states or meta-stable states. In such cases, more than one laser is required in the first excitation step to address all the atoms from their ground state and other low-lying populated states. Hence it is desirable that the atomic beam has collision-less vapor flow and a large fraction of atoms reside in their ground level. In view of the above considerations, an important objective of photoplasma studies is to design an appropriate atom source. It should have the features like long, narrow width, collimated atomic beam that is collision less and has uniform atom density distributions over its dimensions.

In the following sections, the designs of a linear array multichannel atom source, generation of a long collimated atomic beam using the atom source and measurement of average atom density in the atomic beam are described.

3.2 Design Principles of a Linear Array Multichannel Atom Source

3.2.1 Collision-Free Flow through a Cylindrical Channel

Let us consider an enclosed vapor reservoir (i.e. crucible) kept at temperature T and number density n_0. The reservoir is connected to an evacuated vessel through a finite-length channel or tube. The vapor pressure inside the crucible is kept low enough to maintain the condition of molecular flow through the channel. It means that the collision mean free path (λ~ cm) among the neutral atoms is large compared to the dimensions of tube (~mm). The vapors move without undergoing any collision during their passage through the channels as well as their movement within the atomic beam. The vapor flow through a tube was first researched by Knudsen [1909] and Smoluchowski [1910]. For a cylindrical channel of length L and radius r, the Knudsen numbers: $K_{nd} = \frac{\lambda}{2r}$, $K_{nl} = \frac{\lambda}{L}$ determine the nature of vapor flow through the channel. The values of K_{nd} and K_{nl} are chosen to greater than unity and the flow is considered as molecular flow. The source is operated in the transparent mode [Giordmaine and Wang, 1960] which physically signifies that the atoms can enter and exit the tube without suffering any inter-atomic collisions. Only atom-wall collisions occur.

Here all theoretical calculations are confined to such type of sources. Figure 3.1 shows the schematics of geometrical configurations used for the calculation of vapor flow through a cylindrical channel. The atom density is estimated at a point P which is at distance R from the source and at angle θ with the normal.

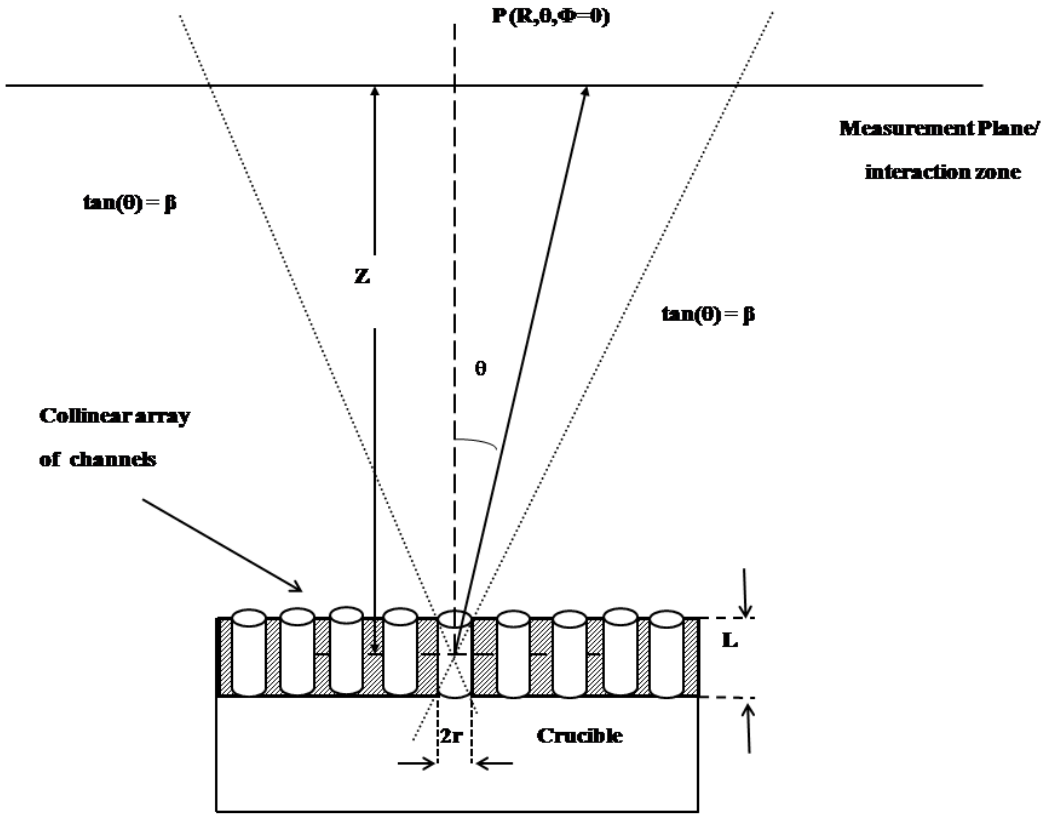

Figure 3.1: Schematics of geometrical configurations for estimating the atom density at any point P from a multi-channel atom source.

The relevant formulae to estimate the barium atom density at point P are ordered below [Scoles, 1988 and Majumder et al, 2009]:

$$\mathrm{Log}(P_{atm}) = 4.478 - \frac{8798}{T(K)} \tag{3.1}$$

$$P = n_0 K_B T \tag{3.2}$$

$$I(\theta) = \frac{n_0 v A}{4} j(\theta) \tag{3.3}$$

$$j(\theta) = \alpha\cos\theta + \frac{2}{\pi}\cos\theta\left[(1-\alpha)R(q) + \frac{2}{3q}(1-2\alpha)\left\{1-(1-q^2)^{\frac{3}{2}}\right\}\right] \quad \text{if } \tan\theta \le \beta \tag{3.4}$$

$$j(\theta) = \alpha\cos\theta + \frac{4}{3\pi q}(1-2\alpha)\cos\theta \quad \text{if } \tan\theta > \beta \tag{3.5}$$

$$\text{Where } q = \frac{\tan\theta}{\beta} \text{ and } R(q) = \cos^{-1} q - q(1-q^2)^{1/2} \tag{3.6}$$

$$\alpha = \frac{1}{2} - \frac{1}{3\beta^2}\left(\frac{1-2\beta^3+(2\beta^2-1)(1+\beta^2)^{\frac{1}{2}}}{(1+\beta^2)^{\frac{1}{2}}-\beta^2\sinh^{-1}\left(\frac{1}{\beta}\right)}\right) \quad (3.7)$$

$$n_a(R,\theta,\varphi=0) = \frac{I(\theta)}{vR^2} \quad (3.8)$$

P is the saturated vapor pressure of barium [Barin,1989] at crucible temperature T, K_B is Boltzmann constant, n_0 is the atom density at the source, v is mean thermal velocity of the atoms and A is cross-sectional area of the channel. I(θ) denotes the angular distribution of atom flux while j(θ) is the angular distribution function. β represents the aspect ratio of the channel and it is defined as β = (2r/L). The parameter α denotes the rate of wall-atom collisions at the exit plane of channel and it is a function of β as represented by Eq. 3.7 due to Clausing [1930]. The atom density at point P (Fig. 3.1) is denoted by n_a. For the regions of tan θ ≤ β [Eq. 3.4], the atoms can reach the point P in two ways: directly from the source without striking the wall and through reflection from the walls. On the other hand, when tan θ > β [Eq. 3.5], only atom-wall collisions contribute to reach the atoms at point P.

3.2.2 Flow Characteristics of a Single Channel

The characteristics of vapor flow through the channel purely depend on its aspect ratio (β). For different β value, the variations of angular distribution function i.e. j (θ) are shown in figure 3.2. It is observed that the distribution is more peaked in forward directions for the lower β value. As the value of β increases, the distribution widens. Asymptotically it tends towards the cosine distribution as the β value tends to infinity. Therefore it is always preferred to choose the low β value to produce a collimated atomic beam. Figure 3.3 shows the variation of half width at half maxima (HWHM) of the angular distribution (i.e. $\theta_{1/2}$) with β. It basically provides the divergence of vapor flow through the channel. The HWHM increases with the increase of β and in the limiting case

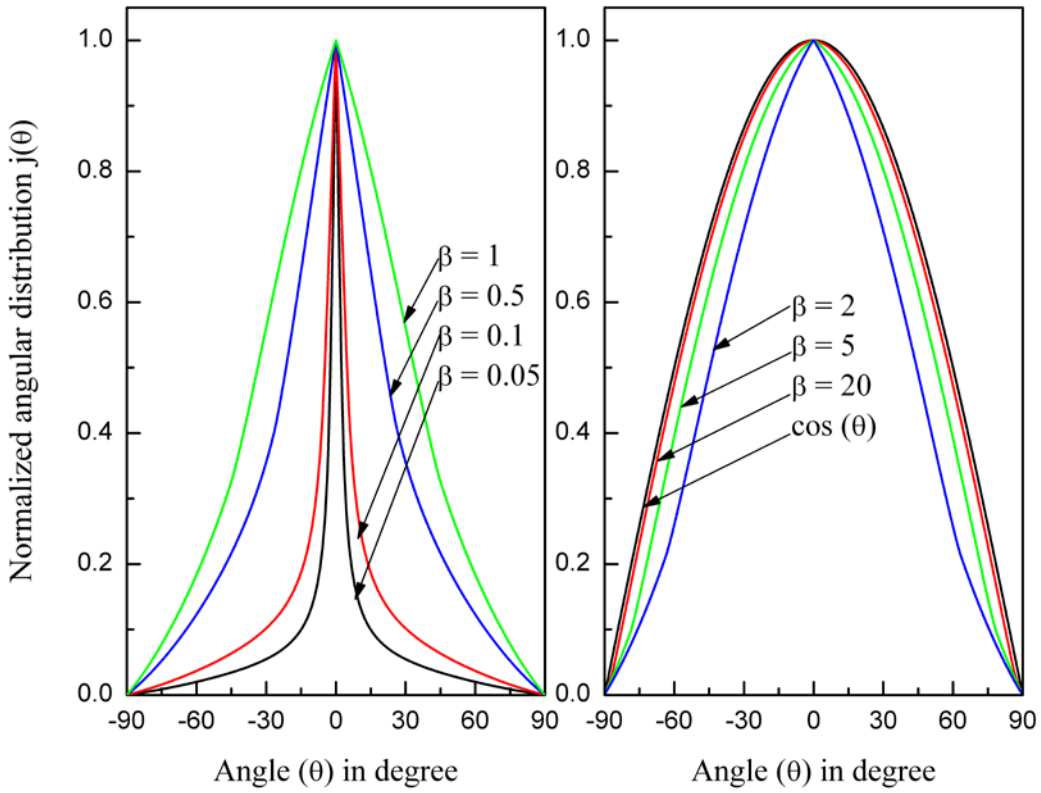

Figure 3.2: Normalized angular distributions of atoms diffused through a single cylindrical channel for different β values of the channel.

of thin orifice, it tends to π/3. For β << 1, the dependence of $\theta_{1/2}$ is given by a linear expression: $\theta_{1/2} = 0.83\ \beta$ [Scoles, 1988]. The divergence of vapor flow is easily estimated from its β value of the long tube.

When the vapors pass through the channel, the ratio of vapor fluxes at the exit plane to entry plane of the channel is defined as transmission probability (W). It is estimated from the expression (3.9)

$$W = \frac{\int I(\theta) d\theta}{0.25\, n_0 v\, A} \qquad (3.9)$$

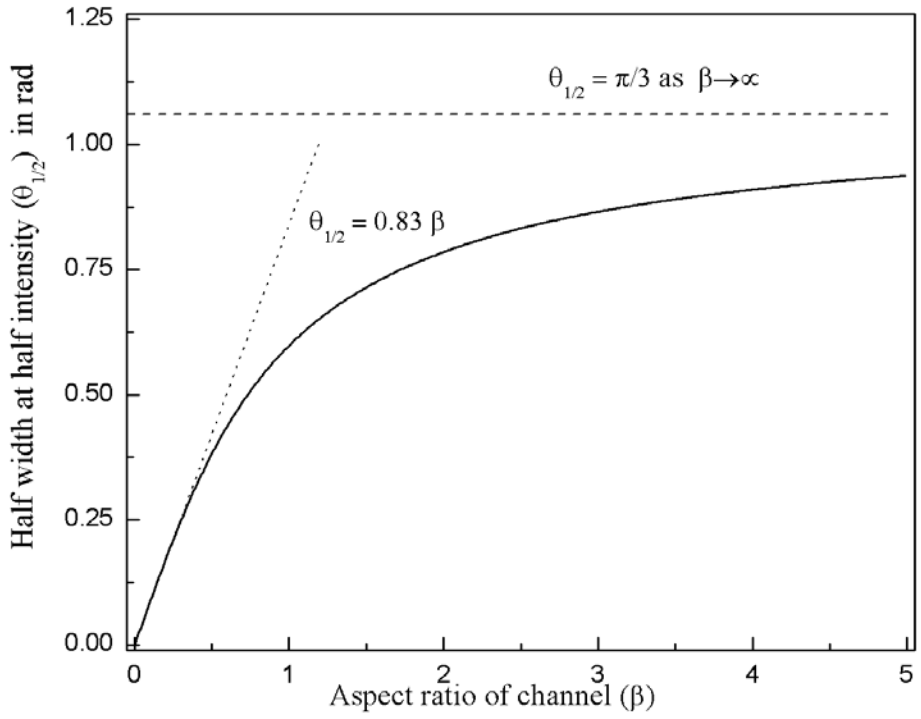

Figure 3.3: Variation of half width at half intensity (i.e. $\theta_{1/2}$) of angular distribution as a function of β.

All parameters were defined in an earlier paragraph. Figure 3.4 shows the change of channel's transmission probability with its β value. It increases as the β value increases and tends to unity for the thin walled orifice. For the long channel, as β→0 the transmission probability decreases and its limiting value is $\frac{4\beta}{3}$. The increment of β value increases both the transmission probability and the divergence of vapor flow in the atomic beam. In other words the collimation of atomic beam decreases. Therefore to make a collimated atomic beam, one has to choose the β value appropriately.

3.2.3 Linear Array of Channels

A linear array of channels is used to make a long extended atom source. Three test examples of linear-array source are considered: (a) single cylindrical channel of β = 0.4

placed at the centre, (b) three identical collinear cylindrical channels of β = 0.4 symmetrically placed with respect to the centre and (c) three channels with the middle one of larger aspect ratio (β = 0.8).

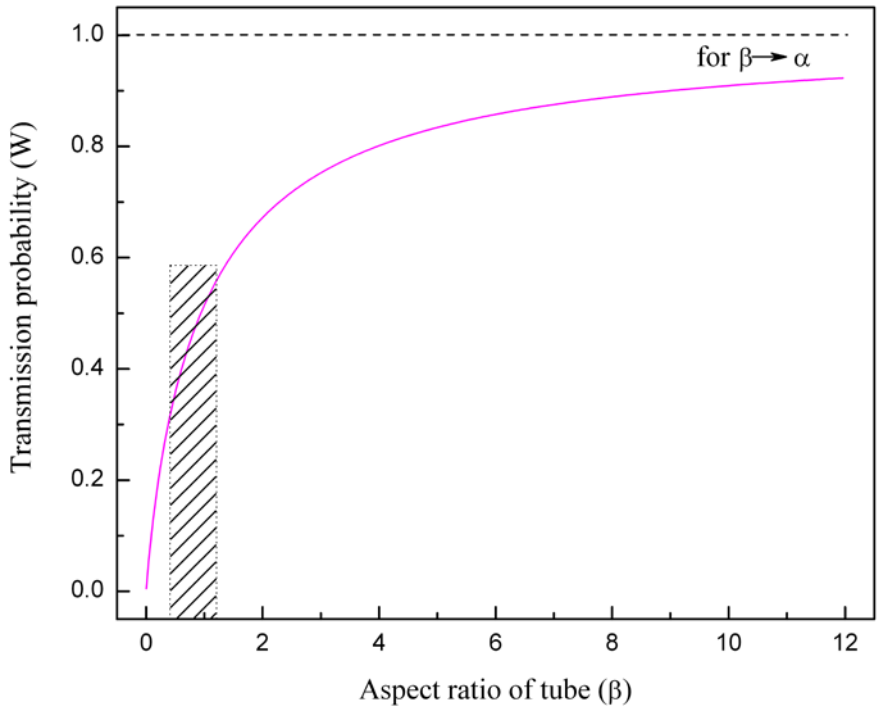

Figure 3.4: Variations of channel's transmission probability with its aspect ratio.

The density distribution at the height of Z = 0.07 m from the source plane are shown in figure 3.5 for the above three cases. The structure of the density profile for a single tube (figure 3.5 (a)) is highly peaked at the centre. Figure 3.5 (b) indicates that the length of the beam increases with increase in the number of channels. Contribution from individual channels adds up.

The role of larger β (= 0.8) of the central channel is clearly noticed from figure 3.5 (c). Due to its larger divergence, it 'makes up' for the low value of density along the length as contributed from a lower β channel. For example, the dip in the density profile in figure 3.5 (b) between 0 to ± 0.02 m is compensated by the central channel thereby

generating the atomic beam to be more uniform along its length. To estimate the elliptical channel's density profile along the direction of its major axis, the elliptical channel is replaced by an equivalent cylindrical channel having same diameter with appropriate cross-section area.

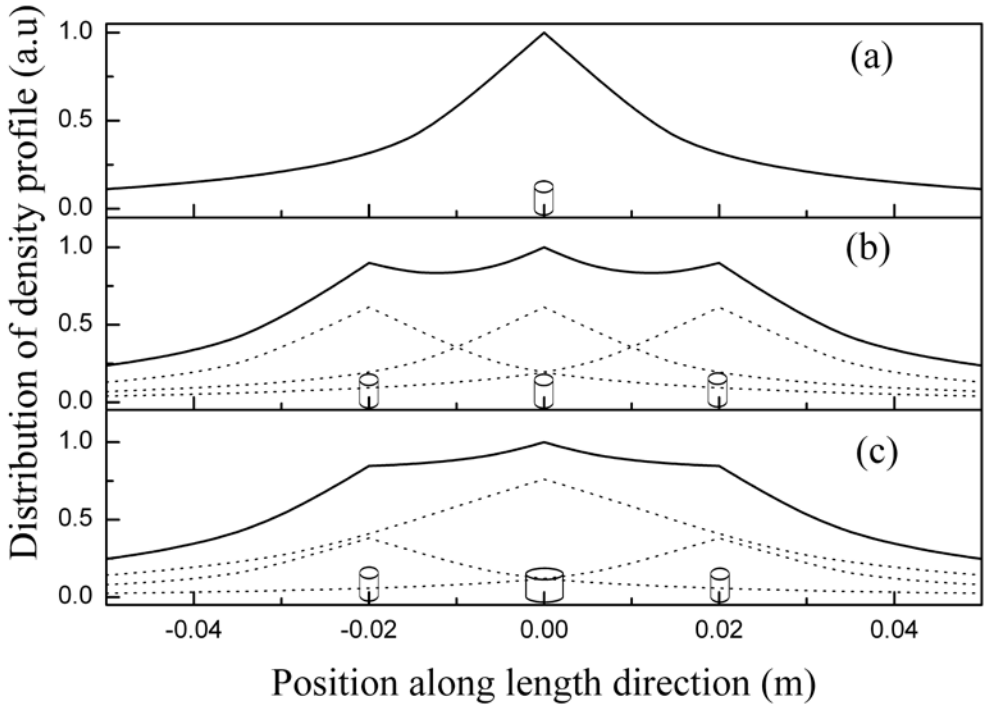

Figure 3.5: Density distribution profile along the length of atomic beam: (a) single channel of β=0.4, (b) three identical channels of β=0.4 and (c) channels with centre one having larger aspect ratio of β=0.8.

3.2.4 Inter-Channel Separation

Inter-channel separation (i.e. centre-to-centre) plays an important role in atom density distribution profile. Figures 3.6(a) and 3.6(b) depict the variation of FWHM of atomic beam and average atom density as a function of relative spacing of the central and end channels as calculated for the case of figure 3.5 (c). It is observed that though the FWHM increases with the increase of inter-channel spacing but the average density

decreases. Both vary linearly. So to attain a high density and a long atomic beam with uniform atom density profile, a compromise in the inter-channel separation is essential.

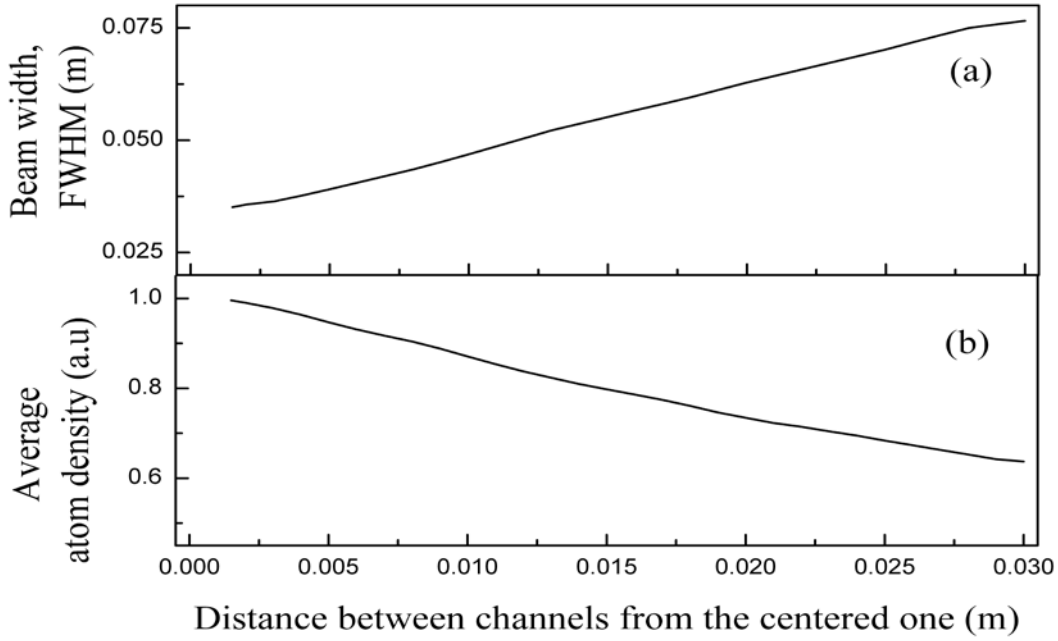

Figure 3.6: (a) Variation of beam-width (FWHM) and (b) average atom density with relative distance between the central channel and the end channels for the case of Fig. 3.5 (c)

3.2.5 Linear Array Multichannel Atom Source

Since we are interested to generate a long extended atomic beam, the above parametric analysis has guided us to design the source in the following manner: 31 collinear channels were drilled on the crucible lid along the mid-section of its length as discussed in section 2.2. The spacing between channels was ~ 0.5 mm. The central one had the largest β (= 1.2) and the rest were symmetrically placed about it. There were three other groups of β (0.8, 0.6 and 0.4) which were placed in a way such that 0.4 was at the extreme ends, 0.8 was nearest to the central channel while 0.6 was in between. The resultant K_{nd} varied from 1.25 to 4.75 which are greater than unity. Figure 3.7 shows the

atom density distribution along the length of the source at different heights Z = 0.03 m, 0.07 m and 0.11 m.

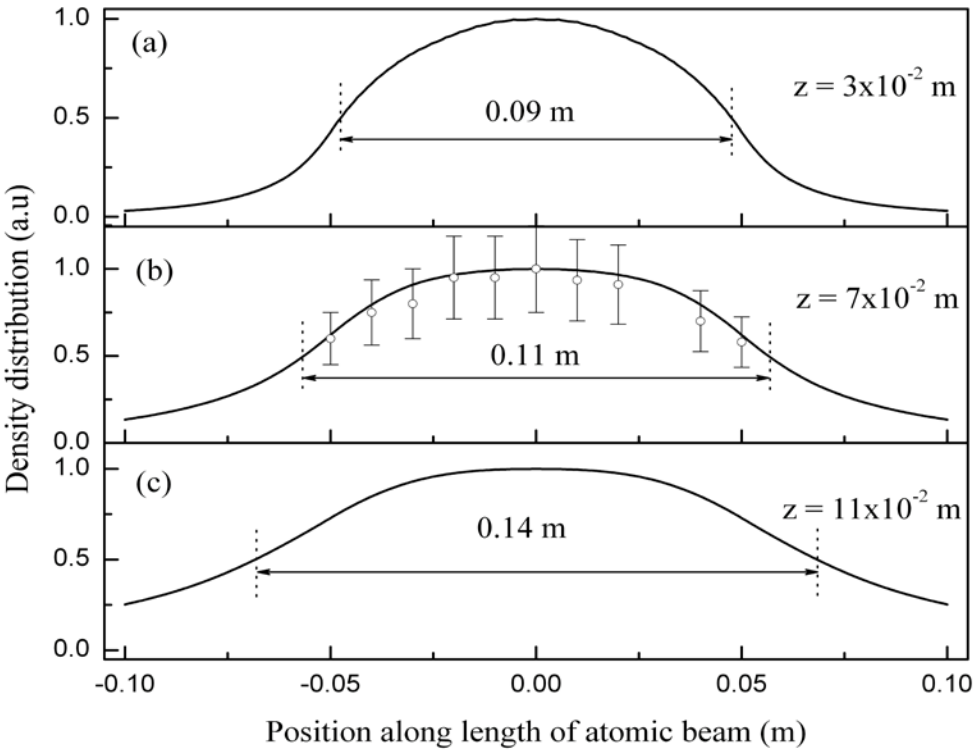

Figure 3.7: Density distributions along the length of atomic beam for a collinear array of 31 channels. (Data points are from the experiments).

The beam lengths are estimated from the full-width-at-half-maximum. Their values are ~ 0.09 m, 0.11 m and 0.14 m respectively. They increase with height from the source plane i.e. the beam is expanding in vertical direction. A distance of z = 0.07 m was chosen as a compromise of the maximum uniform beam length and geometrical constraints of our experimental setup. This large uniformity in the atom density distribution is possible due to the special choice and placement of βs as mentioned above.

The average transmittance is defined as the ratio of n_{avg} at the height of 0.07 m from the crucible to n_0 inside the crucible and it is ~ 0.1% in our case. Thus the linear array of channels generates a long extended atomic source which has a uniform atom density along its length direction. The atomic beam is expanded along the vertical direction.

3.2.6 Average Atom Density with Height from Source

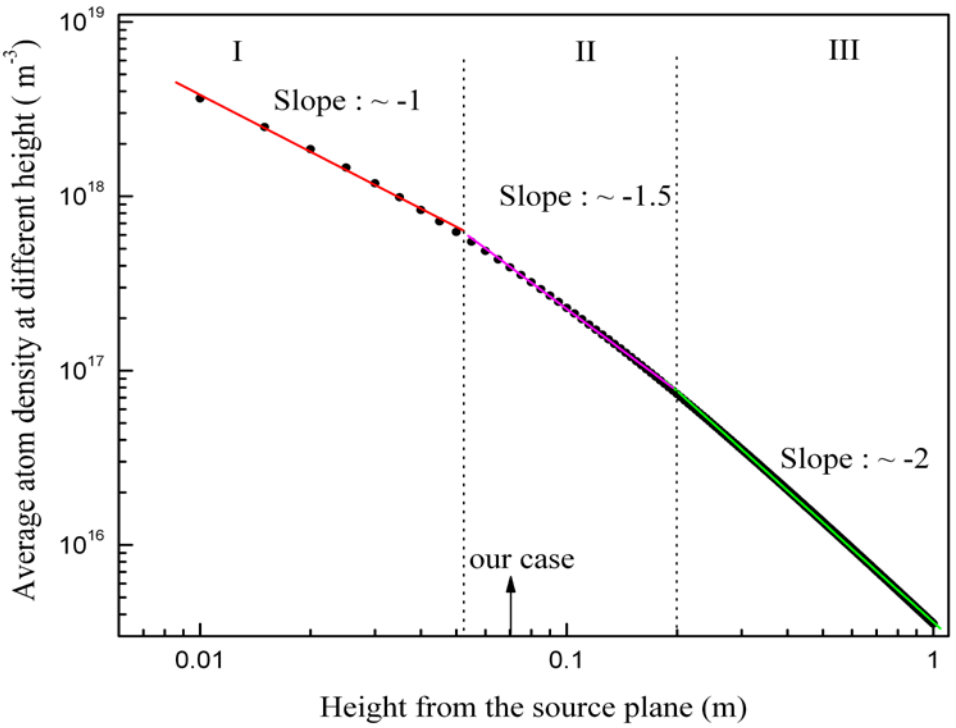

Figure 3.8: Average atom density at various heights from the source.

The atom density is averaged over the length of the atomic beam i.e. FWHM of the atomic beam. The average atom density (n_{avg}) is calculated at different heights (Z) from the source. Its spatial variation with height z is shown in figure 3.8. It is seen that the scaling is $n_{avg} \sim z^{-n}$ where 'n' is the scaling parameter. In the log-log plot of figure 3.8, 'n' represents the slope of the graph which ranges between -1 to -2. The entire height may be divided into three zones for physical understanding: For very low z ($z << L$) in region I, the source appears to be an infinite line and its density varies as z^{-1} [Rogengurd,

1989]. For very large z (z >> L) in region III, the density scales as z^{-2}, a characteristics of a point source. In zone II (z ~ L), the density varies as $z^{-1.5}$ which represents a finite length line source.

3.2.7 Effects of Collimating Slits

To produce a collimated atomic beam with less Doppler width, a base plate having rectangular slit or aperture of 100 mm x 8 mm is placed at a height of ~ 20 mm from the crucible lid. The vapors effused through the channels are further collimated by the slit and its Doppler width is reduced. The plate is kept at relatively lower temperature than the source temperature. The vapors directly striking the plate are lost due to their deposition on the surface. The vapors which are not striking the plate are directly passed through and form a collimated atomic beam. The figure 3.9 shows the length wise variations of atom density in presence and absence of the collimating slit.

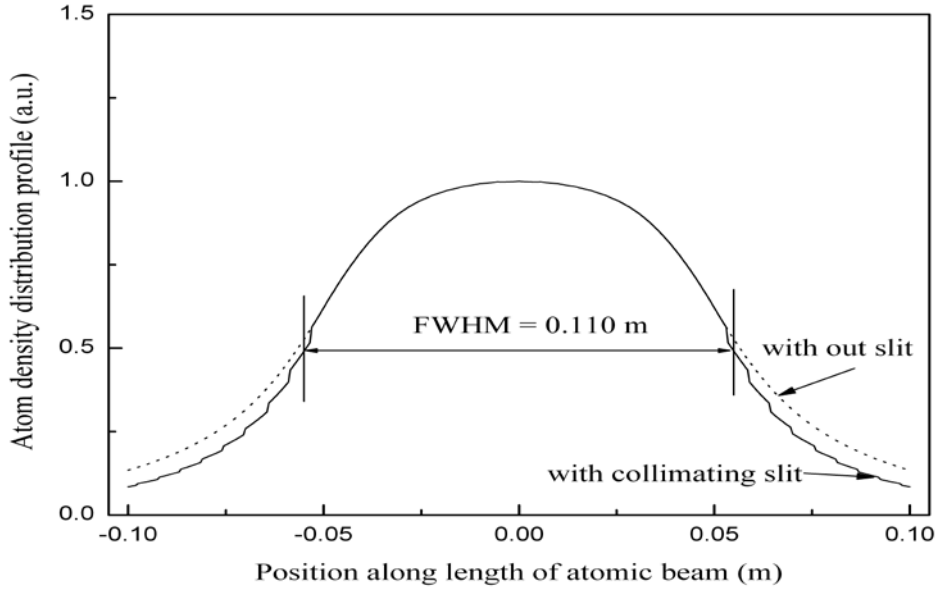

Figure 3.9 Effect of collimating slit in the spatial density distribution of atomic beam along its length direction.

The purpose of collimating slit is also to protect the direct deposition of vapors at different locations due to neutral vapor scattering. The slit does not modify the density distribution profile at the centre portion of atomic beam. In the figure 3.9, the relative distance from the center is plotted in X axis where the origin represents the position of central hole at the source. It shows that the atom density is nearly uniform over a certain length and gradually reduces at the edges of the atomic beam. The length of atomic beam is defined as the distance over which the central value of atom density falls to its 50% value i.e. FWHM of the density distribution. The estimated length of the atomic beam is nearly 0.11 m at the 0.07 m height from the source.

To get the density distribution along the width of atomic beam, the elliptical sources are considered as combination of the multiple cylindrical tubes having aspect ratio of 0.4. The density variation along the width of the atomic beam is shown in figure 3.10. It is almost constant within 90% of its peak value. The estimated width of atomic beam is ~ 25 mm.

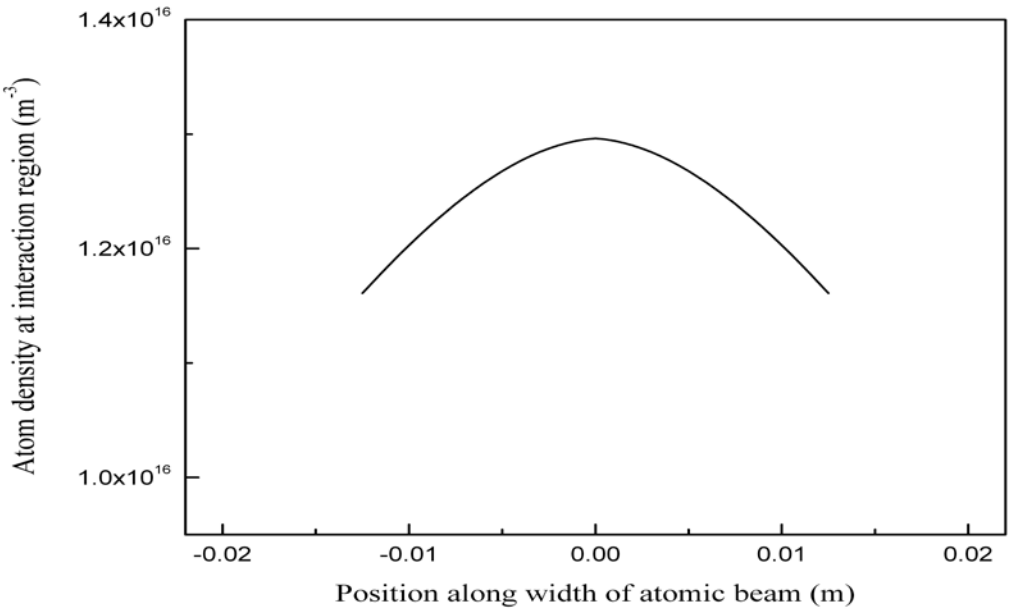

Figure 3.10: Distributions of atom density along the width of atomic beam produced by collinear array.

3.3 Generation of a Long Wedge-Shaped Atomic Beam

The electrical current passes through the filament in a resistively heated furnace. It heats the filament through joule heating. At the high temperature, the thermal radiations from the filament heat the crucible. The temperature of crucible has been measured using a cromel-alumel i.e. K type thermocouple. Figure 3.11 shows the temperature of crucible at different electrical input power fed to the furnace filament. From the plots, it is estimated that the required electrical power to attain the crucible temperature of 1000 K is ~ 1.25 kW. The inset curve in figure 3.11 shows the variation of input power versus temperature in log-log scale.

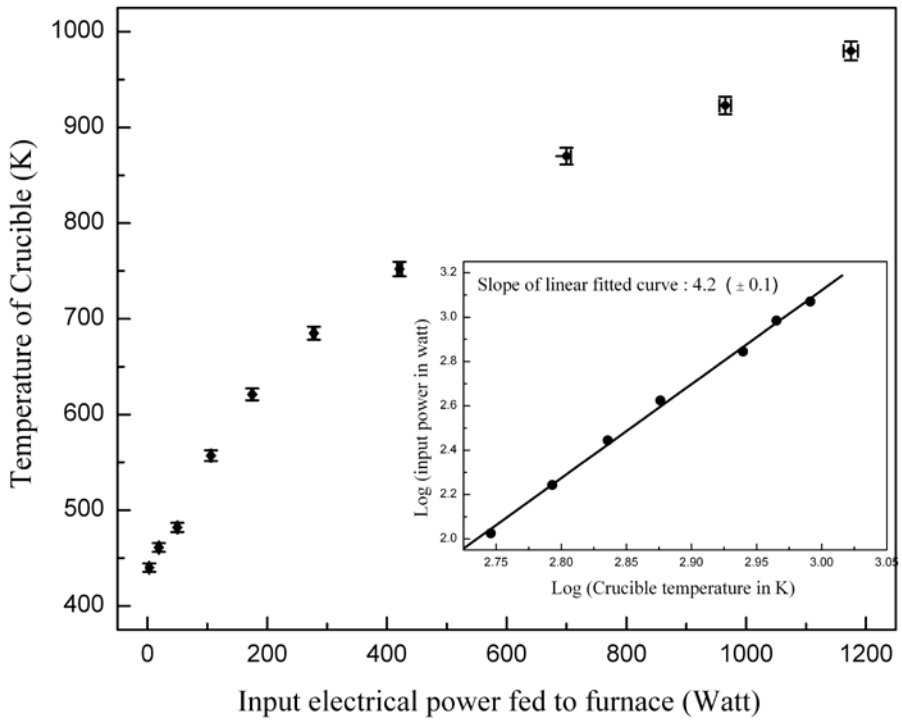

Figure 3.11: Crucible temperature at different electrical power fed to the resistively heated furnace. Same is plotted in log-log scale (inset).

The slope of linear fitted curve is ~ 4.2 (± 0.1). It shows that at equilibrium, the total input power (Q) is nearly proportional to T^4 (i.e. $Q \sim T^4$) where T is the temperature of

hot zone where the crucible was kept. So the crucible is heated mainly through the process of radiation from the filament inside the vacuum chamber. When the crucible is heated to a high temperature (T), the barium metal pieces start to evaporate from the surface of granules kept inside the crucible. The vapors form an enclosed vapor reservoir inside the crucible.

The saturated vapor pressure and the corresponding neutral vapor density of barium at temperature (T) are estimated from the expressions of equation 1 and 2 [Barin, 1989 and Peng et al 2002]. Figure 3.12 shows the variation of neutral vapor density inside the crucible with its temperature. It is estimated that the neutral vapor density (n_0) inside the reservoir is nearly $3.5x10^{20}$ m^{-3} at ~ 1000 K temperature.

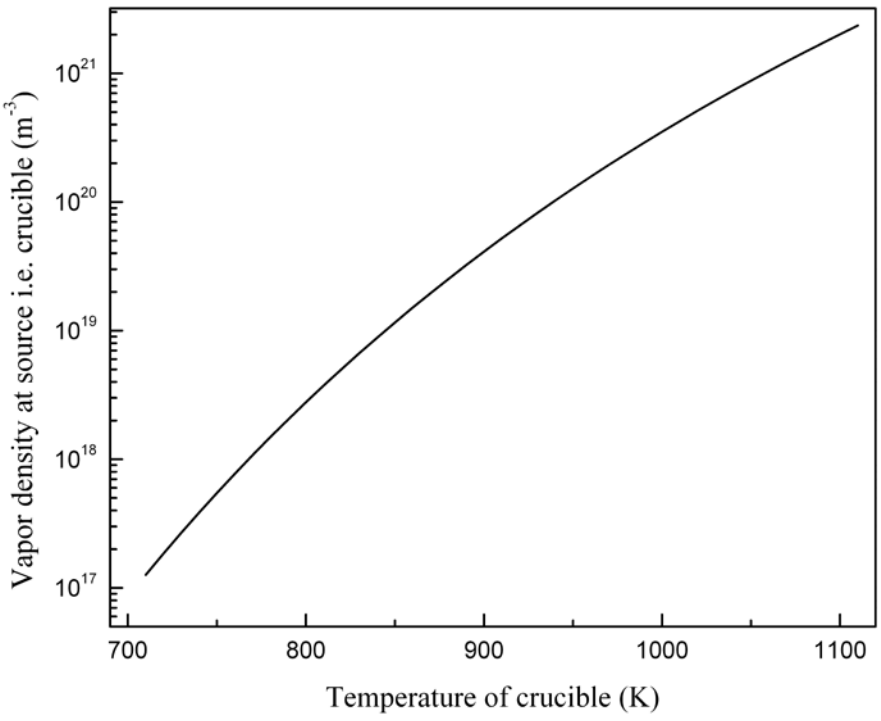

Figure 3.12: Variation of neutral vapor density inside the crucible (i.e. vapor reservoir) with its temperature.

The estimated mean free path of atom-atom collisions at source is ~ 10 mm which is larger than the dimension of channels. The vapors are allowed to effuse through the channels from the crucible to the evacuated vessel. For the cylindrical channels of radius ~ 3 mm and length ~ 5 mm, the Knudsen numbers are K_{nd} ~ 5 and K_{nl} ~ 2. Their values indicate that the barium vapor effuses through channels without undergoing any collisions among themselves.

The vapors are further collimated by a rectangular slit of 100 mm x 8 mm. It expands in the vertical direction and forms a long extended wedge-shaped atomic beam. The beam was characterized in our previous work [Majumder et al, 2009]. The measured atom densities along the length are shown in figure 3.7(b). The atomic beam has the dimension of length ~ 100 mm and width ~ 20 mm at laser-atom interaction region. It has a nearly uniform density distribution over its length. In the expanding beam, the atoms have a flow velocity along the vertical direction. The velocity is nearly equal to the mean velocity of vapor at the crucible temperature.

3.4 Methodology of Atom Density Estimation from Optical Absorption Method

The average atom density inside the atomic beam has been measured by an optical absorption technique using Mitchel-Zemansky [1971] methodology. In this method, the absorbed fraction 'A_s' of the resonant spectral line intensity along the absorption length (L) i.e. length of the atomic beam, is measured by

$$\mathbf{A_s = 1 - \frac{I_t}{I_0}} \qquad (3.10)$$

where I_t and I_0 are the transmitted and incident line intensities. The I_0 is measured in absence of the atomic vapors at the interaction region. The parameter 'A_s' physically denotes the fraction of incoming intensity absorbed in the passage through the atomic beam.

The total intensities integrated over spectral profile for the particular resonant line are given by

$$\boldsymbol{I_o = \int_{-\infty}^{+\infty} I_\sigma \, d\sigma} \text{ and } \boldsymbol{I_t = \int_{-\infty}^{+\infty} I_\sigma \, e^{-k_\sigma L} d\sigma} \quad (3.11)$$

Where σ is the wave number i.e. (σ = 1/λ), I_σ and k_σ are the incident intensity and the absorption coefficient at σ respectively. Then 'A_s' is given by

$$\boldsymbol{A_s = 1 - \frac{\int_{-\infty}^{+\infty} I_\sigma e^{-k_\sigma L} d\sigma}{\int_{-\infty}^{+\infty} I_\sigma d\sigma} = \frac{\int_{-\infty}^{+\infty} I_\sigma (1 - e^{-k_\sigma L}) d\sigma}{\int_{-\infty}^{+\infty} I_\sigma d\sigma}} \quad (3.12)$$

It is assumed that the absorption line profiles in the atomic beam are purely Doppler profiles. Then the absorption coefficient k_σ is expressed as

$$\mathbf{k_\sigma = k_{\sigma 0} e^{-\omega^2}} \qquad \text{with} \quad \boldsymbol{\omega = \frac{2(\sigma - \sigma_0)}{\Delta \sigma_D} \sqrt{\ln 2}} \quad (3.13)$$

Where $k_{\sigma 0}$ is the absorbing coefficient at the center line wave number and $\boldsymbol{\Delta\sigma_D}$ is the Doppler width of the absorption profile in the atomic beam. According to Mitchell-Zemansky, when the emission and the absorption line width of spectral profile are different, the source intensity (I_σ) is given as

$$\boldsymbol{I_\sigma = I_{\sigma 0} e^{-(\frac{\omega}{\gamma})^2}} \quad (3.14)$$

Where $\gamma = (\Delta\nu^S)/(\Delta\nu^B)$, is the ratio of the full widths at half-intensity of the emitting light source ($\Delta\nu^S$) and that of the absorbing atomic beam ($\Delta\nu^B$). A hollow cathode lamp (Ba-HCL) is used as an emission source. The intensity profile of the emission line from the HCL is considered as Gaussian profile. It is assumed that the Doppler broadening is larger than the collision broadening. The influence of self-absorption in the profile is negligible. From equation (3.12), (3.13) (with $\Delta\nu^D = \Delta\nu^B$) and (3.14), it is deduced that

$$\mathbf{A_s = \frac{\int_{-\infty}^{+\infty} e^{-(\frac{\omega}{\gamma})^2} (1 - e^{-k_\sigma L}) \, d\sigma}{\int_{-\infty}^{+\infty} e^{-(\frac{\omega}{\gamma})^2} d\sigma}} \quad (3.15)$$

The equation (3.15) is expressed in the following series:

$$A_s = \sum_{n=1}^{\infty} \frac{(-1)^{n+1}(k_0 L)^n}{n!(1+n\gamma^2)^{1/2}} \quad (3.16)$$

In the atomic absorption profile, when the Doppler width dominants over the other broadening, the optical length "K_0L" is related with the average atom density (n_a) by the following expressions [Mitchel-Zemansky, 1971].

$$\mathbf{k_0 L} = \frac{2}{\Delta\nu^D}\sqrt{\frac{\ln 2}{\pi}}\left(\frac{\pi e^2}{m_e c}\right)\frac{1}{4\pi\epsilon_0} f_{ul} n_a L \quad (3.17)$$

Where $\Delta\nu^D$ is the Doppler width at the resonant absorption line, m_e is the mass of electrons, c is velocity of light, ε_0 is the free space permittivity, f_{ul} is oscillator strength (dimension-less quantity) of the transition and n_a is the atom density at the interaction region. All parameters are in SI units. Putting the value of different constants, the expression in equation (3.17) can be written as

$$\mathbf{k_0 L} = 2.49\mathbf{x}10^{-6}\frac{f_{ul} n_a L}{\Delta\nu_B} \quad (3.18)$$

The atom density (n_a) is estimated in the following steps. First, the co-efficient 'A_s' has been estimated from the measurements of integrated line intensity (equation 3.10). Then the optical length 'K_0L' is calculated from the 'A_s' value (equation 3.16) and at last the average atom density is estimated using equation (3.18), provided the length of interaction zone i.e. length of the atomic beam is known.

3.5 Measurement of Averaged Atom Density inside the Atomic Beam

The line of sight averaged atom density of barium atomic beam has been experimentally measured by a barium hollow cathode lamp (Ba-HCL) based optical absorption method. The details of experimental setup were described in section 2.3. The light emitted from Ba-HCL has been guided and it passed through the barium atomic beam. The transmitted intensity of BaI resonant line 553.5 nm has been measured in the presence and in the absence of atomic vapors at the interaction region. From their ratio,

the absorption coefficient 'A_s' has been estimated using equation 3.10. Figure 3.13 shows the variation of absorption coefficient 'A_s' with optical length 'K_0L' for various value of γ where γ denotes the ratio of FWHM of emission and absorption spectral profile respectively.

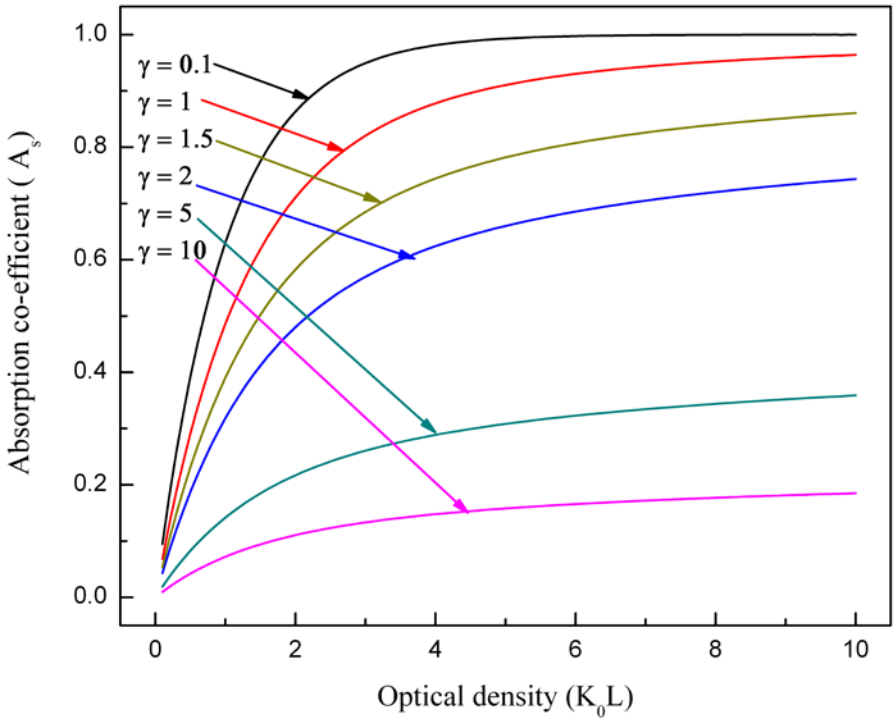

Figure 3.13: Variation of absorbance 'A_s' with optical density (K_0L) for various value of γ.

The line width absorption profile of atomic beam and emission profile from Ba-HCL for 553.5 nm resonant line are estimated as follows. The spectral width of absorption profile ($\Delta\nu^B$) in the collimated and collision-free atomic beam is the convolution of different widths like natural line-width ($\Delta\nu_{NL}$), line-width due to isotope shifts ($\Delta\nu_{IS}$), hyperfine structure ($\Delta\nu_{HF}$) and Doppler width ($\Delta\nu_D$). In our case, the value of various line widths are $\Delta\nu_{NL}$ ~ 20 MHz, $\Delta\nu_{IS}$ ~ 125 - 250 MHz and $\Delta\nu_{HF}$ ~ 300 MHz. Due to the collimation of vapors in the atomic beam, the Doppler width is reduced in the transversal direction [Demtroder, 2002]. The estimated reduced Doppler width ($\Delta\nu_D$) is

nearly 540 MHz at 850 K temperature. The width of absorption profile is expressed as $\Delta\nu_{ABS} = \sqrt{(\Delta\nu_{NL})^2 + (\Delta\nu_{IS})^2 + (\Delta\nu_{HF})^2 + (\Delta\nu_{D})^2}$. The calculated absorption width ($\Delta\nu^B = \Delta\nu_{ABS}$) of the atomic beam is ~ 0.65 GHz at the above resonant line.

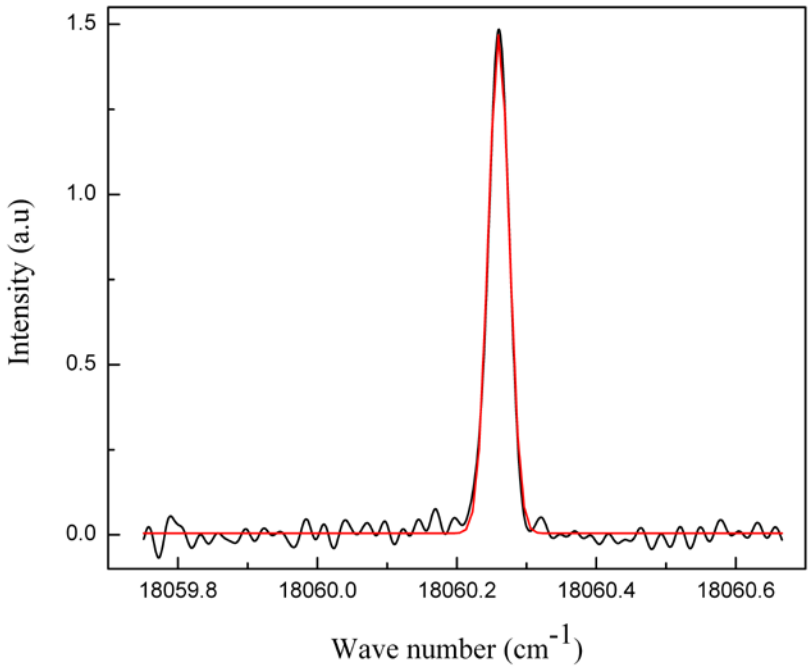

Figure 3.14: Emission profile of barium 553.5 nm resonant line when Ba-HCL is operated at ~15 mA current.

The emission line width ($\Delta\nu^S$) of 553.5 nm line from Ba-HCL operated at ~15 mA current has been measured using a high resolution spectrometer (make: Bruker, model: IFS125 HR) and it is shown in figure 3.14. It clearly shows that there is no signature of self-absorption in the emission profile at the above operating current value. The curve is fitted with Gaussian profile (i.e. distribution of Doppler profile) shown by red line and the estimated line width is ~ 1.06 GHz (i.e. 0.0354 cm^{-1}). It indicates that the Doppler broadening (Gaussian profile) dominates over the collisions broadening of Lorentzian distribution profile.

The estimated γ value is nearly 1.5 in our experimental set up. For γ ~ 1.5, the dynamic range of optical length (k_0L) approximately corresponds to the value of 'A_s'

from 0 to 0.75 as shown in figure 3.13. Beyond the values of $A_s \sim 0.75$, the accuracy in the evolution of k_0L decreases and hence the value of n_a becomes poorer. Even in the above dynamic range, the error mainly occurs in the measurement of transmitted intensity. The intensity is measured by an optical device like PMT where the noise (ΔI_t) is proportional to the square root of the incident intensity (i.e. $\boldsymbol{h\sqrt{I_t}}$ where h is a proportional constant). The percentage error in the atom density measurement is estimated from the following relation assuming the Beer's law is obeyed [Bauman, 1962] and its variation with the absorption coefficient 'A_s' is shown in figure 3.15.

$$\frac{\Delta n_a}{n_a} = -\frac{\Delta I}{I_t \ln\left(I_0/I_t\right)} \tag{3.19}$$

$$\frac{\Delta n_a}{n_a} = -\frac{h\sqrt{I_t}}{I_t \ln\left(I_0/I_t\right)} \tag{3.20}$$

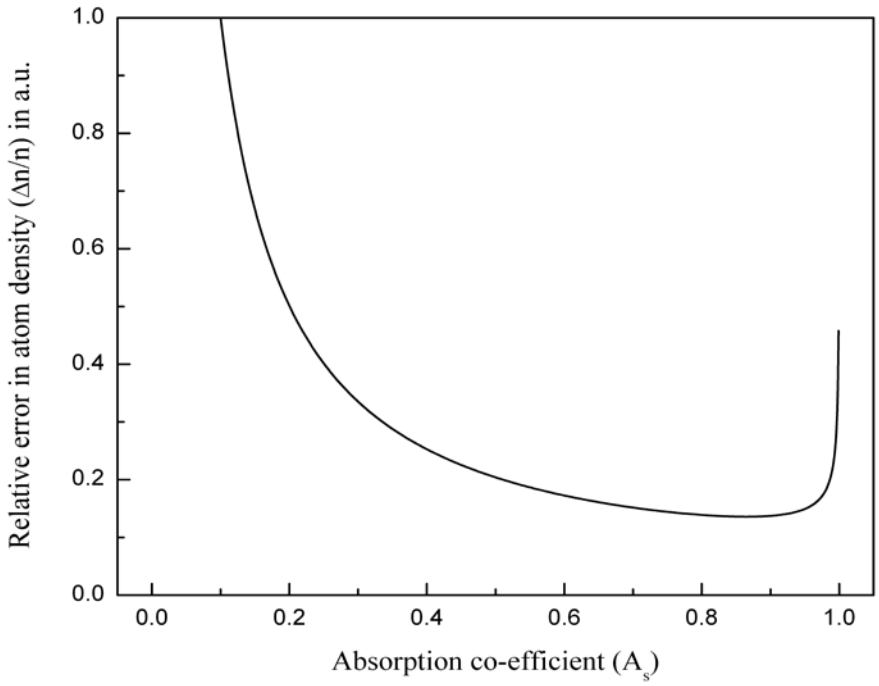

Figure 3.15: Relative instrumental error (i.e. Δn/n) in measurement of atom density against the absorption coefficient as the intensity is measured by photo-emissive detector like PMT.

In order to use the absorption method with minimum error, the experimental datas are chosen carefully such that the co-efficient 'A_s' is to be kept between 0.3 and 0.75. From the linear relationship (i.e. equation 3.18), the average atom density (n_a) in the atomic beam has been estimated. The atom densities are measured with 25% error at various crucible temperatures. The measured values of atom density at different crucible temperature are shown in figure 3.16. The same is also estimated theoretically using the set of analytical expressions discussed in section 3.1.2and its variation is also shown in same figure by the line. The values match in good agreement. From the comparison between figure 3.12 and figure 3.16 at a given temperature, it is observed that the neutral atom density at the interaction region is nearly three orders less than in the crucible.

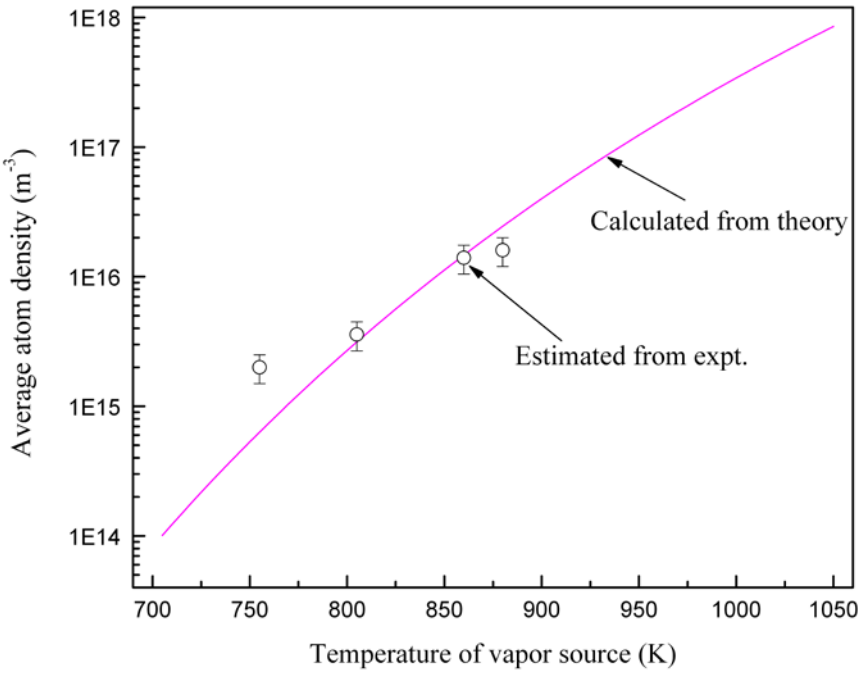

Figure 3.16 Measured average atom density in the laser-atom interaction region at different source temperature.

3.6 Summary

The theoretical basis of designing a liner array multichannel atom source has been discussed. Parametric studies of various design parameters like aspect ratio of the channel, inter-channel separation, beam width and vertical height from the source plane have been carried out. The atom sources are operated in the transparent mode of a long tube regime. The roles of linear array multi-channels have been mathematically computed. Using the atom source, a long wedge-shaped collimated and high density barium atomic beam has been produced. The atomic beam has a length of ~110 mm and width of ~25 mm at the height of ~ 70 mm from the crucible lid. The average atom density has been measured by Ba-HCL based optical absorption technique. The measured values have been compared with the values obtained from theoretical estimation. They are in reasonable good agreement with estimated values.

Chapter 4

Photoplasma Generation and Estimation of Photoionized Yield

This chapter discusses the generation of a finite-sized barium photoplasma through two-step photoionization (TSPI) method and the estimation of photoionization yield in optically thick medium of barium. In the first step, barium atoms get resonantly excited by laser radiations from their ground level to intermediate excited level. The excited atoms are subsequently ionized in the second step by another laser radiation. The kinetics of above photoionization process (i.e. TSPI) has been described using the rate equation based model developed for optically thick medium of barium. The estimated photoionization yields from the model are compared with the measured ionization yield.

4.1 Introduction

Today lasers provide the tunable and intense monochromatic radiations of visible and ultraviolet region in the electromagnetic spectrum. The resonant interaction between light and matter via electro-magnetic dipole radiation leads to the technique of laser resonance ionization spectroscopy (RIS). Two processes namely excitation and ionization of atoms are involved in this method. Firstly, a laser pulse resonantly excites a valence electron in the atomic system from its initial ground level to an intermediate excited level. Secondly, other photons, collisions, internal electron-electron interaction (autoionization) or an electric field causes the ionization of the excited atoms. So the RIS is a multi-step photon absorption process in which the final state is ionization continuum of an atom resulting in creation of ion-electron pair from each atom. The ensemble of generated ion-electron pair forms plasma which is known as photoplasma. In the following sections, the generation of barium photoplasma by two-step photoionization process and the detail

kinetics of the generation processes in the optically thick medium of barium are discussed.

4.2 Two-Step Photoionization Method

Two-step photoionization is the simplest scheme of the multi-step photoionization process. It involves the excitation of a resonant intermediate electronic state and the subsequent ionization of the excited atom. It can be achieved using two different lasers, which simultaneously provide the advantages of individual tuning of wavelengths, fixing their intensities, pulse durations, spectral widths etc. The first two-step RIS experiment was performed on ground state of rubidium atoms in a cavity or cell [Ambartzumian and Letokhov, 1972]. Since then the two-step isotope selective photoionization experiments were carried on various elements like uranium [Tuccio et al, 1974], samarium, europium, gadolinium [Karlov et al, 1977], lithium [Arisawa et al, 1982], potassium [Nygaard et al, 1978], titanium [Maruyama et al, 1987], barium [Yamada et al, 1988 and Majumder et al, 2005] and palladium [Derzhiev et al, 2002] etc. The motivation was to do the feasibility studies of isotope selectivity using both continuous and pulse lasers and to separate the particular isotopes having applications in the nuclear industry. To quantify the photoionization yield and selectivity of isotope, the kinetics of the photoionization process are described either by the density matrix [Milonni, 1988 and Gupta et al, 2004] or by the rate equations [Miller et al, 1983 and Jost et al, 1998]. The applicability of the methods depends on the nature of laser-atom interaction.

When the laser photons interact with atoms, it creates induced dipoles in the atomic medium. If the phase correlation among the dipoles exists during the interactions, the interaction is known as coherent interaction. On the other hand, the atomic dipoles relax and the coherent atomic polarization decays spontaneously. It results the interaction to be incoherent. The density matrix approach is used for the coherent system while the

rate equation approach is applied to study the details kinetics of the incoherent system. The rate equation approach is simpler of the two. Letokhov et al [1977] had solved the rate equations of two-step ionization process analytically for synchronized rectangular laser pulses. The ionization yield has been calculated assuming equal statistical weights of the ground level and excited level. The influences of laser line-width, laser pulse duration and charge exchange processes during ion production and ion-extraction on the isotope selectivity [Jost and Johansen, 1989] have been studied for various elements. In all such calculations, it is assumed that the medium is optically thin where the absorption of laser radiations is ignored. However the effect of optically thick media needs to be accounted in situations where the media are dense and radiation propagates through it. Such cases occur in the laser beam propagation effects in the atomic beams [Chen et al, 1995] and the X-ray emission from galaxies [Dumont et al, 2000]. The details kinetics of the photoionization is investigated in the optically thick medium of barium.

4.3 Relevant Atomic Parameters of Barium

Neutral barium (Ba) is an alkaline earth element with most abundance of $_{56}Ba^{138}$ isotope. It has atomic number 56 and average atomic mass 137.327 amu. In its ground state, 54 electrons are arranged in a closed xenon shell electronic structure with the remaining two 6s electrons available for optical excitation, i.e. [Xe] $6s^2$. The partial energy-level diagram of few low-lying states of barium atoms (BaI) relevant for this study is schematically shown in figure 4.1. The first ionization potential of Ba atom is 5.210 eV. The ground state is designated as $6s^2$: $^1S_0$ while the resonant excited state, 6s6p: $^1P_1$ is at 18060 cm^{-1} [Klose et al, 2002]. The resonant transition of $6s^2$: $^1S_0$ - 6s6p: $^1P_1$ is at wavelength 553.5 nm, with its characteristics light green color. The corresponding transition probability for spontaneous emission is $1.19x10^8$ sec^{-1}. The absorption oscillator strength of 6s6p: $^1P_1$ is 1.59 [Miles and Wiese,

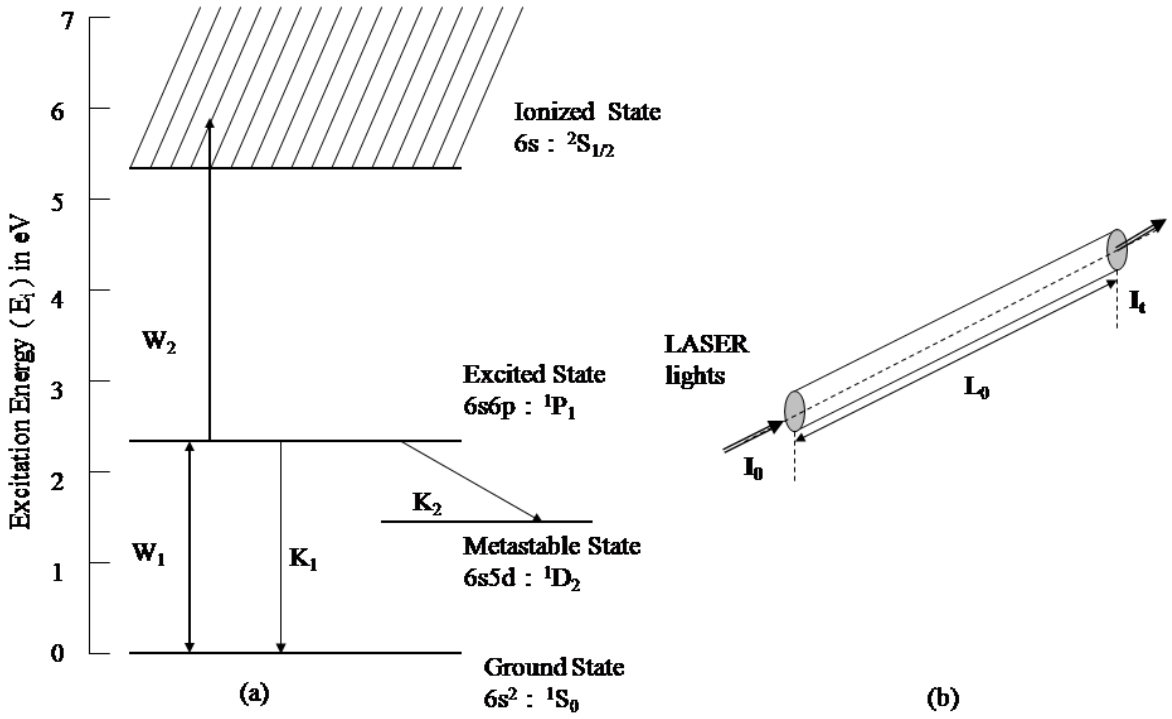

Figure 4.1: (a) Low-lying singlet energy levels of BaI and (b) geometry for laser-atom interaction involved in two-step photoionization process.

1969] and its lifetime is ~ 8.37 ns [Niggli and Hubber, 1987]. The degeneracy factor of ground state (g_o) and resonant state (g_1) are 1 and 3 respectively. The atoms from the 6s6p: $^1P_1$ resonant state can decay to 6s5d: $^1D_2$ (apart from the ground state) with transition probability of 2.5×10^5 sec^{-1} [Klose et al, 2002]. The 6s5d: $^1D_2$ at 11395 cm^{-1} is a metastable state. Decay from its metastable state to the ground state is forbidden by parity but allowed by electric quadrupole transition [Klimouskii et al, 1981]. So the $^1D_2$ level has a long lifetime of ~ 0.5 s [McCavet et al, 1974]. Natural Ba has seven stable isotopes [Lederer et al, 1967]. The heaviest isotope, ^{138} Ba is the most abundant (0.72). The spectral shift in 553.5 nm resonant line of ^{138}Ba from other isotopes is in the range of 125-250 MHz [Baird et al, 1979]. Among the three components of hyperfine structure in odd isotopes (^{135}Ba and ^{137}Ba), the signal strength of first component is significant while

others are negligible. The corresponding shift in the resonant line of ^{138}Ba due to hyperfine structure of odd isotopes is nearly 300 MHz. Barium has large photo-excitation cross-section of the above resonant transition (σ_1) at 553.5 nm radiation and its value is ~ $3x10^{-16}$ m^2 [Ruster et al, 1989]. The ionization cross-section (σ_2) from 6s6p: $^1P_1$ state to the continuum at 355 nm is ~$1.7x10^{-21}$ m^2 [Kalyar et al, 2007].

4.4 Experiments

4.4.1 Generation of Barium Photoplasma

A long collimated atomic beam of barium was generated by the multi-channel atom source as discussed in chapter 3. The barium photoplasma was produced through two-step two-color photoionization schemes by shining laser pulses onto the collimated barium atomic beam.

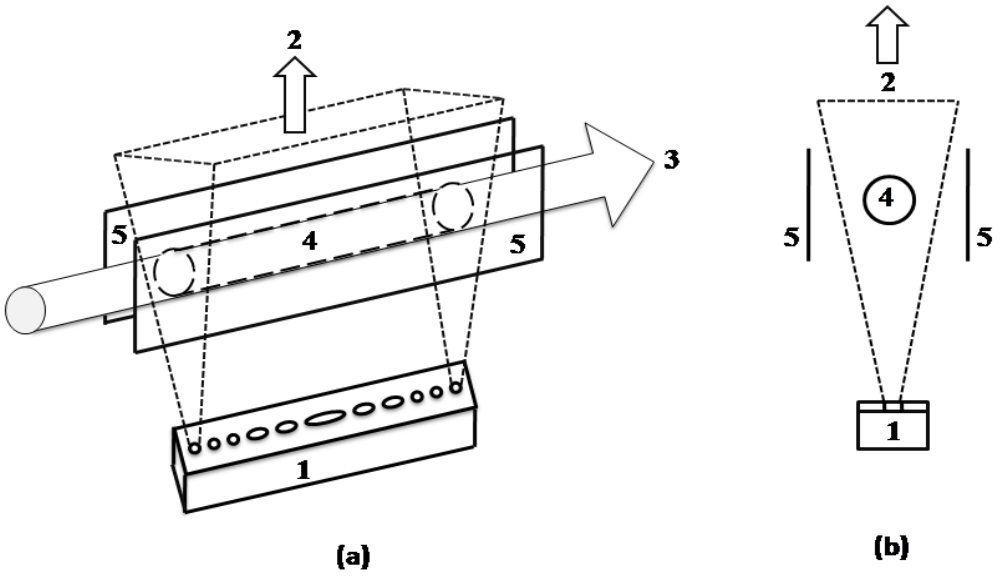

Figure 4.2: (a) Schematic of laser-atom interaction region. 1. Crucible, 2. Atomic beam, 3. Laser beams, 4. Photoplasma, 5.Parallel plate electrodes (b) Width view.

In the first step, the barium atoms get resonantly excited from their ground level ($6s^2$) to an intermediate excited level (6s6p) by absorbing 553.5 nm radiations. In the second step, the excited atoms are ionized to continuum by 355 nm radiation pulse. Although Ba has a lot of autoionization levels, the 355 nm radiations had used for the ionization step because it was easily available from the Nd-YAG laser with large energy of pulses (~ tens of mJ) and no further dye laser was required for the second step. It was configured in a manner such that the direction of vapor flow, combined laser beams and electric field were mutually orthogonal as shown in figure 4.2. Details of the experimental systems were discussed in section 2.4.

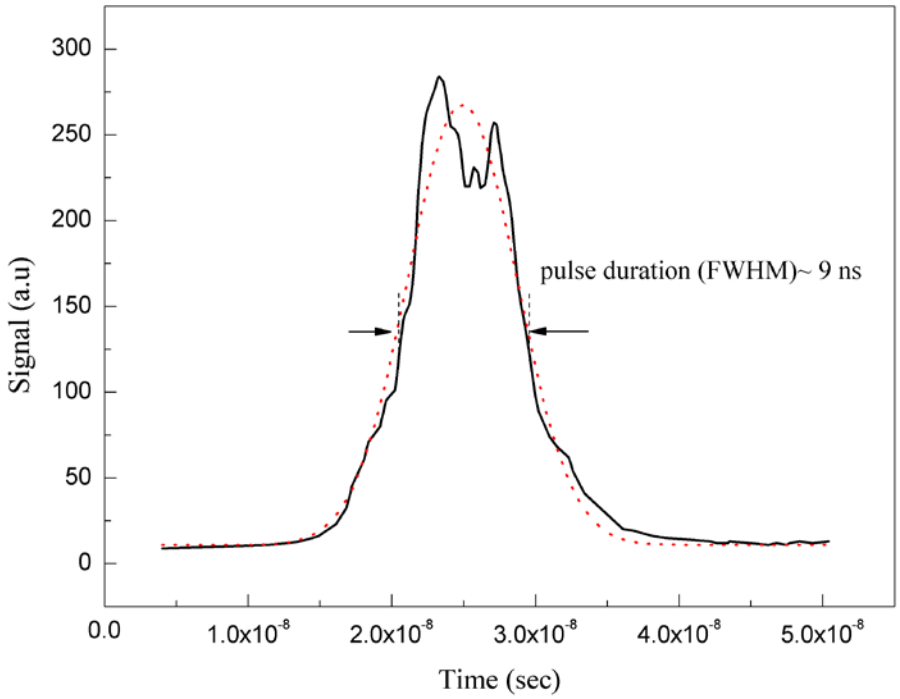

Figure 4.3: Temporal profile of 355 nm pulse from the third harmonic of Nd-YAG laser.

The measured temporal profile of 355 nm radiations is shown in figure 4.3. The profile was fitted with the Gaussian shaped pulse as shown by the red color dotted curve. The estimated pulse duration (FWHM) was ~ 9 ns. Similarly the dye laser radiation pulse of 553.5 nm had pulse duration of ~ 7 ns. The ionization was carried at a height of ~ 0.07

m (i.e. laser-atom interaction region) from the top of the crucible lid. The atomic beam had the dimension of 0.1 m length and 0.025 m width. The circular laser beam of 10 mm diameter interacted with the atomic beam. Thus it produced a long cylindrical shaped Ba photoplasma with diameter of ~ 0.01 m and length of ~ 0.1 m inside the atomic beam.

4.4.2 Estimation of Ion Density from Charge Collection Method

The plasma ion density of barium photoplasma was estimated by the total charge collection method. As the photoplasma is generated by ~ 10 ns laser pulse, it is pulsed in nature. The pulsed photoion current was measured across the series resistors connected to the cathode plates as shown in figure 2.6. The details were discussed in chapter 2. There is a possibility of surface ionization of Ba vapors on tungsten surface in the crucible at 1000 K temperature [Latuszynski and Raiko, 1975] during vapor evaporation. It causes a very small current (~ μA) in the absence of a laser pulse in the electrical circuit and it is known as background current. Since the background current is dc in nature, it does not interfere in detection of the transient photoionization signal.

The photoplasma has nearly uniform photoion density over its entire volume and it was produced at the centre between two electrodes. The estimated mean-free path of the electron-atom collision is ~ 10 m (at electron's energy ~ 500 eV). This is much larger than the length (~ 0.02 m) over which electrons and atoms interact and the inter-electrode separation (~ 0.035 m). Hence the contribution to ionization of Ba atoms by electron impact ionization is negligible. It has been also verified that the effect of secondary electron emission due to the incidence of high energetic photoions on the cathode surface is insignificant [Majumder et al 2005]. The integration of the pulsed photoion current gives the total charge collected on the cathode plate. A relatively large electric field (~

$3x10^4$ V/m) is applied between two plates to collect all photoions on the cathode plate. The photoion density is estimated from the relation of equation 4.1.

$$n_i = \frac{\int V(t)dt}{0.25\pi D^2 L\, R\, q} \tag{4.1}$$

where V(t) is the temporal variation of the voltage drop across the series resistor (R) connected to the cathode plate, n_i is the photoion density in the photoplasma, q is the charge of individual photoions, D and L are the diameter and length of the finite-sized photoplasma respectively. The above charge collection method is used to estimate photoion density in the photoplasma having density less than $5x10^{15}$ m^{-3}. Below this density, all photoions are collected on the cathode plate applying an external electric field. As the plasma density increases, the plasma shields the external electric field through Debye shielding. The motion of plasma particles is governed by ambipolar diffusion due to space charge interactions (discussed in later). As a result, the finite-sized plasma expands in all directions. It is very difficult to collect all the photoions at the particular location (i.e. cathode plate). This increases the measurement errors in the estimation of photoion density.

The typical photoion current signal recorded on cathode plate, biased at -500V is shown in figure 4.4. It shows that the photoplasma evolves under an electric field over a finite time and the time span of the signal is the order of μs. As the strength of electric field increases, more photoions are collected on the cathode plate as shown in figure 4.5. The saturation of collected photoions on the cathode plate indicates that all photoions generated in one laser pulse are collected on the cathode plate. It has also been observed experimentally that the electric field ~ $3.5x10^4$ V/m is sufficient to collect all photoions on the cathode plate for the photoplasma having density less than $5x10^{15}$ m^{-3}. The

measured photoion density from equation 4.1 is ~ $3x10^{15}$ m^{-3} at the crucible temperature of ~ 850 K. The measurement error in photoion density is nearly 20 %.

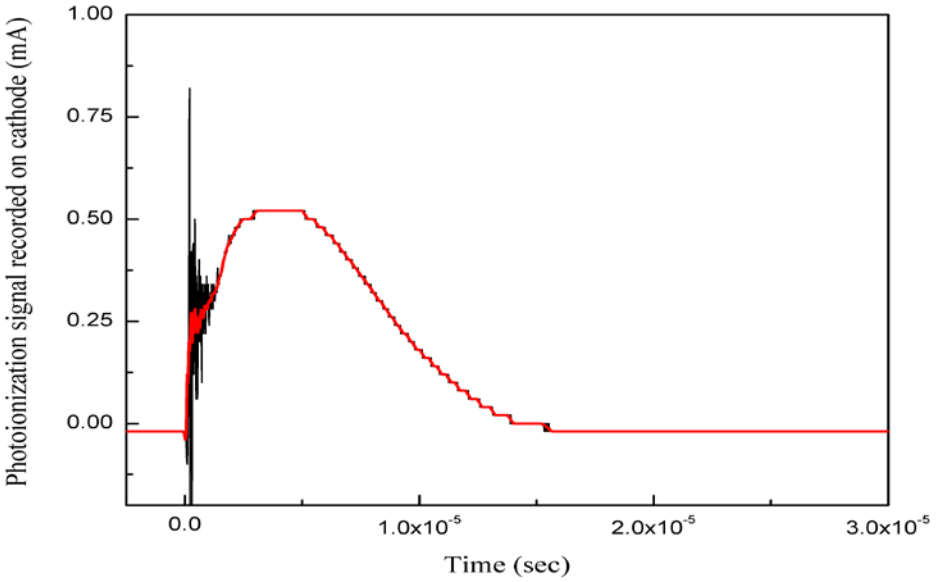

Figure 4.4: Typical photoionization signal recorded on cathode plate biased at -500 V with crucible temperature ~ 850 K.(red color represents smoothen by adjacent 10 points).

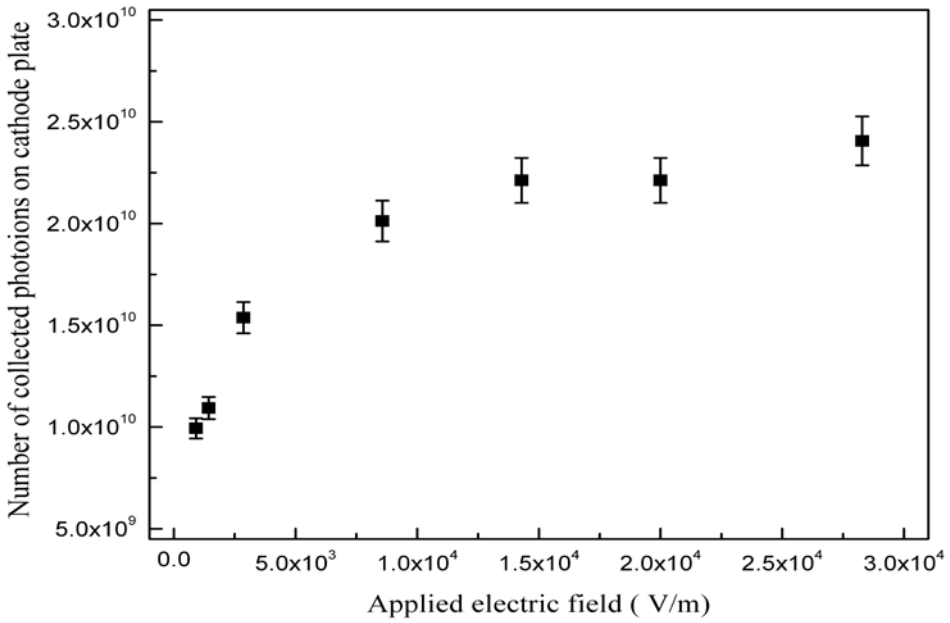

Figure 4.5: Measured photoions collected on the cathode plate at different applied electric field.

4.5 Kinetics of Two-Step Photoionization Process

During the laser-atom interaction, the induced dipole in the atomic medium decay with time and it is known as phase-relaxation time. The phase relaxation time is estimated from the inverse of atomic absorption line-width expressed in frequency unit [Dudley et al 1993]. If the phase-relaxation time is less than the time of laser-atom interaction (~ duration of laser pulse), the coherent atomic induced polarization decays spontaneously. The interaction is said to be incoherent. The opposite case is considered as coherent. In our case, the line-width of atomic absorption profile is ~ 0.65 GHz. The estimated phase relaxation time is ~ 2ns while the laser pulse duration is ~ 10 ns. Hence the laser atom interaction is incoherent and the kinetics of photoionization method has been described by the rate equations.

4.5.1 Formulation of Rate Equations

The transitions of BaI involved in two-step photoionization process are schematically shown in figure 4.1(a). The figure 4.1(b) shows the interaction of the co-propagating laser radiations with a vapor column of length L_0. The absorption of laser radiations depends on the value of optical density in the atomic medium. It is defined as the product of neutral atom density (N_0), absorption cross-section (σ_1) and the interaction length (L_0). When the optical density is greater or equal to unity (i.e $N_0\sigma_i L_0 \geq 1$), there is significant absorption of laser radiations in the atomic medium. The medium is known to be optically thick for the incident radiation. On the other hand, the medium is optically thin and the optical density is very less than unity (i.e $N_0\sigma_i L_0 << 1$). Since the bound to bound level transition is more likely happened than the bound to continuum transition, the excitation cross-section ($\sigma_1 \sim 3x10^{-16}$ m^2) is much larger than the ionization cross-section ($\sigma_2 \sim 2x10^{-21}$ m^2). For a typical atom density $N_0 \sim 5x10^{16}$ m^{-3}, the value of optical density for excitation radiation ($N_0\sigma_1 L_0$) is ~1.5 which is greater than unity. There is significant

absorption of the excitation radiation. The same of ionizing radiation ($N_0\sigma_2L_0$) is ~ $1x10^{-5}$ which is nearly zero and negligible absorption of the ionizing radiation is occurred during its propagation. So only the absorption of exciting radiation is taken into account. Under this condition, the kinetics of photoionization processes is described by the following rate equations [Letokhov et al, 1977].

$$\frac{\partial n_0}{\partial t} = -\sigma_1 J_1 \left(n_0 - n_1 \frac{g_0}{g_1}\right) + K_1 n_1 \tag{4.2a}$$

$$\frac{\partial n_1}{\partial t} = \sigma_1 J_1 \left(n_0 - n_1 \frac{g_0}{g_1}\right) - K_1 n_1 - K_2 n_1 - \sigma_2 J_2 n_1 \tag{4.2b}$$

$$\frac{\partial n_i}{\partial t} = \sigma_2 J_2 n_1 \tag{4.2c}$$

$$\frac{\partial J_1}{\partial z} + \frac{1}{c}\frac{\partial J_1}{\partial t} = -\sigma_1 J_1 N_0 (n_0 - n_1 \frac{g_0}{g_1}) \tag{4.2d}$$

The quantities n(t) represent the time dependent normalized populations of the ground level (n_0), intermediate excited level (n_1) and the ionized level (n_i). J_1 and J_2 are the laser photon fluxes (i.e. photons $m^{-2}s^{-1}$) for the excitation and the ionization step respectively. K_1 and K_2 are the spontaneous transition probabilities from the excited level to ground level and to meta-stable level respectively. It is assumed that the initial atom density (N_0) in the ground state is uniform throughout the interaction volume. The above three equations 4.2(a, b, c) describe the population dynamics of different levels at a particular distance z along the interaction length. The equation 4.2(d) represents the variation of laser photon flux of the excitation radiation, as the atomic medium is optically thick for the excitation radiation. A new local time variable $\tau = (t-z/c)$ is introduced [Comte et al, 1990] in place of global time t for the simplicity in the calculation. The above equations are transformed in the following forms using local variables.

$$\frac{\partial n_0}{\partial \tau} = -\sigma_1 J_1 \left(n_0 - n_1 \frac{g_0}{g_1} \right) + K_1 n_1 \quad (4.3a)$$

$$\frac{\partial n_1}{\partial \tau} = \sigma_1 J_1 \left(n_0 - n_1 \frac{g_0}{g_1} \right) - K_1 n_1 - K_2 n_1 - \sigma_2 J_2 n_1 \quad (4.3b)$$

$$\frac{\partial n_i}{\partial \tau} = \sigma_2 J_2 n_1 \quad (4.3c)$$

$$\frac{\partial J_1}{\partial z} = -\sigma_1 J_1 N_0 (n_0 - n_1 \frac{g_0}{g_1}) \quad (4.3d)$$

The temporal variation of photon flux J (z, τ) at a given z is discussed below.

4.5.2 Numerical Simulation

In our case, the temporal profiles of laser pulse are not rectangular as shown in figure 4.3. They are nearly Gaussian in shape. The temporal variation of energy density $E_i(z, \tau)$ of the Gaussian shaped pulses [Silfvast, 1998] can be written as

$$E_i(z, \tau) = E_{ip}(z) \exp^{-\left(\frac{\tau - \tau_{pi}}{T_i}\right)^2 4 \ln(2)} \quad (4.4)$$

where E_{ip} is the maximum energy densities at a particular z and at time $\tau_{pi,}$ T_i is the pulse duration (FWHM) of the laser pulse. The values of i = 1 for the excitation pulse and i = 2 for the ionizing pulse. For the time varying laser pulses, it is not possible to solve the coupled rate equations analytically. In the experiments, there is a difficulty to achieve the perfectly synchronised laser pulses from two different laser source. So the above coupled differential equations 4.3(a,b,c) are numerically solved using fourth-order Runge-Kutta technique [Chapra and Canale, 2002]. The energy density of excitation radiation is varied along the propagation direction and it is given by the expression of equation 4.5 which is obtained from the solution of equation 4.3(d),

$$E_1(z) = E_{10}(z = 0) \exp^{-(N_0 \sigma_1 z)} \quad (4.5)$$

where E_{10} is the initial energy density of the excitation pulse incident on the medium at z = 0.

A numerical program is written in FORTRAN language. The thick medium of thickness L_0 is divided into many layers of thickness Δz such that $N_0\sigma_1\Delta z \ll 1$. The layer of thickness Δz is considered to be thin medium and the energy density remains unchanged throughout the length of Δz. At each layer the peak energy density of excitation pulse is calculated from the equation 4.5 and the ionization yield is calculated from the simulation. To get a stable solution instead of unstable / periodic solution, the time step should follow the criteria of $\Delta t < (\max [\sigma_1 J_1])^{-1}$. The followings are chosen in the simulation: $\Delta z = 1\text{x}10^{-3}$ m and $\Delta t = 1\text{x}10^{-12}$ sec. It is assumed that the laser beams are co-propagating and remain parallel throughout the interaction length.

4.5.3 Features of Optically Thin / Thick Medium

The criterion for optically thin medium is $N_0\sigma_i L_0 \ll 1$ whereas $N_0\sigma_i L_0 \geq 1$ for the thick medium. The value of $N_0\sigma_i L_0$ physically represents the effective number of atoms interact with the incident radiation within the cross-sectional area of σ_1. In our case, the atomic medium was experimentally varied from optically thin to thick for the excitation radiation by increasing the neutral atom density (N_0) in the interaction region. In case of thick medium, both the required energy to saturate the excitation transition and the corresponding ionization yield depend on the incident number of photons per atom (N_p). The number N_p is defined as the number of photons in an individual laser pulse divided by the number of atoms seen by the pulse [Mitchel and Zemansky, 1971] while it passes through the atomic beam. It is given by

$$N_p = \frac{(W/h\gamma)}{N_0 L_0 A} \qquad (4.6)$$

here W is the incident pulse energy, hν is the photon energy and A is the cross-section area of the laser beam. In the thin medium, the pulse energy does not change significantly along the interaction length as a result the ionization yield remains same over the length. But in the thick medium, the average energy of excitation pulse decreases along the

length due to its absorption. The change in the energy density of excitation pulse is shown in figure 4.6 (curve a) for the optical thick medium of $N_0\sigma_1L_0 \sim 1$ and the incident excitation pulse of $N_p = 1$ at z = 0,. The figure 4.6 (curve b) shows the change in the ionization yield along the interaction path due to variation of energy density of the excitation pulse. An average ionization yield is defined in the optical thick medium. It is obtained from the ratio of total ions produced by the laser radiations to total neutral atoms in the interaction volume.

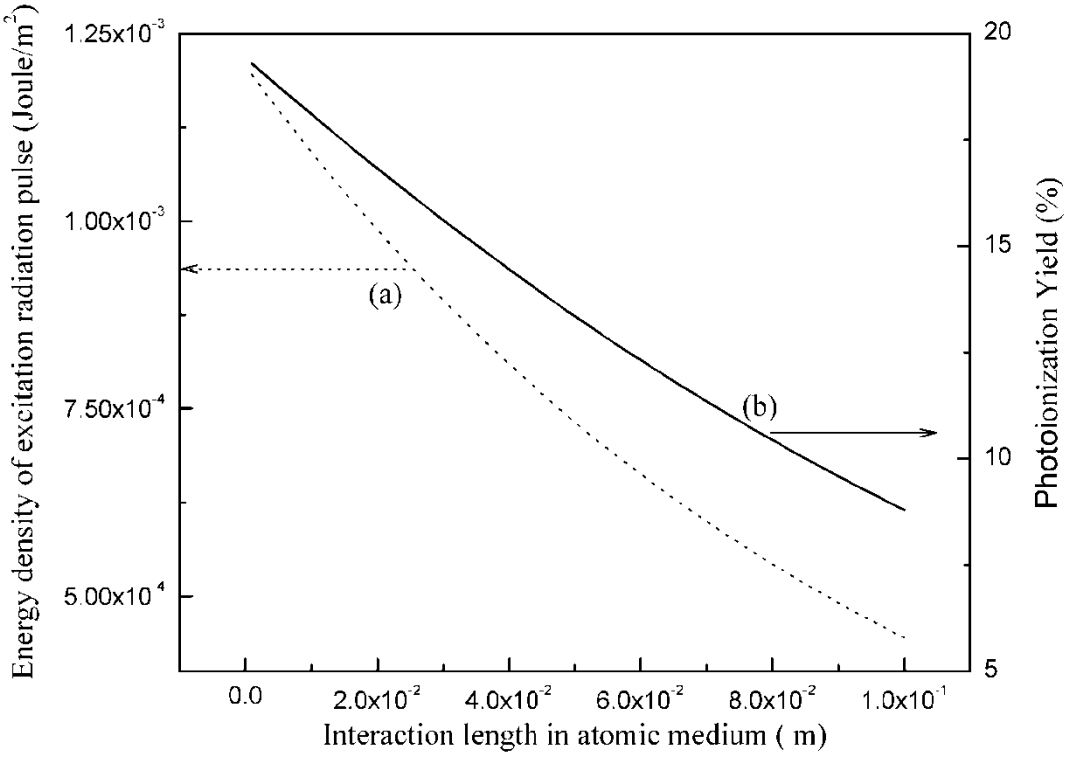

Figure 4.6: (a) Variation of excitation energy density and (b) the corresponding change in photoionization yield along the length of thick medium, $N_0\ \sigma_1L_0 \sim 1$ for $N_p \sim 1$.

Since the ionization yield is directly related to incident photon flux of excitation radiation which can be increased by increasing the value of N_p. The variation of average ionization yield with N_p is shown in figure 4.7 for the medium with $N_0\sigma_1L_0 \sim 1$. When N_p

is sufficiently large, the laser radiation strongly bleaches the working excitation transition in every layer along the length and the population in the excited state gets saturate throughout the length. As a result the ionization yield remains constant over the length. From figure 4.7, it is noticed that the required number of photons per atom (i.e. N_p) is nearly 15 to completely bleach the excitation transition in the optical medium with $N_0\sigma_1L_0 \sim 1$. From simulations it is also observed that the ionization yield will be maximized when both the excitation and ionization transitions are simultaneously saturated by their corresponding laser radiations.

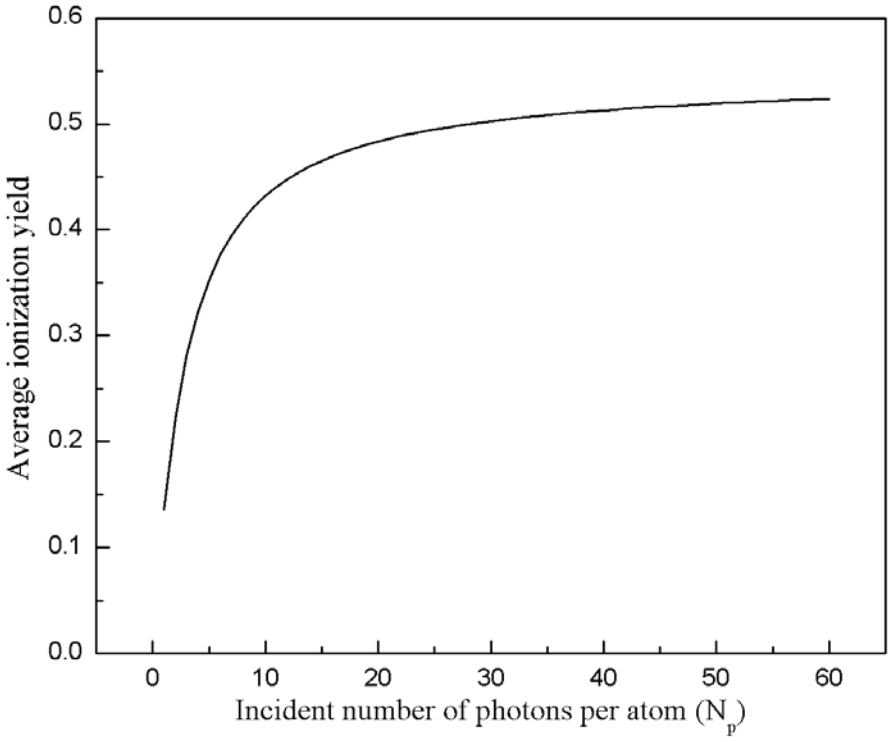

Figure 4.7: Variation of average photoionization yield with incident number of photons per atom (i.e. N_p) for an optically thick medium of $N_0\,\sigma_1L_0 \sim 1$.

4.5.4 Effect of Time Delay between two laser beams

The rate of ionization from the excited level to continuum depends upon the ionization probability and the number of atoms present in the excited level. As the

temporal profile of the laser pulse is nearly Gaussian, it takes a time to get sufficient populations in the excited level during the initial rising part of the exciting pulse. The excited atoms are ionized with greater ionization rate by the second laser pulse which comes with a time delay relative to the first one. Figure 4.8 shows the variation of ionization yield with time delay between the exciting and ionizing pulses.

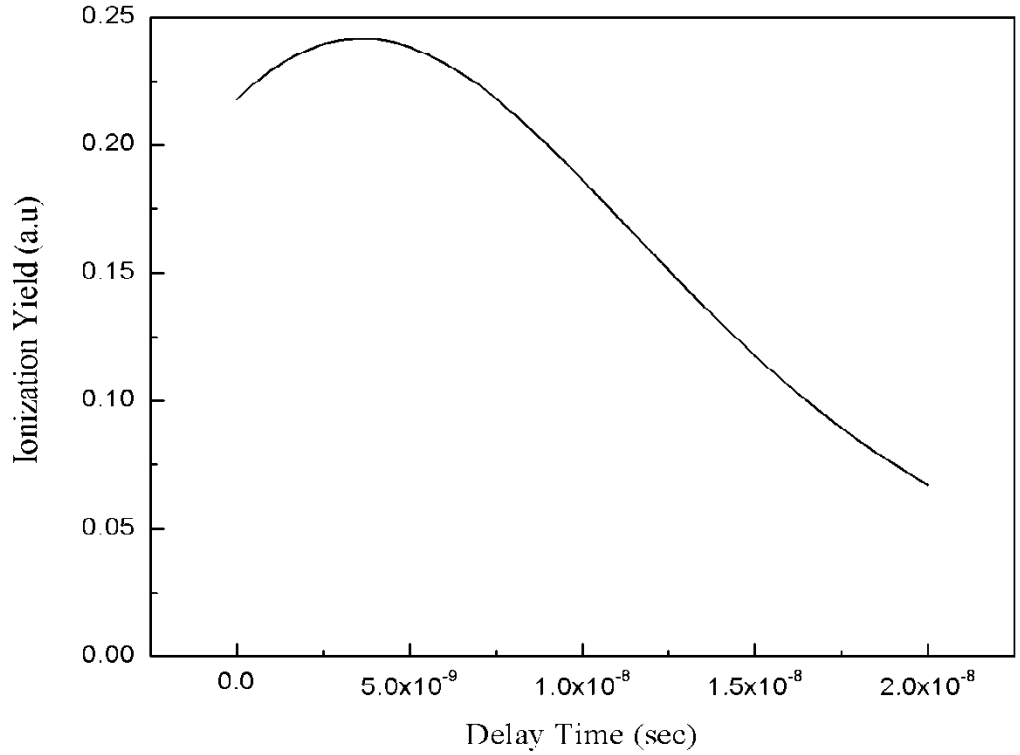

Figure 4.8: Variation of ionization yield with time delay between two laser beams.

The ionization yield increases with time delay, reaches a maxima and then decreases for further delay. Initially the ionization yield increases with time delay due to more atom populations in the excited state.The decrease of ionization yield is due to (1) the less temporal overlap between the pulses and (2) deexcitation of the excited atoms by spontaneous emission process before arival of the ionizing pulse. The ionization yield will be optimum when there is a good temporal overlap as well as a small time delay between the exciting and ionizing laser pulses.

4.5.5 Population Dynamics of Barium Atoms

Figure. 4.9 shows the variation of normalised population densities with time in the ground level (n_o), intermediate excited level (n_1) and ionized level (n_i) for the initial atom density $N_0 = 5x10^{16}$ m^{-3}. For the Gaussian shaped laser pulses, all the photons (~98%) are distributed within a time span of nearly three times of its pulse duration (FWHM). In the experiment, the time spans of excitation and ionization pulses are ~ 21 ns and ~ 27 ns respectively. The ionizing pulse comes after 4 ns with respect to the excitation pulse.

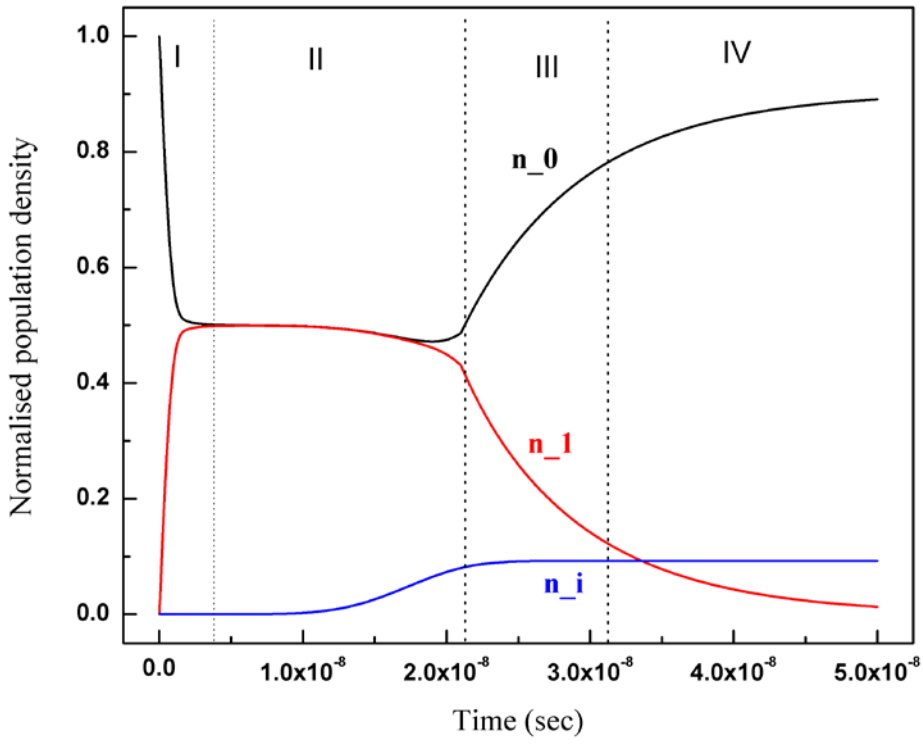

Figure 4.9 Time dependent variation of normalized population density in ground state (n_0), excited state (n_1) and ionized state (n_i) with the measured values of different experimental parameters.

The total time span is divided into four regions. In region I (0 - 4 ns), only the initial rising part of excitation pulse is present. In our case, the energy density of the excitation

pulse is too large (N_p ~ 1100) with respect to the energy density required for the saturation of corresponding transition. As a result it completely bleaches the transition throughout the medium and the population in the excited state gets saturated imeadiately with the initial rising part of the exciting pulse. Almost 50 % atoms are populated in the excited state as the the excited level of J = 0 and mj=0 is connected to ground level J=0 and mj=0 by linearly polarised laser light. In region II (4 - 21 ns), both the excitation and ionization pulses are present. Due to ionization of excited atoms, the population of the excited level decreases and the same of ionized level increases. In region III (21 - 27 ns), there is only ionizing pulse. The available energy density of ionizing pulse is much less than that required to saturate the ionization transition. As a result, a small fraction of atoms (~ 10 %) are ionized. Since the atoms of excited level has a finite life time (~ 8.37 ns), the remaining excited atoms relax through largely populating the ground level. This process is continued till region IV (>27 ns) where no laser pulses are present.

4.6 Comparison of Photoionization Yield

The average atom density of barium atomic beam was measured by the optical absorption method as discussed in section 3.5. The finite-sized photoplasma was produced inside the atomic beam. The photoion density of photoplasma was measured using the technique of total charge collection as described in section 4.4.2. The ratio of measured photoion density to atom density at the laser-atom interaction region gives the photoionization yield. The ionization yield has been measured at different crucible temperatures i.e. different atom densities at the interaction zone. The same has also calculated from the model. For the measured values of pulse energy of excitation pulse ~ 0.2 mJ and of ionization pulse ~ 5 mJ, the computed ionization yield has been compared with the measured values. Their comparison is given in table 4.1. For the plasma density greater than 5x1015 m-3, it is very difficult to collect all photoions on the cathode plate.

So the measurement error increases and the estimated photoionization yield is lower than the actual value. The numerical values comply with the experiment within the error. For our case, the energy density of excitation pulse is very large compared to that required to saturate the excitation transition. So for the above all atom densities, the atomic medium behaves like almost thin layer due to available high energy density. Thus the finite-sized barium photoplasma was generated using this method over a wide density range from ~ 10^{13} -10^{16} m^{-3}.

Table 4.1: Comparisons between experimentally measured and numerically estimated ionization yield of two-step photoionization process.

Experimentally measured atom density N_0 ($/m^3$)	measured ion density N_i ($/m^3$)	Ionization Yield (%) estimated from Experiment	Numerical Simulation
$(4.0 \pm 0.4)x10^{15}$	$(3.8 \pm 0.4)x10^{14}$	9.5 ± 1.9	9.27
$(5.0 \pm 0.5)x10^{16}$	$(5.0 \pm 0.5)x10^{15}$	10.0 ± 2.0	9.26
$(6.0 \pm 0.6)x10^{17}$	$(4.0 \pm 0.4)x10^{16}$	6.7 ± 1.3	9.23

4.7 Summary

A finite-sized barium photoplasma has been generated through two-step photoionization scheme by shining laser pulses onto the barium atomic beam. In the first step, Ba atoms get resonantly excited by laser radiation of 553.5 nm from their ground level to intermediate excited level and subsequently the excited atoms are ionized in the second step by another laser radiation of 355 nm. Experiments have been performed to photoionize all the isotopes. The ionization yield has been measured. The kinetics of two-step photoionization process in optically thick atomic medium of barium (Ba) has been

studied using the rate equation approach. The absorption of exciting radiation (553.5 nm) along its propagation direction has been considered whereas the medium is assumed as optically thin for ionizing radiation (355 nm). The rate equations are solved numerically to estimate the ionization yield for time varying Gaussian shaped laser pulses. The calculated ionization yield has been compared with the experimentally measured values. They match within the experimental errors and it validates the developed rate equation based model.

Chapter 5

Developed One Dimensional Plasma Model based on PIC (particle-in-cell) Technique

The chapter 5 describes about the development of a one-dimensional plasma model based on standard particle-in-cell (PIC) technique to study the motion of a finite-sized photoplasma under an externally applied electromagnetic field. A mathematical problem is formulated to develop the plasma model. It consists of a set of equations like Poisson's equation, Lorentz equation and Newton's equation of motion. The equations are numerically solved. In the model, the plasma is represented by large number of both positive and negative charged super-particles. Their motions are studied in one dimension i.e. along the direction of electric field to investigate the evolution of photoplasma.

5.1 Introduction

In plasma physics, the computer simulations use a mathematical model to simulate the behavior of plasma for detailed understanding of the complex phenomena occurred in the plasma. The computer simulation of plasma comprises two general areas based on fluid and kinetic descriptions. In the fluid description, the plasma is treated as a mixture of two or more interpenetrating fluids. When the plasma particles collide among themselves very frequently, each species maintains a local equilibrium and it is treated as a fluid. The fluid is described by the localized density; macroscopic velocity and temperature. In addition to the usual electromagnetic equations, a set of hydrodynamic equations expressing the conservation of mass, momentum and energy for each type of species in the plasma are numerically solved in the fluid simulations. On the other hand,

the plasma is considered as the collection of large number of interacting particles in the kinetic description. The kinetic simulation involves the particle interactions through the electromagnetic field and it gives a detailed model of plasma motion under the external electromagnetic field. This simulation is achieved either by solving numerically the plasma kinetic equations (e.g. Vlasov or Fokker-Plank equations) or by 'particle simulation'. The particle simulation simply computes the motions of charge particles interacting with each other and their interactions with externally fields [Hockney and Eastwood, 1998].

When the photoplasma decays under an electrostatic field, the plasma particles move along the field direction. To investigate the transient responses of photoplasma to the applied electric field, a one dimensional particle simulation is chosen rather than two dimensional simulation. The one dimensional plasma simulation is relatively simpler. It takes significantly less computational time and memory than that required in the two dimensional simulation. The photoplasma is replaced by an equal number of positive and negative charged super particles. They move along the direction of the external electric field. Thus it simulates the dynamics of photoplasma.

In the following section, a mathematical problem of one dimensional plasma model has been formulated. The numerical techniques to solve the differential equations are described. The algorithm of the plasma model based on standard PIC technique [Birdsall and Langdon, 2005] is discussed.

5.2 Formulation of Mathematical Problem

Though the photoplasma is generated inside a collimated atomic beam, it behaves like fully ionized plasma. In the range of plasma density ~10^{13} m^{-3} – 10^{16} m^{-3}, the direct collisions among the charge particles are negligible. The collision mean free paths of plasma particles (with collision cross-section of electron-electron, electron-ion and ion-

ion ~ $1x10^{-16}$ m^{-2}) is ~ 0.1 m and it is larger than the dimension of the finite-sized photoplasma and the separation gap between the electrodes (i.e. computational length). So in case of photoplasma simulation, the collisions among charge particles are not considered. The charge particles interact with each other via electric field. The 1d Cartesian co-ordinate system is used to simulate the photoplasma motion in one dimension. The motion of plasma particles under the applied electrostatic and magneto static field are described by the following set of equations.

$$\rho = (n_i - n_e)e \tag{5.1}$$

$$\frac{d^2\varphi}{dx^2} = -\frac{\rho}{\epsilon_0} \tag{5.2}$$

$$E = -\frac{d\varphi}{dx} \tag{5.3}$$

$$F = qE + q(v \times B) \tag{5.4}$$

$$m\frac{d^2x}{dt^2} = F \tag{5.5}$$

where ρ is the charge density, n_e and n_i are electron density and photoion density, φ is the potential and E is the electric field along x direction, m and q are the mass and charge of plasma particles, v is the velocity of charged particles and B is the magnetic field applied along z direction. F is the force acting on the charge particles. Thus the mathematical problem consists of a set of equation has formulated for one dimensional plasma model.

5.3 PIC Simulation

Particle approach of plasma simulations is used to develop the model. The photoplasma is replaced by a less number of positive and negative charged super-particles. The super particles are basically a bundle of real charge particles. Each super-particle carries more mass and charge than that of individual photoion or electron. But they have the same charge to mass ratio like the individuals. So the acceleration gain by

the super particles is same as individual charge particles. The motion of charge particle is simulated within a simulation volume known as computational box. In case of one dimension, the computational box is linear as shown in figure 5.1.

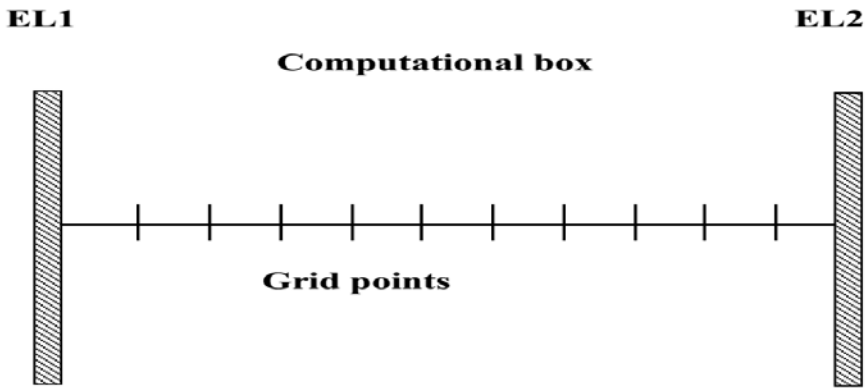

Figure 5.1: Schematics of one dimensional computational linear box discretized into uniformly spaced grid points.

It is discretized into spatial meshes (or grid points) by sets of uniformly spaced points. On the mesh points, the variables like charge density, potential and electric field are defined. Each charge particle interacts with other particles through Coulomb interaction via fields which are defined on the mesh points. Since there is no direct interaction among the particles, it is known as the particle-mesh representation and the method of simulation is called particle-in-cell (PIC) method. In the model, though the particles are moved in one dimension (i.e. along x direction) but their velocities are changed in two dimensions (i.e. V_x, V_y) in order to account the effect of constant magnetic field in z direction. The above model describes the motion of particles in one dimension of the space coordinate but in two dimensions of the velocity coordinates.

The computational procedure in the PIC method consists of following sequential steps: (i).The charge densities at different mesh points are calculated from the particle's initial positions through equation 5.1. A first order linear weighting scheme is applied to

assign the charge of the particles on the adjacent grid points. The values of charge density are used as the source terms in the field equations (eqn. 5.2). (ii). The Poisson's equation is solved to get the potential distribution and electric field at the mesh points. (iii).The values of electric field on the mesh points are used to calculate the forces acted on the particles using Lorentz equation (eqn. 5.4). (iv).The Newton equation of motion (eqn. 5.5) is solved to find the particles' new velocities. (v).The new velocities are used to update the particle positions which are carried forward into the next time step. The computation cycle for one time step is shown in figure 5.2. The iterative execution of the above steps self-consistently calculates the electric field and describes the motions of charge particles.

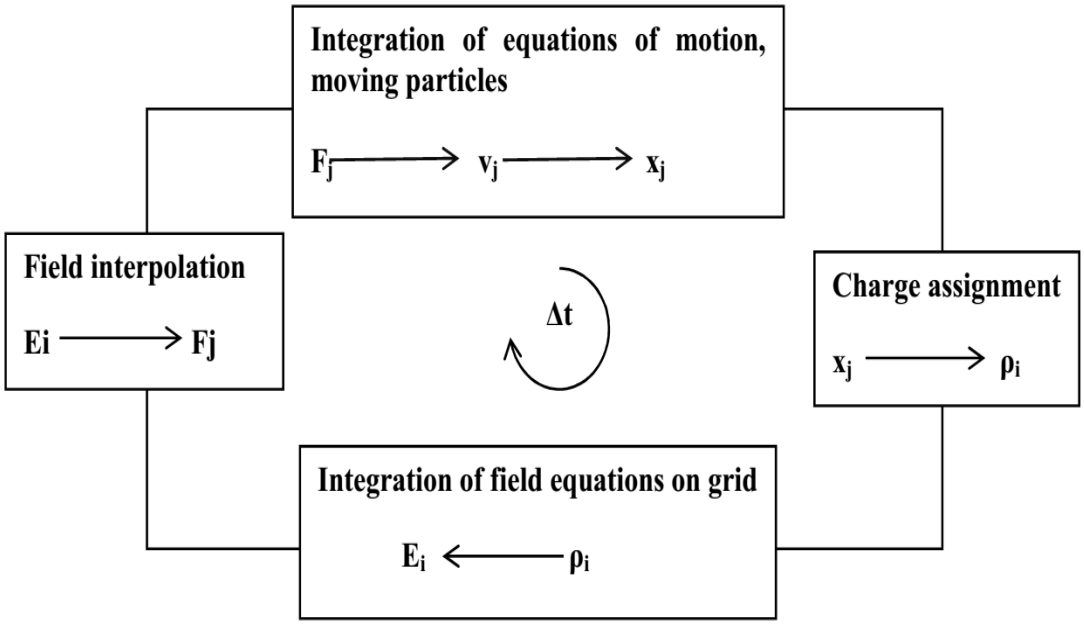

Figure 5.2: A computational cycle for one time step in a particle simulation program. The grid points are numbered as i=0, 1, 2…N and the particles are numbered as j = 1, 2, …..N_P.

5.4 Integration of Field Equation

Equation 5.2 represents the one dimensional Poisson's equation, where φ = φ (x) is the potential and ρ =ρ (x) is the charge density at point x. The charge densities are assigned to the grid points from the particle's positions and the potentials at the grid points are estimated by integrating the equation 5.2. The finite difference form of the Poisson's equation is expressed by the equation 5.6.

$$\frac{\partial^2 \varphi_i}{\partial x^2} = \frac{\varphi_{i+1} - 2\varphi_i + \varphi_{i-1}}{\Delta x^2} = -\frac{\rho_i}{\epsilon_0} \tag{5.6}$$

where ρ_i and φ_i are the charge density and potential at the i^{th} grid point, φ_{i+1} and φ_{i-1} are the potential at $(i+1)^{th}$ and $(i-1)^{th}$ grid points respectively. The second order differential equation 5.6 is solved numerically by Gauss-Seidel method with proper boundary conditions. The Gauss-Seidel method is an iterative method used to solve the linear system of equations [Chapra and Canale, 2002]. It starts with an initial guess value. The iterations are repeated until the absolute values of all the percentile of relative errors $(\varepsilon_a)_i$ fall below a pre-specified stopping criterion ε_s (i.e. $\varepsilon_a < \varepsilon_s$). These percentile relative errors are estimated by

$$|(\epsilon_a)_i| = \left|\frac{\varphi_i^{new} - \varphi_i^{old}}{\varphi_i^{new}}\right| 100\%. \tag{5.7}$$

To accelerate the rate of convergence, a technique of over relaxation is employed where the new guess value for the next iteration is estimated using the relation 5.8.

$$\varphi_i^{new\ guess} = \lambda \varphi_i^{new} + (1 - \lambda)\varphi_i^{old} \tag{5.8}$$

Where φ_i^{new} and φ_i^{old} are the potential values from the present and the previous iteration respectively, and λ is a weighting factor that is set between 1 and 2. Thus the potentials of different mesh points under the certain boundary conditions are estimated by solving the Poisson's equation using Gauss-Seidel iterative technique.

5.5 Integration of Equations of Motion

The trajectories of plasma particles are calculated from the Newton's equation of motion. The second order differential equation (eqn. 5.5) is equivalently written by two first order differential equations as.

$$m\frac{dv}{dt} = F \tag{5.9}$$

$$\frac{dx}{dt} = v \tag{5.10}$$

They are solved using leap-frog integration method. The centered finite divided difference form of the equations 5.9 and 5.10 are as follows.

$$m\ \frac{v_{t+\Delta t/2} - v_{t-\Delta t/2}}{\Delta t} = F_t \tag{5.11}$$

$$\frac{x_{t+\Delta t} - x_t}{\Delta t} = v_{t+\Delta t/2} \tag{5.12}$$

The notations of various variables and flow of time used in the leap-frog integration method are shown in figure 5.3.

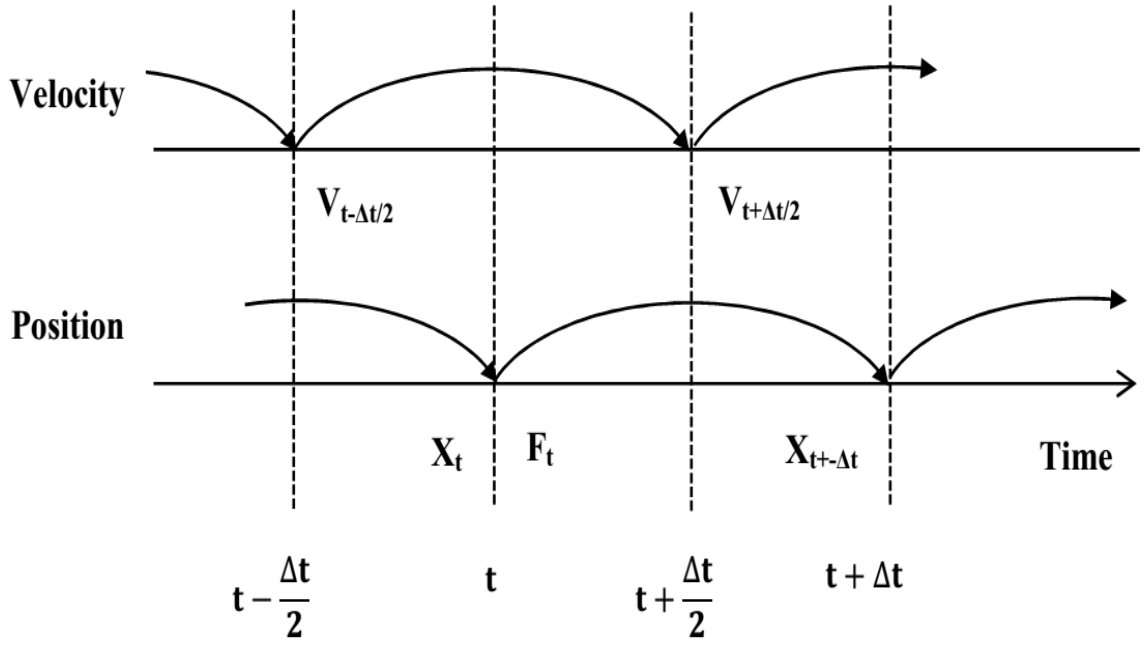

Figure 5.3: Sketch of leap-frog integration method showing the time-centering of force F while advancing velocity (v) and that of 'v' while advancing position (x).

The position of particles is updated at integer time steps while the velocity is updated at integer-plus-a-half time step. It shows the time centering of force F while advancing the velocity v and similarly the advancing of position x using time centre of velocity v. The leap-frog integration updates the positions and the velocities of particles at interleaved time points, staggered in such a way that they 'leapfrog' over each other. The leap frog integration method is a second order method, in contrast to Euler integration, which is only first order, though both require the same number of function evaluations per one time step. Unlike Euler integration, it is stable for oscillatory motion, as long as the criterion of $\Delta t.\omega_0 \leq 2$ is satisfied, where ω_0 is the frequency of oscillation. The leap-frog integration has an important feature. It has the time-reversibility. One can integrate forward *n* steps, and then reverse the direction of integration and integrate backwards *n* steps to arrive at the same starting position. It also conserves the energy of dynamical systems. This is especially useful when computing orbital dynamics, as many other integration schemes, such as the fourth order Runge-Kutta method, do not conserve energy and allow the system to drift substantially over time [Birdsall and Langdon, 1985].

The applied force (F) on the charge particles has two parts as expressed by equation 5.13,

$$F = F_{electrical} + F_{magnetic} = qE + q(v \times B) \quad (5.13)$$

here the electric field **E** and magnetic field **B** are to be interpolated at the particle position from their values at the grid points. The charge particle moves in the direction of electric field i.e. along x direction. Under the constant magnetic field B_0 along z direction, the force q (**vxB**) simply gives a rotation of the velocity v as shown in figure 5.4.

Due to the magnetic force, the velocity of particle does not change in magnitude but it changes its direction. Whereas the electrostatic force q**E** = qE_x does alter the

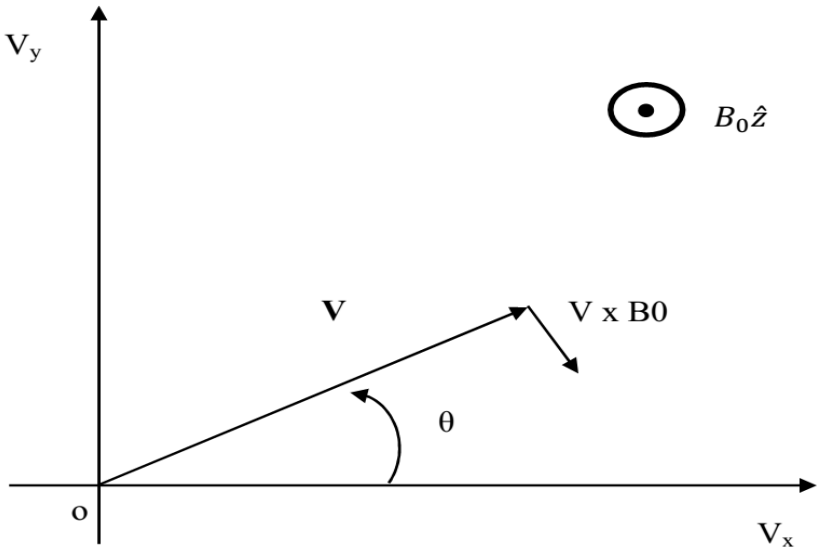

Figure 5.4: The V_x, V_y plane showing the magnetic force q(vxB) force normal to **V** which results in a rotation of **V** with no change in speed with $\frac{d\theta}{dt} < 0 \; for \; \left(\frac{q}{m}\right) > 0, B_0 > 0$.

magnitude of v (i.e. v_x) along x direction. Therefore a physically reasonable scheme which is centered in time is used to advance the velocity of particle. It consists of three step calculation with t' and t''used as dummy variables within one time step i.e. $\left(t - \frac{\Delta t}{2}\right) < t' < t'' < \left(t + \frac{\Delta t}{2}\right)$.

1. Half acceleration (in time of Δt/2) due to electrical force

$$v_x(t') = v_x\left[t - \frac{\Delta t}{2}\right] + \left[\frac{q}{m}\right] E_x(t) \left[\frac{\Delta t}{2}\right] \tag{5.14a}$$

$$v_y(t') = v_y\left[t - \frac{\Delta t}{2}\right] \tag{5.14b}$$

2. Rotation due to magnetic force

$$\begin{bmatrix} v_x(t^{"}) \\ v_y(t^{"}) \end{bmatrix} = \begin{bmatrix} \cos(w_c\Delta t) & \sin(w_c\Delta t) \\ -\sin(w_c\Delta t) & \cos(w_c\Delta t) \end{bmatrix} \begin{bmatrix} v_x(t') \\ v_y(t') \end{bmatrix} \tag{5.14c}$$

3. Half acceleration ((in time of Δt/2)) due to electrical force

$$v_x\left(t + \frac{\Delta t}{2}\right) = v_x[t^{"}] + \left[\frac{q}{m}\right] E_x(t) \left[\frac{\Delta t}{2}\right] \tag{5.14d}$$

$$v_y\left(t+\frac{\Delta t}{2}\right)=v_y\left[t^{"}\right] \qquad (5.14e)$$

The angle of rotation is $\Delta\theta=-w_c\Delta t$ i.e. $\frac{d\theta}{dt}=-w_c$. The cyclotron frequency w_c (rad/sec) is defined as $w_c\equiv\left[\frac{q}{m}\right]B_0$ and it carries the sign of q and B_0. In leap frog method the main loop runs with position x leading velocity v by time Δt/2, so one need to take care of the initial conditions of the particles' velocities and positions. In order to fit in the time flow, the v(0) is moved backward to v(-Δt/2), by first rotating v(0) through the angle $\Delta\theta=+w_c\Delta t/2$ and then applying a half acceleration using -Δt/2 based on E(0) obtained from x(0) as shown in figure 5.5

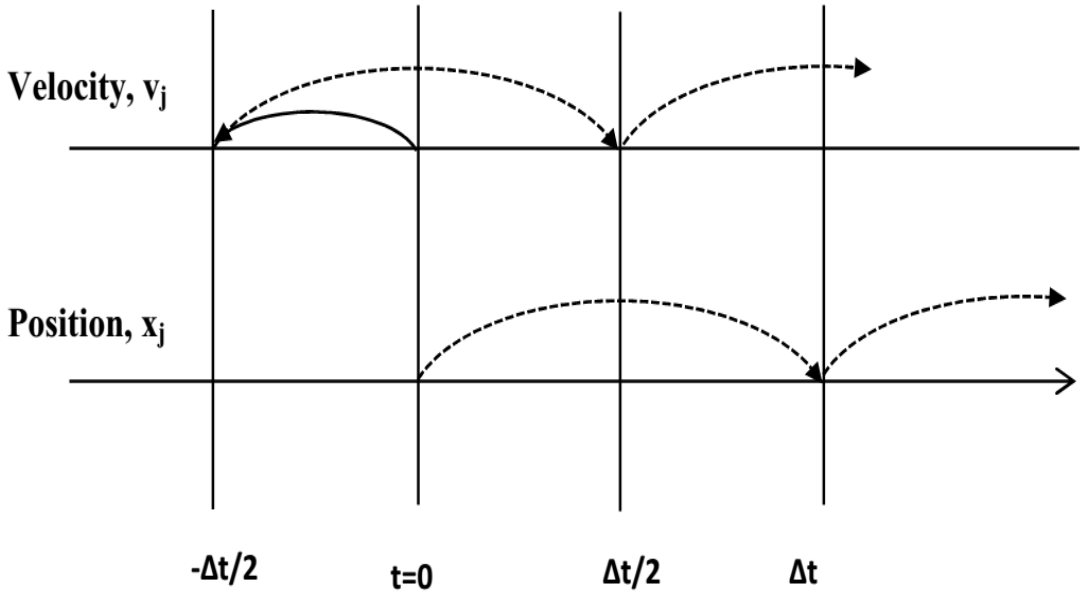

Figure 5.5: Backward movement of particles' initial velocity by a half time-step (shown by solid line) using the field at time t=0 to fit in the time flow in leap-frog method.

5.6. Charge Assignment

The charges of super particles are assigned to the nearby grid points from their positions to estimate the charge density at grid points. In charge assignment procedure, each grid point has a finite domain of influence. If the charge particle lies within the

domain of a grid point, either a part or all of the charge carried by the particle is assigned to that point. The charge assignment scheme has several effects on the physics of plasma simulation. Firstly, the particles acquire a finite size (Δx) as the particles have limited domain of influence though they are considered as point charge, secondly the force law at short distances gets modified, thirdly, the scheme introduces discontinuities in the system which results in 'noise'. All these effects depend crucially on the exact nature of the charge assignment scheme.

The simplest scheme is called the nearest grid point scheme or zero-order weighting scheme. In this scheme, the charge of a super particle is assigned to the nearest grid point only. For example the particles which reside within distance $\pm \Delta x/2$ (one cell width) about the i^{th} grid point, are assigned to that point. The charge density ρ_i is simply estimated through the total charge accumulated on i^{th} grid point divided by the cell length (Δx) in one dimension. The particle moves into the i^{th} cell through cell boundaries at ($x_i \pm \Delta x/2$) and the density on grid point jumps up due to that particle. Similarly it jumps down as the particle moves out from the cell i.e. $x_j < x_i + \Delta x/2$ or $x_j < x_i - \Delta x/2$, where x_j is the position of particle. This jump up and down in the density makes it noisy both in space and time. This noise may be intolerable in many plasma problems.

The first order weighting scheme has smoothen out the density fluctuations by distributing the charge between two nearby grid points. It reduced the noise relative to zero order weighting. In this scheme, the charge is assigned to a grid point on the basis of its distance from the particle. Lesser the distance between grid point and the particle's position, higher the fraction of charge is assigned to the grid point. In figure 5.6, the position of a particle x_j lies between the i^{th} and $(i+1)^{th}$ grid points and its domain of influence is confined within the length of x_i and x_{i+1}. The charge (q_j) of particle is distributed on i^{th} and $(i+1)^{th}$ grid points in following manner.

$$q_i = q_j \left(\frac{x_{i+1} - x_j}{\Delta x}\right) \tag{5.15}$$

$$q_{i+1} = q_j \left(\frac{x_j - x_i}{\Delta x}\right) \tag{5.16}$$

It is noted that the point charge q_j at the position x_j is assigned to its nearest grid points by the linear interpolation. It is seen that $\sum_i^{i+1} q_i = q_j$. When $|\delta x| = |x_j - i.\Delta x| = 0$, i.e. the particle resides on the i^{th} grid point, and $q_i = q_j$. After finding the total charge on all the grid points, the charge accumulated at every grid point is divided by the cell length to estimate the charge density at the grid points. Using the charge density, the potential and electric field are estimated at the grid points.

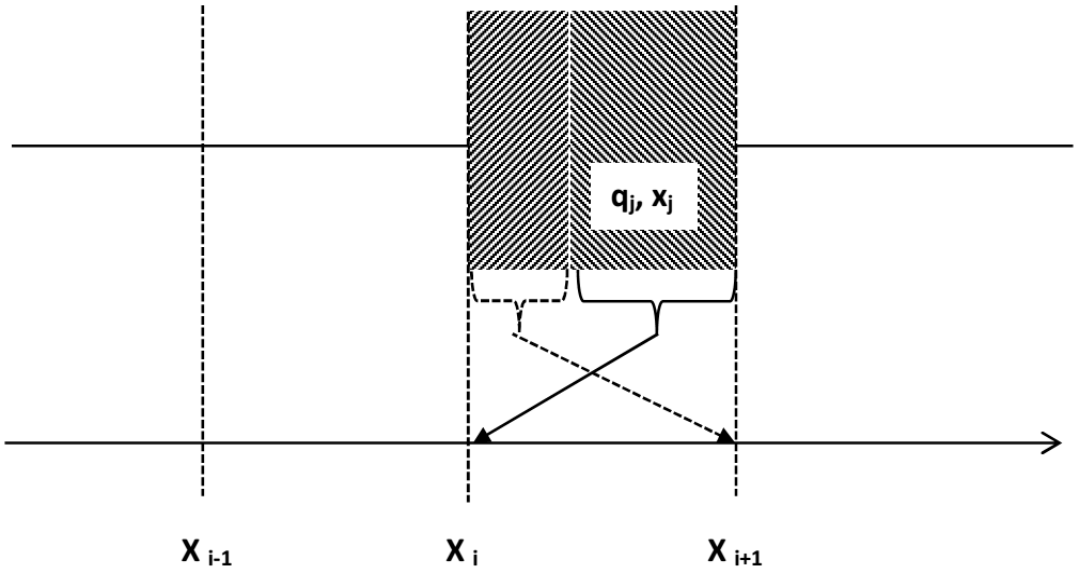

Figure 5.6: Charge assignment to grid points from particle's position using the first order linear charge weighting scheme.

5.7 Field Interpolation

The fields are computed at the grid points of the computational volume. In order to calculate the force acting on the charge particle, the electric field is to be estimated at

the position of particle. The interpolation of the electric field at the particle's position from their values at the nearby grid points is the reverse of charge assignment. The estimated electric field (E_j) at the position (x_j) of particle is given by

$$E(x_j) = \left(\frac{x_{i+1}-x_j}{\Delta x}\right) E_i + \left(\frac{x_j-x_i}{\Delta x}\right) E_{i+1} \quad (5.17)$$

Where E_i and E_{i+1} are the electric field at i^{th} and $(i+1)^{th}$ grid points and the position x_j is lies between the above two points.

5.8 Simulation Algorithm

In simulation algorithm, all variables are initialized, input parameters are defined, sets of equations are numerically solved and some output data are saved in the desired output files. At first it is necessary to decide the number of super particles (N_p), the separation between grid points (Δx) and the time step (Δt) to be used in the simulation. In arriving at these numbers, there are some criteria which should be followed so that the plasma is represented in the appropriated manner [Patel, 1989].

- The number of super particles representing the finite-sized photoplasma should be much larger than the number of grid cells. This ensures that each cell always contains several particles on an average during the simulation i.e. the no of particles over the space of Debye length should be more that 10-20 particles for macroscopic quasi-neutrality. If the number of super particles present inside the computation volume is too low, the simulation will be noisy. The condition is satisfied when the total number of super particles (N_p) is greater than number of grid points (N_g) (i.e. $N_p \gg N_g$). In our case, 50000 positive charged super particles and 50000 negative charged super particles are considered.

- The separation between grid points should not be very much greater that Debye length (λ_D) in the plasma, so that the potential setup by the charge separation can be resolved. As a rule of thumb, $\Delta x \leq 5\lambda_D$. In our case Δx is chosen as 0.07 mm.
- The time-step should be less than the period of plasma electron frequency, so that the particle oscillations are faithfully reproduced and the energy is conserved for the system. Hence $\Delta t < W_p^{-1}$. In simulation it is considered that $\Delta t\, w_p = 0.2$
- The initial positions of particles are defined inside the computational box. Their positions are randomly or uniformly assigned through the grid points as per the size of plasma. It is considered that the super-particles are distributed randomly over the finite-width of photoplasma. The width of photoplasma is ~ 10 mm.
- The initial velocities of super-particles are defined using a velocity distribution function. In the photoplasma, the electrons are initially mono-energetic whereas the photoions are nearly cold. Since the electrons are emitted in all direction after the ionization. They have the initial velocity of same magnitude. In the model of one dimensional PIC simulation, it is considered that the half of negative super particle has velocity in positive x direction and other half has velocity in negative x direction. Whereas the positive super-particles have zero velocity.
- As discussed in earlier that the main loop of leap-frog integration method runs with the particles position leading its velocity by time $\Delta t/2$. In order to fit in the time flow, the v(0) is moved backward to v($-\Delta t/2$) using the value of electric field at t = 0.
- From the initial positions of charge particles, the appropriate charge densities are assigned at each grid points using the first order charge assignment scheme. The Poisson's equation (eqn. 5.6) is solved with appropriate boundary conditions.

- From the above potential value, the electric fields at each grid points are calculated.
- The array of particles is scanned and the electric field at the position of each particle is obtained by using the same weighting scheme used for the charge assignment.
- After getting the force on charge particle, the component of velocity at the later time $(t + \frac{\Delta t}{2})$ for every particle is then calculated in three steps as discussed in section 5.5 from its value at $(t - \frac{\Delta t}{2})$. The position of each particle at the later time $(t + \Delta t)$ are found using equation like $x(t + \Delta t) = x(t) + v_x \left(t + \frac{\Delta t}{2}\right) \Delta t$. It is noted that the particle positions are calculated at integral multiples of Δt whereas the velocities are found at integral multiplies of Δt/2.
- If the super particle crosses the boundary, they lost from the computational volume.
- From the new position of the remaining charge particle, again the charge densities at the grid points are calculated and subsequently the electrical field is estimated.
- This completes one time step. The iterative calculation of above procedures simulates the decay of finite-sized photoplasma in the constant electromagnetic field.
- The output data obtained from the program is saved in files for post run analysis.

5.9 1d PIC Code

The set of equations (i.e. 5.1-5.5) are numerically solved to develop a code based on particle-in-cell (PIC) technique for the study of plasma motion in one dimension. The code is written in the FORTRAN language. It contains several subroutines like (i)

initialization of various input parameters, (ii) charge assignment on grid points from the particle position, (iii) Poison 1d solver, (iv) interpolation of electric field from grid points to the particles' positions and (v) Newton's equation solver to get the position and the velocity of particles. The potentials at the boundary of computational volume are defined. The boundary EL1 is grounded whereas EL2 is negatively biased to an external potential. During their motion, the super particles cross the boundary or electrode and lost from the computational volume. Thus a fully kinetic model has been developed using 1d PIC simulation. Though the external magnetic field is incorporated in the model, its value is set to zero to study the decay of pulsed photoplasma in an external electrostatic field.

The various output variables and parameters of the programs are written in the several files. At a particular time, the dynamic variables like the phase space (v_x versus x) and velocity distribution function of particles, spatial distribution of charge density $\rho(x)$, particle density n(x), potential $\varphi(x)$, field E(x) and particles energy are calculated. The time history of various quantities such as electrostatic energy, particle kinetic energy, particle thermal energy, plasma potential, number of particles cross the boundaries, the current signal on electrodes are recorded. In this way a sufficient data has been stored or accumulated like the experiment performed in a laboratory. They are used to verify the correctness of the physics and to provide the insight desired into the photoplasma problem.

5.10 Summary

A fully kinetic one dimensional model based on particle simulation has been developed to study the evolution of photoplasma. The mathematical problem consisting of a set of equations has been formulated. The equations are solved numerically. The photoplasma has been replaced by an equal number of both positive and negative

charged super-particles. The particles are randomly distributed over the photoplasma volume. The charge densities at the grid points have been calculated from the particles' positions. The Poisson's equation has been solved to get the potential and electric fields using the charge densities at the grid points. The fields at particle's positions are calculated from their values at grid points using linear interpolation. Using the fields the velocity and position of super particles have been calculated. The iterative execution of the above steps has computed the electric field self-consistently and described the motion of charge particles. This model is being used to study the decay of the finite-width photoplasma in the electrostatic field.

Chapter 6

Motion of Low-density Photoion-bunch in Linear Electrostatic Potential Wells

The chapter 6 presents the motion of a low-density (~ $1x10^{13}$- $5x10^{14}$ m^{-3}) photoplasma in electrostatic potential wells created by the plate-grid-plate geometry. Under the external electric field, all electrons get removed from the photoplasma within a time scale of few ns and only the ion bunch remains left. It shows an oscillatory behavior like single particle kinetics while the ion-bunch evolves in the potential wells. The oscillation behavior gets modified as the photoplasma density increases. The motion of photoplasma is governed by both the externally applied electric field and the space charge produced internal field. The transition of plasma behavior from the single particle kinetics to collective motion due to space-charge interaction is explained using PIC simulations.

6.1 Introduction

Motion of charge particles under electromagnetic field is an elementary problem in physics. Though the plasma is an ensemble of charge particles, but its characteristics are distinctly different from that of the single charge particle due the long range Coulomb interactions among the charge particles. The interactions among charge particles are relatively weak in low-density plasma. So the low density plasma behaves as single charge particle under the external electric field. Its single particle behavior changes to the collective motion while the density of plasma increases. Therefore in plasma physics, it is important to understand the basic characteristics of plasma over its wide range of density. The motions of photoplasma are studied in electrostatic potential wells with various electric field configurations. The potential wells are produced by plate-grid-plate

geometry where the different biasing configurations are created using the grid to control the photoplasma motion. The use of grid (meshed electrode) geometry is also found in manipulation of ion motions in the time-of-flight mass spectrometer [Opsal et al, 1985], double plasma device [Barrett et al, 1989 and Rohde et al, 1997] and vacuum triode tube.

In the following section, the motions of a finite-sized low-density photoplasma in linear electrostatic potential wells are discussed. The structures of experimentally recorded photoion current signals are explained using single particle motion. As the plasma density increases, its behavior deviates from that of single particles in the external electric field. The plasma behaviors in the potential wells are described using PIC simulations.

6.2 Theoretical Description

6.2.1 Analytical Solution

When the photoplasma density is quite low (~10^{12} m^{-3}), the interactions among charge particles are neglected. The ion-bunch is considered as an ensemble of independent charge particles. They move independently in the external electric field. The equations of motion for a single particle are solved analytically to get its velocity and position. Thus the motion of low-density photoplasma is explained by single particle motion. As the density of photoplasma increases, the space charge interactions among the charge particles become significant. The motion of charge particle is not only governed by the externally applied electric field but also by the internal field due to space charge interactions. In such situation, it is difficult to solve the equations of motion analytically. It requires the numerical simulation to understand the plasma dynamics.

6.2.2 PIC Simulation

The plasma simulations based on PIC techniques, discussed in chapter 5 have been considered to simulate the photoplasma motion in the linear electrostatic potential wells. The code has been modified accordingly for the plate-grid-pate geometry. When the super particles move in the electrostatic potential wells, the electrical current is generated in the circuit. The rate of induce charge formation on the parallel plates and grid (i.e. meshed electrode) gives the convection current. While the charge particles are in zone I, they induce their image charges on plate no. 1 and grid. No charge is induced on plate no 2. The similar phenomena are happened between the grid and plate no. 2 when the charge particles are in zone II. For an example, if a particle of charge Q is positioned at a distance x_0 from the plate no. 1 in zone I, the charge Q_1 and Q_2 are induced on plate no.1and grid respectively. They are given by [Spangenberg, 1948] following relations.

$$Q_1 = -Q\frac{d-x_0}{d} \tag{6.1}$$

$$Q_2 = -Q\frac{x_0}{d} \tag{6.2}$$

here d is the separation gap between plate no.1 and grid frame. It is noted that (Q_1+Q_2) =-Q. The current (I_g) on the grid electrode is given by the relation of $I_g = \left|\frac{dQ_2}{dt}\right| = Q\frac{v}{d}$, where v is the velocity of charge particle with respect to the grid position. In reality, the grid electrode has a finite transmission factor T. As the super-particles cross through the grid from one zone to another zone, they are replaced by a new super-particle of charge TQ and mass Tm. After certain number of cross-over, the super-particles below an arbitrary minimum size have negligible contribution. Therefore they are discarded in the simulation.

6.3 Removal of Electrons from Low-Density Photoplasma

It has been already discussed that the photoplasma is generated with mono-energetic electrons which carry the excess absorbed energy as their kinetic energy. They fly and escape from the very low-density finite-size photoplasma even in the absence of any external field. The photoions bunch remains left. In our case, it happens at the plasma density $\leq 8x10^{12}$ m^{-3}, when the electrostatic potential energy of electrons at the plasma boundary is equal to the initial kinetic energy of the electrons (~0.54 eV). When an external electrostatic field (E_{ext}) is applied, it aids to remove the electrons from the photoplasma at density > $8x10^{12}$ m^{-3}. As the plasma density increases, the internal space charge field (i.e. E_{int}) created in the photoion bunch pools the electrons. Thus it prevents the electrons from escaping the photoplasma. The E_{ext} and E_{int} fields are estimated from following relations.

$$E_{ext} \approx \frac{V}{d} \tag{6.3}$$

$$E_{int} \approx \frac{n_i\, e\, D}{4\, \epsilon_0} \tag{6.4}$$

where V is applied potential on plate, d is the separation between the plate and grid, n_i is the plasma ion density, D is the diameter of cylindrical ion-bunch and ε_0 is free space permittivity. A parameter α is defined as the ratio of internal field to external field i.e. $\alpha = E_{int}/ E_{ext}$. When the external field dominates over the internal field i.e. $\alpha < 1$, all electrons get removed from the photoplasma and only a photoion bunch remains left. It is calculated that the electrons remove from the plasma of density < ~ $1.5x10^{14}$ m^{-3} in presence of E_{ext} ~ $7x10^3$ V/ m. The same is also estimated from the PIC simulation where the fields are obtained self-consistently from the Poisson's equation. The corresponding plasma density is ~ $3x10^{14}$ m^{-3} and it agrees well with the above estimation. As the plasma density further increases, only a fraction of electrons is removed from the photoplasma. The unbalanced positive charge in the photoplasma produces an electric field which

creates the potential well for electrons and prevents them from escaping the photoplasma. Therefore the photoplasma having a certain plasma density satisfies all plasma criteria.

6.4 Motion of Photo Ion Bunch in Potential Wells

The motion of photoion bunch having density of ~$2x10^{13}$ m^{-3} has been studied in the electrostatic potential wells (symmetric and asymmetric) created in plate-grid-plate geometry as discussed in section 2.5.1. A symmetric linear potential well is formed when the grid is biased at - 200 V and the plate no. 1 and plate no. 2 are grounded. The Laplace equation is solved analytically to get the potential distribution over the space and it is shown in figure 6.1(a) by the dotted line. In presence of finite-width photoion bunch the potential distribution is also obtained from PIC simulation by solving the Poisson equation as shown in fig 6.1(a) by the solid line. The potential at any points is the superposition of externally applied potential (from Laplace equation) and the internally produced potential due to the positive ion-bunch.

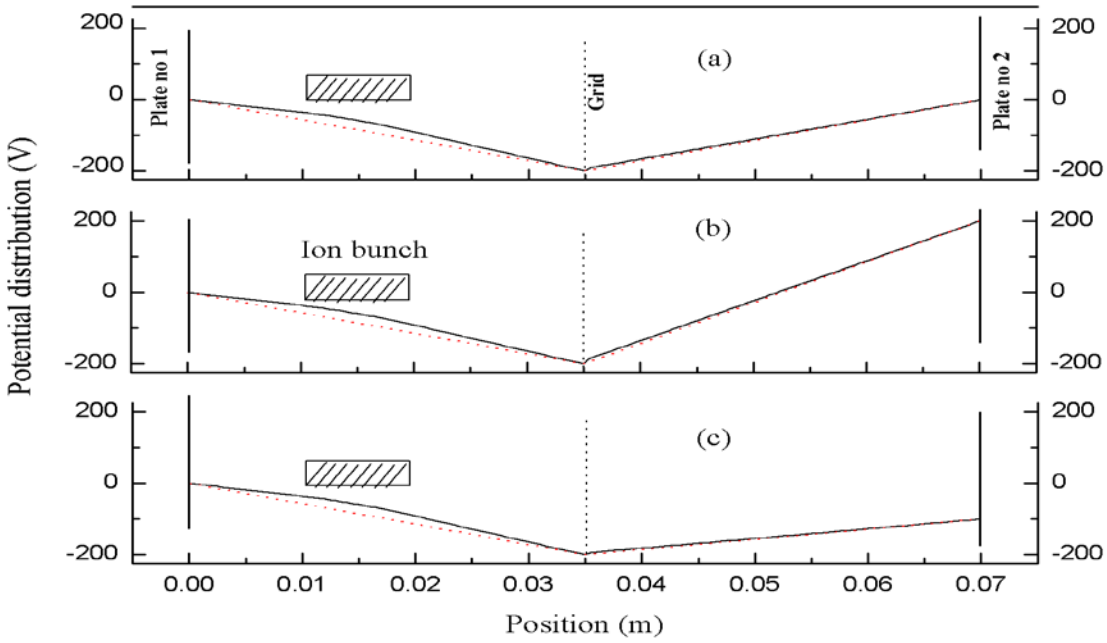

Figure 6.1: Potential distribution of symetric (a) and asymmetric potential wells (b and c).obtained from analytical solution (⋯⋯), PIC simulation (——) with ion-bunch of density ~$2x10^{13}$ m^{-3}

It is noticed that a small change is occurred in the potential distribution of zone I due to the presence of ion-bunch. In similar fashion the asymmetric potential wells are also created by changing the biasing voltages on plates and grid. Two such asymmetric potential wells are shown in fig. 6.1(b) and fig. 6.1(c). In both cases, the grid is biased at -200 V and plate no. 1 is grounded. The plate no.2 is biased at +200 V in fig. 6.1(b) and -100 V in fig. 6.1(c).

To understand the dynamics of photoion bunch, the phase-space trajectory of photoions is calculated for different potential configurations of fig. 6.1. They are shown in fig. 6.2(a, b, c) respectively.

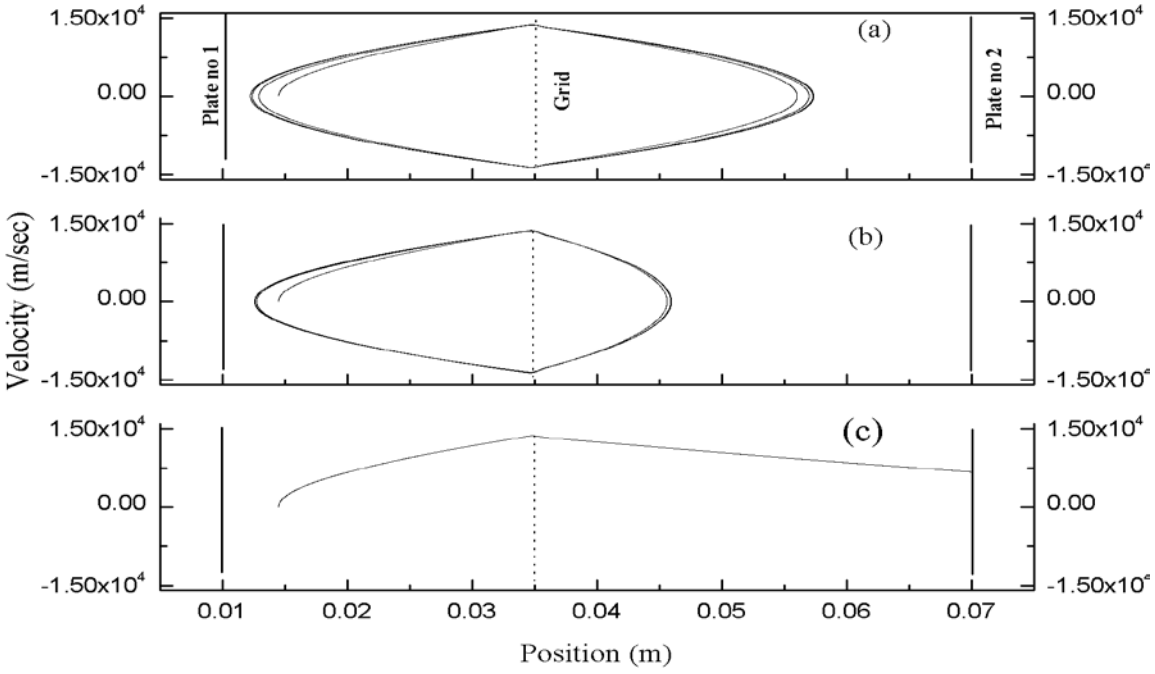

Figure 6.2: Trajectory of photoion in phase-space plane for different potential wells as shown in figure 6.1.

In fig. 6.2 (a), the photoion forms a close loop trajectory in phase space. It means that the photoion moves from zone I to zone II through grid and vice versa. It shows an oscillatory periodic motion in the potential well. In fig. 6.2(b) the photoion bunch shows a non-periodic oscillation for the asymmetric potential well in fig. 6.1(b) due to different

electric field in different zone. When the potential well is more asymmetric as shown in fig. 6.1(c), the phase-space trajectory does not form the closed loop as shown in fig. 6.2(c). During their evolution, the photoions strike on the plate no.2 and get absorbed there.

6.5 Experimental Observations

The details of experimental set-up used to study the motion of photoplasma in plate-grid plate (PGP) geometry have been discussed in section 2.5.1. The electrostatic potential wells were experimentally created using different biasing configurations and the photoion current signals were individually measured on grid and plates. The photoplasma was generated in zone I between plate no. 1 and grid. The measured photoion current signal on different electrodes are shown in fig. 6.3 when the photoion bunch moves in potential well of fig. 6.1 (a).

The structure of current signal recorded on the grid electrode shows an oscillatory motion. The ion bunch moves in the potential well over the grid position and it is reflected on the current structure. During the crossover of ion bunch from one zone to another zone, some charge particles are absorbed and get lost on grid due to its finite transmission factor. The amplitude of oscillation decreases. Therefore the oscillation is damped in nature. From the current signals, it is also observed that no current is recorded on the plate no. 2 as long as the ion-bunch remains in zone I. It means no lines of force originating from the charge particle of zone I penetrate to zone II. It forms the induced charges on the plate no. 1 and the grid. The motion of ion bunch is studied analytically as well as through PIC simulation. In analytical solution, the ion bunch is considered as a point charge whereas in PIC simulation the finite-width ion bunch is considered as the ensemble of macro charged particles distributed over the width. The temporal structures

of current signal obtained from theory and PIC simulation are also plotted in figure 6.3 by dotted lines with grid transmission factor of 0.5.

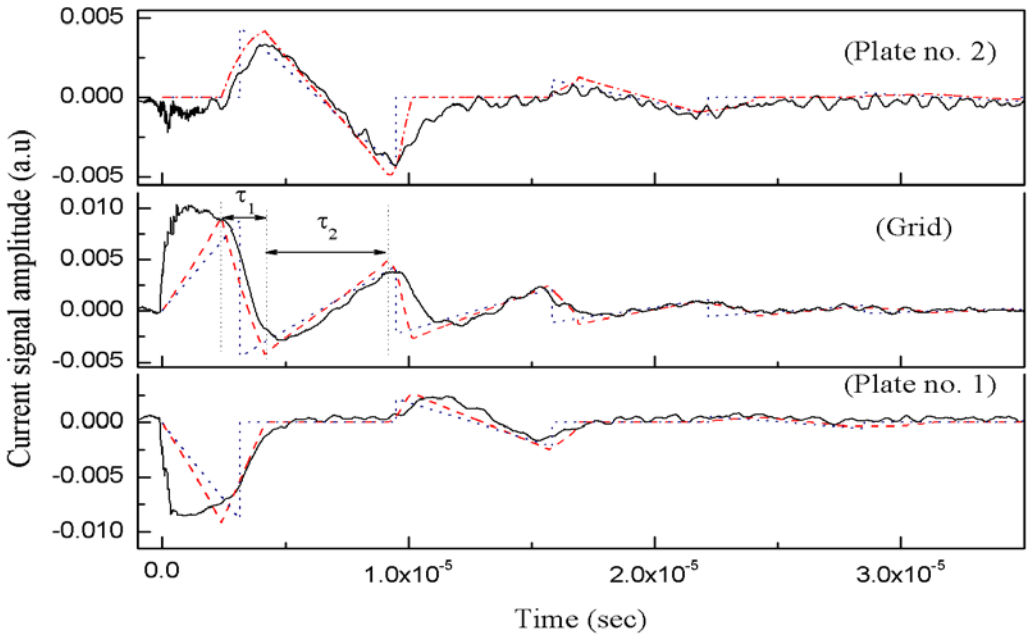

Figure 6.3: Photoion current signal recorded on various electrodes when the photoion bunch of density ~ $2x10^{13}$ m^{-3} evolves in the symmetric potential well as shown in figure 6.1(a): ····· analytical solution, ---------- PIC simulation and —— experiment.

The ion bunch travels in potential well. The period of oscillation is estimated from its transit time which consists of time τ_1 and τ_2. The $\boldsymbol{\tau_1}$ represents the transit time of the finite-width ion-bunch to traverse from one zone to another zone through grid whereas the $\boldsymbol{\tau_2}$ is the travel time of ion-bunch in one zone. For the case of analytical solution, the value of $\boldsymbol{\tau_1}$ is zero as the ion-bunch is represented by a single charge particle. Whereas in PIC simulation, the photoions are distributed over the initial width of ion-bunch, hence the photoion-bunch takes a finite time to crossover the grid and it is reflected on fig. 6.3. The time period of oscillation observed on grid electrode is the sum of $\boldsymbol{\tau_1}$ and $\boldsymbol{\tau_2}$. It is noticed that the simulated current structures from PIC simulation reasonably match with the experimentally observed current signals.

The period of oscillation of a charge particle in the symmetrical linear 'V' shaped potential well is analytically solved. The oscillation frequency (f) of current pulse on the grid is obtained analytically from the transit time of photoions. It is given by

$$f = \sqrt{\frac{QV}{32\, m_i\, d\, x_0}} \qquad (6.5)$$

where x_0 is the initial distance of charge particle from the grid, m_i is the mass of photoion. All other notations are described earlier. The oscillation frequency varies with square root of applied potential but independent of plasma density. It agrees with the experiments [Majumder et al 2003] in low density (~10^{13} m^{-3}) plasma regime.

The photoion current signals recorded on the grid electrode for the asymmetric potential wells of fig.6.1 (b, c) are shown in fig. 6.4(a) and 6.4(b) respectively.

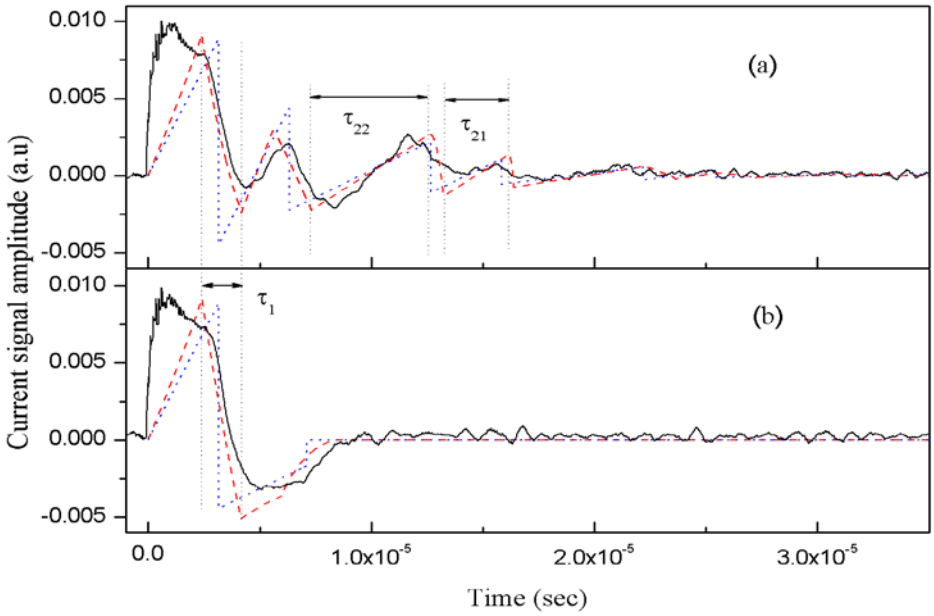

Figure 6.4: Current signal of grid electrode while the photoion bunch of density ~ $2x10^{13}$ m^{-3} is undergone in an assymetric potential well of fig. 6.1(b) and 6.1(c): ·····, analytical solution, ---------- PIC simulation and —— experiement.

Figure 6.4(a) shows a non-periodic oscillation. In asymmetric potential well, the electric field in zone I and zone II are different. Therefore the time τ_2 has different magnitude in different zone (say τ_{21} in zone I and τ_{22} in zone II) as indicated in figure 6.4. As discussed in earlier section, though the phase space trajectory forms a closed loop but its curvature varies from one zone to another zone due to the different electric field in different zone and it shows a non-periodic oscillation. In case of fig. 6.4 (b), as the ions strike on plate no. 2 and get absorbed. As a result, no oscillation in current signal recorded across the grid is observed.

6.6 Effect of Photoplasma Width

To know the effect of plasma width on its oscillation characteristics, the ion bunch of 12 mm and 6 mm width were studied in the symmetric potential well. The width of ion bunch was varied experimentally using the adjustable iris placed in front of chamber window. The measured current signals on the grid electrode are shown in figure 6.5 by solid curve for 12 mm and 6 mm width of photoplasma.

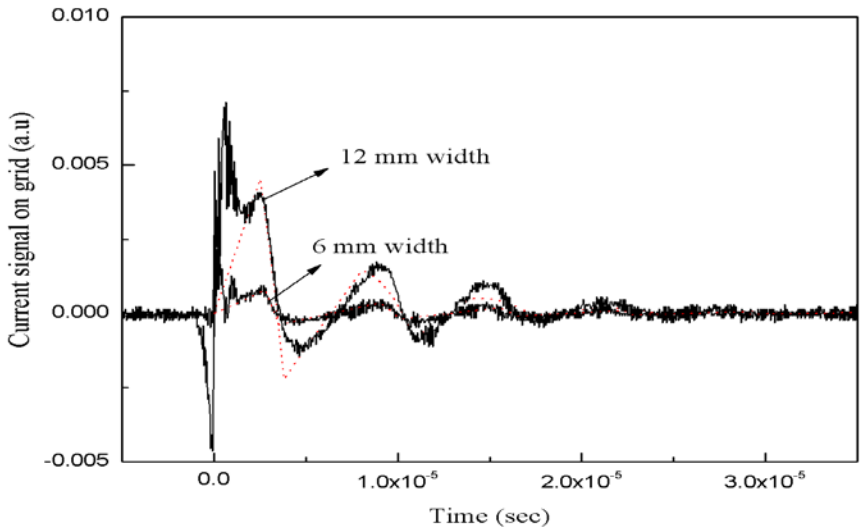

Figure 6.5: Photoion current signal measured on grid electrode for different width of photoion bunch of density ~ $2x10^{13}$ m^{-3} evolved in symetric potential well shown by figure 6.1(a): _____ experiment and --------- PIC model

The dotted line represents the same obtained from the PIC simulation. It is observed that though the signal's amplitude is increased for 12 mm width of ion bunch, the period of oscillation remains nearly same for both plasma widths. This is due to the fact that the total number of photoions in the ion-bunch increases as the width of ion-bunch increases. For the larger width of photoplasma, it takes longer time to cross the grid window while it spends lesser time in each individual zone. The time $\boldsymbol{\tau_1}$ and $\boldsymbol{\tau_2}$ vary in a way such that their sum (i.e. the period of oscillation) remains almost same for the different plasma width. Though the strength of internal field increases as the width of photoion bunch increases, but its contribution remains very less compared to the external field in the density range of ~10^{13} m^{-3}.

6.7 Space-Charge Effect (Collective Behavior)

When the density of photoplasma increases to a certain density (> ~ $5x10^{14}$ m^{-3}), the space charge interaction among charge particles builds up. Not all electrons are removed from the photoplasma; only a small fraction of electrons fly from the plasma. An ambipolar field is produced by the unbalanced positive charge which forms a potential well for electrons and prevents the remaining electrons from escaping the photoplasma. During its evolution in the externally produced potential well the motion of photoions is governed by not only the externally applied field but also by the space charge created internal ambipolar field. The resultant potential distribution gets deformed from the "V" shaped linear potential well. The frequency of oscillatory motion is obtained from the following relation.

$$\boldsymbol{f} = \sqrt{\frac{\boldsymbol{Q}}{\boldsymbol{32\, m_i\, x_0}}\left(\frac{\boldsymbol{V}}{\boldsymbol{d}} + \frac{\boldsymbol{\delta_e\, n_i\, Q\, D}}{\boldsymbol{4 \in_0}}\right)} \qquad (6.6)$$

This expression is an extension of the formula which is derived from particles' independent motion under the external electric field. Here δ_e is defined as the fraction of

electrons (i.e. N_e/N_i), removed from the photoplasma and its value lies between 0 and 1 (i.e. $0<\delta_e \leq 1$). The n_e and n_i are the number of electrons and ions present inside the photoplasma. For the plasma density of ~ $1x10^{14}$ m^{-3}, the variation of estimated oscillation frequency from the analytical expression of equation 6.6 with applied grid potential is shown by dotted curve in figure 6.6. The same is also calculated using PIC simulation and plotted by solid curve in figure 6.6.

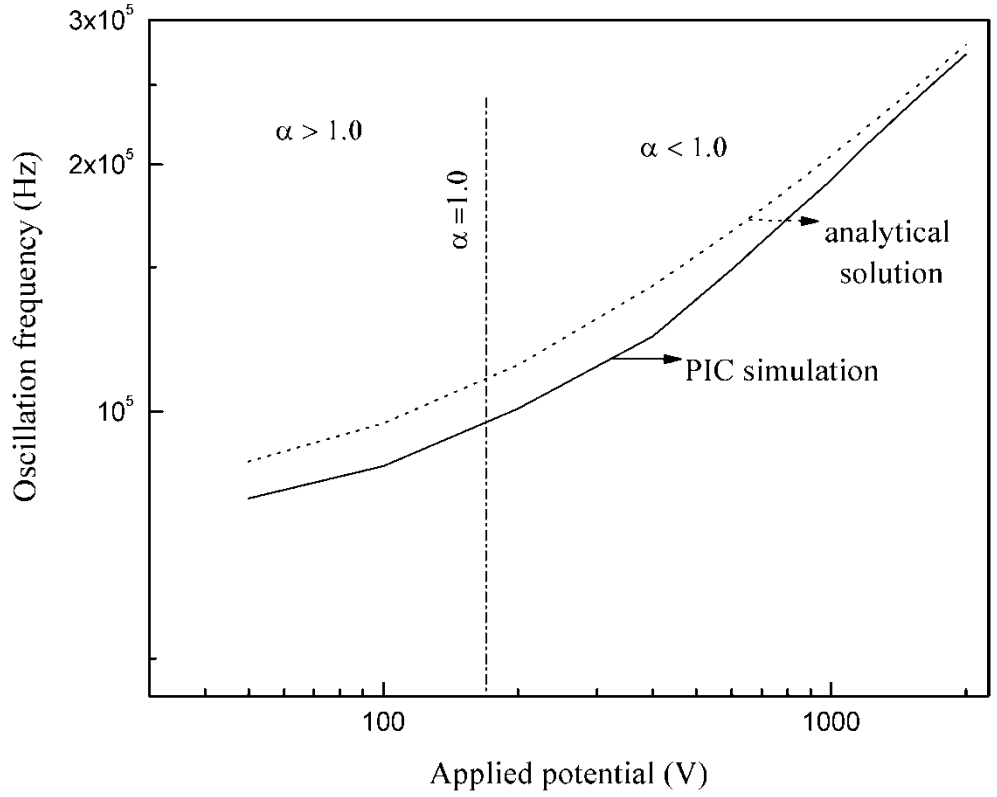

Figure 6.6: Variation of oscillation frequency with the applied negative voltage on grid when the photoplasma of density $1x10^{14}$ m^{-3} evolves in symetric potential well.

When the value of α is very less than unity (i.e $\alpha<<1$) which means the external electric field dominates over the internal field, the oscillation frequency obtained from analytical expression (with δ_e =1) matches with that of PIC simulation. Whereas in case of $\alpha \geq 1$, the strength of external electric field is nearly equal to the internal field, the

estimated oscillation frequency is slightly higher side than that obtained in PIC simulation. In analytical expression, it is assumed that the δ_e value is ~1 but in actual case it is not strictly true for the value of $\alpha > 1$. Only a fraction of electrons get removed from the plasma. The value of δ_e is < 1 and the resulted frequency is slightly lesser than that calculated using relation 6.6 with the value of $\delta_e = 1$.

When the ambipolar field plays a significant role in the motion of photoplasma, the oscillation frequency depends on the plasma density. The variation of oscillation frequency with the plasma density in symmetric potential well with -500 V applied on the grid is shown in figure 6.7. The dotted line represents the results of analytical expression and the solid line data is from PIC simulation. The values are matched in reasonably good agreement. The magnitude of oscillation frequency is a fraction of plasma ion frequency.

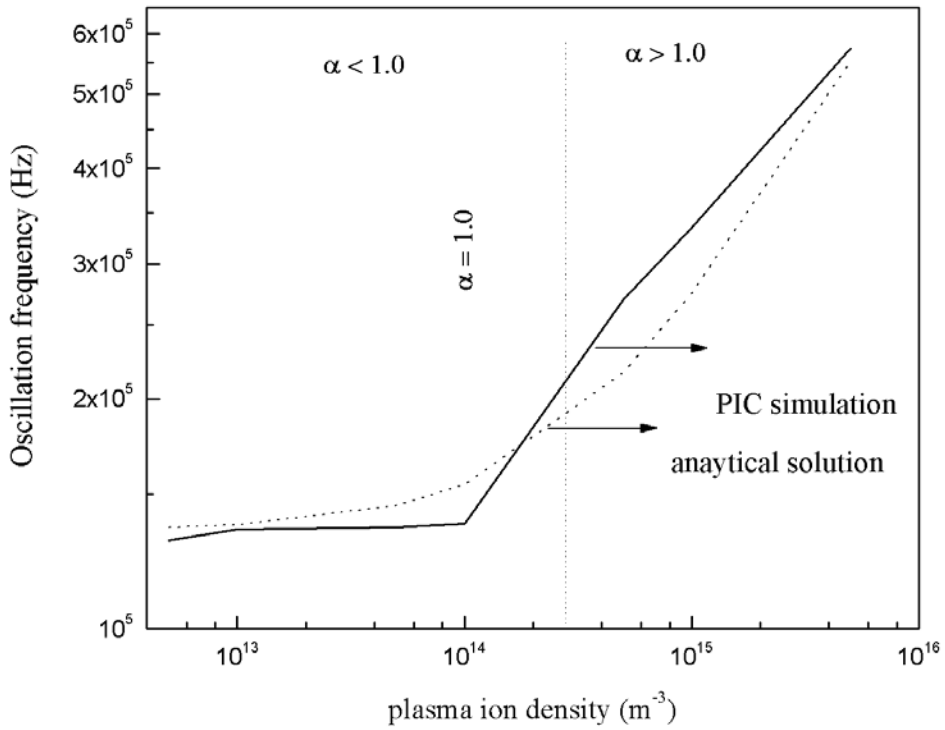

Figure 6.7: Variation of oscillation frequency with plasma density during the evolution of photoplasma in symmetric potential well produced by biasing with -500 V on the grid electrode.

As the plasma density further increases, the electrons and ions are strongly coupled in the plasma (i.e. $\alpha >> 1$). The plasma motion is governed by the space charge created ambipolar internal field. It decays due to ambipolar diffusion and does not show any oscillatory behavior in the potential well. Thus the collective behavior due to space charge interactions among charge particles dominates over the single particle motion under the external electric field. During its evolution the photoion density gradually decreases with time due to their absorption on the grid and plates. The strength of internal ambipolar field decreases. As a result the plasma's collective behavior changes to single particle behavior.

6.8 Summary

The motion of low-density photoplasma of $\sim 10^{13}$-10^{15} m^{-3}, has been investigated in the linear electrostatic potential wells. For low density plasma ($\leq 3x10^{14}$ m^{-3}), all electrons get removed from the plasma by the external electric field, leaving behind a photoion bunch. The photoion bunch has been considered as a collection of non-interacting independent charge particles as the interactions among them are very less. The photoions move in the potential well and exhibit a damped oscillation in the current signal recorded on the grid electrode. The amplitude of oscillation decreases due to their absorption on the grid during their passage through the grid window. As the density in plasma increases, the interactions among charge particles become significant. Then the oscillation frequency is governed by both the externally applied field and by the internal field produced by space charge interactions. The photoion bunch behaves differently from that of independent particle. As the plasma density further increases, the ensemble of charge particles exhibits the collective behavior of plasma governed by the space-charge interactions.

Chapter 7

Decay of Photoplasma in Electrostatic Field

The chapter 7 describes the decay of finite-sized photoplasma in an electrostatic field. During its decay the photoplasma passes through different transient stages. The various physical process happened in the direction of electric field are investigated and discussed. The transient responses of photoplasma to the external electric field and its temporal evolutions are studied using 1d PIC simulation.

7.1 Introduction

Photoplasma is transient in nature. To understand the complex characteristics of the photoplasma, it has been studied in literature under various electric field configurations over its wide range of plasma density as discussed in section 1.5. Though it has been studied extensively, but the complex transient behaviors of the photoplasma are not clearly understood. The transient stages through which it decays are also not fully explained. To understand the transient aspects of photoplasma decay, the simulation of the finite-sized photoplasma in the electrostatic field has been carried out using a fully kinetic 1d PIC model. In the following section, the different physical processes occurred along the electric field direction during its decay in the electrostatic field have been investigated and discussed.

7.2 Input Parameters to PIC Simulation

The initial input parameters of the PIC simulation are listed in table 7.1. The various plasma parameters like Debye length (λ_D), plasma electron frequency (ω_{pe}), plasma ion frequency (ω_{pi}) and number of particles in Debye sphere (N_D) are estimated from the input parameters. Their values are given in table 7.2. The electrons in the plasma

response to the external field in timescale of ω_{pe}^{-1}. Therefore the time step (Δt) in numerical simulation should be less than ω_{pe}^{-1} to capture the electrons' motion. In our case, the value of Δt is chosen as 0.2 times ω_{pe}^{-1} to properly describe the plasma collective behavior and to ensure the energy conservation. Regarding the spatial step, the separation between grid points should be smaller than the Debye length to describe the collective phenomena in plasma. Here Δx = 0.07 mm is chosen which is less than λ_D= 0.08 mm as given in table 7.2.

Table 7.1: Input parameters for 1d PIC simulations of the finite-sized photoplasma

Name of element	: Barium
Mass of photoions	: 138 amu
Plasma density ($n_e = n_i$)	: $5x10^{15}$ m^{-3}
Kinetic energy of electrons (KT_e)	: 0.54 eV
Kinetic energy of photoions (KT_i)	: 0 eV
Separation between electrodes (L)	: 35 mm
Photoplasma width (W)	: 10 mm
Electric field (E_{ext})	: $1.5x10^4$ Volt/ m
Magnetic field (B_0)	: 0 Tesla
Separation between grid points (Δx)	: 0.07 mm
Time step (Δt)	:0.2 W_{pe}^{-1}
No. of negative super particles (N_{pe})	: 50000
No. of positive super particles (N_{pi})	: 50000

Table 7.2: Calculated plasma parameters of the above photoplasma

Debye length (λ_D)	: 0.08 mm
No. of particles in Debye sphere (N_D)	: 9600
Plasma electron frequency (W_{pe})	: $4x10^9$ rad
Plasma ion frequency (W_{pi})	: $8x10^6$ rad

The initial plasma density distribution in the photoplasma is shown in figure 7.1. It is clearly shown that there is a sharp density gradient at the plasma boundary. The photoplasma has the finite width of ~ 10 mm. There is a vacuum gap between the plasma boundary and the electrode. In the photoplasma, the electrons initially have same kinetic energy which is the excess absorbed energy of neutral atoms over its ionization energy. They emit in all directions [Yamada et. al., 1990 and Patel et. al., 1995]. The initial velocities (i.e. v_x) of plasma electrons are chosen corresponding to the energy of ~ 0.54 eV. In 1d PIC simulations, the electrons are emitted in either x direction or opposite to that. The photoions have zero velocity (i.e. cold ions) at time t = 0.

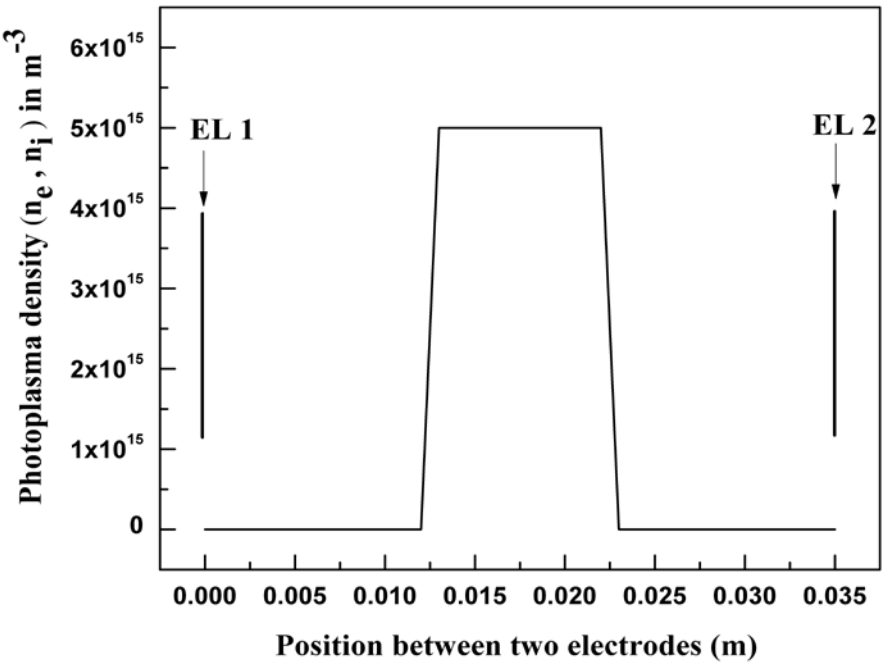

Figure 7.1: Density distribution of plasma particles in photoplasma between two electrodes at t=0.

7.3 Relaxation of Electrons' Velocity Distribution

The initial velocity distribution of mono-energetic plasma electrons is shown in fig. 7.2(a). Two streams of electrons move in opposite direction. Due to two stream

instability in the plasma, the width in velocity distribution of each beam increases as shown in fig. 7.2(b). It clearly indicates the increase in the temperature of each beam. The drift or mean velocity of each stream decreases. The electrons also interact with each other through Coulomb interaction. They relax among themselves with time. The distribution becomes nearly Maxwellian. The figure 7.2(b-d) show the evolution of velocity distribution function $f_v(v_x)$ of plasma electrons at time (b) $t = 5\omega_{pe}^{-1}$, (c) $t = 5x10^1$ ω_{pe}^{-1} and (d) $t = 1x10^2$ ω_{pe}^{-1} respectively. The plasma evolution time (t) is normalized with respect to ω_{pe}^{-1} where ω_{pe} is the plasma electron frequency in radian unit. The fitted Gaussian curves are shown by red color lines. The figures 7.2(c) and 7.2(d) show that there is a rapid relaxation of the electrons' velocity distributions. It is also observed in the simulation that the energy distribution follow the Boltzmann distribution. Therefore the plasma electrons get equilibrated within a time-scale of ~ $1x10^2\omega_{pe}^{-1}$.

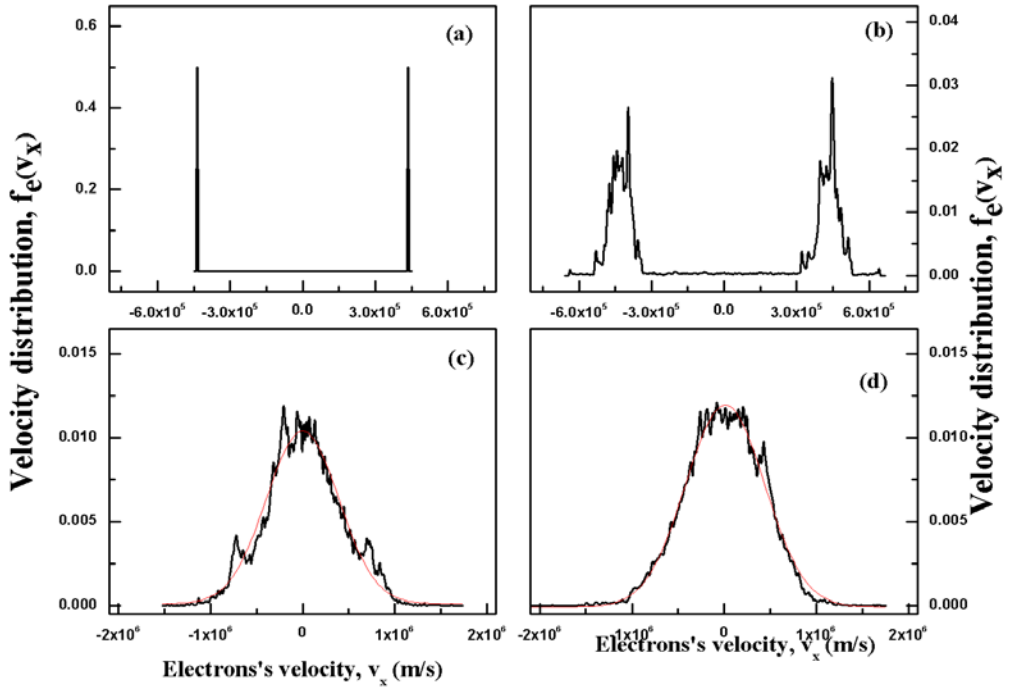

Figure 7.2 Velocity distribution functions of plasma electrons at time: (a). t = 0, (b). $t = 5\omega_{pe}^{-1}$, (c). $t = 5x10^1$ ω_{pe}^{-1} and (d). $t = 1x10^2$ ω_{pe}^{-1}. The fitted one dimensional Maxwell velocity distributions are shown by red color curves.

The electron temperature is directly proportional to the thermal energy of electrons. The temporal variation of the mean thermal energy per electron is shown in figure 7.3. The initial mean value represents the excess absorbed energy of the atom. In absence of external electric field, it remains nearly constant as shown in figure 7.3(a) which shows the conservation of total energy for an isolated system. In presence of the external electric field, the mean thermal energy increases and attains a stable value which is higher than its initial value. Its stable value also increases with increase of applied electric field as shown in the figure 7.3(b) and 7.3(c) for electric field of ~2.8×10^3 V/m and ~1.4×10^4 V/m respectively.

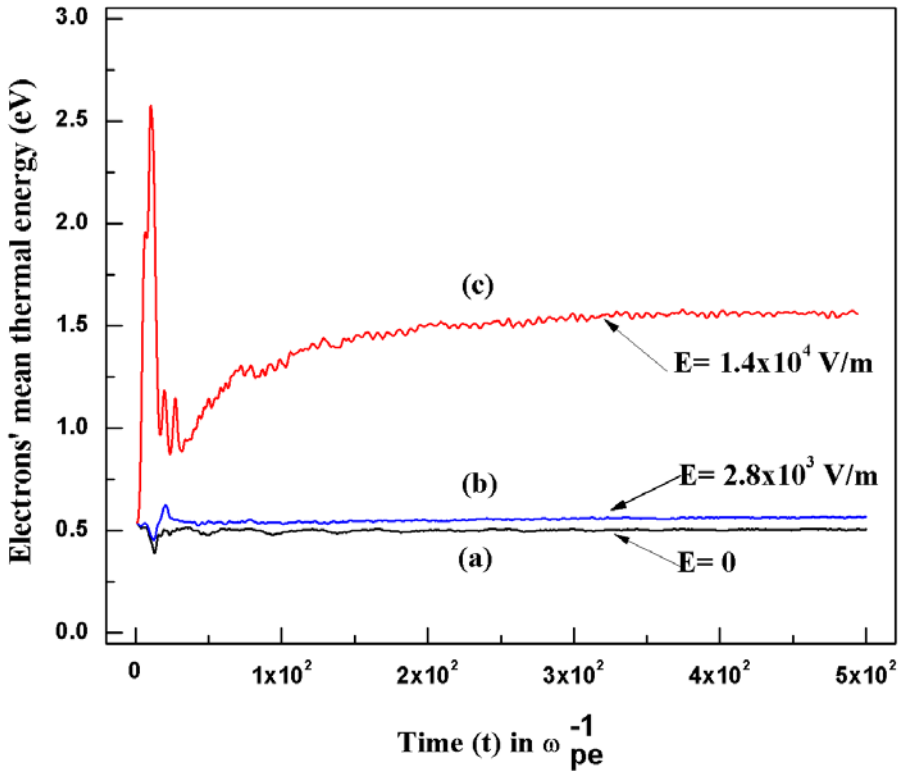

Figure 7.3 Temporal variation of electrons' average thermal energy when the applied electric field is (a) $E_0 = 0$, (b) $E_0 \sim 2.8 \times 10^3$ V/m and (c) $E_0 \sim 1.4 \times 10^4$ V/m.

The initial transient peak represents the electrons' fast response to the externally applied electric field. They accelerate under the external electric field. The average

kinetic energy increases. A fraction of high energetic electrons cross the anode boundary before build up of an internal ambipolar field and subsequently the electrons average kinetic energy decreases. As the electrons start to move towards the anode, an internal field builds up due to the space-charge interaction among the charge particles. It pulls the electrons towards the plasma. With time the remaining plasma electrons get equilibrated. The average thermal energy attains a stable value of nearly 1.5 eV at the applied electric field of ~ 1.4×10^4 V/m.

7.4 Transient Effect in Plasma Potential

Due to the initial response of plasma electrons to the externally applied electric field, a transient effect is observed in plasma-space-potential and the spatial distribution of potential over the computational volume. The plasma-space-potential is defined as the potential averaged over the quasi-neutral region of plasma volume. In case of finite-width photoplasma, it is calculated as the averaged potential over the central 80% region of its initial photoplasma width. Figure 7.4 shows the initial temporal variation of the plasma-space-potential (i.e. φ_p) during the plasma evolution under the external electric field. The plasma-space-potential oscillates and after a few cycles (10-15 nos) of oscillations, it acquires a stable value close to the anode potential. The period of oscillation in the plasma-space-potential is estimated and it is around ~ 6.8 ω_{pe}^{-1}. It is in good agreement with the period of the plasma electron oscillation i.e. $\tau_{pe} = \frac{2\pi}{\omega_{pe}} = 6.28\ \omega_{pe}^{-1}$. It means that the oscillations observed in the plasma-space-potential are due to the oscillations of plasma electrons in the background of cold photoions. As the time increases, the electrons are distributed over the photoion background. Though the oscillation of electrons remains in the background of photoions, the amplitude of oscillation is very less. The plasma potential oscillates over a slightly positive potential than the anode potential (i.e. ground

potential). Kurosawa et al [2001] discussed the parametric study of plasma potential in presence of the electric field using the fluid model.

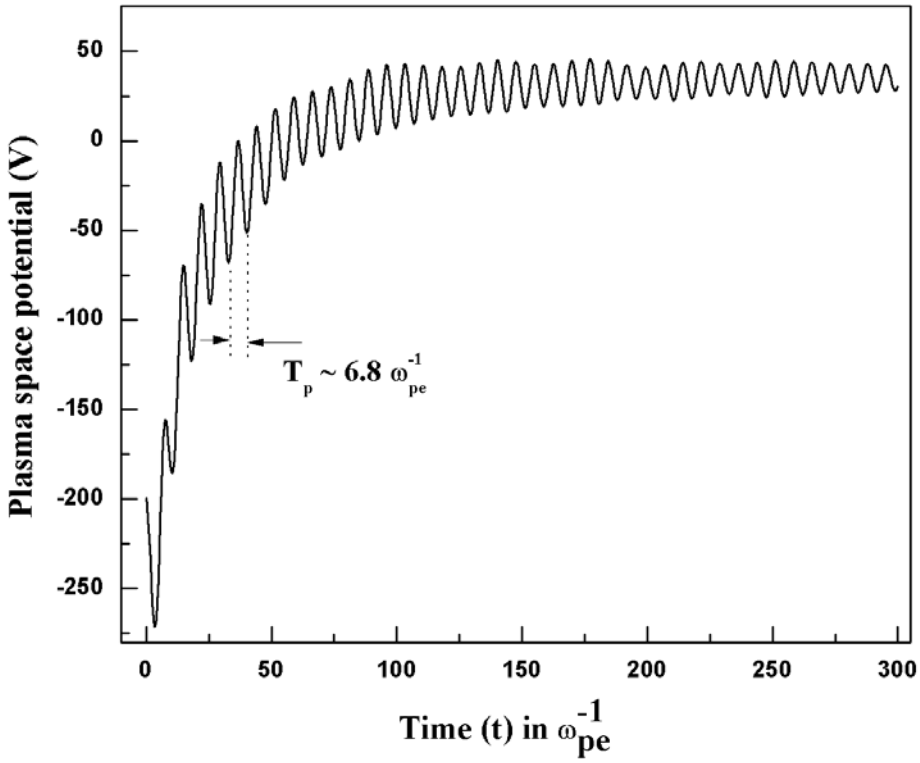

Figure 7.4: Oscillatory motion of the plasma space potential before it attains a stable value close to the anode potential.

The distribution of potential over the computational space between two electrodes is varied with time. The time dependent evolutions of potential distribution are shown in figure 7.5. The potential distribution changes as the charge densities change over the grid points. At time t = 0, the net charge density is zero (i.e. n_i-n_e=0) throughout the photoplasma region as each electron's charge is compensated by the positive charge of photoions. The potential profile (obtained from Laplace equation) falls down linearly from the anode potential to cathode potential. The electrons response to the external electric field and they move towards the anode. It makes an electron rich zone near the plasma vacuum boundary towards the anode while it lefts behind the positive ion

background at the other end of the plasma towards the cathode. The charge density profile over the space is changed from its initial value. It has the negative value towards the anode and positive value towards the cathode. Therefore the potential falls at the anode side and rises at the cathode side of the photoplasma, as shown by the potential profile at time t = $2\omega_{pe}^{-1}$ and t = $4\omega_{pe}^{-1}$. With time, the electrons distribute over the space. The potential profile is changed. It gets a certain distribution profile. The potential towards the anode side increases with time and it attains a value close to the anode potential (ground potential) within the timescale of ~ $1x10^{2}\omega_{pe}^{-1}$. The potential over the plasma region has marginally positive potential with respect to anode potential as the plasma has unbalanced positive charged particles.

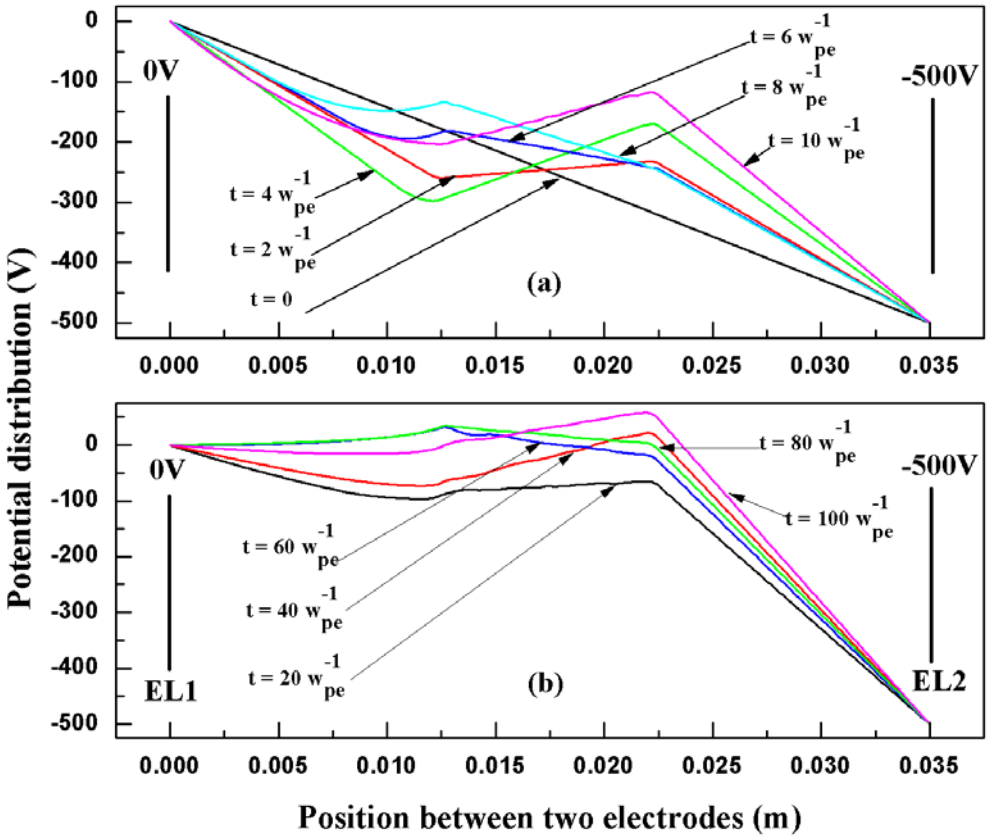

Figure 7.5: Spatial variations of potential profile between two electrodes before obtaining a stable profile.

In order to understand the potential profile in details, the distributions of electron density and photoion density at time t = $1x10^2$ ω_{pe}^{-1} are plotted in figure 7.6. It is noticed that the electrons fill the vacuum gap between the anode and photoplasma boundary, whereas the massive photoions remain at their initial positions. Due to the displacement of charge inside the plasma volume, the photoplasma is polarized in a fashion so that the internal space charge field shields the photoplasma from the applied external electric field. Inside the plasma volume, there is no electric field. The potential distribution has a flat profile over the quasi-neutral region of photoplasma. The entire applied potential drops between the plasma boundary and the cathode. It is shown by the curve of time t = $1x10^2\omega_{pe}^{-1}$ in figure 7.5.

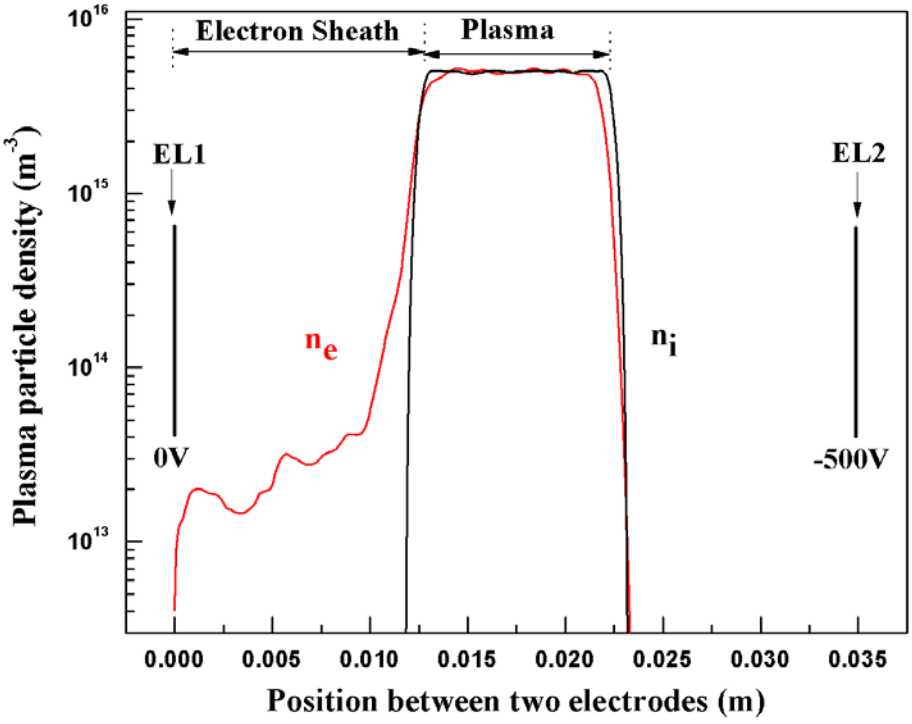

Figure 7.6: Density distribution of plasma electrons (n_e) and photoions (n_i) at time t = $1x10^2$ ω_{pe}^{-1}.

7.5 Formation of Photoion-Sheath and its Structure Analysis

The response time of photoions to the external electric field is order of ω_{pi}^{-1} (i.e. ~ $5x10^2$ ω_{pe}^{-1}), where the ω_{pi} is the plasma ion frequency. Though the photoplasma shields the external electric field, the photoions at plasma edge towards the cathode are affected by the external electric field. They move towards the cathode and fill up the vacuum gap with photoions between the photoplasma and the cathode boundary. It results to form a positive ion-sheath between the plasma and the cathode within the ion-flight time (i.e. ~ $2x10^3\omega_{pe}^{-1}$) under the external electric field.

The distribution of plasma particles' density at time t = $4x10^3$ $\omega_{pe}^{-1}$is shown in figure 7.7(a). The entire space between two electrodes is distinctly divided into four regions. From the cathode towards the anode, they are (I). Langmuir sheath region that is filled only with the streaming photoions, (II). Debye sheath region where the electron density falls from its initial value (n_e) to a negligible fraction of n_e, (III). Plasma region where the quasi-neutrality condition holds (i.e. $n_i \sim n_e$), and (IV). Electron-sheath region towards anode plate. Except the region II, all regions (I), (III) and (IV) have macroscopic scale-length of the order of plasma dimension. The region (II) has a much smaller scale-length. It is the order of Debye length (λ_D) in the plasma.

Figure 7.7(b) shows the variation of potential and electric field over the above four regions at time t = $4x10^3$ ω_{pe}^{-1}. It is observed that both potential and electric field are monotonically varied over the region I and region II. The region (III) has a slightly positive potential above from the grounded anode potential. It is also noted that in the region (II), the absolute value of potential is relatively less compared to that in region (III). So the potential $\varphi(x)$ has a negative curvature at the plasma-ion sheath boundary (i.e. between region II and III). In order to get the right sign of $\frac{d^2\varphi(x)}{dx^2}$, the value of ρ must have positive value (i.e. greater than zero). Therefore the electron density always

remains less than the photoion density over the Debye sheath region (II) [Chen, 1982] and it is clearly seen in figure 7.7(a). From the figure 7.7(b), it is observed that the electric field is nearly zero over the plasma region (III) and the electron sheath region (IV). The electric field only exists over the photoion-sheath region (I).

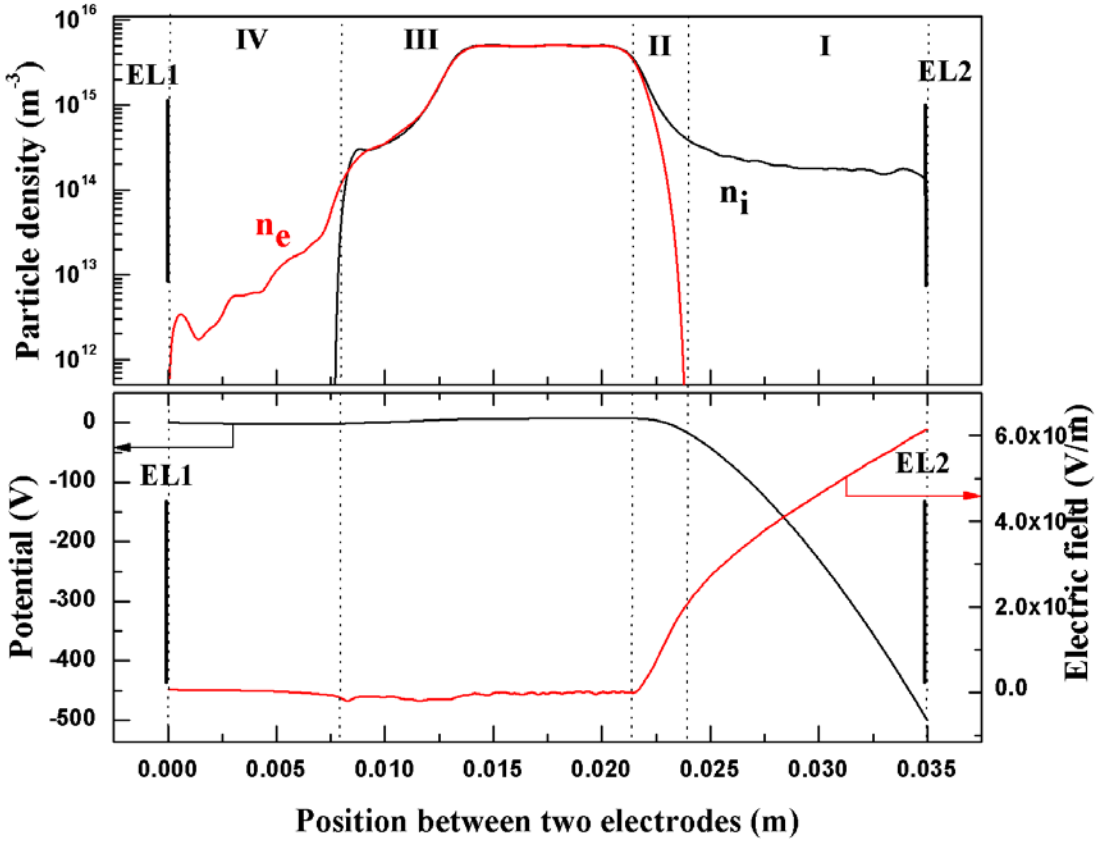

Figure 7.7: Distribution of (a) electron density (n_e) and photoion density (n_i), (b) potential and electric field at time t = $4x10^3$ ω_{pe}^{-1}.

When the photoion-sheath is formed, the Bohm-sheath criterion is satisfied at the plasma-sheath boundary. The photoions in the region (III) must fly to the region (II) with a velocity greater than the Bohm velocity [Chen, 1981]. The Bohm velocity (v_B) is defined as $v_B = \sqrt{\frac{K_B T_e}{M_i}}$, where T_e is the plasma electron temperature, M_i is the mass of photoion and K_B is Boltzmann constant. The cold photoions accelerate in the plasma region (III) and they attain the Bohm velocity from their initial zero velocity. So there must be a small electric field in the quasi-neutral region of photoplasma. The region over

which the photoions gain the energy of at least ½ KT_e (i.e. the energy of photoions corresponds to the Bohm velocity) is known as pre-sheath region [Chen, 1982 and Lieberman et al, 1994]. The pre-sheath region extends over a distance on the order of plasma dimensions. The field in the pre-sheath region is so weak that the 'quasi-neutrality' condition does not have to be violated to create the above small electric field. The plasma-sheath boundary is defined as the boundary where the condition of $e\varphi(x) = ½ kT_e$ is fulfilled. The photoions cross the plasma-sheath boundary and enter to the Langmuir sheath region (I) with kinetic energy of ½ KT_e . The potential energy '$e\varphi(x)$' rises to few times of kT_e within few Debye lengths from the boundary in the Debye sheath region (II). When the photoplasma evolves under a large external electric field where $e\varphi_0 >> KT_e$ (φ_0 is the applied potential), the Debye sheath region (II) may be neglected. The plasma region (III) is directly connected to Langmuir region (I) through the plasma-sheath boundary.

7.6 Motion of Plasma-Sheath Boundary

The photoions cross the plasma-sheath boundary and move toward the cathode. Their motion in the Langmuir region (I) is governed by space-charge limited Child-Langmuir law. The corresponding flux of photoions is known as Child-Langmuir flux (Γ_{CL}) which depends on the applied potential and the sheath-thickness. At the plasma sheath boundary, the Γ_{CL} is supplied by the Bohm flux (Γ_B) of photoions in the plasma region. The Bohm flux is the product of the photoion density and the Bohm velocity. The difference in the two flux values controls the movement of the plasma sheath boundary and according it moves. When $\Gamma_{CL} < \Gamma_B$, the plasma-sheath boundary moves towards the cathode to increase the value of Γ_{CL} by decreasing the thickness of sheath region. The finite-width photoplasma expands towards the cathode. In the case of $\Gamma_{CL} > \Gamma_B$, the plasma-sheath boundary moves away from the cathode plate. It reduces the Child-

Langmuir flux by increase the photoion-sheath thickness. The plasma-sheath boundary stagnates at the condition of $\Gamma_{CL} = \Gamma_B$. The position of the plasma-sheath boundary (S) and its velocity (ds/dt) during the decay of photoplasma are estimated from the simulation. They are shown in figure 7.8(a) and 7.8(b). It is observed that the plasma-sheath boundary initially moves fast, then it stagnates and again it moves slowly away from the cathode plate. The negative value of velocity means that the plasma-sheath-boundary moves towards the negative x direction. Its motion depends on various parameters like density of plasma (n_i), plasma electron temperature (T_e) and applied external electric field.

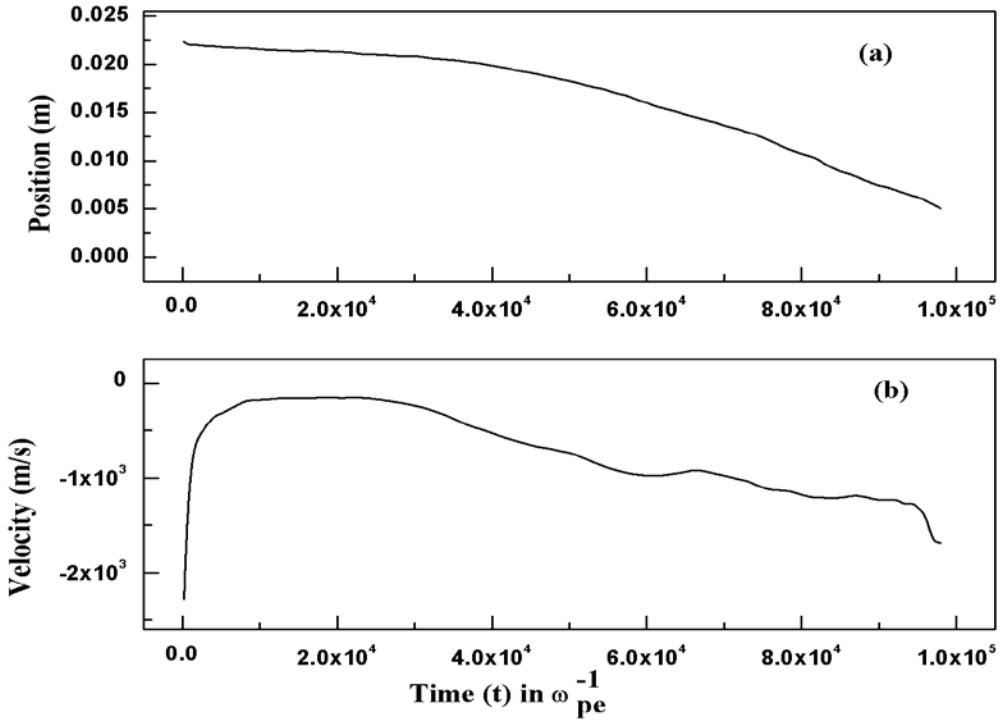

Figure 7.8: Time dependent (a) position and (b) velocity of the plasma-sheath boundary during the decay of photoplasma.

To understand the motion of the plasma-sheath boundary qualitatively, the relative temporal balance between Γ_{CL} and Γ_B is examined at the position of plasma-sheath boundary. It is estimated that the value of Γ_{CL} is ~ $2.1 \times 10^{18} m^{-2}.sec^{-1}$ with initial thickness

of photoion sheath ~ 12.5 mm whereas the value of Γ_B is ~ 1.9x10^{18} m^{-2}.sec^{-1}. This is the case of $\Gamma_{cl} > \Gamma_B$. The initial difference between the two fluxes (Γ_{CL} and Γ_B) is balanced by fast moving of plasma-sheath boundary towards the plasma region (i.e. away from the cathode plate). The thickness of photoion-sheath increases, the corresponding value of Γ_{CL} decreases to match with Γ_B. As long as the condition $\Gamma_{cl} = \Gamma_B$ is satisfied, the plasma-sheath boundary remains idle. As time increases, the photoplasma decays in the external electric field. Its density decreases and Γ_B also decreases. The Γ_B is insufficient to balance the Γ_{CL} at the plasma-sheath boundary. Again the plasma-sheath boundary moves towards the plasma region as shown in figure 7.8(a).

7.7 Plasma Expansion towards Anode

To know the phenomena happened towards the anode, the distributions of charge particles and potential over the space at time (a) t= 2x10^4 ω_{pe}^{-1}, (b) t= 4x10^4 ω_{pe}^{-1}, (c) t= 6x10^4 $\omega_{pe}^{-1}$and (d) t= 8x10^4 ω_{pe}^{-1} are shown fig. 7.9. The plasma region is defined as the region where the photoion density is nearly equal to the electron density (i.e. $n_i \sim n_e$). It is observed that the finite-width photoplasma expands towards the anode. This is due to the process of ambipolar diffusion. In plasma, the electrons move towards the anode. They create an internal electric field and it drugs the photoions towards the anode. As a result, the photoplasma expands towards the anode. The photoions defuse due to density gradient and the process is known as ambipolar diffusion.

The photoions also diffuse towards the cathode and the corresponding flux is called as Bohm flux. The Bohm flux supplies the Child-Langmuir flux at the plasma-sheath boundary. From the figure 7.9, it is observed that the photoion density decreases with time during the evolution of photoplasma. Thus it decreases the Bohm flux as it is directly proportional to the photoion density. The dotted vertical line represents the plasma-sheath boundary. It moves toward the plasma. When the plasma density further

decreases, the photoplasma is unable to shield the external electric field. The plasma criteria are not fulfilled. The charge particles move independently under the external electric field and collected on the cathode. Therefore it is concluded that during the transient evolution of the photoplasma, the plasma behavior changes from its collative motion to the single particle behavior.

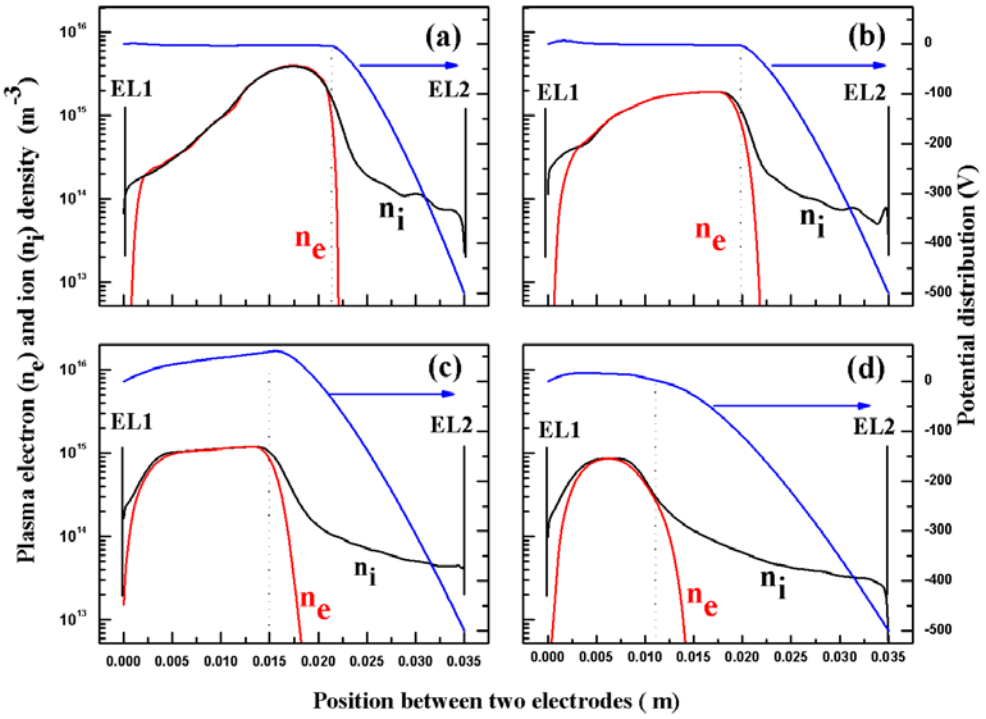

Figure: 7.9: Distributions of electron density (n_e), photoion density (n_i) and potential near sheath boundary at time (a) t = $2x10^4$ ω_{pe}^{-1}, (b) t = $4\ x10^4$ ω_{pe}^{-1}, (c) t = $6\ x10^4$ ω_{pe}^{-1}, (d) t = $8\ x10^4$ ω_{pe}^{-1}.

7.8 Temporal Shape of Current Signals on cathode and anode plate

When the charge particles move, they generate current. The structure of the current signals reflects all the phenomena happened on the charge particles during the decay of photoplasma. Here the temporal shapes of the current signals are simulated. In the simulation, the charge particles cross the boundary of the computational volume. They are collected on the electrodes and lost from the computational particles. The rate of total

charge-collection on the electrode gives the current on that electrode. Thus the currents on the electrodes are calculated from the expression of $I_e = \frac{dQ_e}{dt}$ and $I_i = \frac{dQ_i}{dt}$ for electrons and photoions, where Q_e and Q_i are the total charge of electrons and photoions collected on the electrode respectively. It is noticed that the electrons are collected only on the anode plate whereas the photoions are collected on both the cathode and the anode. The simulated current structure of photoion current to the cathode (I_{iC}), photoion current to the anode (I_{iA}) and electron current to the anode (I_{eA}) are shown in figure 7.10 (a,b,c) respectively.

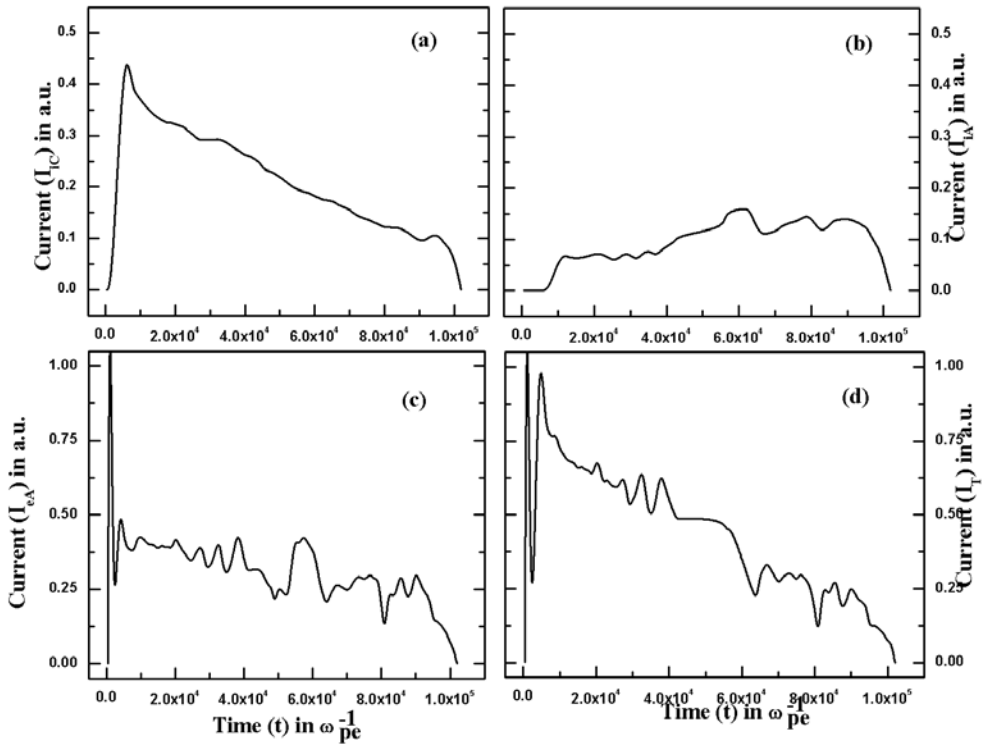

Figure 7.10: Temporal variations of simulated currents obtained from 1d PIC model: (a). photoion current to the cathode (I_{iC}), (b). photoion current to the anode (I_{iA}), (c). electron current to the anode (I_{eA}) and (d). total current on the cathode ($I_T = I_{iC} - I_{iA} + I_{eA}$).

The photoion current signal towards the cathode (I_{iC}) initially fast increases and attains a value after passing through a small peak. It remains nearly constant over a time span and then it decreases slowly. The peak represents the initial response of photoions to

the electric field and their collections on the cathode plate during the formation of the photoion sheath. The current towards the cathode plate is governed by the Child-Langmuir flux which mainly depends on the thickness of ion sheath (i.e. distance of plasma sheath boundary from the cathode surface). After formation of the photoion sheath, the Child-Langmuir flux is balanced by the Bohm flux. The current attains stable value. As long as, the plasma-sheath boundary stagnates or moves very slowly, the I_{iC} remains nearly unchanged. As the time increases, the density in plasma decreases so Bohm flux. To balance the shortfall, the plasma-sheath boundary moves away from the cathode. The thickness of ion sheath increases. As a result, the photoion current (I_{iC}) is decreased.

From the figure 7.10(b) and 7.10(c), it is cleared that the electrons and photoions are simultaneously collected on the anode plate. The initial transient peak in the electron current signal (fig. 7.10(c)) represents the initial response of electrons to the electric field. After formation of the electron sheath, the electrons are collected on the anode plate under a small electric field. From the figure 7.10 (b), it is clearly indicated that the photoions reach to the anode plate after a time delay whereas they reach the cathode plate very quickly due to the external electric field. The photoions move towards the anode due to ambipolar diffusion and it takes a time to reach the anode. The collection of more photoions per unit time shows the more current on the anode. The photoplasma expands towards the anode. The photoions and electrons both are simultaneously collected on the plate. The plasma particles lost from the plasma volume in nearly equal number to maintain the charge neutrality in the plasma.

The total current (I_T) in the circuit which can be a measurable quantity in the experiments is the resultant of all individual currents. The total current is estimated from the expression of $I_T = (I_{iC} - I_{iA}) + I_{eA}$ and the corresponding time structure is shown in

figure 7.10(d). The current signal is pulsed in nature which means the charge particles are collected on the plates over a time span. The time interval to collect all the photoions after generation of the plasma at t=0 is known as ion-extraction-time. The structure of the current signal and the ion-extraction-time depend on the applied electric field, photoplasma density, plasma width etc.

7.9 Collection of Photoions on cathode and anode plate

From the simulation, it is observed that, the plasma-sheath boundary moves very fast in case of low-density photoplasma (~ 10^{13}-10^{14} m^{-3}). It is unable to shield the external electric field. The photoions move independently and collect on the cathode plate. As the density in plasma increases, the photoplasma having density > $5x10^{14}$ m^{-3}, it shields the external electric field. The motion of photoions is governed by both external field and the internal ambipolar field. The photoions diffuse in both direction and they collect on both electrodes. The fraction of total photoions collected on the anode plate and the cathode plate depend on the relative strength between the ambipolar field and the external electric field. When the external electric field is greater than the ambipolar field, the ion-extraction regime is termed as Langmuir regime. On the other hand, it is Bohm regime where the internal field dominants over the external field.

To distinguish the process of ion-extraction at different regime like Langmuir regime and Bohm regime, a dimensionless parameter normalized density 'ρ' is defined [Okano, 1992]. The 'ρ' is basically the ratio of initial Bohm Flux (Γ_B) to the Child-Langmuir flux (Γ_{CL}) when the sheath thickness is the sum of plasma width and the one side gap between plasma and cathode. Using one dimensional PIC model, the percentage of photoions collected on the cathode and the anode are estimated at different value of ρ. The same is also measured experimentally using Faraday cups (i.e. F2 and F6) placed behind the electrodes at the same height of the photoplasma location. The details of experiments are

discussed in section 2.5.2. In experiments, when the charge particles are collected on the electrode, some fractions of them are also collected on the Faraday cups as they are placed behind the electrode. The integrated current signal recorded on the Faraday cup samples the total charge collected on the corresponding electrodes. The variations of the normalized fraction of total photoions collected on the anode and the cathode plate with ρ are shown in fig. 7.11.

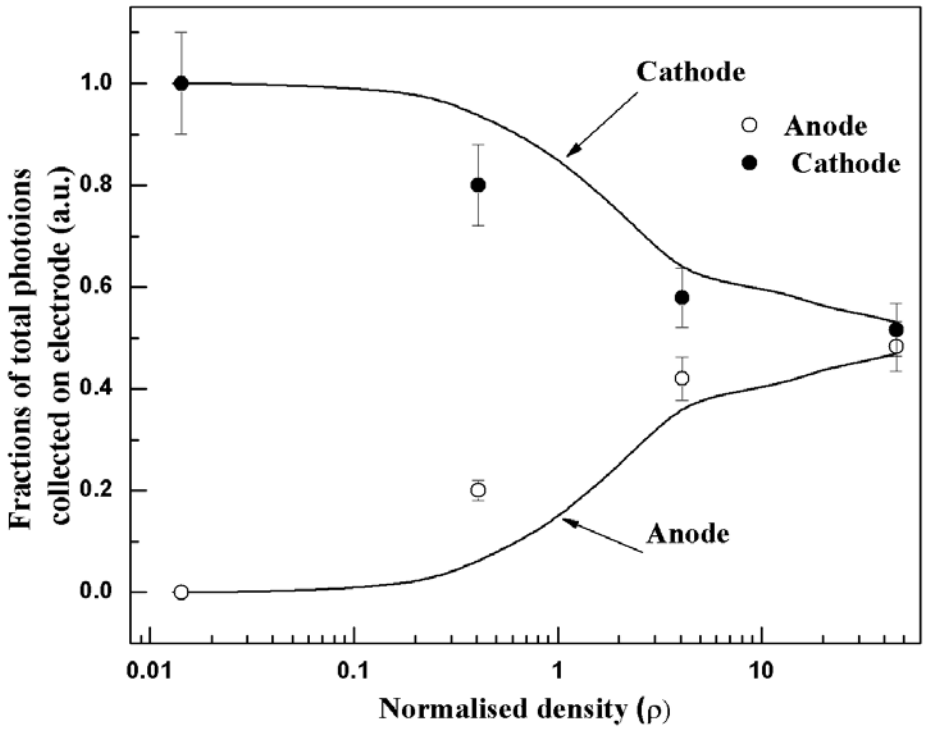

Figure 7.11: Normalized fraction of total photoions collected on the cathode and anode plate at different normalized density (ρ). (Simulations, data points are from the experiments).

It is clearly seen that all photoions collect on the cathode in case of $\rho << 1$. As the value of ρ increases, the number of photoions collected on the cathode decreases and the same on the anode plate increases. The ρ value further increases ($\rho >> 1$), nearly equal fraction of total charge particles are collected on both electrodes. The experimental data reasonably matches with the simulated values obtained from the 1d PIC simulations.

From the analysis, it is concluded that in the applications like laser based isotope separation, the value of '$\rho < 1$' is always preferred to collect all the photoions to a desired location.

7.10 Summary

The decay of the finite-sized photoplasma in an electrostatic electric field has been studied using one dimensional PIC (particle-in-cell) model. During its evolution, the various processes occurred along the direction of the electric field has been investigated. The photoplasma has been evolved through a series of quasi-steady states. The mono-energetic electrons of the photoplasma get thermalised through the electron-electron collisions within a few cycles of plasma oscillations. The electrons fast response to the electric field. An electron sheath is formed between the anode and the photoplasma gap. The plasma is polarized in a fashion that it shields the external electric field to penetrate inside the plasma. The plasma-space-potential initially oscillates and attains a stable value close to the anode potential. The field over the plasma and the electron sheath region is negligible. The entire applied potential drops between the plasma and the cathode. The photoions at the plasma boundary move towards the cathode. They form a positive ion-sheath between the plasma and the cathode. The motion of photoions inside the sheath is governed by the space charge limited Child-Langmuir law. The Child-Langmuir flux is supplied by the Bohm flux at the plasma-sheath boundary. The difference between them controls the movement of the plasma-sheath boundary. Towards the anode side, the photoions diffuse due to the ambipolar diffusion and the photoplasma plasma expands towards the anode. During its decay the charge particles are collected on the boundaries i.e. cathode and anode. The plasma density decreases with time. At the low density, the photoplasma is unable to shield the applied external potential. The charge particles are

moved independently. The fractions of total photoions collected on the electrodes depend on the relative strength of the internal ambipolar field and the external electric field. When the external electric field is predominant over the internal ambipolar filed, all photoions are collected on the cathode, whereas they are collected on both sides as the internal filed dominants at higher density of the plasma.

Chapter 8

Two Dimensional Evolution of Photoplasma in Electrostatic-Ion-Extractor

The chapter 8 presents two dimensional evolution of the finite-sized barium photoplasma in an electrostatic-ion-extractor. The various processes contributing to its decay in 2d are identified. Their relative contributions are quantified from the measured ion current signals recorded on electrode plates as well as Faraday cups placed behind the electrodes. The results are also compared with the 2d PIC simulations.

8.1 Introduction

Ion-extraction from the photoplasma is an important issue in many research fields and technological applications like laser based isotope separation and metal alloys purifications. The aim is to collect all ions of the finite-sized photoplasma to a desired location of the ion-extractor with an excellent efficiency. A simple electrostatic ion-extractor is produced by two parallel plate electrodes placed on both side of photoplasma. The edge effects are neglected and it creates a uniform electrostatic field over the extractor. In chapter 7, it has been already discussed the decay phenomena of photoplasma in the direction of external electric field. Since the photoplasma is produced inside a collimated atomic beam, it is embedded with the atomic beam. It has a bulk motion along the vertical direction. Therefore the photoplasma has two-dimensional (2d) motion in the plane of the electric field and vapor flow. The third dimension that is along the direction of laser is considered to be infinite. Due to its cylindrical symmetry, the motion of photoplasma is investigated on the middle cross-sectional plane. For designing

of an efficient ion-extractor, the primary requirement is to know the various processes contributing to decay of photoplasma in 2d.

In this chapter, the two dimensional motion of the finite-size (circular cross-section) barium photoplasma is investigated in the electrostatic ion-extractor. From the measured current signals on the electrodes and Faraday cups, the processes contributing to the 2d expansion are studied. Their relative magnitudes are quantified and compared with the results obtained from 2d PIC simulations.

8.2 Physical Picture of Photoplasma expansion in two dimension

Due to its sharp density gradient at the plasma boundary, the photoplasma expands in two dimensions. A physical picture of photoplasma expansion is discussed below. It highlights the various processes like bulk plasma motion, ambipolar diffusion, Coulomb repulsion and Child-Langmuir flux which are responsible for the motion of photoplasma in the electrostatic ion-extractor. Figure 8.1 summarizes the different mechanisms and their role. During its decay with time, the density of photoplasma decreases, these mechanisms are time dependent (except bulk motion) and superimposed. Their relative magnitudes decide the spatial destination of photoions. For example, it is determined whether the photoplasma motion is one-dimensional or two-dimensional.

The bulk flow and free ambipolar diffusion contribute in the vertically upwards direction whereas Coulomb repulsion is in radial. The atomic beam has a mean thermal velocity and it determines the plasma bulk motion in vertical direction. For free ambipolar diffusion, the driving force is provided by the electron temperature. The photoplasma expands in vacuum with ion-acoustic velocity. The external electric field interacts with the photoplasma and removes a fraction of electrons from it. The uncompensated positive photoions then undergo Coulomb repulsion resulting in plasma expansion. In the horizontal direction, the spatial evolution of photoplasma is greatly modified due to the

presence of electric field and physical boundaries (i.e. electrodes). The Child-Langmuir flux towards cathode side and bounded diffusion towards anode side decide the photoion evolution in horizontal direction. When the external electrostatic field is dominant, all photoions are directed towards the cathode by Child-Langmuir flux with negligible vertical spread. The motion is predominantly one-dimensional. On the other hand, when collective effects dominate due to internal ambipolar field, the photoplasma spreads over larger region. The processes like Coulomb repulsion, free and bounded diffusion become comparable and compete with Child-Langmuir flux. The expansion then becomes two dimensional.

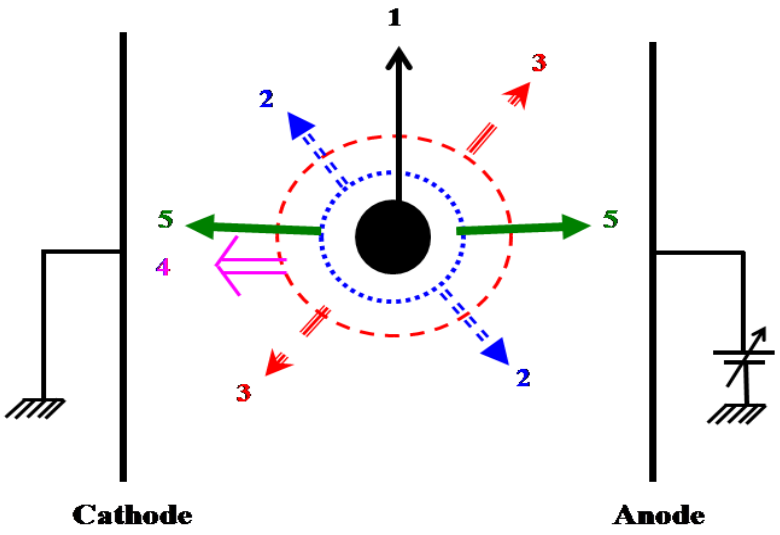

Figure 8.1: Various mechanisms contributing to two-dimensional expansion of photoplasma. 1: bulk motion, 2: free ambipolar diffusion, 3: Coulomb repulsion, 4: Child-Langmuir flux and 5: bounded diffusion.

8.3 2d PIC Simulations

To study the details of 2d evolution of photoplasma in the electrostatic ion-extractor, a 2d-PIC code developed in our group [Patel and Mago, 1995] has been used.

The details of PIC simulation techniques have been discussed in chapter 7 and they are extended to 2d PIC simulation. The 2d computational area of 45 mm x 150 mm is discretized into a 2d square mesh of 1 mm x 1 mm resolution. Around $1x10^5$ particles each are assigned to the photoions and electrons of the photoplasma. They are randomly distributed within a circle of 10 mm diameter. The positive particles have an upward drift velocity of ~ $4x10^2$ m/s while the negative particles are assigned to a Gaussian velocity distribution. Binary collisions among the particles are neglected. The iterative execution of the computational steps leads to self-consistent evolution of the photoplasma. Using the code, the motion of photoplasma is visualized in two-dimensions.

The motion of charge particles generate electrical currents which were measured on electrodes and a series of faraday cups placed behind the electrodes. The details experimental set-up of ion-extractor was discussed in section 2.6. The results obtained from experiments and simulations are discussed below.

8.4 Bulk Motion of Plasma

Figure 8.2 shows the typical photoion current signal recorded on Faraday cups along the vertical direction. The plasma density for this experiment was ~ $5x10^{15}$ m^{-3} and applied field was ~ $2.8x10^3$ V/m. It is noticed that the photoions are collected on the three Faraday cups (i.e. F1, F2 and F3) though they are produced in front of the F2 only. It implies that the finite-sized photoplasma expands along the vertical axis. The signal on Faraday cups shows peak after some initial oscillations (striations) which are identified as electromagnetic interference from the Q-switch of the laser. The curves are smoothening by averaging of adjacent 10 points and they are shown by red lines.

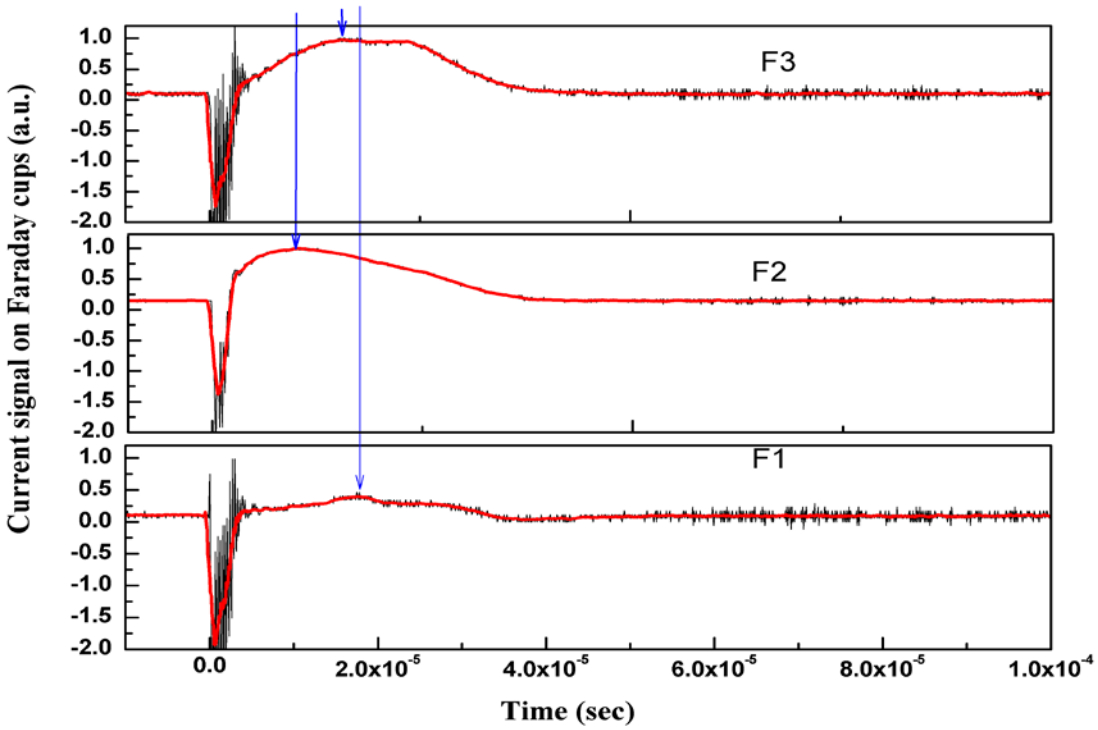

Figure 8.2: Temporal variation of current signals as recorded on Faraday cups with photoplasma density ~ $5x10^{15}$ m^{-3} and applied potential ~ 100 volts.

The peaks in the Faraday cup signals (shown by blue arrow) represent the arrival time of the maximum number of photoions at the corresponding aperture location of the electrode. Since Faraday cup F2 is nearest to the photoplasma, the photoions reach it earlier than at F1 and F3. It is also seen that the peak of F3 comes marginally earlier than that of F1 and the amplitude of F3 signal is greater than that of F1 though they are symmetrically placed with respect to the photoplasma. This means more photoions are collected on F3 than F1 at the same time. Thus the photoplasma has a preferred bulk motion in upward direction. It is assumed that the vertical motion is a superposition of bulk motion and free expansion of the plasma. The expansion is happened in both upward and downward direction. From the time delays in peaks of fig. 8.2, it is estimated that the bulk plasma velocity is ~ (3.32 ± 0.8) $x10^2$ m/s. The calculated mean free path of barium atoms inside the crucible at ~1000 K temperature is ~10 mm. It is larger than the

dimensions of collimator thickness and holes sizes. So the vapors have an effusive (i.e. collision-less) flow. They move vertically upwards with an average speed of ~3.9×10^2 m/s (at 1000 K) which is in reasonable agreement with the experimental value. Thus the photoplasma embedded in the atomic beam, moves upwards with a bulk velocity equal to the vapor flow velocity.

8.5 Free Ambipolar Diffusion

The mobile plasma electrons move fast than the ions as they have very less mass and try to escape from the plasma. It creates an electric field which accelerates the photoions and the plasma particles diffuse along the field. The process is known as ambipolar diffusion. In absence of the external electric field, the photoions move due to ambipolar diffusion. In horizontal direction, since there are boundaries on both side of the plasma, the diffusion process is greatly modified and it is called as bounded diffusion. Whereas in the vertical direction, there are no boundaries, the plasma particles move due to free diffusion. In our experimental setup, the separation gap between the plasma and boundary in horizontal direction is ~ 13 mm whereas the top plate is located at a large distance (~ 113 mm from the plasma) in the vertical direction. To examine the role of free ambipolar diffusion, the photoplasma is allowed to expand in absence of any external electrostatic field. A typical waveform of photoion current recorded on top plate for plasma density ~2×10^{15} m^{-3} is shown in figure 8.3. The original signal was quite noisy. The digital smoothening techniques have been applied to extract the information. The present signal is smoothen by adjacent averaging of 100 points. The peak of signal corresponds to the arrival time of the maximum photoions at the top plate. The velocity of plasma in vertical direction is a superposition of the bulk velocity of the plasma and its expansion velocity due to free ambipolar diffusion.

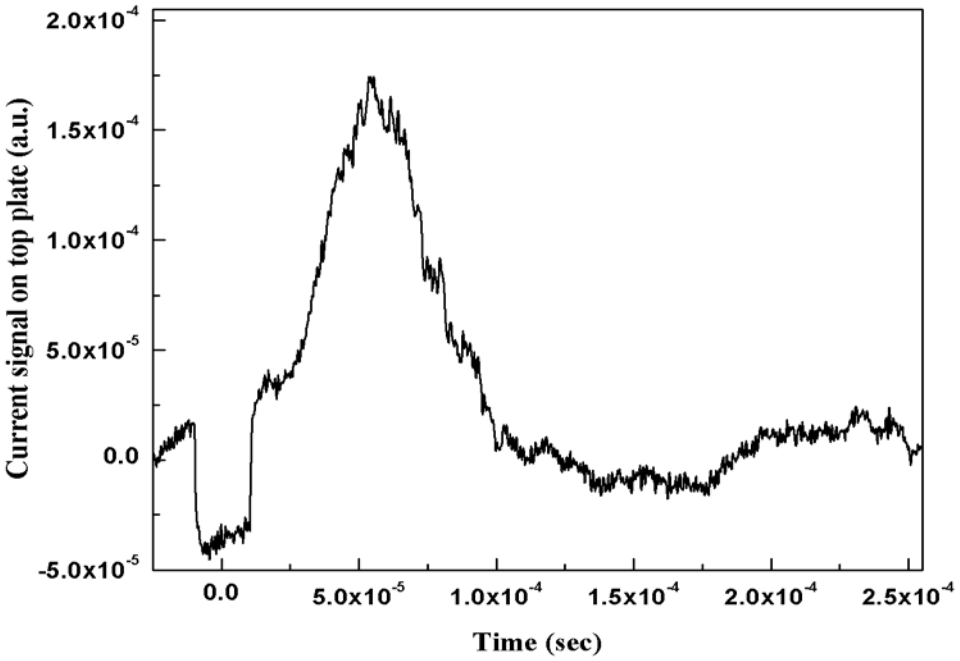

Figure 8.3: Measured photoion current signal on top plate while the photoplasma of density ~ $2x10^{15}$ m^{-3} decays in absence of electric field.

It is estimated that the photoplasma diffuses in vacuum with an average velocity ~ (1.2 ± 0.4) $x10^3$ m/s. This ambipolar expansion velocity of the plasma is equivalent to ion acoustic velocity which is estimated to be ~$0.8x10^3$ m/s for the barium photoplasma with electron temperature of ~ 0.36 eV and ion temperature of ~ 0.1 eV. The discrepancy is probably due to the contribution of other process occurred in the vertical direction. One of them is Coulomb repulsion.

8.6 Coulomb Repulsion

The Coulomb repulsion is an important mechanism, which plays a vital role in the 2d motion of photoplasma. Figure 8.4 depicts the distribution of photoions collected on Faraday cups as a function of normalized plasma density (ρ). The normalized density (ρ) [Okano, 1992] is defined as

$$\rho = \frac{n_0 \, d^2 \, T_e^{1/2}}{k^{\,2} V^{3/2}} \qquad (8.1)$$

$$k = \left(\frac{4\,\epsilon_0\sqrt{2}}{9\,e}\right)^{1/2} \tag{8.2}$$

where n_0 is the initial plasma density, V the applied potential, d is the sum of one side of vacuum gap and photoplasma width, T_e is the electron temperature (in eV), ε_0 is dielectric constant in free space and e is the electronic charge.

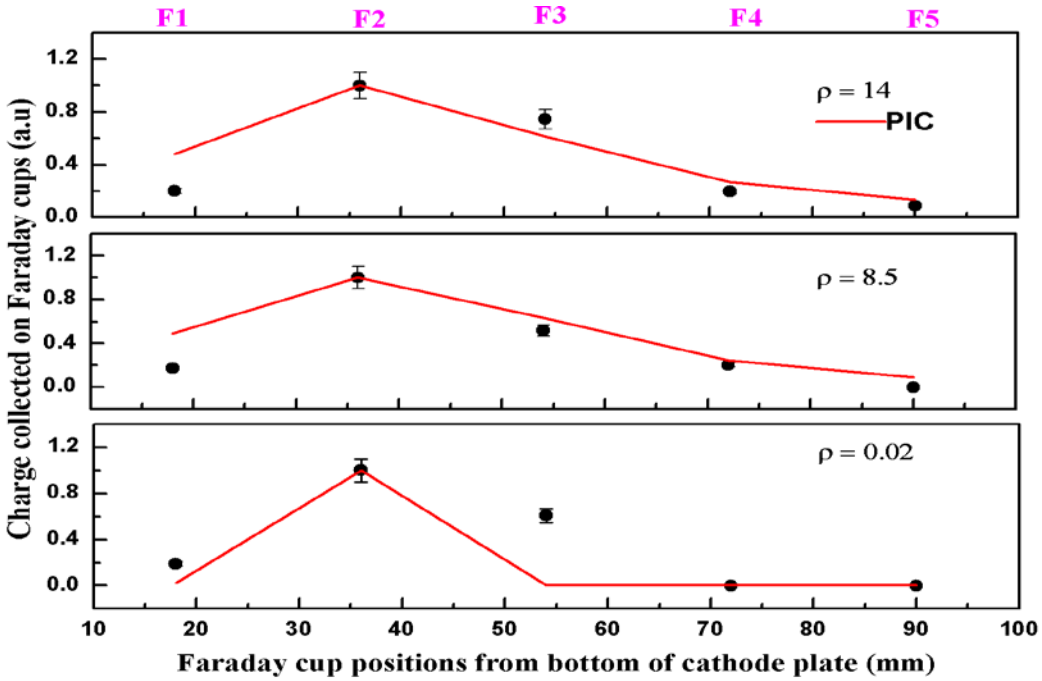

Figure 8.4: Distribution of photoions over the Faraday cup locations in the vertical direction at different ρ values. (Red lines represent the results of 2d simulation and data points are from experiments).

The parameter ρ represents the ratio of initial value of Bohm flux to Child-Langmuir flux with maximum sheath thickness. It physically signifies the competition between collective plasma effects and the external electric field. The value of ρ is varied by changing the value of plasma density (n_0) and applied potential (V). When ρ = 0.02, the external field is strong enough to collect the photoions over a small region (i.e. between F1 and F3) before it expands significantly. With the increase of ρ, the photoplasma expands in the vertical direction with the photoions reaching F4 (ρ = 8.5) and F5 (ρ = 14).

The results from 2d-PIC simulation are also shown in figure 8.4 by solid red lines for comparison. In the simulation, the electrodes are divided into different segments corresponding to the actual Faraday cup locations. The photoions reaching these segments are considered to be collected by the Faraday cups.

The Coulomb repulsion is one of the processes causes to expand the plasma. In presence of external electric field, a small fraction of plasma electrons get removed from the plasma leaving behind an equivalent amount of uncompensated photoions. These photoions undergo Coulomb repulsion resulting in the plasma expansion. Using the time values of the peaks from the corresponding waveforms of Faraday cups, it is estimated [Tkachev and Yakovlenko, 1993] that a cylindrically shaped photoplasma will have an expanded radius of ~20 mm due to Coulomb repulsion only. It is in good agreement with the Faraday cup separation of 18 mm. It is also observed that the amount of charge collected on a particular Faraday cup (say F2) increases with the increase of ρ. As the value of ρ increases, the initial Bohm flux in ambipolar diffusion increases. The difference between the Bohm flux and the Child-Langmuir flux moves the plasma-sheath boundary towards the cathode. It increases the value of Γ_{CL}. Thus more amount of charge is collected on F_2 as ρ increases.

The expansion velocity due to Coulomb repulsion is time-dependent as the fraction of uncompensated charge in plasma varies with time. The 2d-PIC simulated temporal dependence of the uncompensated photoions for plasma density ~ $5x10^{15}$ m^{-3} and applied potential 300 volts is shown in figure 8.5 together with three regions marked in Roman numerals.

In region I (i.e. till ~3μs) only electrons are removed from the system while no photoions are collected. This increases the percentage of uncompensated ions with respect to the

initial number of photoions. Hence the expansion velocity due to Coulomb repulsion increases linearly.

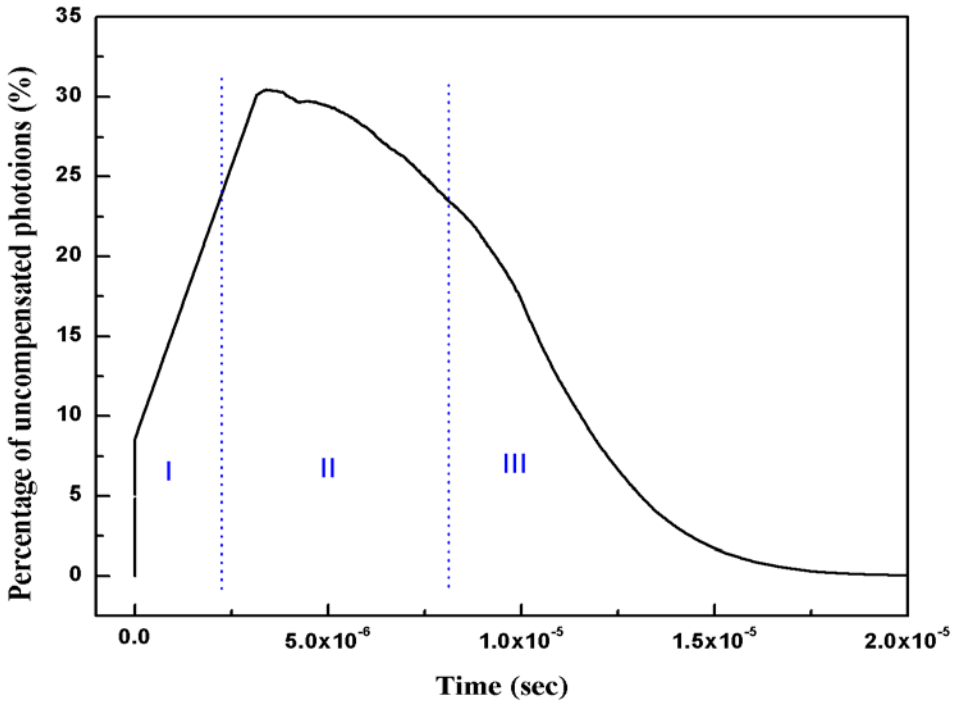

Figure 8.5: PIC simulated temporal dependence of uncompensated ions responsible for Coulomb repulsion.

Between 3μs to 9μs (region II) both electrons and photoions are collected implying the contributions from superposition of Child-Langmuir flux on the Coulomb repulsion. The number of photoions and electrons are collected on electrode in almost equal fashion. It results in the gradual decrease of the uncompensated photoion-fraction and so in the velocity of Coulomb repulsion. In region III i.e. after ~9μs almost all electrons are removed and a small fraction of ions is left. The average velocity for Coulomb repulsion is estimated from the average value of the percentage of uncompensated positive photoions. The calculated velocity from the simulation is ~$3x10^3$ m/s with the averaged 20 % uncompensated charge in the plasma.

8.7 Child-Langmuir Flux and Bounded Diffusion

The photoplasma motion in the horizontal direction is greatly modified due to the presence of electric field and boundaries like the electrodes. The mechanisms of photoion motion on the cathode are different from that on the anode side. On the cathode side, the motion is predominantly governed by the Child-Langmuir flux (discussed in chapter 7) while on the anode side it is largely due to bounded diffusion. The Faraday cups F2 and F6 are placed behind the cathode and anode respectively at the same height of photoplasma. The magnitudes of charge collected on F2 and F6 for different values of ρ are plotted in figure 8.6. Photoions reaching both F2 and F6 increase attain a maxima and then decrease with ρ. When ρ is small, the photoions are efficiently repelled by the external electric field towards F2 and none reaches F6. As ρ increases, the photoplasma expands in the horizontal direction. A significant fraction of photoions diffuse towards the anode as it is evident from the finite number of charges collected on F6.

The increase in the photoions reaching F6 depends on ρ. It indicates that the bounded diffusion and/or Coulomb repulsion are the photoion motion mechanisms on the anode side. In this regime of ρ (~ 0.01 - 5), the photoions reaching F2 almost remains constant implying that the dominant mechanism of photoion motion on the cathode side is Child-Langmuir flux. As it has been discussed in chapter 7 that the electric field exists on the cathode side as determined by space-charge effects and negligible field is on the anode side. The plasma evolution occurs on the anode side in nearly field-free environment. With further increase of ρ (>10), the collected charges on F2 and F6 rapidly decrease. A situation is reached when almost equal numbers of photoions get collected on the anode and the cathode. The decrease is due to the onset of plasma expansion in the vertical direction that is the signature of 2d motion. Under such 2d effects, the fractional charges sampled by F2 and F6 are decreased.

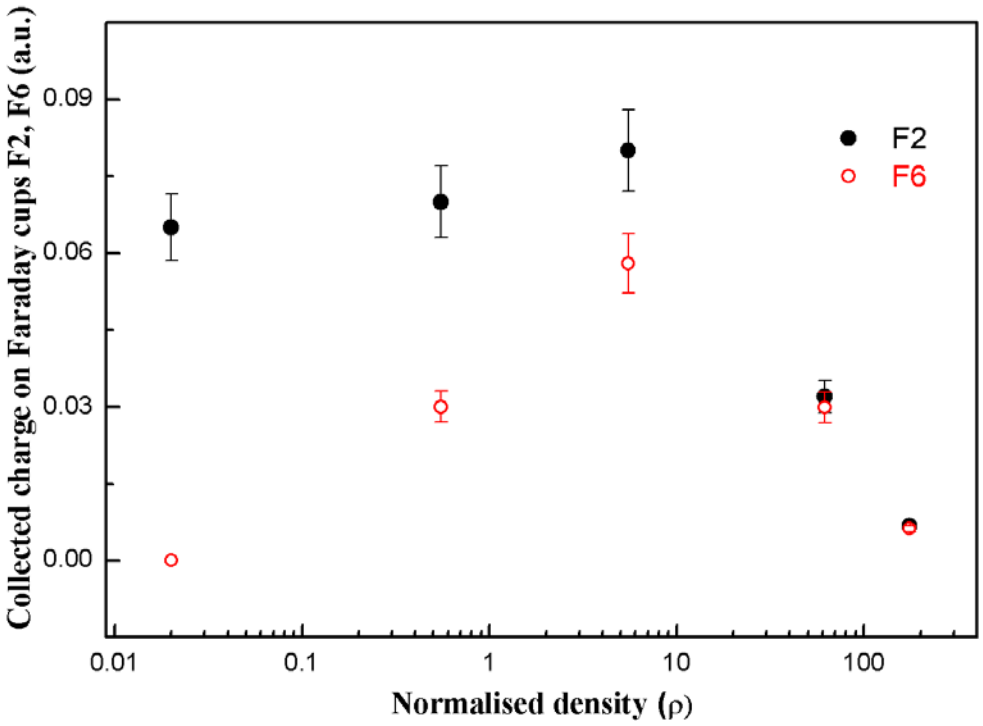

Figure 8.6: Photoions collected on cathode and anode plate as sampled by Faraday cups placed behind the electrode for different ρ values.

It is very difficult to uniquely quantify the role of bounded diffusion for this kind of integrated measurements. Nonetheless, an estimate can be provided if it is assumed that the photoions reaching F6 are only due to diffusion. The time dependent photoion density can be represented as $n(t)= n_0 e^{-t/\tau}$, where t is the time counted from the photoplasma generation. The time constant (τ) is defined as the time taken to decay of the initial plasma density to its 1/e value. In our case, the photoplasma dimension was ~ 10 mm and the electrode separation was ~35 mm. It is seen that by the time the plasma reaches F6, the initial photoion density is decreased by a factor of 3.5. Using linear interpolation and the corresponding F6 waveform, the decay time τ can be determined. Approximating the plasma to be infinite along the laser propagation direction with a boundary, the diffusion coefficient D is given by

$$D = \frac{L^2}{\pi^2 \tau} \tag{8.3}$$

where L in the electrode separation. The estimated value is ~19 m^2/s. This is in good agreement with that obtained by LIF [Yamada. 1990] and in the PIC simulation experiments [Patel and Mago, 1995].

8.8 2d Evolution from PIC Simulation

The 2d PIC code was run for various combinations of plasma densities and electric fields. Figure 8.7 shows the snapshots of computational volume during the evolution of photoplasma of density $5x10^{15}$ m^{-3} and electric field of ~$8.5x10^3$ V/m.

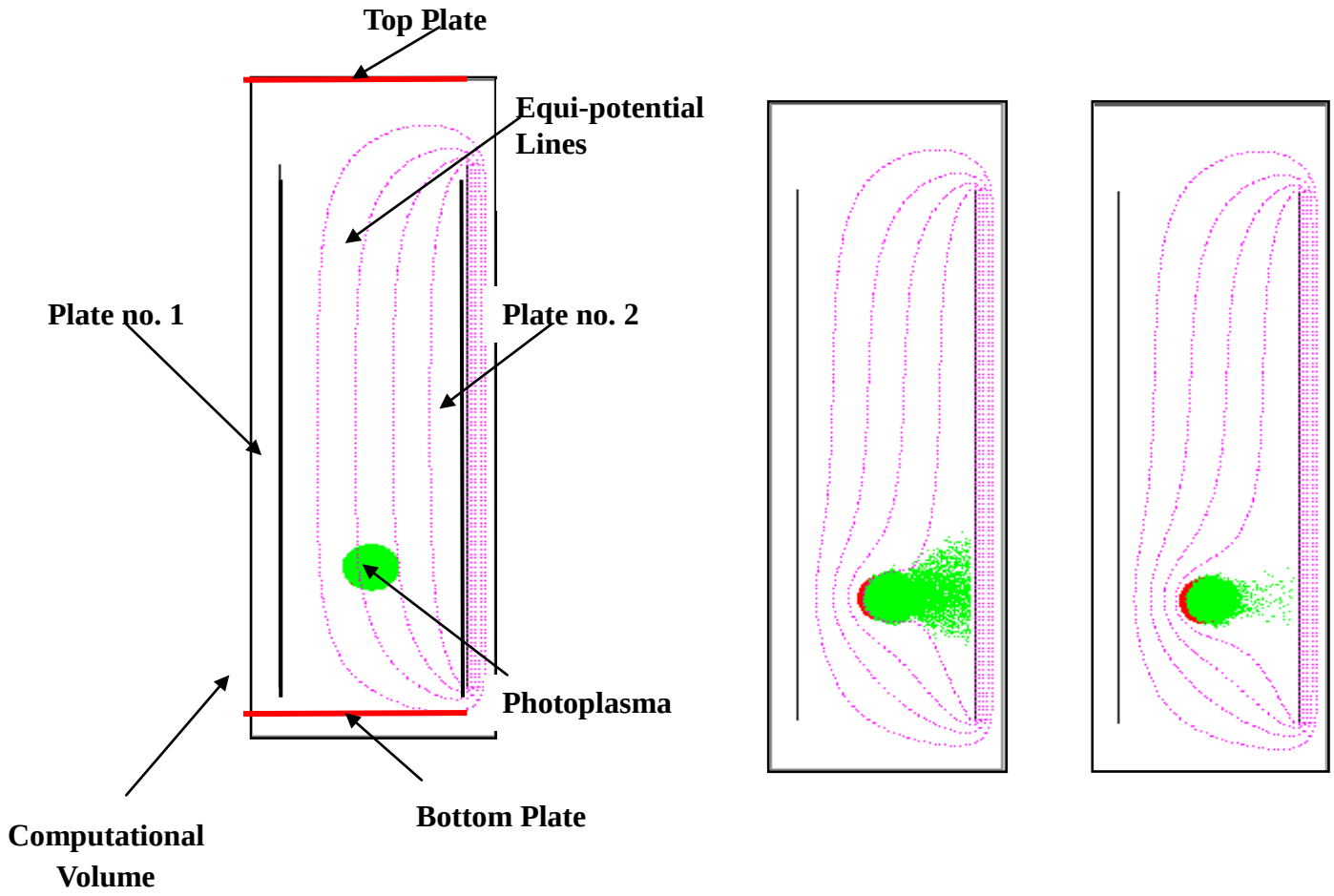

Figure 8.7: Snapshots (a-k) of the 2d evolution of photoplasma at different time obtained from PIC simulation. (Green dots represent electrons and red dots represent photoions).

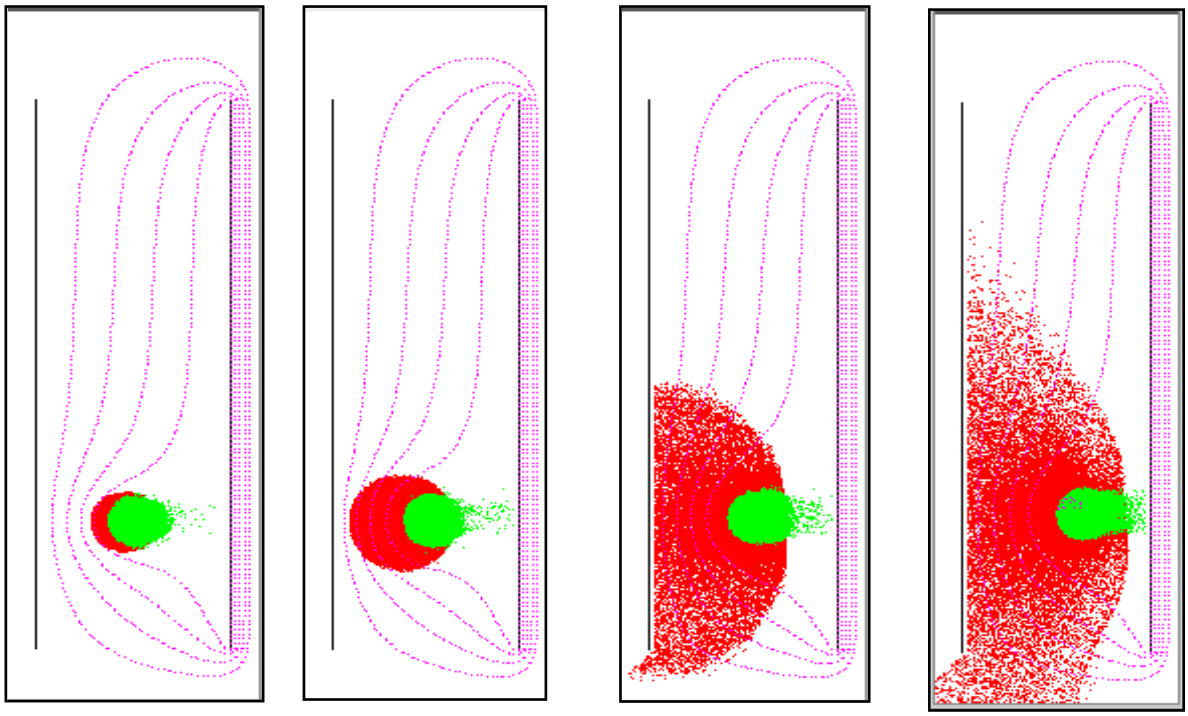

(d). t= $5x10^{-7}$ s **(e). t= $1x10^{-6}$ s** **(f). t= $2.5x10^{-6}$ s** **(g). t= $5x10^{-6}$ s**

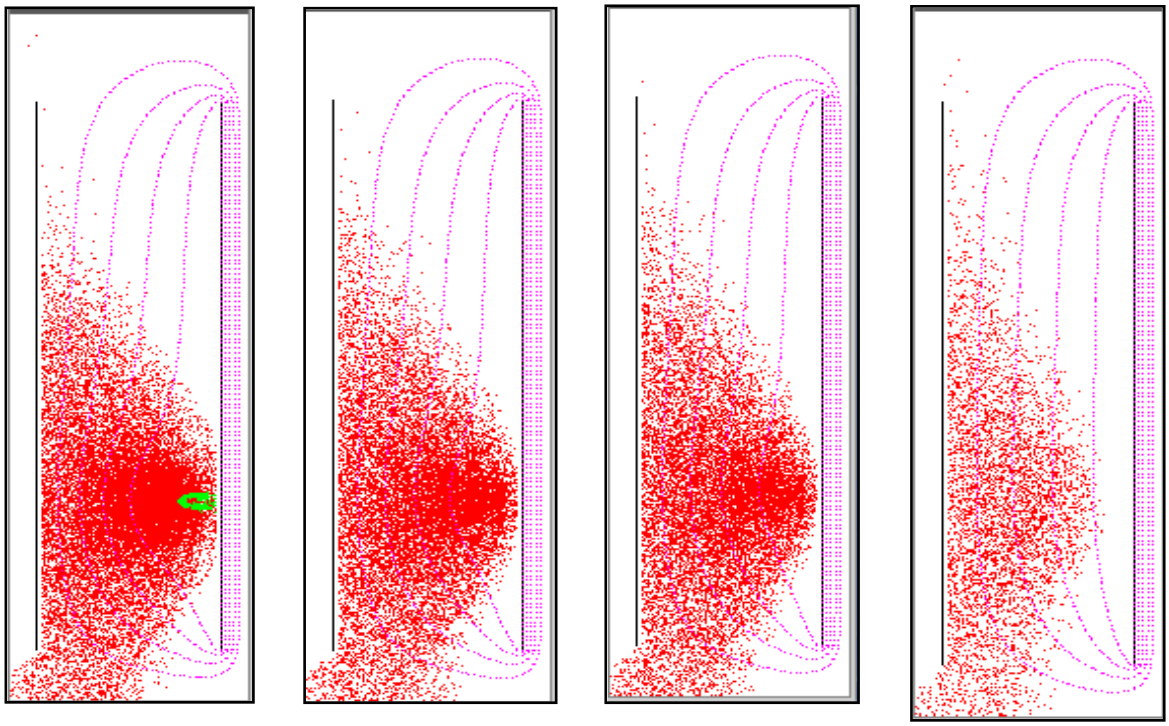

(h). t= $8.6x10^{-6}$ s **(i). t= $9.6x10^{-6}$ s** **(j). t= $1x10^{-5}$ s** **(k). t= $1.3x10^{-5}$ s**

The red color dots represent the positive charged super particles and the green color dots are negative charged super particles. A positive potential is applied on plate no. 2 whereas plate no. 1, bottom plate and top plate are grounded. The computational geometry along with the initial position of photoplasma is shown in fig. 8.7 (a). The pink color dotted lines represent the equi-potential lines under the external electric field. The plasma electrons (green dots) move towards the anode (i.e. plate no.2). They form an electron sheath within a time scale of few ns as seen in fig. 8.7 (b) and (c). It clearly indicates that the finite-sized (circular) photoplasma expands in two dimensions during its evolution in the electrostatic ion-extractor. The photoions are collected on both cathode and anode plate. Since positive bias voltage on plate no. 2 to repel the photoions towards the plate no. 1, the photoions are collected on plate no. 1. A significant fraction of photoions are also collected on the bottom plate as it was close to the cathode plate.

8.9 Audit of Photoions in Ion-Extractor

To make an efficient ion-extractor, it is important to know the photoions audit at different location of the ion-extractor. The photoions move in the electrostatic field and reach various electrodes and plates. The extent of their reach is determined by the competition between collective effect and the external field. As an estimate of photoion audit, a set of experiments was carried out with a slight modification of the experimental arrangement. A bottom plate was introduced with appropriate insulation between the vertical electrodes and base slit so that photoion signal could be recorded for this bottom plate. Table 8.1 shows the percentage of photoions on different locations (top, bottom plates and electrodes) as a function of plasma density when +1kV was applied on plate no. 2 and all other plates are grounded. The 2d-PIC simulation data is also shown within parenthesis in the same table.

Table.8.1 Percentage distribution of photoions on different locations in ion-extractor as a function of plasma density when +1kV is applied. The values have error of ~10%. The values in parenthesis are that of 2d-PIC simulation.

Density (m^{-3})	Percentage of photoions reaching (%)			
	Cathode	Anode	Bottom plate	Top plate
$1.5x10^{15}$	70 (80)	18 (12)	12 (8)	0 (0)
$4x10^{15}$	63 (69)	23 (17)	14 (13)	0 (1)
$3.5x10^{16}$	54 (63)	27 (20)	17 (15)	1 (2)

It was observed that negligible photoions reached the top plate as compared to that of the bottom plate. This was because the top plate was placed at about three times the distance from the photoplasma as that of the bottom plate. When the density was increased by one order of magnitude (from ~ 10^{15} to 10^{16} m^{-3}), there was ~ 20% loss of photoions from the cathode. These were lost to the anode and bottom plate due to bounded diffusion and Coulomb repulsion. With the dominance of collective effects, the photoplasma expands in two-dimensions and reach the cathode, anode, bottom and top plates. Such studies of photoions audit in 2d assume significance when the photoions need to be collected on predetermined size of cathode.

For low $\rho \sim 10^{-2}$ i.e. when the external electrostatic field is dominant, the photoions are mostly directed towards the cathode with negligible expansion. As an example, for photoplasma density of $1x10^{14}$ m^{-3} and electric field ~$2.85x10^{4}$ $V.m^{-1}$, 99% of the ions are collected on the cathode (by Child-Langmuir flux), 1% on anode and no ions reach the bottom and top plates. The motion can then be approximated as one-dimensional. The numerical figures are matched with the data obtained from 1d PIC simulation. When ρ is

high (~1-10), i.e. as collective effects dominate, various processes contributing to photoion motion become comparable leading to 2d motion. Contribution due to the bulk flow has the least magnitude and remains constant. All other processes are time-dependent.

The relative magnitudes of the dynamical processes responsible for photoion distribution were estimated. For a particular magnitude of photoplasma density and external electric field, the currents on the cathode, anode and the bottom plate were experimentally measured. For the same conditions, the velocities of various processes are estimated and corresponding currents are evaluated. As an example for photoplasma density of $5x10^{15}$ m^{-3} and electric field ~$8.5x10^{3}$ V/m, it is estimated that the relative magnitudes of the mechanisms responsible for photoion distribution on the cathode side are as follows: bounded diffusion (55%), Coulomb repulsion (23%) and Child-Langmuir flux (22%). On the anode side, the contribution from bounded diffusion is 71% while Coulomb repulsion is 29%. On the bottom plate, Coulomb repulsion contributes 77% whereas 23% is from free diffusion. For the same density (i.e. $5x10^{15}$ m^{-3}) when the external electric field was increased to ~$2.85x10^{4}$ V/m, 66% of the photoions were collected on the cathode, 24% on the anode and 10% on bottom plate. With increase of external electric field, photoions are collected more efficiently on the cathode and Child-Langmuir flux is the dominant mechanism.

8.10 Summary

The two dimensional evolution of barium photoplasma has been experimentally studied in the electrostatic ion-extractor, produced by parallel plate geometry. The various processes contributed to its decay have been identified by measuring the current signal recorded on the electrodes and Faraday cups those were placed behind the electrodes. They are bulk plasma motion, free ambipolar diffusion, Coulomb repulsion, Child-

Langmuir flux and bounded diffusion. As the photoplasma is generated inside the atomic beam, it has a bulk velocity in vertical direction. Due to its sharp density gradients at the plasma boundary, the plasma particles diffuse from its higher concentrated region to low density region. The process is known as ambipolar diffusion. Since there is no boundary in vertical direction, the process is known as free diffusion where as in horizontal direction the diffusion is called bounded diffusion. Due to collection of charge particles at the boundary, a sharp density gradient of plasma particles exists at the position of boundary. So the diffusion constant of bounded diffusion is larger than the free diffusion. In presence of electric field, a fraction of plasma electrons gets removed from the photoplasma leaving behind an uncompensated positive charge cloud. The Photoplasma expands in radial direction due to Coulomb repulsion. Towards the cathode, the photoion sheath is formed. The motion of charge particles in the sheath is controlled by Child-Langmuir law. All above said processes are superimposed. Many of them are time variant. Their relative magnitudes depend on the applied electrostatic field, plasma density and flow velocity. They also determine the spatial extent of the photoions in two dimensions. When the external field is dominant the photoions are collected almost completely by the cathode with negligible loss. In such a case, the expansion is considered to be one-dimensional. However at large photoplasma densities, the collective effects dominate and the various processes become comparable leading to 2d motion. This study quantifies the expansion dynamics of the photoplasma in the electrostatic field and some results are compared using a 2d-PIC code.

Chapter 9

Conclusions and Future Directions

This thesis investigated the physics of photoplasma motion in the electrostatic ion-extractors. Photoplasma is a special class of plasma. It is transient in nature. It has finite volume and it is produced by multi-step photoionization method. Its characteristics are unique and different from that of conventionally produced thermal plasma and discharge plasma. This type of plasma is involved in applications like laser based isotope separation, material purification using lasers, laser ion-source etc. In such applications, a particular isotope or element is selectively photoionized through multi-step resonant photoionization method and it produces the photoplasma. The photoions from the photoplasma are extracted in the efficient manner using the external fields and they are collected to the desire location in the ion-extractors. Thus the photoplasma plays a crucial role in the above applications. During its decay in the external electric field, the photoplasma shows its complex behaviors and it passes through the several transient stages. It is essential to understand the complex characteristics of the photoplasma while it decays in the electrostatic ion-extractors.

9.1 Summary of Present Studies: Contributions

This thesis addressed the issues of photoplasma generation by irradiating atomic beam using pulsed lasers. It investigated the various physical processes involved in the transient decay of the photoplasma. It discussed the distributions of photoions and two dimensional evolutions of the photoplasma in the electrostatic ion-extractor. Both numerical simulations and experiments were carried out to investigate the photoplasma dynamics

under the electrostatic field. In the experiments, Barium element was used. The works done under the thesis are summarized in below.

- **Design of Linear Atom Source : Generation of a Long Wedge-Shaped Atomic Beam**

In photoplasma study, a long, collimated, collision-less high-density atomic beam is required. For this an atom source has been designed using a collinear array of multi-channels. The characteristics of vapor flow through the channels under collision-free conditions have been discussed. Parametric studies have been carried out on various design parameters like aspect ratio of channel, inter-channel separation, beam width and vertical distance from the source plane. The channels of different aspect ratio ranges from 0.4 to 1.2 have been chosen to get the uniform atom density distributions over the length of atomic beam. The higher aspect ratio channels have more divergence and they are placed at the middle whereas the lower aspect ratio channels are located the ends.

According to the design of atom source, the crucible lid of the vapor source was fabricated. The barium (Ba) granules were kept inside the crucible. It was heated by the resistively heating furnace. The barium vapors effused through the channels and made a long wedge-shaped atomic beam of length ~ 100 mm and width ~ 25 mm at the height of ~ 70 mm (i.e. laser-atom interaction region) from the crucible lid. To measure the average atom density inside the barium atomic beam, a sensor based on optical absorption technique has been developed where the barium hollow cathode lamp was used as the emission source. The sensor was integrated with the experimental chambers. The line of sight integrated barium atom density at their ground state was measured at different crucible temperatures. The measured values of atom density have been compared and validated with the values obtained from the theory. It was found that the atom density in

laser-atom interaction region was ~ 10^{17} m^{-3} at the highest temperature (~ 1000 K) of the above designed vapor source.

- **Kinetics of Two-Step Photoionization Method : Generation of Barium Photoplasma**

By shining laser pulses onto the collimated barium (Ba) atomic, the finite-sized photoplasma was produced inside the atomic beam through two-step photoionization method. In the first step, the Ba atoms got resonantly excited from their ground state ($6s_2$: $^1s_0$) to the intermediate excited state (6s6p: $^1p_1$) by 553.5 nm radiation. The resonant line was obtained from a tunable dye laser pumped by 532 nm radiation of Nd:YAG laser. In the second step, the excited atoms were subsequently ionized from their excited state (6s6p: $^1p_1$) to continuum by the 355 nm radiation of Nd: YAG laser. The two laser beams were propagated collinearly and overlapped with the atomic beam to generate the photoplasma. In experiments, all isotopes of barium were photoionized due to broad bandwidth of available lasers and the photoions were collected to the electrodes. The ion density of photoplasma was measured using the technique of total charge collection method. Thus the ionization yield of the process was measured from the ratio of photoions density to neutral atom density at the laser-atom interaction region.

To study the kinetics of two-step photoionization process in the optically thick atomic medium of barium and to estimate the ionization yield in the photoplasma study, a model based on rate equations has been developed. The absorption of exciting radiation has been taken into account along its propagation direction (optically thick). However, the medium has been assumed to be optically thin for the ionizing radiation. The rate equations are solved numerically to estimate the ionization yield for the time varying Gaussian shaped laser pulses. The required energy density of the laser pulse has been estimated to saturate the excitation transition throughout the thick atomic medium. The effect of the optical

delay between the laser beams on the ionization yield has been simulated. The calculated ionization yields from the simulations have been compared with the measured values in the experiments. They agree with the experiments within the errors. Thus the developed model has been validated.

- **Development of One Dimensional Plasma Model based on PIC Technique:**

The photoplasma has a finite-volume and it is transient in nature. To study its transient decay in the electromagnetic field, the mathematical problem consists of a set of equations has been formulated. A 1d model has been developed based on standard PIC technique. The photoplasma has been replaced by an equal number of both positive and negative charged super particles. The set of equations have been solved numerically to study the motion of super particles in one dimension (i.e. along the direction of electrostatic field). The computational volume (i.e. a linear box) is discretized by sets of uniformly spaced points known as grid points. Initially the particles are randomly distributed over the photoplasma volume. The charge density has been assigned to the grid points from their positions of the particles. The Poisson's equation has been solved to get the potential and electric fields at the grid points. The fields at grid points have been interpolated to get their values at the particle's position. The forces on the super particles have been estimated from the Lorentz equation. The velocity and position of the super particles have been calculated by solving Newton's equations. The iterative execution of the above steps self-consistently has computed the electric field and described the motion of the finite-width photoplasma in the external electromagnetic field. Thus a one dimensional fully kinetic model based on PIC (particle-in-cell) simulations been developed. This model has been used to study the decay of photoplasma in the electrostatic field.

- **Motion of Low-Density Photoplasma in Linear Electrostatic Potential Wells: Transition of Plasma Behaviors from Single Particle Motion to Collective Phenomena**

Though the plasma is a collection of charge particles, but it shows a complex behavior in the external electric field. It is completely different from that of a single charge particle. To understand the transition of the plasma behavior from its independent particle motion to its collective effect, the motion of a finite-sized low-density ($\sim 10^{13}$-10^{14} m^{-3}) photoplasma has been investigated in the linear electrostatic potential wells. For the low-density plasma ($\leq 3x10^{14}$ m^{-3}), all electrons are removed from the plasma by the external electric field, leaving behind a photoion bunch. The photoion bunch has been considered as a collection of non-interacting independent charge particles as the interactions among themselves are very less. The photoions move in the potential well and exhibit a damped oscillation in the current signal recorded on the grid electrode. The amplitude of oscillation decreases due to their absorption on the grid during their passage through the grid window. As the density of plasma increases, the interactions among charge particles become significant. Then the oscillation frequency is not only governed by the externally applied field but also by the internal field produced by space-charge interactions. The photoion bunch behaves differently from that of independent particle. As the plasma density further increases, the ensemble of charge particles exhibits the collective behavior governed by the space-charge interaction.

- **Decay of Photoplasma under External Electric Field : Investigation of various Physical Process**

The decay of the finite-sized photoplasma in an electrostatic electric field has been studied using one dimensional PIC (particle-in-cell) model. During its evolution, the various processes occurred along the direction of the electric field has been investigated.

The photoplasma has been evolved through a series of quasi-steady states. The mono-energetic electrons of the photoplasma get equilibrated through the electron-electron collisions within a few cycles of plasma oscillations. The mobile electrons fast response to the electric field. An electron sheath is formed between the anode and the photoplasma gap. The plasma is polarized in a fashion that it shields the external electric field to penetrate inside the plasma. The plasma-space-potential initially oscillates and attains a stable value close to the anode potential. The field over the plasma and the electron sheath region is negligible. The entire applied potential drops between the plasma and the cathode. The photoions at the plasma boundary move towards the cathode. They form a positive ion-sheath between the plasma and the cathode. The motion of photoions inside the sheath is governed by the space-charge limited Child-Langmuir law. The Child-Langmuir flux is supplied by the Bohm flux at the plasma-sheath boundary. The difference between them controls the movement of the plasma-sheath boundary. Towards the anode side, the photoions diffuse due to the ambipolar diffusion and the photoplasma expands towards the anode. During its decay the charge particles are collected on the boundaries i.e. cathode and anode. The plasma density decreases with time. At the low density, the photoplasma is unable to shield the applied external field. The charge particles are moved independently.

- **Evolution of Photoplasma in Electrostatic Ion-Extractor: Two Dimensional features of Plasma Motion**

The two dimensional evolution of barium photoplasma has been experimentally studied in an electrostatic ion-extractor, produced by parallel plate geometry. The various processes contributed to its evolution have been identified by measuring the current signal recorded on the electrodes and Faraday cups placed behind the electrodes. They are bulk plasma motion, free ambipolar diffusion, Coulomb repulsion, Child-Langmuir flux and bounded diffusion. Since the photoplasma is generated inside the atomic beam, it has a

bulk velocity in vertical direction. Due to its sharp density gradients at the plasma boundary, the plasma particles diffuse from its higher concentrated region to low density region. The diffusion process in plasma is known as ambipolar diffusion. In the vertical direction there is no boundary, the process is known as free diffusion where as in horizontal direction, the diffusion is called bounded diffusion. Due to collection of charge particles at the boundary, a sharp density gradient of plasma particles exists at the position of boundary. So the diffusion constant of bounded diffusion is relatively larger than the free diffusion. In presence of the electric field, the plasma electrons fast response to the electric field. A fraction of them gets removed from the photoplasma leaving behind an uncompensated positive charged cloud. The Photoplasma expands in radial direction due to Coulomb repulsion. Towards the cathode, the photoion sheath is formed. The motion of charge particles in the sheath is controlled by Child-Langmuir law. All above said processes are superimposed. Many of them are time variant. Their relative magnitudes depending upon the electrostatic field, plasma density and flow velocity, determine the spatial extent of the photoions in two dimensions. When the external field is dominant, the photoions are collected almost completely by the cathode with negligible loss. In such a case, the expansion of photoplasma can be considered to be one-dimensional. However at higher photoplasma density, the collective effects dominate and the various processes become comparable leading to 2D motion. This study quantifies the expansion dynamics of the photoplasma in the electrostatic field and the results are compared with 2D-PIC simulation.

9.2 Future Scope :

In the thesis, the generation of barium photoplasma and its evolutions in an electrostatic ion-extractor has been investigated in details. It has mainly described the various physical processes through which the transient photoplasma undergoes when it

evolves in an electrostatic electric field. The ion-extraction efficiency has been evaluated in the electrostatic ion-extractor. It has found that at very high plasma density (> 10^{16} m^{-3}), there is a difficulty to extract the photoions from the plasma to a particular location using the electrostatic field. The plasma shields the applied electric field within the length-scale of its Debye length. The external electric field could not penetrate inside the bulk plasma. So the photoions only at the plasma boundary are affected by the external electric field. As a result, the ion-extraction-efficiency decreases in case of high density plasma. The corresponding ion-extraction time increases. To improve the ion-collection-efficiency, it is proposed that future studies may concentrate on fast photoion extraction.

- Application of time varying electric field in radio frequency (RF) resonance method is a promising scheme to extract the photoions from the high density photoplasma. The RF field is to be applied along with the DC electrostatic field. The frequency of RF field will be chosen to excite an Eigen mode of the plasma wave in a low magnetic field. As a result, a large electric field penetrates inside the plasma. It aids to extract the photoions more efficiently. To include the magnetic field and the RF field in present experimental setup, the existing set-up is to be modified. A weak magnetic field (~ few tens of Gauss) is to be produced along the length of photoplasma. The RF field is to be applied along with the DC electric field to extract the photoions. The results may be compared with the electrostatic method of photoion extraction. It is expected that the RF based resonance method shall provide higher photoion extraction efficiency for ion density > 10^{16} m^{-3}.

  In high plasma density, the process like electron-ion recombination, resonance charge exchange and other collision effects play a significant role in the process of

ion-extraction. The contributions of the above process can be estimated from the numerical simulations and that is to be validated with the experiments.

- It has been discussed that the Bohm flux in the plasma region supplies the Child-Langmuir flux at the plasma sheath boundary during the decay of transient photoplasma. The Bohm flux depends on the electron temperature of the plasma. If the electron temperature increases, the ion-extraction will be faster for the high density plasma and the ion-collection time decreases. The electron temperature in the plasma could be increased by using the laser radiation of shorter wave length at the ionization step or plasma electron heating through radio frequency field during the process of ion-extraction. The use of 266 nm radiation i.e 4^{th} harmonic of commercial Nd:YAG laser to generate the barium photoplasma at the ionizing step will increase the electron temperature in barium photoplasma. The expected results are to be compared with the present analysis.
- In transient photoplasma study, the sheath physics plays an important role. It is necessary to understand the photoions' behaviors and their dynamics at the plasma-sheath region. Plasma diagnostics like laser based absorption technique where the resonant line of barium 493.5 nm or 455.4 nm radiations pass through the photoplasma, is to be used for detection of the photoions at the plasma-sheath region. It can be used to study the details of sheath dynamics. The laser photons interact with the photoions, a part of the incident laser intensity is absorbed by the photoions and the remaining fraction is transmitted through the plasma. By measuring the transmitted and incident intensities, the photoion density in the ground state is to be measured. Using this technique, the spatial and temporal evolutions of the photoplasma, the motion of the plasma sheath boundary are to be

investigated. The absorption set up is to be integrated with existing system and the experimental results may be compared with the present study.

- In large scale operations of laser based isotope separation or material purification process, the plant needs to be operated for a long durations to obtain weighable amount of interested isotope or material. For collection of the materials to a desired location in a continuous mode, the ambient temperature of the ion-extractor is to be kept at higher temperature than the melting point of the element. The photoions are extracted from the photoplasma, deposited on the extractor plate. As the deposited amounts increase, it forms droplet at the high temperature and will be collected at the desired location through liquid flow. When the ion-extractor is operated at the high temperature, the processes like thermionic emission from the hot electrode plate, re-evaporation of materials from the deposited electrode, application of high voltage on the electrodes, high temperature insulation etc play an important role along with the various processes discussed in this thesis.

Bibliography

Ambartzumian R. V. and Letokhov V. S. (1972), "Selective two step photoionization of atoms and photodissociation of molecules by laser radiation" *Applied Optics***, Vol. 11,** pp. 354-358.

Anisimov S. I. and Medvedev Y. V. (1990), "Decay of plasma cloud in electric field", *Physica Scripta*, Vol. 42, pp. 719-724.

Arisawa T., Maruyana Y., Suzuki Y. and Shiba K. (1982), "Lithium isotope separation by laser", *Appl. Phys. B***, vol. 28**, pp. 73-76.

Baird P. E. G., Brambley R. J., Burnett K., Stacey D. N., Warrington D. M. and Woodgate G. K. (1979), " Optical isotope shifts and Hyperfine structure in 553.5 nmm of barium", *Proc. R. Soc. Lond. A.* vol. 365, pp. 567-582.

Barin I.(1989), *Themochemical data for pure substances*, Verlagsgesellschaft Weinheim, Germany.

Barrett P. J. and Greaves R. G. (1989), "Double-plasma instability near the ion plasma frequency," *Phys. Fluids B*, vol. 1, pp. 1776-1179.

Bauman R. P. (1962) *Absorption spectroscopy*, NY: John Wiley & Sons.

Birdshall C. K. and Langdon A. B. (1985), *Plasma Physics Via Computer Simulation,* McGraw-Hill, New York.

Bittencourt J. A. (2004), *Fundamentals of plasma physics*, Springer-Verlag, New York.

Bokhan P. A., Buchanov V. V., Fateev N. V., Kalugin M. M., Kazaryan M. A., Prokhorov A. M., and Zakrevskii D. E. (2006) *Laser Isotope Separation in Atomic Vapor*, WILEY-VCH Verlag GmbH & Co. KGaA.

Chapra S. C. and Canale R. P. (2002), *Numerical methods for engineers,* Tata Mc.Graw. Hill Edition 2002, P-707.

Chen F. F. (1982), " Decay of a plasma created between negatively biased walls," *Phys. Fluids*, Vol. 25, pp. 2385- 2387.

Chen F. F. (1984), *Introduction to plasma physics and controlled fusion*, Plenum Press, New York.

Chen H. L. and Borzileri C. (1981), "Laser induced flurosence studies of UII produced by photoionization of uranium", *Journal of Chemical Physics*, Vol. 74, pp. 6063-6069.

Chen Y. W., Izawa Y., Nakai S. and Yamanaka C. (1995), "Analysis of laser beam propagation effects in atomic laser isotope separation", *Jpn. J. Appl. Phys*. Vol.**34**, pp. 504-509.

Clausing P.(1930), "Uber die strahlformung bei der molekularstromung" *Z. Physik* **,** Vol. 66, pp. 471-476.

Comte M., Graillot H. and Kupecek P. (1990), "Some aspects of propagation phenomena in an optically thick medium of two level atoms with a complementary leak transition from the upper state", *Optics Communications*, Vol. 79, pp**.** 235-240.

Demtroder W. (2002), *Laser spectroscopy* , Springer 3rd Edition.

Derzhiev V. I., Dyakin V. M., Il'kaev R. I., Mikhal'tsov L. A., Selemir V. D., Sidorov I. I., Tkachev A. N., Chaushanskii S. A. and Yakovlenko S. I. (2002), " Two-step photoionization of palladium", *Quan. Elect*. Vol. **32**, pp. 619-622.

Doneddu F. (1993), "Numerical experiments of ion extraction in laser separation using a particle-mesh simulation",*SPIE*, Vol.1859, pp. 98-106.

Dudley J. M, Harvey J. D. and Leonhardt R. (1993), "Coherent pulse propagation in a mode-locked argon laser", *J. Opt. Soc. Am. B* , vol. **10,** pp. 840-851.

Dumont A. M., Abrassart A. and Collin S. (2000), "A code for optically thick and hot photoionized media", *Astron. Astrophys*. Vol.**357**,pp. 823-838.

Fedoseyev V. N., Huber G., Koster U., Lettry J., Mishin V. I., Ravn H., Sebastian V. and the ISOLDE Collaboration. (2000), "The ISOLADE laser ion source for exotic nuclei", *Hyperfine Interactions*, Vol. 127, pp. 409-416.

Fedosseev V. N., Kudryavtsev Y.and Mishin V. I. (2012), " Resonance laser ionization of atoms for nuclear physics", *Physica Scripta*, Vol. 85, p. 058104.

Furtlehner J. P., Blanchet A. and Leloutre B. (1994), "Electron temperature measurement of Ba photoplasma by using an electrostatic probe", *Review of Scientific Instruments*, Vol. 65, pp. 2984-2990.

Giordmaine J. A. and Wang T. C. (1960), "Molecular beam formation by long parallel tubes", *J. App. Phys*. Vol. **31**, pp. 463-471.

Golyatina R. I., Sytsko Y. I. and Yakovlenko S. I. (1998), "On ion extraction from a low-density plasma through grid meshes," *Laser Physics*, Vol. 8, pp. 860-863.

Greenland P. T. (1990), "Laser isotope separation" ,*Contemporary Physics,* vol. **31, pp.** 405-424.

Hasegawa HS., Takei M., Suzuki A. And Kurosawa H. (2001). "Influence of charge exchange on the collection of the laser produced ions", *Journal of Applied Physics*., Vol. **90**, pp. 5878-5883.

Hazak G., Gell Y., Boneh Y. and Goshen S. (1980), "Fast ion extraction in laser isotope separation", *Journal of Applied Physics*., Vol. **51**, pp. 5207-5211.

Hockney R. W. and Eastwood J. W. (1981), *Computer simulation using particles*, McGraw-Hill, New York.

Ishikawa T., Kawakami H. and Mori, H. (1997), "Laser purification of metals (I); high Rydberg states of Ni, Ag, and Pd", *Nuclear Instruments and Methods in Physics Research Section B: Beam Interactions with Materials and Atoms*, Vol. 121, pp. 437-441.

Johst K. and Johansen H. (1989), "Resonant two-step photoionization of molecules: Effects of pulse sequence, pulse duration and delay time of two lasers on ionization probability and selectivity", *Appl. Phys. B*, vol. 48, pp. 479-484.

Kalyar M. A., Rafiq H., Haq S. and Baig M. A. (2007), "Absolute photoionization cross section from the 6s6p $^{1,3}P_1$ excited states of barium", *J. Phys. B, vol.* **40**, pp.2307-2319.

Karlov N. V. , krynetskii B. B., Mishin V. A., Prokhorov A. M, Savelev A. D. and Smirnov V. V.(1977), "Isotope separation of some rare-earth elements by two step photoionization", *Optics Communication* **, Vol. 21**, pp.384-286.

Killian T. C. (2007), "Ultra-cold neutral plasma", *Science* Vol. 316, pp. 705-708.

Killian T. C., Kulin S., Bergeson S. D., Orozco L. A., Orzel C. and Rolston S. L. (1999), "Creation of an ultra-cold neutral plasma", *Physical Review Letters*, Vol. 83, pp. 4776-4779.

Klimouskii I. I., Minaev P. V. and Morozov A. V. (1981), "Measurement of the probabilities of forbidden radiative transition in the barium atom", *Optics and Spectroscopy*. Vol. **50**, pp. 464-467.

Klose J. H., Fuhr J. R. and Wiese W. L. (2002), "Critically evaluated atomic transition probabilities for Ba I and Ba II", *J. Phys. Chem. Ref. Data*. Vol. **31**, pp. 217-230.

Knudsen M. (1909), " Die molekularstromung der gase durch offnungen und die effusion ", *Annln. Phys*., Vol. 28, pp. 75.

Kulin S., Killian T. C., Bergeson S. D. and Rolston S. L. (2000), "Plasma oscillations and expansion of an ultra-cold neutral plasma", *Physical review Letters*, Vol. 85, pp. 318-321.

Kurosawa H., Hasegawa S and Suzuki A. (2001), "Plasma potential in the presence of an external electric field" *Journal of Applied Physics*., Vol. **90**, pp. 3713-3719.

Kurosawa H., Hasegawa S and Suzuki A. (2002), "Ion extraction from a laser ionized plasma produced between parallel plate cathodes and an anode above them" *Journal of Applied Physics*., Vol. **91**, pp. 4818-4823.

Langmuir I. (1928), "Oscillations in ionized gases", *Proc. N. A. S*., Vol. 14, pp. 627-637.

Latuszynski A. and Raiko V. I. (1975), "Studies of the ion source with surface-volume ionization", *Nucl. Instr. Meth*, Vol. 125, pp. 61-66.

Lederer C. M., Hollander J. M. and Perlman I. (1967), *Tables of isotopes*, 6th edition, Wiley, New York.

Letokhov V. S. (1987) *Laser Photoionization Spectroscopy*, Academic, New York.

Letokhov V. S., Mishin, V. I. and Puretzky A. A.(1977), "Selective photoionization of atoms by laser radiation and its applications", *Progress in Quantum Electronics*, Vol. **5**, pp.139-203.

Lieberman M. A. And Lichtenberg A. J. (1994), *Principles of Plasma Discharges and Materials Processing*, John Wiley & Sons, Inc., New York.

Litvinov I. I. (1997), "Theory of ion extraction from plasma by an external electric field in systems of laser isotope separation" , *Journal of Russian Laser Research*, Vol. **8**, pp. 87-99.

Majumder A., Mago V. K., Kathar P. T. and Das A. K. (2003), "Oscillations of low–

density barium photoplasma in electric field," *J. Appl. Phys*., vol. 94, pp.7044-7049.

Majumder A, Mago V. K., Ray A. K. Kathar P. T. And Das A. K. (2005), "Generation of low density plasma by two-step photoionization method of barium and its evolution in electric field", Appl. Phys. B, Vol.81, pp. 669-674.

Majumder A., Jana B., Kathar P. T., Das K. K. and Mago V. K. (2008), "Two-dimensional expansion of finite-size barium photoplasma in an electrostatic field", *Physics of Plasma*, Vol. 15, pp. 12350508.

Majumder A. Jana B., Kathar P. T. Das A. K. and Mago V. K. (2009), "Generation og a longwedge shaped barium atomic beam and its density characterization", *Vacuum*, Vol 83, pp. 989-995.

Marsh B. A. (2014), "Resonance ionization laser ion sources for online isotope separators", *Review of Scientific Instruments*, Vol. 85, p. 02B923.

Maruyama Y., Suzuki Y., Arisawa T. and Shiba K. (1987), "Laser isotope separation of titanium by two step photoionization", *Appl. Phys. B* , vol.44, pp.163-166.

Marzevet S., Collins L. A., Kress J.D. (2002), "Evolution of ultra-cold neutral plasmas", *Physical Review Letters*, Voll. 88, p. 55001.

Matsui K., Tsuchida K., Tsuda S., Suzuki K. and Shoji T. (1997a), "Ion extraction from plasma by using a radio frequency resonant electric field", Physics of Plasma, Vol. 3, pp. 4367-4375.

Matsui K., Tsuchida K., Tsuda S., Suzuki K. and Shoji T. (1997b), "Ion extraction characteristics from photoionized plasma by radio frequency resonant method", *Journal of Nuclear Science and Technology,* Vol. 34, pp. 923-929.

McCavet P. and Trefftz E. (1974), "Oscilator strengths of some Ba lines, calculated in MCHF approximation", *J. Phys. B*, vol. 7, pp.1270-1278.

Miles B. M. and Wiese W. L. (1969), "Critical evaluation of transition probabilities", *Atomic Data*, Vol. **1**, pp. 1-17.

Miller C. M. and Nogar N. S. (1983), "Calculation of ion yields in atomic multiphoton ionization spectroscopy", *Anal. Chem*. Vol. **55,** pp. 481-488.

Milonni P. W. and Eberly J. H.(1988), *Lasers,* Wiley, New York.

Mitchel A. and Zemansky M. (1971), *Resonance Radiation and Excited atoms,* Cambridge University press.

Moore I. D., Nieminen A., Billowes J., Champbell P., Geppert Ch., Jokinen A., Kessler T., Marsh B., Penttila H., Rinta Antila S., Tordoff B., Wendt K. D. A. and Aysto J. (2005), " Development of laser ion source at IGISOL", *Journal of Physics G: Nuclear and particle physics,* Vol. 31, pp. S1499- S1502.

Mori H. (1998), "Laser purification of Ag using a time-division collection method", *Applied Physics Letters,* Vol. 72, pp. 1948-1950.

Mori H., Ishikawa T. and Kawakami H. (1997), "Laser purification of metals (II); Purification of Ni and Ag", *Nuclear Instuments and Methods in Physics Research Section B: Beam Interactions with Matterials and Atoms,* Vol. 121, pp. 442-445.

Murakami M. and Nishihara K. (1993), "Sheath dynamics induced by ion-acoustic rarefaction wave", *Phys. Fluids B,* Vol. **5**, pp. 3441-3446.

Niggli S. and Huber M. C. E. (1987), "Transition probabilities in neutral barium", *Phys. Rev. A* , vol. 35, pp. 2908-2918.

Nishio R., Yamada K. Suzuki K. and Wakabayshi M. (1995), "Ion transport from laser induced metal plasma to ion extraction electrodes", *Journal of Nuclear Science and Technology,* Vol. 32, pp. 180-190.

Nygaard K. J., Corbin R. J. and Jones Jones J. D.(1978), "Two step photoionization of potassium atoms", *Phys. Rev. A* , vol. 17,pp.1543-1544.

Ogura K., Arisawa T. and Shibata T. (1992), "Ion collection from laser induced plasma using positively biased wire electrode", *Japanese Journal of Applied Physics,* Vol. 31, pp.1485-1490.

Ogura K., Kaburaki H. and Shibata T. (1993), "Two-dimensional numerical simulation of ion collection from pulsed laser induced plasma", *Journal of Nuclear Science and Technology,* Vol. 30, pp. 1248-1255.

Ogura K. and Shibata T. (1994), "Initial plasma density dependence of kinetic energy of ions collected on electrode", *Japanese Journal of Applied Physics,* Vol. 33, pp.131-134.

Okano K. (1992), “Theory of ion-extraction time from a plasma by a static electric field”, *Journal of Nuclear Science and Technology,* Vol. 29, pp. 601- 607.

Opsal R. B., Owens K. G. and Reilly J. P. (1985), “Resolution in linear TOF massspectrometer,” *Anal. Chem*. Vol. 57, pp. 1884-1889.

Paisner, J. (1988), “Atomic vapor laser isotope separation”, *Applied Physics B: Laser and Optics*, Vol. 46, pp. 253-260.

Patel K. (1989), “particle simulation of a two dimensional electrostatic plasma’, BARC report-1489, Mumbai, India.

Patel K. and Mago V. K.(1995), “ Two-dimensional particle simulation of plasma expansion Between plane parallel electrodes,” *Journal of Applied Physics s.* Vol.78, pp. 4371-4381.

Patel K. (1997), “Observation of ion waves in two dimensional particle simulation of field assisted plasma expansion”, *Journal of Applied Physics s.* Vol.81, pp. 6622-6634.

Peng X. L., Curry J. J. Lister G. G. and Lawler J. E.(2002), “Radiometric efficiency of low pressure barium discharges”, J. Appl. Phys, Vol. 91, pp. 1761-1771.

Piel A. Klostermann H , Rohde A., Jelic N. and Schrittwieser R. W. (1996), “Ion sheath oscillatios in double plasma machines,” *Phys. Lett. A*, vol. 216, pp.296-302.

Rohde A., Klostermann H. and Piel A. (1997),“Particle-in–cell simulatio of grid sheath oscillations in a double plasma device,” *IEEE Trans. Plasma Sci.*, vol.25, pp.1144-1149.

Rosengard A. (1989), “Three dimensional freejet flow from a finite length slit”, 16th rare field gas dynamics conf (AIAA). pp. 312-326.

Ruster W, Ames. F, Kluge H. J., Otten E. W., Rehklau D., Scheerer F., Herrmann G. Muhleck C., Riegel J., Rimke H., Sattelberger P., Trautmann N. (1989), “A resonance ionization mass spectrometer as an analytical instrument for trace analysis”, *Nuclear Instruments and Methods in Physics Research,* Vol. 281A, pp. 547-558.

Savelev V. V. And Yakovlenko S. I. (1997), “Passage of a low density plasma through transparent grids”, *Quantum Electronics*, Vol. 27, pp. 913-917.

Scoles G. (1988), *Atomic and Molecular Beam Method*, Vol. 1, chapter 4, Oxford University Press.

Sheridan T. E. (1997), "Model for ion oscillations at negatively–biased grid," *Phys. Lett. A*, vol.235, pp.253-258.

Siemien C. E., Chen Y. C., Gupta P., Laha S., Martinez Y. N., Michelson P. G., Nagel S. B. and Killian T. C. (2004), "Using absorption imaging to study ion dynamics in an ultra-cold neutral plasma", *Physical Review Letters*, Vol. 92,p. 143001.

Silfvast W. T. (1998), *Laser fundamentals*, Cambridge University press, 1st edition, P-103.

Smoluchowski V. M. (1910), "To the kinetic theory of transpiration and diffusion of dilute gases" Ann. d. Phys. Vol. 33, pp. 1559-1570.

Spangenberg K. R. (1948), *Vacuum Tubes* , Mcgraw-Hill Book Company, Inc. New York.

Tkachev A. N. And Yakovlenko S. I. (1993), "Coulomb explosion of a laser plasma", *Quantum Electron*, Vol. 23, pp. 972-974.

Tuccio S. A., Dubrin J. W, Peterson O. G. and Snavely B. B. (1974) " Two step selective photoionization of 235U in uranium vapor", *IEEE J. Quantum Electronics, (Q-*10), pp. 790.

Vitello P., Cerjan C.and Braun D. (1992), " Flow: A two-dimensional time dependent hydrodynamical ion extraction model,", *Physics of Fluids. B* Vol. 4, pp. 1447-1456.

Watanabe J. and Okano K. (1993), "Particle simulation of the ion-extraction process from a plasma by a static electric field", *Phys. Fluids B*, Vol. 5, pp. 3092-3096.

Yamada K., Tetsuka T. and Deguchi Y. (1990), " Ion extraction characteristics by an electric field on laser produced barium plasma" , Journal of applied physics, Vol. **67**, pp. 6734-6739.

Yamada K., Tetsuka T. and Deguchi Y. (1991a), "New scaling relation for ion extraction by external electric field on a barium plasma produced between parallel-plate electrodes", Journal of applied physics, Vol. **69**, pp. 6962-6967.

Yamada K., Tetsuka T. And Deguchi Y.(1991b), "Ion extraction characteristics on a

barium plasma produced between grounded plate electrodes nad a positively biased upper electrode", *Journal of Applied Physics*., Vol. 6**9**, pp. 8064-8071.

Yamada K., Okada H., Tetsuka T. and Yoshioka K. (1993), "Ion behavior in photoionization plasma originating from one-directional atomic vapor flow under external electric field", *Journal of Nuclear Science and Technology*, Vol. .30, pp. 143-153.

Yamada K. and Ozaki N.(1988), " Separation of barium isotopes by selective two step photoionization process", *J. Nucl. Sci. Technol*., vol.**25,** pp. 641-648.

Zhidkov A. G. (1998), "Simulation of ion extraction from laser-induced plasma by electromagnetic fields", Physics of Plasma

Abstract of Publications in International reviewed Journals

Eur. Phys. J. D (2015) 69: 62
DOI: 10.1140/epjd/e2015-50276-8

THE EUROPEAN PHYSICAL JOURNAL D

Regular Article

Decay of a finite-sized transient photoplasma in an electrostatic field

Biswajit Jana[a], Abhinandan Majumder, Kiran B. Thakur, and Ashoka K. Das

Laser & Plasma Technology Division, Bhabha Atomic Research Centre, Trombay, Mumbai 400085, India

Received 2 April 2014 / Received in final form 29 November 2014
Published online 6 March 2015 – © EDP Sciences, Società Italiana di Fisica, Springer-Verlag 2015

Abstract. Photoplasma is produced through multi-step resonant photoionization method by shining the laser pulses onto a collimated atomic beam. It has finite size having a sharp density gradient at its boundary. It is created within the duration of laser pulse (~10 ns) while it lasts for few tens of micro-seconds. During its decay in an external electrostatic field, the photoplasma passes through various physical phenomena happened along the direction of the electric field. The transient responses of photoplasma to the external electric field and its temporal evolutions are studied using a one dimensional model based on standard particle-in-cell (PIC) technique. The various processes like relaxation of mono-energetic electrons, spatial and temporal variations in plasma potential, plasma-sheath formation, charge particles distribution near the plasma-sheath boundary, motion of plasma-sheath boundary, expansion of the finite-width photoplasma and collections of charge particles at the boundaries (i.e. electrodes) are investigated and discussed.

IOP Publishing — Measurement Science and Technology
Meas. Sci. Technol. **25** (2014) 015003 (9pp) — doi:10.1088/0957-0233/25/1/015003

Measurement of photoionization yield in low-density barium photoplasma study

B Jana[1], P T Kathar, A Majumder, K B Thakur and A K Das

Laser and Plasma Technology Division, Bhabha Atomic Research Centre, Trombay, Mumbai 400 085, India

E-mail: biswajit@barc.gov.in

Received 28 May 2013, in final form 5 October 2013
Published 26 November 2013

Abstract
A finite-sized barium (Ba) photoplasma is generated through a two-step resonant photoionization method by shining laser pulses onto an atomic beam of Ba. The photoionization yield is estimated from the ratio of photoion density to neutral atom density measured in the laser–atom interaction region. The neutral atom density in the atomic beam is measured by an optical absorption technique where a Ba hollow cathode lamp (Ba-HCL) is used as an emission source. Since the photoplasma has a finite volume and it is pulsed in nature, the photoion density in the photoplasma is estimated through the collection of charge from the photoplasma. The measured ionization yield is compared with the calculated value that is obtained from an in-house developed code. It is observed that the values are in good agreement.

Keywords: photoionization yield, photoplasma, optical absorption method, hollow cathode lamp, electrostatic ion-extractor

(Some figures may appear in colour only in the online journal)

Abstract of Publications in International reviewed Journals

REVIEW OF SCIENTIFIC INSTRUMENTS **84**, 106113 (2013)

Note: Design principles of a linear array multi-channel effusive metal-vapor atom source

B. Jana,[a] A. Majumder, K. B. Thakur, and A. K. Das
Laser and Plasma Technology Division, Bhabha Atomic Research Centre, Trombay, Mumbai 400 085, India

(Received 17 July 2013; accepted 2 October 2013; published online 29 October 2013)

Atomic beams can easily be produced by allowing atoms to effuse through a channel. In an earlier investigation [A. Majumder *et al.*, Vacuum **83**, 989 (2009)], we had designed, fabricated, and characterized an effusive metal-vapor source using collinear-array of multi-channel. In this note, we describe the theoretical basis of designing the source. Atom density in atomic beam has been estimated using a set of analytical expressions for long-channel operated in transparent mode. Parametric studies on aspect ratio of channel, inter-channel separation, beam width, and vertical distance from the source are carried out. They are useful in providing physical picture and optimizing design parameters. © *2013 AIP Publishing LLC*. [http://dx.doi.org/10.1063/1.4825343]

Motion of Finite-Sized Low-Density Photoion Bunch in Electrostatic Potential Wells

B. Jana, A. Majumder, P. T. Kathar, A. K. Das, and V. K. Mago

***Abstract*—A finite-sized low-density photoplasma is produced by a two-step resonant photoionization method. Its density is varied in the range of $\sim (10^7-10^9)$ cm^{-3}. The motion of photoplasma is studied in a linear electrostatic potential well that is created by plate–grid–plate geometry. To understand its dynamics, a 1-D particle-in-cell model has been developed. For density range $\sim (1 \times 10^7-5 \times 10^8)$ cm^{-3}, an electric field $\leq$100 V/cm is sufficient to remove all the electrons from the photoplasma within a time of few nanoseconds, leaving behind an ion bunch. When a photoion bunch evolves in a potential well, a damped oscillation is observed on the current signal recorded on a grid electrode. The structure is explained by single-particle behavior of the photoion bunch. For densities $> 3 \times 10^8$ cm^{-3}, the oscillation frequency depends on both externally applied electric field and internal field that is produced by space-charge interactions among charge particles. This is because, at higher densities, collective behavior dominates and the dynamics is governed by space-charge interactions.**

***Index Terms*—Electrostatic potential well, particle-in-cell (PIC) simulation, photoplasma.**

etry [14], [15] were studied. In PGP geometry, different biasing configurations were created to control the ion motion. The use of grid (meshed electrode)-type geometry is also found in time-of-flight mass spectrometer [16], double-plasma device [17], [18], and vacuum Tube like triode. To know the basic characteristics of photoplasma, a potential well is formed using PGP geometry. When the photoplasma evolves in the electrostatic potential well, it shows an oscillatory behavior such as classical periodic motion. The oscillation is governed by the strength of both externally applied field and the internal field produced by space charge. The ion oscillation at negatively biased grid and corresponding sheath dynamics play an important role in the behavior of double-plasma machines [19], [20].

In this paper, we discuss the evolution of finite-sized low-density photoplasma in electrostatic potential well created by PGP geometry. A 1-D particle-in-cell (1-D-PIC) code is developed to understand photoplasma dynamics. In the external field, the electrons are removed from the plasma and an ion

Abstract of Publications in International reviewed Journals

Appl Phys B
DOI 10.1007/s00340-010-4194-4

Applied Physics B
Lasers and Optics

Ionization yield of two-step photoionization process in an optically thick atomic medium of barium

B. Jana · A. Majumder · P.T. Kathar · A.K. Das · V.K. Mago

Received: 7 May 2010 / Revised version: 21 July 2010

Abstract The kinetics of a two-step photoionization process in optically thick atomic medium of barium (Ba) is studied using the rate equation approach. In the first step, Ba atoms get resonantly excited by laser radiation from their ground state to an intermediate excited state and subsequently are ionized in the second step by another laser radiation. The absorption of exciting radiation is taken into account along its propagation direction (optically thick). However, the medium is assumed to be optically thin for the ionizing radiation. A numerical simulation is done to estimate the ionization yield for time-varying Gaussian shaped laser pulses. The required energy density of the laser pulse to saturate the excitation transition throughout the thick medium is calculated. The effect of optical delay between the laser beams on the ionization yield is simulated. The calculated ionization yield from the simulation is compared with the measured values.

excites an electron in an atom from an initial ground state to an intermediate excited state. Secondly, other photons, collisions or an electric field causes ionization of the excited atoms. So the RIS is a multi-step photon absorption process in which the final state is ionization continuum of an atom resulting in creation of an ion-electron pair from each atom. This enables the RIS technique [1, 2] to be highly sensitive (single atom/molecule detection) and extremely selective (10^{10}–10^{20}). The RIS has widespread application in isotope separation [3] and metal purification [4] etc. It also makes it possible to measure on-line isotope shifts and hyperfine structures of short-lived radioactive isotopes. This generates knowledge of nuclear properties (nuclear spin, magnetic and quadrupole moment) of elements [5].

Two-step photoionization is the simplest of the multi-step photoionization schemes involving the excitation of a resonant intermediate electronic state and the subsequent ionization of the excited atom. It can be achieved using two different lasers, which simultaneously provide the advantages

PHYSICS OF PLASMAS **15**, 123508 (2008)

Two-dimensional expansion of finite-size barium photoplasma in an electrostatic field

A. Majumder, B. Jana, P. T. Kathar, A. K. Das, and V. K. Mago
Laser and Plasma Technology Division, Bhabha Atomic Research Centre, Trombay, Mumbai 400085, India

(Received 24 July 2008; accepted 21 November 2008; published online 22 December 2008)

Two-dimensional evolution of finite-size barium photoplasma, produced using multistep-resonant ionization is experimentally investigated in an externally applied electrostatic field. Several processes like bulk motion, ambipolar diffusion, Coulomb repulsion, Child–Langmuir flux, bounded diffusion, etc. that contribute to its expansion, have been identified. They are quantified with the help of signals recorded by Faraday cups, electrodes and plates and by two-dimensional particle-in-cell simulation. These processes are superimposed and their relative magnitudes decide the evolution of the photoions. When external field is dominant, a significant fraction of ions reach the cathode with negligible vertical spread and the plasma motion can be considered as one-dimensional. However, when plasma collective effects are dominant, then the different mechanisms become comparable and the photoplasma expands in two dimensions. The spread of photoions at different locations in parallel plate geometry is determined as a function of plasma density and compared with simulation. © *2008 American Institute of Physics*.
[DOI: 10.1063/1.3050059]